Doctoral Thesis

Kristian Etienne Einarsrud

ISBN 978-82-471-3699-7
ISBN 978-82-471-3700-0
ISSN 1503-8181

Doctoral theses at NTNU, 2012:201

Kristian Etienne Einarsrud

A Treatise on Interpolar Transport Phenomena

NTNU
Norwegian University of Science and Technology
Thesis for the degree of Philosophiae Doctor
Faculty of Engineering Science and Technology
Department of Energy and Process Engineering

Doctoral theses at NTNU, 2012:201

NTNU

NTNU – Trondheim
Norwegian University of
Science and Technology

NTNU – Trondheim
Norwegian University of
Science and Technology

Kristian Etienne Einarsrud

A Treatise on Interpolar Transport Phenomena

Thesis for the degree of philosophiae doctor

Trondheim, May 2012

Norwegian University of Science and Technology
Faculty of Engineering Science and Technology
Department of Energy and Process Engineering

NTNU – Trondheim
Norwegian University of
Science and Technology

NTNU
Norwegian University of Science and Technology

Thesis for the degree of philosophiae doctor

Faculty of Engineering Science and Technology
Department of Energy and Process Engineering

ISBN 978-82-471-3699-7 (printed version)
ISBN 978-82-471-3700-0 (electronic version)
ISSN 1503-8181

Doctoral Theses at NTNU, 2012:201

Printed by Skipnes Kommunikasjon as

Dedicated to the light at the end of the tunnel.

Abstract

This thesis contributes to the understanding of mechanisms for mass transport in aluminium electrolysis cells. Fundamental studies are undertaken of flow patterns and mass transport in the interpolar region under various operating conditions. A coupled model predicting the turbulent electrolyte flow, under the influence of both electromagnetism and forces from buoyant gas bubbles, crucial for better prediction of mass transfer mechanisms and voltage oscillations, has been developed from first principles. The model is validated against experiments performed on a lab scale electrolysis cell. Both modelling and experiments are performed within the scope of this thesis.

Experiments on lab- and industrial scale cells have been conducted in order to study the behaviour of anodic gas bubbles under various operating conditions. On industrial scale, bubble related signals show typical frequencies in the range 0.5 to 2 Hz, with amplitudes up to $\pm 5\%$ around the mean voltage. Results indicate that the bubble related voltage oscillations increase in both frequency and magnitude with increasing anode age, the latter of which due to the diminishing influence of slots. No significant correlation between anode pairs is identified, suggesting that models treating individual anodes are meaningful also on an industrial scale.

Due to challenges related to multiple simultaneous phenomena occurring on industrial scales, a series of lab scale measurements have been performed, in order to obtain quantitative data for model validation. The lab scale experimental cell allowed for different current densities, interpolar distances and inclination angles, thus spanning ranges typically encountered on the industrial scale. Lab scale frequencies are found to be in the range 0.25 to 0.65 Hz, with magnitude of up to $\pm 4\%$ around the mean voltage. The magnitude of the oscillations decreases with increasing anode age, due to increased rounding of the initially sharp anode edges.

The traditional voltage measurements have been supplied with high-speed video recordings of the bath surface showing a good correspondence between voltage fluctuations and escaping gas bubbles. On average, 0.5 and 2 bubbles were observed per second on lab and industrial scales, respectively, significantly higher than frequencies obtained by a FFT of the voltage signal. It is shown that this discrepancy can be due to large variations in the bubble release times, thus violating the assumption of a periodic signal required for an FFT. For industrial anodes, the possibility of overlapping bubbles is investigated as an alternative effect resulting in the mismatch between observed and calculated frequencies.

A phenomenological, coupled, model for the creation and transport of anodic gas bubbles is developed from first principles. The proposed model is a multiscale approach in which molecular species are produced by Faraday's law and transported by diffusion and advection through a supersaturated electrolyte. Sub grid bubbles are allowed to form through nucleation on the anode surface and the resulting bubble population evolves through mass transfer and coalescence. As sub grid bubbles reach a certain size they are transferred

to a macroscopic phase which evolution is governed by the volume of fluid method, thus allowing for the treatment of complex bubble topology.

The model is validated against results from the lab scale experiments in a 2D model, showing that essential features of the voltage signal can be reproduced by the proposed approach. The influence of various parameters such as bath properties, anode microstructure and mass transfer properties are investigated by means of a factorial design analysis. The factorial design indicates that the contact angle, Sherwood number (and molecular diffusivity) and the porosity of the anode that have the most significant influence on the frequencies of the resulting bubble induced voltage fluctuations. Furthermore, resulting frequencies appear to be dominated by these selected factors, as coupling is present only at low significance. Considering the amplitude of the signal, the dominating factors are the bath viscosity, contact angle and pore diameter. Although the influence of these factors is large, significant coupling between factors is observed, indicating that the physics determining the amplitude of the signal is of a more complex nature than that of the frequencies. The mean voltage is relatively insensitive to the factors studied in this analysis.

Simulations are able to reproduce the essential behaviour found experimentally on the lab scale cell, that is: increasing frequencies with increasing current densities and anode inclination, increasing amplitudes with decreasing anode inclination and increasing current densities and finally increasing mean voltages with increasing ACD and current density.

Considering individual bubbles, the influence of electromagnetic forces is small when compared to other forces such as buoyancy and surface tension. However, when considering the system as a whole, the Lorentz forces are found to yield enhanced gas departure rates due to favourable pressure gradients in the bath. This feature is necessarily enhanced further by the significantly elevated current densities found in the proximity of large bubbles, as the influence of the Lorentz forces is found to increase with increasing current densities.

Simulations indicate that steady state bubble production on the anode does not imply a direct transfer of all the molecular gas to bubbles. Instead, a balance between bubble production and transport by diffusion and advection away from the anode appears to describe this state, resulting in a CO_2 supersaturated region greatly extending the bubble layer. The presence of a CO_2 enriched region yields a possible explanation to the observed reduction of current efficiency if the anode-cathode distance is reduced beyond a critical limit.

Preface

This thesis is submitted to the Norwegian University of Science and Technology (NTNU) for partial fulfilment of the requirements for the degree of philosophiae doctor.

The doctoral work has been performed at the Department of Energy and Process Engineering, NTNU, Trondheim, between August 2008 and May 2012 under the supervision of Professors Stein Tore Johansen and Iver H. Brevik.

Much of the work presented in this thesis had not been as successful without the collaboration with and initiatives taken by other research groups. The primary collaborators and initiators have been Drs. Ingo Eick and Nancy Jorunn Holt at Hydro Aluminium, Primary Metal Technology, Dr. Eirik Manger at Acona Flow Technology, and Asbjørn Solheim and Egil Skybakmoen at SINTEF Materials and Chemistry.

The present work was financed by Hydro Aluminium, Primary Metal Technology with support from the Research Council of Norway, through the project "Process Innovations for High Current Densities" (PI-HCD).

Acknowledgements

As four years of intensive research comes to an end, it becomes evident that the progress made would not have been possible without the encouragement and support from my supervisors, fellow researchers, colleagues, relatives and friends.

First and foremost, I would like to thank my supervisors, Professors Stein Tore Johansen and Iver H. Brevik, for their engagement, fruitful discussions and guidance during my work. Their recommendations, revisions and suggestions to increase the scientific level of my work has been truly invaluable during the years we have worked together. I would also like to thank them for their trust in me to pursue my own ideas and thoughts. I am truly honoured to have had the opportunity to have supervisors with such a deep knowledge, understanding and intuition of the physical world. I look forward to further joint scientific adventures in the future!

My involvement towards aluminium and Hydro had probably not occurred, had it not been for Dr. Eirik Manger who in autumn 2007 asked me "why I wasn't already recruited". I would like to thank him for giving me this opportunity, making the arrangements prior to the onset of the PhD, his interest in my research and for his revisions of central parts of my work.

This project had not been possible without the generous grant given by Hydro Aluminium Primary Metal Technology, with support from the Research Council of Norway, through the Process Innovations for High Current Density (PI-HCD) project, for which I am deeply thankful.

Within Hydro, I would like to thank the project manager Dr. Nancy Jorunn Holt for taking interest in my work, introducing me to other researchers in Hydro and for arranging workshops and seminars from which I have had great benefit. I would also like to thank Drs. Espen Sandnes and Arne Klaveness (formerly in Hydro) for interesting discussions and assistance with experiments and modelling, respectively. Lastly, I would like to express my extended gratitude to Dr. Ingo Eick for his engagement and enthusiasm, his arrangements during the workshops in Neuss, his revisions of my work and for giving me the opportunity to participate in the lab scale experiments. Much of the progress presented in this thesis had not been possible without his efforts.

Parts of the work presented in this thesis, especially the experiments, has been in close collaboration with SINTEF Materials and Chemistry. I would like to thank everyone in the group for making me feel welcome and for guiding me whenever I had questions. An extended acknowledgement goes to Asbjørn Solheim and Egil Skybakmoen for their assistance during the experiments, sharing good ideas and for their good company during our travels.

Over the last four years, one year has been spent on teaching duties at the Department of Energy and Process Engineering. Thanks to the Professors at the department, Lars

Sætran, Tor Ytrehus, Reidar Kristoffersen, Bernhard Müller and Helge Andersson, I have had the opportunity to do meaningful things at times when my research gave none. I would also like to thank my former students for asking good questions, inspiring me to go deeper into matters which I thought I had already understood.

The administration at the department, Gerd Randi, Ingrid, Wenche, Nina, Anita and Gunnhild, are acknowledged for always being helpful with any non-academic issue I might have had. Special thanks also to Eugen Uthaug for all his efforts to provide me with stable and reliable hardware to perform the simulations presented in this thesis.

Besides the academic and administrative staff at the department, I would like to thank my fellow PhD students (former students for some), Simen, Joris, Claudio, Jan Fredrik, Michael, Ignat, Luca, Fabio and many more for countless lunch and coffee breaks as well as joint ventures into more applied branches of fluid mechanics. When research doesn't converge, it always helps to relax. A special thanks to Simen, whom I have had the pleasure of sharing an office with during my PhD, for all the interesting discussions we have had, ranging from corridor cricket to quantum mechanics, and for showing me the wonders of vector graphics.

Outside the safe walls of the university, I would like to thank all my friends, near and far, for support and initiating all sorts of activities allowing me to take my mind off working. If you are reading these lines, and we have shared a glass or two, it is very likely that this paragraph is for you. A special thanks to *Tirsdagsklubben* for taking such good care of me during my long long distance relationship year.

I would not be here at all had it not been for my dear family, always supporting me and showing interest in my work and well-being. A special thanks to my parents, Aline and Terje, my sister Ingrid and Mamie, for raising me well and always encouraging me. I would also like to thank my aunt and uncle, Mari-Ann and Jon, for being my reserve parents in Trondheim.

Finally, the deepest gratitude to Marthe, the moon of my life, for shining a light for me in hours where I could not see and for giving me something to look forward to every day, evening, night and morning for the past years, and many more to come.

Contents

List of Tables

List of Figures

Chapter 1

Introduction

1.1 On the production of aluminium

Today more aluminium is produced than all other non-ferrous metals combined (IAI [54]). Due to attractive properties such as low weight and nearly 100% recyclability, the aluminium industry has grown to an international multibillion business since the discovery of the element some 200 years ago. The production of primary aluminium is carried out in aluminium reduction cells by the Hall-Héroult process, named after its inventors who, independently of each other, in 1886 developed and patented an electrolytic process by which alumina (Al_2O_3) is dissolved in an electrolyte consisting mainly of molten cryolite (Na_3AlF_6) (Thonstad et al. [116]). The Hall-Héroult process is the only method by which aluminium is produced industrially today and according to Thonstad et al. [116], no other process appears to threaten its position for the next twenty years. A sketch of a Hall-Héroult electrolysis cell is given in figure 1.1.

In the Hall-Héroult process, cryolite acts as a dissolvent for alumina, yielding complex ions of oxide and aluminium. By passing an electrical current through the system, positive complexes are transported to the negative electrode (the cathode) where they are reduced whereas negative complexes are transported to the positive electrode (the anode) where they are oxidized. The anode is made of carbon, which when reacting with oxide containing complexes yields carbon dioxide.

The net reaction in the Hall-Héroult cell can thus be written as

$$\frac{1}{2}\mathrm{Al_2O_{3,d}} + \frac{3}{4}\mathrm{C}_s \rightarrow \mathrm{Al}_l + \frac{3}{4}\mathrm{CO_{2,g}}, \tag{1.1}$$

where s , l and g represent solid, liquid and gaseous phases of state, and d represents dissolved species. By means of gravity, liquid aluminium, which in general is denser than the cryolite bath, remains in the lower regions of the cell, forming an interface between the electrolyte and liquid metal as sketched in figure 1.1. The produced gas is lighter than the

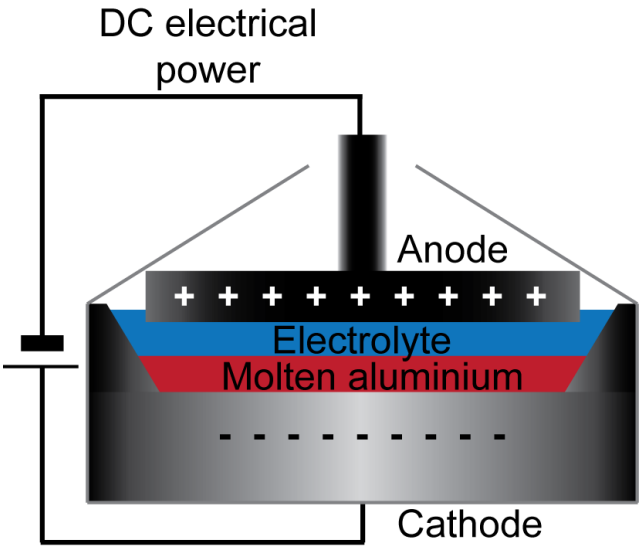

Figure 1.1: Sketch of the Hall-Héroult process. The figure shows an industrial reduction cell consisting of an anode, a cathode and an electrolyte (bath). Electrochemical reactions of the raw-material (alumina) occur within the electrolyte yielding liquid aluminium. The cell is powered by an external DC energy source.

other phases, and is set in motion due to buoyancy. The motion of gas bubbles induces a flow field in the cell, as gas is evolved and escapes through a side channel at the anode edge.

A higher current flow in the cell means that more electrons will be passing through it at any given moment. This implies a higher reaction rate at the electrodes and thus a greater number of moles of product. High current cells are thus sought by the aluminium industry in order to increase productivity.

The energy necessary to produce aluminium is one of the main factors when evaluating the economy of the total process (Thonstad et al. [116]). The specific electric energy consumption, W_{el}, is typically given as

$$W_{el} \propto \frac{U}{\chi_{Al}}, \tag{1.2}$$

where U is the cell voltage and χ_{Al} is the corresponding current efficiency fraction[1], with respect to aluminium. As equation 1.2 shows, the energy consumption can be reduced either by a reduction in cell voltage, or by an increase in current efficiency. Considering a simple Ohmic law for the system

$$U = RI, \tag{1.3}$$

[1]The current efficiency is the ratio of produced aluminium to the (ideal) value predicted by Faraday's laws.

where R is the resistance of the cell and I is the electrical current, it is obvious that an increased amperage will *increase* the cell voltage U, and thus energy consumption, if the resistance is kept constant.

Cell resistance can be reduced by decreasing the distance between anode and cathode (the interpolar region), as the main contribution to resistance is due to the cryolite bath. However, a direct reduction of the interpolar distance can have negative consequences for the current efficiency.

In commercial aluminium reduction cells waves and disturbances of the bath-metal interface, especially vertical oscillations, have a great influence on efficiency (Tang et al. [114] and Bearne et al. [4]). The influence of the interpolar region upon current efficiency has been studied by several authors, cf. Grjotheim et al. [44], Fellner et al. [37] and Alcorn et al. [101], showing how current efficiency drops abruptly if the interpolar regions becomes smaller than a certain value, thus increasing energy consumption. This effect is explained by means of the so-called back-reaction, which can occur if molten aluminium comes in contact with CO_2, which is produced at the anode.

Another important point related to the cell voltage is the contribution to the electrical conductivity from the (essentially) non-conductive gaseous bubbles, effectively screening the active anode area and increasing the cell voltage (cf. Cooksey et al. [21]) and consequently increasing the energy consumption by as much as 10%.

According to Grjotheim and Kvande [47], energy costs have increased more than other manufacturing costs since 1973 and for most smelters in the world, energy is neither cheap nor plentiful. Thus, in order to improve existing designs with respect to energy efficiency, detailed knowledge of the physics governing the flow in the interpolar region is imperative, motivating the present work.

1.2 Modelling the Hall-Héroult process

The large scale motion of the bath and molten aluminium is due to the joint effect of buoyant bubbles and so called Lorentz-forces, arising from the electrical currents passing through the cell and its surroundings. Thus, the Hall-Héroult cell can essentially be described as a turbulent, magnetohydrodynamic three-phase system where complex chemical reactions occur. Combined with the dynamical nature of the governing phenomena and strong dependence upon cell geometry, it is evident that the Hall-Héroult cell is a highly complex system to study. Because of the harsh environment of a Hall-Héroult cell, quantitative experimental data of relevant phenomena are not easily obtained. One thus relies upon extensive modelling to describe the system.

Broadly speaking, the system can be divided into four sub-systems, each of these being governed by

- Chemical reactions (CH)
- Electromagnetism (EM)
- Thermodynamics (TD)
- Hydrodynamics (HD)

Furthermore, the dynamic nature of the boundaries of the system yields an additional sub-system to be studied, the nature of which necessarily is inherently coupled to the other four. This inherent coupling between phenomena yields an additional level of complexity to the system, as it a priori is difficult to determine to what degree phenomena can decouple. The coupling between the five described sub-systems is shown schematically in figure 1.2.

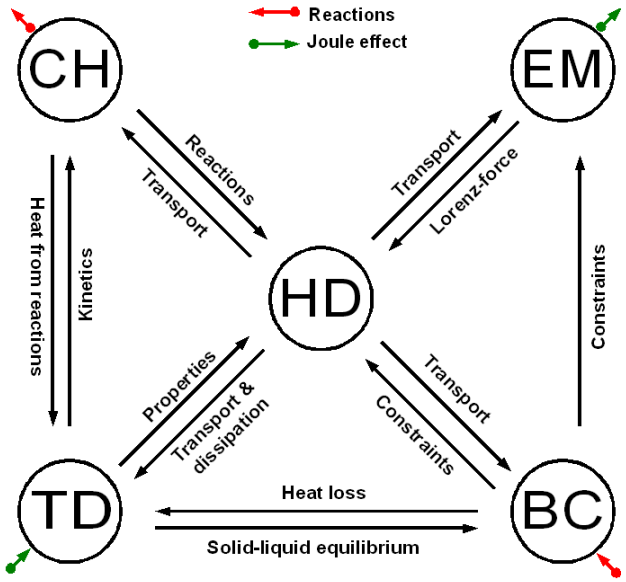

Figure 1.2: Principal coupling diagram. The figure sketches the coupling between different phenomena in Hall-Héroult cells; chemical reactions (CH), electromagnetism (EM), boundary conditions (BC), thermodynamics (TD) and hydrodynamics (HD) for the Hall-Héroult cell. Diagonally opposite systems (i.e. TD-EM and CH-BC) are coupled via the Joule effect (green arrow) and chemical reactions (red arrow), respectively.

Practical models are often based on judicious decoupling of some parts of the physics, treating these as separate phenomena. The importance of this uncoupling can be checked and rectified to some extent a posterior (Evans and Ziegler [36]).

The focus of this thesis will be on the computation of the coupled bubble driven magneto-hydrodynamic system in a nontrivial geometry. Due to the importance of hydrodynamics, determining the overall mass- and heat transfer processes, it is evident that a model which

combines the electrolyte flow and resulting transport mechanisms is of fundamental interest.

1.3 Significance

Increasing the knowledge of transport phenomena in the Hall-Héroult cell by advanced numerical techniques will be decisive for further improvements of the process. This thesis will aid to identify state of the art models and algorithms and determine whether or not these can be coupled to describe the process as a whole.

The vision is that this thesis will contribute to the fundamental knowledge of transport processes in the Hall-Héroult cell in such a way that future design choices, and current operational decisions, are taken in such a way that the aluminium industry can contribute further to a sustainable future.

The thesis is multidisciplinary, as it involves scientific computing, fluid dynamics, electromagnetism, non-equilibrium thermodynamics and experimental work.

1.4 Objectives and scope

The main goal of this thesis is to simulate transport processes in the Hall-Héroult cell using advanced numerical techniques in order to obtain a deeper fundamental knowledge of the process. The basis for these simulations are the Navier-Stokes equations. As the problem is multiphase by nature, multiphase modelling will be of major concern.

The hydrodynamic model will be restricted to the incompressible case with simplified species transport, in which thermoelectric effects and detailed treatment of chemistry is neglected. Furthermore, the outer boundaries of the system will be assumed to be fixed for each case considered. The influence of different (fixed) geometries will however be considered. Finally, most physical properties such as density, solubility, viscosity etc. are assumed to be constant for a given simulation, in order to isolate the influence of the phenomena of interest.

As the large scale dynamics in the Hall-Héroult cell arise mainly due to buoyant gas bubbles and Lorentz forces, these phenomena will be studied in detail, especially concerning bubble generation and evolution.

As experimental measurements are crucial to validate essential parts of the model, new experiments will be performed within the scope of the thesis. Due to time limitations, the main focus of the thesis will however be on modelling and simulations, and not on the experiments.

The main objectives of the thesis are

- To present a review of the current knowledge and possible modelling approaches.
- To obtain quantitative data regarding bubble evolution on lab and industrial scales.
- To develop a framework for the treatment of electromagnetic forces in Hall-Héroult cells.
- To develop and validate a framework for the treatment of anodic gas bubbles.
- To investigate the effect of bubbles and electromagnetic forces in Hall-Héroult cells.

1.5 Research method

The model of hydrodynamics in the Hall-Héroult cell is based on the 2D/3D incompressible Navier-Stokes equations. Due to the complexity of the system and high degree of coupling, numerical simulations are sought rather than simplified analytical solutions, an approach denoted as Computational Fluid Dynamics (CFD) .

There are several ways to obtain a numerical simulation for a given fluid flow. One possibility is to develop an entirely new code, often combined with multipurpose software such as for instance MATLAB [80]. This strategy is of often adopted by researchers focusing on the development of discretization methods, new solution algorithms or the study of convergence.

For simulating the Hall-Héroult process, the software should, as a minimum, be able to handle

- Complex geometries.
- Transient phenomena.
- Multiphase flows.
- Turbulence.

In addition, suitable post-processing tools are required in order to visualize the results. Needless to say, the development of a new code covering all the above points in addition to the study of new phenomena is neither feasible within the allocated time, nor required, as several software packages such as openFOAM [88], COMSOL [20] and ANSYS FLUENT [1] already exist and have been extensively used and validated for many CFD applications.

Due to previous experience and the ability to include additional models through user defined subroutines, scalar fields and functions, the commercial CFD package ANSYS FLUENT [1] is used throughout this thesis. The multiphase nature of the flow will be treated by means of the Volume of Fluid (VOF) method, allowing for direct simulations

of interfacial behaviour, rather than relying upon empirical exchange laws required for alternative multiphase models.

The default models available in FLUENT will be extended through the development of models treating electromagnetism and evolution of bubbles. In order to keep the formalism on a comprehensible level, the models for each of the two phenomena are developed in a modular fashion, allowing for coupled simulations only where required. Furthermore, the modular approach allows for simple integration of further extensions, such as for instance heat balance calculations, if required. Finally, the modular approach allows for extensive verification of each sub-routine before a complete validation is performed.

Validation is performed with comparison to existing numerical results and/or experimental data where these exist. As gas evolution is of a major concern in the current thesis, new experiments based on optical methods and voltage measurements are performed in order to yield further means for validation.

1.6 Organization of thesis

This thesis is organized in the following five parts:

Part I: Background and Theory This part gives an introduction to the five nodes shown in the principal coupling diagram. Heat balance is considered to be outside the scope of the current work, so the discussion related to thermodynamics is restricted only to kinetics. Finally, a review of previous modelling approaches and experimental results is given.

Part II: Experimental work This part describes the setup and results from experiments related to gas bubble evolution on industrial- and lab scale electrolysis cells. Lab scale results are used extensively for the validation of the bubble evolution model presented in Part IV.

Part III: Electromagnetism This part gives an extensive introduction to various electromagnetic approaches. Following the introduction, various case studies are presented in order to verify the features of the proposed model. Results from this part are used further in Part IV.

Part IV: Gas generation and evolution of bubbles This part describes the underlying theory for a multiscale approach for the treatment of anodic bubbles. Following the theoretical part, verification and validation studies are presented. Validation is performed by comparison to lab scale experiments presented in Part II.

Part V: Concluding remarks and issues for further work The final part of the thesis provides general conclusions from the previous parts and describes points relevant for future research.

Each of the above parts begins with a brief outline and description of following chapters. Following main part of the thesis, a list of references and an appendix is given.

1.7 List of publications

This thesis is organized as a monograph. Parts of the thesis have been published at international conferences and peer reviewed journals. The papers with a brief outline as well as an explanation of the co-authors' role is given in the following. In all the below papers, professors Stein Tore Johansen and Iver H. Brevik have contributed with initiating ideas, support, recommendations and suggestions to increase the scientific level of the publications.

1.7.1 Primary publications

[35]: K. E. Einarsrud and E. Sandnes (2011). Anodic Voltage Oscillations in Hall-Héroult Cells. Light Metals, pages 555–560.

This paper describes experiments on lab- and industrial scale cells in order to study the behaviour of anodic gas bubbles under various operating conditions. Traditional voltage measurements have been supplied with high-speed video recordings of the bath surface showing a good correspondence between voltage fluctuations and escaping gas bubbles. For industrial anodes, the possibility of overlapping bubbles is investigated.

The first author (Kristian Etienne Einarsrud) planned and performed the experiments together with E. Sandnes, evaluated and analysed the results, wrote the paper and submitted it to TMS2011, where he gave a presentation of the findings.

[32]: K. E. Einarsrud and S. T. Johansen. On the Modelling of Anodic Bubbles in Hall-Héroult cells (2011). Proceedings of the 8th Int. Conf. on CFD in Oil & Gas, Metallurgical and Process Industries, SINTEF/NTNU, Trondheim, Norway.

This paper describes a new approach to the modelling of gas evolving anodes in the production of primary aluminium, based on a multiscale approach. A preliminary verification study is presented, showing the potential of the suggested approach.

The first author (Kristian Etienne Einarsrud) developed and wrote the model, planned and performed simulations, wrote the paper and submitted it to CFD2011, where he gave a presentation of the findings.

[29]: I. Eick, A. Klaveness, C. Rosenkilde, M. Segatz, H. Gudbrandsen, A. Solheim, E. Skybakmoen and K. E. Einarsrud (2011). Voltage and Bubble Release Behaviour in a Laboratory Cell at Low Anode-Cathode Distance. In: Proceedings of the 10th AASTC, Launceston, Tasmania.

This paper describes the bubble release and overvoltage in a laboratory cell setup. By means of video equipment, bubbles escaping from the anode where recorded in parallel to voltage measurements, allowing for additional interpretation of the bubble release behaviour.

The current author (Kristian Etienne Einarsrud) participated in all the measurements and performed high speed video recordings of the bath surface in order to study bubble release behaviour and was involved in the interpretation of the results. The final section of the paper ("Bubble release") was written by the current author.

[33]: K. E. Einarsrud and S T. Johansen (2012). Modelling of bubble behaviour in aluminium reduction cells. Progress in Computational Fluid Dynamics, Vol. 12:2/3, pages 119-130.

This paper is an extension of publication [32], where the influence of the various parameters of the model is investigated by means of factorial analysis. Based on the parameters investigated, it is found that the supersaturation concentration and pore density of the anode contribute significantly to gas evolution.

The first author (Kristian Etienne Einarsrud) developed and wrote the model, planned and performed simulations, wrote the paper and submitted it to Progress in Computational Fluid Dynamics.

[34]: K. E. Einarsrud, S. T. Johansen and I. Eick (2012). Anodic bubble behaviour in Hall-Héroult cells. Light Metals, pages 875–880.

This paper is an extension of publication [33], where the influence of Lorentz forces are investigated. Lorentz forces are found to have an increasing importance with increasing current densities, increasing the mean bubble release frequencies due to favourable pressure gradients arising in regions with several bubbles.

The first author (Kristian Etienne Einarsrud) developed and wrote the model, planned and performed simulations, wrote the paper and submitted it to TMS2012, where he gave a presentation of the findings.

1.7.2 Secondary publication

[31]: K. E. Einarsrud (2010). The effect of detaching bubbles on aluminium-cryolite interfaces: An experimental and numerical study. Metallurgical and Materials Transactions B, Vol. 41:3, pages 560-573.

This paper is an extension of the authors Master's Thesis [30]. Using dimensional analysis it is found that similarity could be claimed for the original experimental setup for the ranges studied. Furthermore, an extension to 3D allowed for an explanation of discrepancies found in the 2D simulations performed in [30].

Part I: Background and Theory

Outline of Part I

Part I of this thesis describes the background and selected theoretical issues relevant to the Hall-Héroult process, and thus serves as an extensive review. It is divided into six chapters which cover:

- Introduction to hydrodynamics and multiphase flows.
- Introduction to CFD.
- Introduction to electromagnetism.
- Kinetics and chemical reactions.
- Typical boundaries and properties of the Hall-Héroult cell.
- Review of mathematical and physical modelling.

In addition to the review, this part thus treats the five nodes shown in the principal coupling diagram, figure 1.2, with the exception of heat balance calculations, which details are outside the current scope.

Part I includes several figures and graphs of data found elsewhere in the literature which have been digitally re-mastered for use in this thesis. The original source of the figure (or data, where applicable) is referenced in the caption of the corresponding figure as "..as of Author [reference]".

Chapter 2

Introduction to hydrodynamics

The governing equations for a general fluid flow are the equation of continuity (mass conservation), the Navier-Stokes equations (momentum conservation) and the energy equation (conservation of energy). An excellent derivation of and introduction to these equations can be found in for instance Oertel [86], while more advanced subjects can be found in for instance Landau and Lifshitz [71]. Considering a Newtonian fluid with density ρ and constant viscosity μ, the equation of continuity is given as

$$\frac{\partial \rho}{\partial t} + \nabla \cdot \rho \boldsymbol{u} = 0, \tag{2.1}$$

while the Navier-Stokes equations take the form

$$\frac{\partial}{\partial t}\left(\rho \boldsymbol{u}\right) + \nabla\left(\rho \boldsymbol{u}\boldsymbol{u}\right) = -\nabla p + \mu \nabla^2 \boldsymbol{u} + \boldsymbol{f}, \tag{2.2}$$

where $\boldsymbol{u}$ and p represent velocity and pressure fields, respectively, and $\boldsymbol{f}$ represents external force densities. For the Hall-Héroult cell, the principal external force densities are gravity and Lorentz forces (equation 4.3), that is

$$\boldsymbol{f} = \rho \boldsymbol{g} + \boldsymbol{f}_L = \rho \boldsymbol{g} + \boldsymbol{j} \times \boldsymbol{B}. \tag{2.3}$$

The Hall-Héroult cell consists of different phases, meaning that the above (single phase) equations must be modified if the multiphase nature of the cell is to be captured. The following sections give an introduction to multiphase flows and flows containing species. Parts of the following sections are based on previous work [30], but are included here for completeness. The energy quation is not treated, as heat balances are considered to be outside the current scope.

2.1 Multiphase flows

Multiphase flows occur frequently in nature. The word *phase* is to be understood in a thermodynamic sense, being a solid, liquid or gas like state that can occur simultaneously in one- or multicomponent systems (Oertel [86]). Multiphase flows can fundamentally be described in two different ways. One approach is to describe the multiphase flow as a continuum where the different constituents form a perfect mixture. Modelling these systems is straight forward, as the equations basically are reduced to single phase equations, where the single phase now has the properties of the mixture. These models are useful if the large scale behaviour of the multiphase flow is to be described. However, these mixed fluid models fail to describe the dynamics between the phases, as the interactions are "mixed out". Such interactions must thus be introduced by some suitable sub-model.

The motion of each phase can also be described separately with a coupling term between phases. This approach is frequently referred to as a two-fluid model (or more generally an N-fluid model). The two-fluid models are useful if the interactions between the phases are of special importance, for instance if mass transfer is present due to dissolution. Besides the fact that N-fluid models have N times more equations to solve than the mixed fluid equations, they are necessarily more complex as they need sub-models to describe the interaction between phases.

Micro structural and interaction effects complicate the theory of multiphase flows to an almost overwhelming level. In order to simplify the formalism, the presence of more than one phase is modelled with the concept of phase fractions (Drew [28]). Definitions vary in the literature, but one intuitive definition is

$$\alpha_k \equiv \frac{V_k}{V} \tag{2.4}$$

which states that the phase fraction of the k-th phase is the total volume, V_k, occupied by this phase divided by the total volume, V. The phase fraction can in other words be interpreted as a relative volumetric fraction. The concept is easily understood from two-phase flow in a pipe of unit volume $\pi r^2 dz$ as shown in figure 2.1.

In the geometry of figure 2.1, the phase fractions are found to be

$$\alpha_g = \frac{V_g}{V} = \frac{A_g dz}{A dz} = \frac{A_g}{A_g + A_l} \tag{2.5}$$

and equivalently

$$\alpha_l = \frac{V_l}{V} = \frac{A_l}{A_g + A_l}, \tag{2.6}$$

where indices g and l represent the gas and liquid phase, respectively. For simple geometries or two-dimensional systems, the void fraction can thus be interpreted as the relative area fraction. The phase fraction is subject to the constraint

$$\sum_k \alpha_k = 1, \tag{2.7}$$

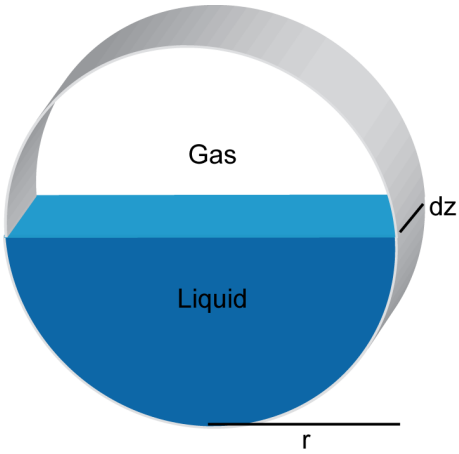

Figure 2.1: Two phase flow (stratified flow) through a pipe of radius r and length dz.

where the sum is taken over all phases present.

2.1.1 The N-fluid model

Interpreting the phase fraction as a weighting function between phases, it is possible to formulate a set of transport equations for the system, analogous to the transport equations for a single phase fluid. Details of the derivation can be found in for instance Drew and Passmann ([28]), and only key results are presented here.

The mass balance equation of the k-th phase can be expressed as

$$\frac{\partial(\alpha_k \rho_k)}{\partial t} + \nabla \cdot (\alpha_k \rho_k \boldsymbol{u}_k) = \dot{R}_k. \tag{2.8}$$

where $\boldsymbol{u}_k$ represents the velocity and $\dot{R}_k$ is the rate of production of component k per unit volume, due to phase changes or chemical reactions. For a system consisting of N phases, $N-1$ equations on the form of equation 2.8 are solved, the final phase fraction being governed by the constraint given in equation 2.7.

The Navier-Stokes equations of the k-th phase can be expressed as

$$\frac{\partial(\alpha_k \rho_k \boldsymbol{u}_k)}{\partial t} + \nabla \cdot (\alpha_k \rho_k \boldsymbol{u}_k \boldsymbol{u}_k) = \dot{R}_k \boldsymbol{u}_{ki} + \nabla \cdot (\alpha_k \boldsymbol{T}_k) + \alpha_k \boldsymbol{f}_k + \boldsymbol{M}_{ki}, \tag{2.9}$$

where $\boldsymbol{M}_{ki}$ is the force per volume acting on the k-th phase due to interactions with other phases and $\dot{R}_k \boldsymbol{u}_{ki}$ is a momentum source due to mass sources. The velocity $\boldsymbol{u}_{ki}$ represents the velocity at the interface at which mass transfer occurs. Finally, $\boldsymbol{T}_k$ represents the stress tensor acting on the phase in question, i.e. pressure and viscous stresses. One momentum

equation on the form of equation 2.9 must be solved for each of the phases, yielding a total of $4N - 1$ equations for the system as a whole.

In addition to involving all the complexity related to solving the full Navier-Stokes equations, an N-fluid model necessarily involves constitutive relations in order to describe interactions between phases. For the momentum equations, this could for instance be done by introducing a Drift Flux model (cf. Brennen [10] chapter 14) to treat momentum exchange between phases. Constitutive relations rely to some degree on empirism and/or idealizations, for instance assuming spherical particles in order to obtain a simplified drag law.

2.1.2 The mixture model

An alternative to the N-fluid models is the mixed fluid model, motivated by the fact that the complicated *internal* interactions should cancel when considering the fluid as a mixture of the phases present. The mixed fluid model is obtained by using the following averaging convention from Drew and Passmann [28]

$$\rho = \sum_k \rho_k, \tag{2.10}$$

$$\rho \boldsymbol{u} = \sum_k \alpha_k \rho_k \boldsymbol{u_k}, \tag{2.11}$$

$$\boldsymbol{T} - \rho \boldsymbol{u}\boldsymbol{u} = \sum_k \alpha_k \boldsymbol{T} - \alpha_k \rho_k \boldsymbol{u}_k \boldsymbol{u}_k \tag{2.12}$$

and

$$\boldsymbol{f} = \sum_k \alpha_k \boldsymbol{f}_k. \tag{2.13}$$

The assumption of cancelling internal interactions yields

$$\sum_k \dot{R}_k = 0 \tag{2.14}$$

and

$$\sum_k \boldsymbol{M}_k + \dot{R}_k \boldsymbol{u}_{ki} = 0 \tag{2.15}$$

Summation over the k phases in equations 2.8 and 2.9 results in

$$\frac{\partial \rho}{\partial t} + \nabla \cdot \rho \boldsymbol{u} = 0 \tag{2.16}$$

and

$$\frac{\partial \rho \boldsymbol{u}}{\partial t} + \nabla \cdot \rho \boldsymbol{u}\boldsymbol{u} = \nabla \cdot \boldsymbol{T} + \boldsymbol{f}. \tag{2.17}$$

The mixed fluid equations are analogous to the classical Navier-Stokes equations for single phase flows, differing only in the physical meaning of the properties, representing average values of all phases present in the mixed fluid formalism.

As the name suggests, the mixed fluid formalism is especially useful in systems where mixing of phases is significant or in cases where a gross balance is needed. However, by definition, internal interactions cancel, yielding the full mixed formalism unsuitable if such interactions are of interest.

2.1.3 The VOF model

In order to avoid the somewhat complex N-fluid model described previously, but still be able to differentiate between phases, a compromise is met by means of the Volume of Fluid method, first introduced by Hirt and Nichols [50]. The VOF model is designed for free-surface and interface tracking between two or more immiscible fluids. As for the mixture model a single set of momentum equations is solved and a special routine is used to compute the shape of the interface (Troshko and Mohan [121]). In the VOF formalism the calculation of momentum exchange is based on first principles, i.e. the actual flow field around some immersed body, and constitutive momentum exchange laws are thus not necessary.

The fields for all variables and properties are *shared* by the phases and represent volume-averaged values as long as the phase fraction, α_k, is known at each location. Variables and properties in any given control volume are thus purely representative for one phase or for a mixture of phases.

Phase fraction equation

In the VOF-formalism, the phase fraction is used as a weighting function when determining average fluid properties. Given some fluid property, ψ_k of the k-th phase, the volume average of this property, ψ, is given by the sum[1]

$$\psi = \sum_{k=1}^{N} \alpha_k \psi_k \tag{2.18}$$

where the sum is to be taken over the N phases present in the volume. The phase fraction α_k is determined from the transport equation

$$\frac{\partial}{\partial t}(\alpha_k \rho_k) + \nabla \cdot (\alpha_k \rho_k \boldsymbol{u}) = \dot{R}_k, \tag{2.19}$$

analogous to the N-fluid model.

[1]Provided that arithmetic averaging is applicable.

Momentum equation

The momentum equation of the VOF model is equivalent to that of the mixture model. Assuming that the mixed flow field is incompressible, the incompressible continuity equation must be satisfied by the flow field, i.e. the following constraint must be met:

$$\nabla \cdot \boldsymbol{u} = 0. \tag{2.20}$$

Under this assumption, the VOF momentum equation is reduced to

$$\frac{\partial}{\partial t}\left(\rho u_i\right) + \frac{\partial}{\partial x_j}\left(\rho u_j u_i\right) = -\frac{\partial}{\partial x_i}p + \frac{\partial}{\partial x_j}\left(\mu \frac{\partial u_i}{\partial x_j}\right) + f_i, \tag{2.21}$$

for the i-th momentum component. The momentum equation (shared by all phases) is dependent on the phase fractions of all present phases through the (volume averaged) properties ρ and μ, defined by equation 2.18.

The main challenge of the VOF method is that of representing interfaces in an adequate way. This can be considered to be a numerical issue, and is treated further in chapter 3.

2.1.4 Euler-Lagrange models

An alternative to the mixture model, allowing for phase interaction, denoted the Euler-Lagrange model has been developed and extensively used for dispersed or particulate flows. An introduction to this formalism can be found in Johansen et al. [56] and further topics are treated in Clift et al. [19].

The momentum equation for the *fluid* is in the Euler-Lagrange formalism obtained by a *volume* averaging of the momentum equation over a domain containing particulates. Letting $\langle \ldots \rangle$ denote volume averaged fields in a volume V, the resulting momentum equation is

$$\frac{\partial}{\partial t}\left(\alpha_f \rho_f \left\langle \boldsymbol{u}_f \right\rangle^i\right) + \nabla \cdot \left(\alpha_f \rho_f \left\langle \boldsymbol{u}_f \right\rangle^i \left\langle \boldsymbol{u}_f \right\rangle^i\right) = \alpha_f \boldsymbol{f}_f - \nabla \cdot \left\langle \boldsymbol{T} \right\rangle^i - \frac{1}{V}\sum_{p \in V} \boldsymbol{F}_I, \tag{2.22}$$

where index f refers to fluid properties and

$$\boldsymbol{F}_I = \int_{A_p} \boldsymbol{T} \cdot \boldsymbol{n}_p dA, \tag{2.23}$$

is a fluid-particulate interaction force for a particulate with area A_p and normal vector $\boldsymbol{n}_p$. The final term on the right hand side of equation 2.22 is the sum over all particles present in the volume V.

Several models exist for the fluid-particulate forces, covering for instance

- Drag forces.
- Virtual mass and Basset forces.
- Pressure forces.
- Lift forces.

As the name suggests, particulates are in this formalism treated in a Lagrangian framework, i.e. their motion is governed by (the classical form of) Newton's 2nd law. Thus, the velocity of a particle with mass m_p is determined by

$$m_p \frac{d\boldsymbol{u}_p}{dt} = \boldsymbol{F}_I + V_p \boldsymbol{f}_p, \tag{2.24}$$

which is solved for each individual particle, resulting in particle streamlines as time evolves.

Depending upon features such as for instance particulate phase fraction, Lagrangian models can be one-, two- or four-way coupled. One-way coupling (valid for low particulate phase fractions) signifies that that the influence from the particles on the fluid can be neglected, opposed to a two-way coupling where such effects are important. Four-way coupling implies that particle-particle interactions are important.

As for the N-fluid model, the Lagrangian models necessarily involves constitutive relations in order to describe the particle-fluid interactions, often involving simplifying assumptions such as spherical particles.

2.2 Flows containing species

The final class of multiphase models involves the treatment of species. As details regarding chemistry (and thus also species transport) is beyond the scope of this thesis, only a simplified treatment is given here. Detailed descriptions are found in for instance Bird et al. [6].

Considering a concentration C_i, the mass conservation of species can be written as

$$\frac{\partial C_i}{\partial t} + \nabla \cdot (C_i \boldsymbol{u}_i) = \dot{R}_i, \tag{2.25}$$

where $\boldsymbol{u}_i$ is the velocity and $\dot{R}_i$ is the production rate of species i. The computation of each of the i-th velocity is a task with challenges similar to those related to the N-fluid model. In order to simplify the formalism, the i-th velocity is assumed to be given by the *fluid* velocity, $\boldsymbol{u}$, and some drift velocity $\delta\boldsymbol{u}_i$:

$$\boldsymbol{u}_i = \boldsymbol{u} + \delta\boldsymbol{u}_i, \tag{2.26}$$

so that the mass balance can be written as

$$\frac{\partial C_i}{\partial t} + \nabla \cdot (C_i \boldsymbol{u}) + \nabla \cdot (C_i \delta \boldsymbol{u}_i) = \dot{R}_i. \tag{2.27}$$

The final term on the left hand side can be interpreted as the divergence of a diffusive mass flux vector

$$\boldsymbol{J}_i = C_i \delta \boldsymbol{u}_i, \tag{2.28}$$

resulting in

$$\frac{\partial C_i}{\partial t} + \nabla \cdot (C_i \boldsymbol{u}) + \nabla \cdot \boldsymbol{J}_i = \dot{R}_i. \tag{2.29}$$

The mass diffusion flux can be arbitrarily complex and is in principle dependent upon gradients of *all* fields present (cf. Callen [13]). The formalism can however be simplified, assuming a generalized Fick's law,

$$\boldsymbol{J}_i = -\mathcal{D}_{i,eff} \nabla C_i, \tag{2.30}$$

stating that the mass flux is proportional to the gradient in concentration, the factor of proportionality being the effective diffusivity $\mathcal{D}_{eff}$. The above assumption results in an advection-diffusion equation for the i-th species concentration,

$$\frac{\partial C_i}{\partial t} + \nabla \cdot (C_i \boldsymbol{u}) - \nabla \cdot \mathcal{D}_{i,eff} \nabla C_i = \dot{R}_i, \tag{2.31}$$

which serves as a basis for species transport in the current work.

2.3 Turbulence

Turbulent phenomena are readily observed in Hall-Héroult cells (cf. for instance Dernedde and Cambridge [25], Tørklep et al. [119], Bilek et al. [5]) and needs to be modelled in order to capture the important features of the flow. A brief discussion of turbulence modelling is given in the following. Extensive treatments of turbulence modelling can be found in for instance Tennekes and Lumley [115] and Davidson [24].

The $k - \epsilon$ model has previously been successfully adopted by several authors in the field (Solheim et al. [111], Hua and Wang [52], Doheim et al. [26]) and is the standard approach for turbulence modelling in many industrial applications. The basic idea behind the $k - \epsilon$ model is that of eddy viscosity. In brief, this simply asserts that, as far as the mean flow (i.e. the flow field where turbulence is averaged out) is concerned, the net effect of turbulence is to increase the molecular viscosity and replace it with a larger "eddy viscosity" (Davidson [24]).

Due to turbulence, the molecular viscosity μ in the momentum equation is substituted for an effective viscosity, μ_{eff}, given by:

$$\mu_{eff} = \mu + \mu_t, \tag{2.32}$$

where μ_t is the eddy viscosity defined by

$$\mu_t = C_\mu \frac{\rho k^2}{\epsilon} \tag{2.33}$$

where k and ϵ are the turbulent kinetic energy and turbulent dissipation rate, respectively, and C_μ is a model parameter.

Three different variants of the $k-\epsilon$ model are found in the literature, differing in the way the transport equations for k and ϵ as well as how the parameter C_μ is defined. In the standard $k-\epsilon$ model C_μ is taken as an empirical constant (Davidson [24]), whereas in the RNG (Renormalization Group Theory) (Yakhot et al. [140]) and Realizable $k-\epsilon$ models (Shih et al. [109]), C_μ is allowed to depend on flow features.

Although the (standard) $k-\epsilon$ model appears in many publications, it has some shortcomings (cf. Davidson [24]). Alternative formulations such as the $k-\omega$ model (Wilcox [136]), Reynolds stress model (Launder et al. [72]) or filtered URANS (Johansen et al. [55]) could in principle resolve some of the problems related to the $k-\epsilon$ approach, but require additional modelling and validation.

Ultimately, for realistic predictions of the turbulent flow, a Large Eddy Simulation (LES, cf. for instance Sagaut [104]) is sought. The LES approach is not extensively used for Hall-Héroult modelling, possibly due to relatively high computational requirements. Piovic and Lakehal [75], [76] and Piovic et al. [77] treats both stratified and bubbly flows by means of a LES model and the techniques developed for those purposes could possibly be used for simulations of the Hall-Héroult process, provided computational facilities are available.

Chapter 3

Introduction to CFD

Applying the fundamental laws of mechanics to a fluid continuum gives the governing equations of a flow as described in the previous sections. Unfortunately, the coupled set of non-linear differential equations has no analytical solutions for most engineering problems. It is possible, however, to find approximate solutions to the problem at hand with help of a computer. Broadly speaking, this is the subject of matter in computational fluid dynamics, CFD.

A detailed study of CFD in general is well beyond the scope of the present work and should be sought in comprehensive text books such as Versteeg and Malalasekera [124] while specific details on CFD treatment in FLUENT can be found in the FLUENT User Guide [2]. In the following a brief introduction to the concepts behind CFD will be given. This section is in essence a summary of the corresponding chapter found in Einarsrud [30], included here for reference purposes.

3.1 Introduction to the finite volume method

As a computer performs operations in a discrete manner, the first challenge of a CFD simulation is to replace the continuous problem with a discrete domain. In the continuous domain, all variables are defined at every point, whereas in the discrete case, variables are represented only in discrete grid points. Thus, in a CFD code one would solve for the relevant flow variables only at these points and use some interpolation scheme to obtain intermediate values.

In the present work, a *finite volume* scheme is used. In the finite volume formalism, the computational domain (i.e. the grid) is represented by means of cells, faces and nodes, as sketched in figure 3.1.

The main feature of the finite volume method is that the governing equations are solved

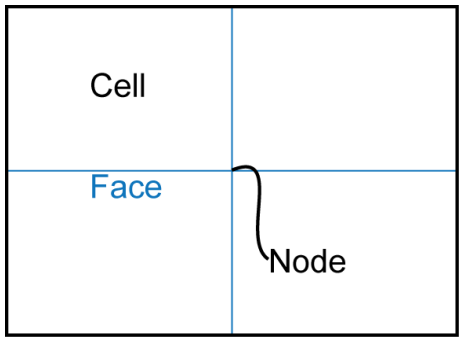

Figure 3.1: The figure shows a computational domain (solid black lines) divided into four cells that are defined by their boundaries (solid blue lines), denoted as faces. Intersections between cell-boundaries are denoted as nodes.

in *integral form*. As an example, the integral form of the steady incompressible continuity equation is considered:

$$\int_{CV} \nabla \cdot \boldsymbol{u} dV = \int_{CS} \boldsymbol{u} \cdot \boldsymbol{n} dA = 0, \tag{3.1}$$

where the divergence theorem has been used to obtain a surface integral. The last integral is taken over the control surface CS enclosing the control volume CV and $\boldsymbol{n}$ is the outward normal of the surface.

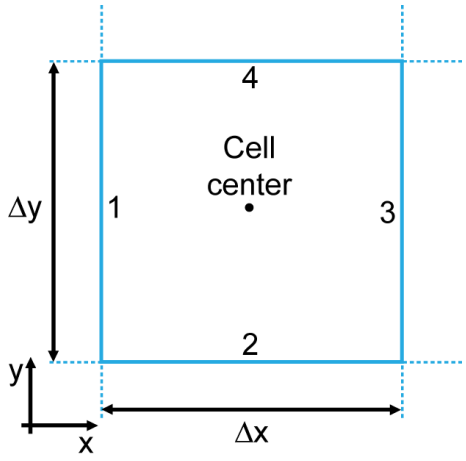

Figure 3.2: Sketch of a typical 2D cell. The cell center is surrounded by four faces denoted 1-4 with dimensions Δx and Δy in respective directions.

Representing equation 3.1 in a 2D-flow field with a grid as sketched in figure 3.2, and assuming that the velocity at the i-th face is given by

$$\boldsymbol{u}_i = u_i \boldsymbol{i} + v_i \boldsymbol{j}, \tag{3.2}$$

equation 3.1 can be rewritten as

$$-u_1\Delta y - v_2\Delta x + u_3\Delta y + v_4\Delta x = 0, \tag{3.3}$$

which is an algebraic expression for mass conservation for the cell in question. One can think of the finite volume method as a code which finds solutions such that relevant quantities are conserved for each cell. It is clear that a domain consisting of more than one cell will yield a system of coupled algebraic equations, as each face is shared by at least two cells.

In a general situation one would apply discrete equations to grid points or cells in the interior of the domain and a combination of discrete equations and boundary conditions for grid points or cells near the boundaries. This yields a system of simultaneous algebraic equations, with the number of equations being equal to the number of discrete variables. The general problem can thus be reduced to a simple matrix equation of the form

$$\boldsymbol{A}\cdot\boldsymbol{x} + \boldsymbol{b} = \boldsymbol{y} \tag{3.4}$$

where $\boldsymbol{A}$ is the system matrix and $\boldsymbol{x}$ is a vector containing the unknown parameters. In a finite volume formalism, the task of solving the integral conservation equations is in principle reduced to that of inverting the system matrix. However, in a practical application of CFD one would typically have millions of unknowns in the discrete system, yielding a direct inversion method like Gaussian elimination at best useless.

Fortunately, most system matrices are sparse, meaning that most entries in the matrix are zero. Several iterative procedures for sparse matrices exist and an introduction to the theory is given in Press et al. [98]. In the present work, matrices are inverted iteratively using the Gauss-Seidel method in conjecture with FLUENT's algebraic multigrid (AMG) solver. A review of the AMG scheme is given in Stüben [112].

3.2 Spatial discretization of steady governing equations

The steady conservation law for the transport of a scalar quantity ψ (the steady advection-diffusion equation) can be written as

$$\nabla\cdot(\rho\boldsymbol{u}\psi) = \nabla\cdot(\mathcal{D}\nabla\psi) + S_\psi \tag{3.5}$$

where $\mathcal{D}$ is a diffusion coefficient and S_ψ is a source term. Setting $\mathcal{D}$ and S_ψ equal to zero and $\psi = \alpha_k$, the phase fraction equation (equation 2.19) is obtained. Equivalently, the transport equations for momentum and turbulent quantities can be obtained by choosing $\mathcal{D}$, S_ψ and ψ appropriately. Equation 3.5 thus serves as the generic form for *all* simulated equations.

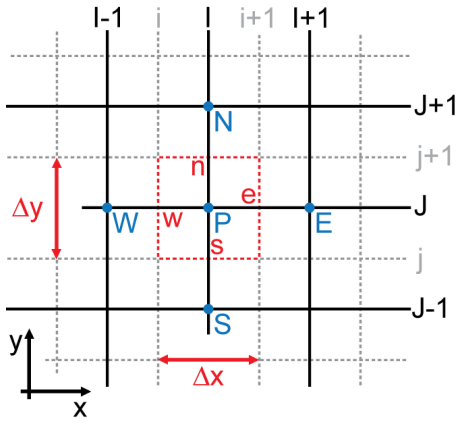

Figure 3.3: Domain for solving 2D scalar transport equation. The figure shows the grid (black solid lines) and five nodal points (marked with blue dots) denoted with capital letters. The central node P is enclosed by a volume (red dashed lines) defined by four faces denoted with lower-case letters. The sketched control volume has dimensions Δx and Δy in respective directions.

Integrating equation 3.5 over the control volume enclosing the central node P (sketched in figure 3.3) one obtains

$$\int_{CS} (\rho \boldsymbol{u}\psi)\, \boldsymbol{n} dS = \int_{CS} (\mathcal{D}\nabla\psi)\, \boldsymbol{n} dS + \int_{CV} S_\psi dV \tag{3.6}$$

where the divergence theorem is used to express volume integrals as surface integrals. The surface integrals are easily discretized

$$\int_{CS} (\rho \boldsymbol{u}\psi)\, \boldsymbol{n} dS = (\rho_e u_e \psi_e - \rho_w u_w \psi_w)\, \Delta y + (\rho_n u_n \psi_n - \rho_s u_s \psi_s)\, \Delta x \tag{3.7}$$

$$\int_{CS} (\mathcal{D}\nabla\psi)\, \boldsymbol{n} dS = \left(\mathcal{D}_e \left.\frac{\partial\psi}{\partial x}\right|_e - \mathcal{D}_w \left.\frac{\partial\psi}{\partial x}\right|_w \right) \Delta y + \left(\mathcal{D}_n \left.\frac{\partial\psi}{\partial x}\right|_n - \mathcal{D}_s \left.\frac{\partial\psi}{\partial x}\right|_s \right) \Delta x \tag{3.8}$$

where faces A_e and A_w are set to Δy and A_n and A_s are set to Δx for simplicity. Source terms are represented by their volume average

$$\bar{S}_{\psi p} = \frac{1}{\Delta V} \int_{CV} S_\psi dV. \tag{3.9}$$

The discretized version of the scalar transport equation for the cell surrounding node P can further be written as

$$\sum_f \rho_f u_f \psi_f A_f = \sum_f \mathcal{D}_f \nabla\psi_f A_f + \bar{S}_{\psi p} \Delta V, \tag{3.10}$$

where the sums are taken over all faces surrounding node P. The values at the faces need to be determined in order to obtain discretized equations of a useful form. Face values can

typically be obtained by linearly interpolated values. For instance, the value of $\mathcal{D}$ at the west face w can be approximated by the average of adjacent nodal values $\mathcal{D}_W$ and $\mathcal{D}_P$, i.e.

$$\mathcal{D}_w = \frac{\mathcal{D}_W + \mathcal{D}_P}{2}. \tag{3.11}$$

An obvious approximation of the gradients at the faces is obtained by central differencing

$$\left.\frac{\partial \psi}{\partial x}\right|_w = \frac{\psi_P - \psi_W}{\Delta x_{PW}} \tag{3.12}$$

where Δx_{PW} is the distance between nodes P and W.

In practical situations, the source term S may be a function of the dependent variable. In such cases it is useful to approximate the source terms by means of a linear function

$$\bar{S}_{\psi p} \Delta V = S_u + S_p \psi_p \tag{3.13}$$

By substitution of equations 3.11 - 3.13 in equation 3.10 and carrying out some algebra, the following algebraic equation for the scalar quantity ψ at node P is obtained:

$$a_P \psi_P = \sum_n a_n \psi_n + S_u \tag{3.14}$$

where the sum is to be taken over all neighbouring nodes. Coefficients a depend of nodal values of $\mathcal{D}$, ρ and u, face areas A and the spacing between the nodes.

As shown in Versteeg and Malalasekera [124] the general form of equation 3.14 can be obtained for the steady convection-diffusion problem for all discretization schemes, differing only in the way the coefficients a are defined.

3.3 Pressure-velocity coupling

Considering the phase fraction equation (equation 2.19) and momentum equation (equation 2.21) one observes an apparent paradox. The gradient of the pressure field appears on the right hand side of the momentum equations, but evidently there is no equation for it. For compressible flows, the pressure can be obtained by some suitable equation of state, $p = p(\rho, T)$, by solving the continuity equation for density and the energy equation for temperature. However, if the flow is incompressible, the density is constant and hence not coupled to pressure. In this case the pressure field introduces a constraint on the flow-field: If the correct pressure field is applied to the momentum equation, then the obtained velocities should satisfy the incompressible continuity equation (equation 2.20) (Versteeg and Malalasekera [124]). The pressure field can thus be interpreted as a correction to the momentum equation, forcing the velocity field to satisfy continuity. The basic idea behind pressure-velocity coupling is to introduce *guessed* values of pressure and velocity fields and to progressively improve the guessed values using an iterative scheme as sketched in figure 3.4, until an acceptable solution is obtained.

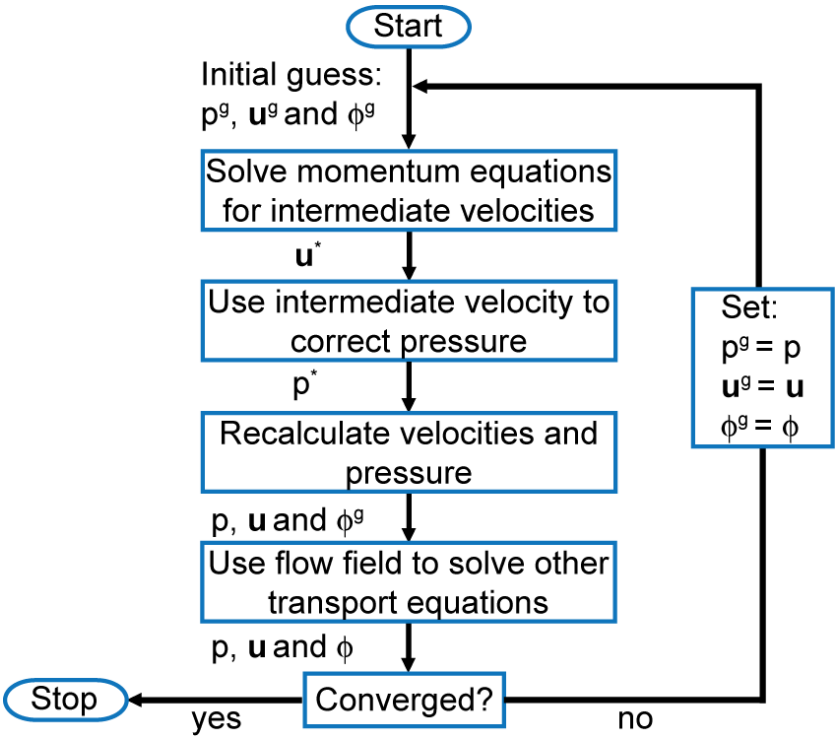

Figure 3.4: Simplified flow diagram for pressure-velocity coupling. Superscripts g signify guessed values.

3.4 Convergence

A CFD simulation relies heavily on iterative procedures in order to obtain a representation of the flow field. This is the case for handling non-linearities, pressure velocity coupling and matrix inversions. In all cases, the discretized equations are solved until convergence is achieved. Considering a discretized equation of the form

$$a_P \psi_P = \sum_f a_n \psi_f + b, \tag{3.15}$$

the *unscaled* residual R^ψ is defined as

$$R^\psi = \sum_{cells} \left| \sum_f a_f \psi_f + b - a_P \psi_P \right|, \tag{3.16}$$

where $\sum_{cells}$ is to be taken over *all* cells in the computational domain. The residual is thus an indication of how far the current solution is from the correct one. In general, this formulation makes it difficult to judge if overall convergence is achieved. This is especially evident if conserved quantities are small, yielding small residuals even if the relative error is large. A *scaled* residual is thus adopted, defined by

$$R^\psi = \frac{\sum_{cells} \left| \sum_f a_f \psi_f + b - a_P \psi_P \right|}{\sum_{cells} |a_P \psi_P|}. \tag{3.17}$$

A CFD simulation is converged when the residuals of *all* transported properties fall below a user defined limit.

3.5 Numerics of the VOF-method

Given the fully discretized equations of previous sections, the solutions of *single* phase flow field can in principle be obtained. In the present work additional equations need to be solved due to the multiphase nature of the flow.

In general, a VOF algorithm solves the problem of updating the phase fraction α_k (i.e. equation 2.19) based on the velocity field and the phase fraction α_k obtained at the previous iteration. It is clear that the description of cells that are entirely filled by one single phase is given by the formalism described in previous sections, as the multiphase nature of the flow is present *only* at cells that are close to an interface. Broadly speaking, the goal of the VOF model is to describe the behaviour of these interfaces. The interface propagation is simulated in two separate steps:

- The advection step.

- The reconstruction step.

The advection step involves the (discrete) solution of equation 2.19, advecting the phase fraction according to local fluid velocities, while the second step involves the reconstruction of a (sharp) interface based on local gradients in phase fraction. In two dimensions, an interface can be considered to be a continuous, piecewise smooth line. The problem at hand is thus to find an approximation to the section of the interface present in each cell, given information of the phase fraction in that and neighbouring cells only.

The scheme used in the present work is based on a piecewise linear reconstruction (PLIC). The idea behind the PLIC method of Youngs [142] is to use a piecewise linear reconstruction of the interface at each cell, as sketched in figure 3.5.

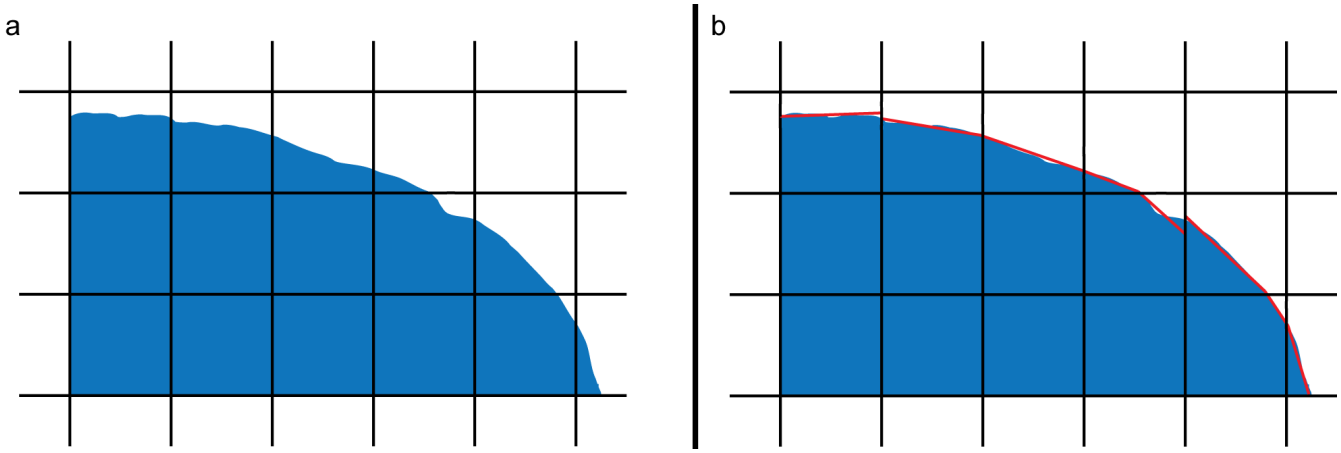

Figure 3.5: Piecewise linear interface reconstruction. The figure shows an actual interface (a) and a piecewise linear reconstruction of the same interface (b). The reconstructed interface is emphasized by red line segments in (b).

As figure 3.5 shows, the line segments representing the interface are not joined. This is the main simplifying feature of the PLIC scheme; one does not attempt to reconstruct the interface as a chain of joined segments. Whenever curvature is relatively small (i.e. the radius of curvature is large when compared to the size of the cell) the method is accurate.

The essential part of the reconstruction step is to determine the orientation of the segment, that is the unit normal vector $\boldsymbol{n}$ of the surface. The normal vector of the interface and the phase fraction α uniquely determine a straight line, which gives the approximated interface in the cell in question (cf. Scardovelli and Zaleski [105]).

3.6 Time advancement

For transient simulations, the governing differential equations must be discretized in both space and time. The spatial discretization for transient flows is identical to that of the steady flows described in previous sections, yielding the temporal discretization rather simple. The prototype time-dependent equation for some quantity ψ can be written as:

$$\frac{\partial \psi}{\partial t} = F(\psi) \tag{3.18}$$

With a first order discretization of the derivative on the left hand side, equation 3.18 can be written as

$$\frac{\psi^{n+1} - \psi^n}{\Delta t} = F(\psi) \tag{3.19}$$

where Δt is the discrete time-step, ψ^{n+1} and ψ^n are the values of ψ at the next time level $t + \Delta t$, and current time level t, respectively.

3.6.1 Explicit schemes

In an explicit scheme the function on the right hand side of equation 3.19 is taken to be at the current time level, yielding:

$$\frac{\psi^{n+1} - \psi^n}{\Delta t} = F(\psi^n). \tag{3.20}$$

As discussed thoroughly in Versteeg and Malalasekera [124], explicit schemes are only conditionally stable making them prone to oscillations if time steps are chosen inadequately. Implicit schemes (as described in the following) are thus preferred in order to avoid this problem.

To the author's best knowledge, there exists no general implicit VOF scheme yielding sharp interfaces, and time integration of stepping of the phase fraction equation is thus done following an explicit scheme. The fully discretized, explicit version of equation 2.19 for a node (node indices dropped for clarity) is given by:

$$\frac{\alpha_k^{n+1}\rho_k^{n+1} - \alpha_k^n \rho_k^n}{\Delta t}\Delta V + \sum_f \rho_k^n u_f^n \alpha_{k,f}^n = \dot{R}_i^n \tag{3.21}$$

where the sum is to be taken over neighbouring faces.

3.6.2 Implicit schemes

In implicit schemes, the value of ψ is taken at the next time level, i.e.

$$\frac{\psi^{n+1} - \psi^n}{\Delta t} = F(\psi^{n+1}). \tag{3.22}$$

The benefit of the implicit scheme is that it is un-conditionally stable (Versteeg and Malalasekera [124]). The drawback, however, is that the equations need to be solved iteratively, as the unknown value ϕ^{n+1} is present on both sides of equation 3.22.

A fully implicit scheme is in the present work chosen for time advancement of the momentum, turbulent kinetic energy and turbulent dissipation equations in order to obtain stable solutions. The fully discretized, implicit version of equation 3.14 for a node P is given by:

$$\frac{\psi^{n+1} - \psi^n}{\Delta t}\Delta V + a_P^{n+1}\psi_P^{n+1} = \sum_f a_f^{n+1}\psi_f^{n+1} + S_\psi^{n+1} \tag{3.23}$$

where the first term on the left hand side represent volume averaged quantities and the sum is to be taken over all (relevant) neighbouring cells. The source term S_u will depend on which scalar property is transported, and must thus be chosen appropriately.

3.7 Accuracy in time and space

The numerical solution of any continuous problem necessarily introduces a limit to its accuracy, due to discretization. Considering for instance the above explicit time integration, equation 3.20, and comparing to the corresponding Taylor expansion of the continous derivative,

$$\frac{\partial \psi}{\partial t}\Delta t = \psi\left(t + \Delta t\right) - \psi\left(t\right) - \left(\frac{\partial^2 \psi}{\partial t}\right)\frac{\Delta t}{2} - \ldots, \tag{3.24}$$

it is evident that equation 3.20 is an *approximation* of the derivative, with first order accuracy:

$$\frac{\partial \psi}{\partial t} = \frac{\psi\left(t + \Delta t\right) - \psi\left(t\right)}{\Delta t} + \mathcal{O}\left(\Delta t\right). \tag{3.25}$$

Correspondingly, higher order discretizations (for instance the QUICK for spatial discretization) have a lower discretization error and are consquently more accurate. As seen from equation 3.25, besides increasing the order of the method, the accuracy of a solution can be improved by choosing a smaller time step (for time accuracy) or by mesh refinement (for spatial accuracy), at the cost of increased CPU time and memory consumption. In addition, time and spatial resolution must be chosen in such a way that the numerical solution is *stable*, a requirement given by the so-called CFL-condition

$$\frac{u\Delta t}{\Delta x} \leq C, \tag{3.26}$$

where C is the Courant-number, depending upon which equations are solved and what numerical schemes are used.

For practical engineering problems, commonly involving several simultaneous phenomena, the resolution requirements typically become more involved and no well-established theory exists on necessary conditions to maintain a specified space-time accuracy. Hence, the grid and time-step are often chosen based on intuition or expert knowledge, allowing for phenomena of interest to be resolved in both time and space, while maintaining numerical stability and restricting CPU-time.

3.8 On verification and validation

The literature defines an *error* as a recognisable deficiency in a CFD model that is *not* caused by lack of knowledge, whereas *uncertainties* are potential deficiencies in a CFD model that *are* caused by the lack of knowledge (Versteeg and Malalasekera [124]). Typical causes of errors are numerical errors, coding errors and user errors. Typical causes of uncertainties are input uncertainties (e.g. limited knowledge of geometry, boundary conditions, properties etc.) and physical model uncertainties (i.e. discrepancies between real flows and CFD due to inadequate representations of physical processes).

Errors are quantified by *verification* of the model, a process determining that the implementation of the model accurately represents the conceptual description of the problem (i.e. "solving the equations right"). Uncertainties are quantified by *validation*, a process determining to which degree a model is an accurate representation of the real world (i.e. "solving the right equations").

Validation is traditionally carried out by means of comparison with experimental data, comparing some key features of the flow that also are obtainable from the CFD model, while verification traditionally is performed by evaluating global and local conservation equations and comparing simplified parts of the model to analytical solutions.

3.9 Hardware and software used in the thesis

Hardware and operative system

The majority of the calculations performed in this thesis were computed on a Hewlett-Packard $\mathcal{Z}800$ workstation. The workstation was equipped with two Intel Xeon W5590 processors, running at 3.33 GHz and 24 GB of Random Access Memory. The operating system was Windows Vista Enterprise, 64-bit.

ANSYS FLUENT

ANSYS FLUENT is a state-of-the-art computer program used for modelling of fluid flow and heat transfer in complex geometry, and has for many applications become the industry standard. The ANSYS FLUENT environment provides all the tools needed to implement a finite volume problem, ranging from mesh-generation and discretization of the governing equations to detailed options concerning turbulence models.

FLUENT is based on a graphical user interface (GUI), allowing the user to choose various models, set boundary conditions, solver options, post process results etc. More advanced options are available through a text user interface (TUI) allowing users to tweak models so that they fit their needs. Further extensions are available through the C or C++ programming language combined with FLUENT's built in compiler to include user defined functions (UDF). In a UDF, calculated values can be stored in a user defined memory (UDM). In addition to user defined functions, FLUENT allows the user to specify a number of user defined scalar (UDS) functions, given by the general advection-diffusion equation

$$\frac{\partial}{\partial t}\left(\rho\psi_k\right) + \frac{\partial}{\partial x_i}\left(f(u_i)\psi_k - \rho\mathcal{D}_k\frac{\partial\psi_k}{\partial x_i}\right) = S_{\psi_k}, \tag{3.27}$$

where $f(u_i)$ is a general advection function and S_{ϕ_k} is a general source term, both specified by an appropriate UDF.

For the UDS equations, one essentially has the choice between Dirichlet or Neumann boundary conditions, i.e.

$$\psi \quad \text{is known.} \quad \text{or} \quad \boldsymbol{n}\cdot\mathcal{D}_k\nabla\psi \quad \text{is known,} \tag{3.28}$$

where $\boldsymbol{n}$ is the boundary normal pointing *into* the computational domain.

Two points should be noted regarding the use of UDFs:

1. Although the possibility to use UDFs provides a certain flexibility, they must be specified within the frame of special macros provided by the software. Thus, the source code of the software is not accessible to the user.

2. For cells in the interior of the computational domain, *only* cell centred values are available to the user. Node and face values can thus be obtained only by means of an appropriate interpolation scheme. On boundaries, the face values are however accessible in order to specify for instance boundary conditions.

Grid generation

The grids (or meshes) used in this thesis have been constructed using GAMBIT [39] and ANSYS Workbench [1]. Both tools provide a large range of grid generation techniques as well as boundary value specification for multi-purpose CFD solvers such as FLUENT.

Meshing can be performed following a "bottom up" or "top down" approach. The top down approach allows to automatically design a mesh for some given geometry. However, this approach tends to generate unstructured grids (cf. Versteeg and Malalasekera [124]) which are prone to high skewness and low quality for non-trivial geometries. A bottom up approach is thus chosen in order to maintain control of grid quality. An overview of the bottom up approach is given in figure 3.6.

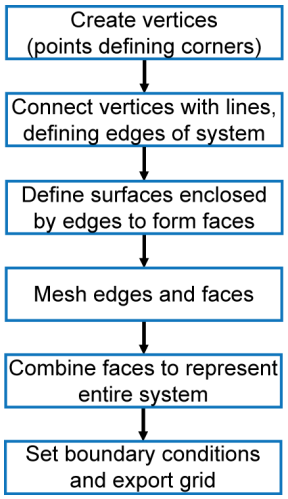

Figure 3.6: Overview of bottom up approach for mesh generation.

Most grids used in the present work are *structured* (cf. Versteeg and Malalasekera [124]) for computational efficiency. Structured grids are characterized by topologically rectangular cells, meaning that all grid lines continue from one boundary to the next (as opposed to unstructured grids where this needs not be the case). Curved edges are meshed by means of a non-orthogonal meshing technique, allowing grid lines to intersect at angles different from 90°.

Chapter 4

Introduction to electromagnetism

The principal chemical reactions in the Hall-Héroult cell rely upon the transfer of electrical charge, that is, an electrical current must pass through the cell for the reactions to occur. An electromagnetic field is induced in the cell as a result of the electrical current, which gives rise electromagnetic forces causing fluid flow. In the following sections, the basis for these phenomena is treated. A more comprehensive treatment is given in Part III of the thesis.

4.1 Electromagnetic fields and the electrical current

Electric and magnetic fields (denoted $\boldsymbol{E}$ and $\boldsymbol{B}$) are governed by the Maxwell equations (cf. Griffiths [43]) and constitutive closure relations. The closure relation used in the present work is the continuum form of Ohm's law, stating that the electrical current density $\boldsymbol{j}$ is given as

$$\boldsymbol{j} = \sigma \left(\boldsymbol{E} + \boldsymbol{u} \times \boldsymbol{B} \right). \tag{4.1}$$

where $\boldsymbol{u}$ is the velocity of the substance considered, i.e. the fluid velocity, and σ is the corresponding electrical conductivity.

The electrical current density is of fundamental importance to the Hall-Héroult cell as it dictates the electromagnetic force density (the Lorentz force) and serves as a driving force for electrochemical reactions, as described in the following two sections.

4.2 The Lorentz force

A fluid through which an electrical current passes is subject to a Lorentz force given as

$$\boldsymbol{f}_L = \boldsymbol{j} \times \boldsymbol{B} - \varrho_e \nabla \phi, \tag{4.2}$$

where ϱ_e is the density of *free* charges. For a fluid with zero net charge, as in the present case, the Lorentz force term is simply

$$\boldsymbol{f}_L = \boldsymbol{j} \times \boldsymbol{B}, \tag{4.3}$$

where $\boldsymbol{j}$ is given by equation 4.1 and $\boldsymbol{B}$ is calculated from the Maxwell equations or given as an external field. The inclusion of electromagnetic forces is the prime requisite of a special field of fluid mechanics, denoted magnetohydrodynamics or more commonly, MHD.

4.3 Faraday's law of electrolysis

As stated by Grjotheim and Kvande [47], when current passes from the anode to the cathode through an electrolyte, the following laws apply for the amount of electrode products formed:

1. The amount of products formed at each electrode will be proportional to the number of charges passing through the cell.

2. The amount of each electrode product will be proportional to the equivalent mass of the product.

In electrolytic production, where an electrical current density $\boldsymbol{j}$ passes through a surface with area $\boldsymbol{A}$, the laws of Faraday can be combined to

$$\dot{m}_i = \frac{M_i \boldsymbol{j} \cdot \boldsymbol{A}}{z_i F}, \tag{4.4}$$

where $\dot{m}_i$ is the mass production rate of species i, with molar mass M_i , z_i is the valency number for ionic species i and F=96483C/mol is Faraday's constant.

Chapter 5

Chemical reactions

The chemistry of the Hall-Héroult cell is highly complex and at the present time not fully understood. However, relatively simple reaction mechanisms can be constructed, capturing the essence of the process. Considering these simplified reaction mechanisms, two limiting factors arise; the presence of reacting species and the rate at which the reaction occurs.

5.1 Species in the cell

Cryolite (Na_3AlF_6) is the dominant constituent of the electrolyte. The cryolite has to main functions; acting as a solvent for alumina (Al_2O_3) and acting as a medium for passing an electrical current. In addition, cryolite provides a physical boundary between aluminium produced at the cathode and gas produced at the anode. Cryolite is *not* consumed during normal operation.

While the electrolyte essentially is molten cryolite, certain additions are present. As discussed in Prasad [97], a typical electrolyte contains excess AlF_3 and CaF_2. The role of the additives is to increase the conductivity of the electrolyte and lower the liquidus temperature, resulting in favourable energy conditions. The additives however decrease the solubility of alumina. In addition to the mentioned additives, several further additions are made, both for operational reasons and as impurities from alumina and the anode. Due to the increased complexity of involving further species, only the primary system Na_3AlF_6-Al_2O_3 will be considered in the present work.

According to Thonstad et al. [116] and Evans [36], 2 - 3 wt% of alumina is dissolved in the cryolite. This ratio is kept close to constant by continuous feeding of alumina to the cell. As cryolite is not consumed during operation, the overall (net) reaction in the cell in the cell affects *only* alumina. As previously stated, the overall reaction can be written as

$$\frac{1}{2}Al_2O_{3,d} + \frac{3}{4}C_s \rightarrow Al_l + \frac{3}{4}CO_{2,g}. \tag{5.1}$$

As pointed out by Popov et al. [95], there is no experimental data suggesting that alumina disassociates into free ions of aluminium and oxygen. It is however postulated [95] that aluminium is present as a mixture of oxy-fluoride complexes.

5.2 Dissolution of alumina

The primary ionization of cryolite melt is represented by

$$Na_3AlF_6 \rightarrow 3Na^+ + AlF_6^{3-}. \tag{5.2}$$

According to Popov et al. [95], the hexafluoraluminate ion dissociates further by the following reaction

$$AlF_6^{3-} \rightarrow AlF_4^- + 2F^-. \tag{5.3}$$

The cryolite melt is thus believed to contain mainly Na^+, AlF_6^-, F^- and AlF_4^-.

The nature and number of ionic species formed as alumina dissolves in the melt is still not completely understood [95], though it is believed that dissolution occurs with the formation of complex oxyfluoroaluminates. According to Grjotheim and Kvande [47], species with bridging Al-O-Al bonds are more important. At low alumina concentrations, the following complexes are suggested

$$4AlF_6^{3-} + Al_2O_3 \rightarrow 3Al_2OF_8^{4-} \tag{5.4}$$

$$4AlF_6^{3-} + Al_2O_3 \rightarrow 3Al_2OF_6^{4-} + 6F^-. \tag{5.5}$$

Grjotheim and Kvande [47] suggest further possible complexes at higher alumina concentrations. Other sources however present other plausible complexes. For instance, Evans and Ziegler [36] suggest the following two to be formed during dissolution

$$F^- + 2AlF_6^{3-} + Al_2O_3 \rightarrow 3AlOF_3^{2-} + AlF_4^- \tag{5.6}$$

$$3F^- + 4AlF_6^{3-} + Al_2O_3 \rightarrow 3AlOF_5^{4-} + 3AlF_4^-. \tag{5.7}$$

Even further suggestions are given by Popov et al. [95]. The discrepancies in the literature concerning oxyfluoroaluminates yield an obvious challenge for modelling the species in the Hall-Héroult cell.

5.3 Anode reaction

At the anodic current densities used in industrial cells, gaseous CO_2 is the primary product at the anode (Popov [95]). While carbon is supplied by the anode, oxygen is transported

to the anode through oxyfluoroaluminates. Considering the suggested complexes for low alumina concentrations, the anode reactions may be written as

$$2\mathrm{Al_2OF_8^{4-}} + \mathrm{C} \rightarrow \mathrm{CO_2} + 4e^- + 4\mathrm{AlF_4^-} \tag{5.8}$$

$$4\mathrm{F^-} + 2\mathrm{Al_2OF_6^{2-}} + \mathrm{C} \rightarrow \mathrm{CO_2} + 4e^- + 4\mathrm{AlF_4^-}. \tag{5.9}$$

Following Thonstad et al. [116], the complexes suggested by Evans and Ziegler [36] could react by the following steps

$$\mathrm{AlOF_x^{1-x}} + \mathrm{C} \rightarrow \mathrm{CO}_{ads} + \mathrm{AlF_x^{3-x}} + 2e^- \tag{5.10}$$

$$\mathrm{AlOF_x^{1-x}} + \mathrm{CO}_{ads} \rightarrow \mathrm{CO_2} + \mathrm{AlF_x^{3-x}} + 2e^-, \tag{5.11}$$

where CO_{ads} is an intermediate adsorbed species and $\mathrm{AlOF_x^{1-x}}$ is an oxyfluoride complex ion.

5.4 Cathode reaction

Following Thonstad et al. [116], the cathode process can be written as
Diffusion towards the electrode

$$\mathrm{AlF}^-_{4,bulk} \rightarrow \mathrm{AlF}^-_{4,surf}. \tag{5.12}$$

Charge transfer reaction

$$\mathrm{AlF}^-_{4,surf} + 3e^- \rightarrow \mathrm{Al} + 4\mathrm{F}^-_{surf}. \tag{5.13}$$

Counter transport of charge

$$4\mathrm{F}^-_{surf} \rightarrow 4\mathrm{F}^-_{bulk}, \tag{5.14}$$

with corresponding steps for $\mathrm{AlF_6^{3-}}$.

5.5 Loss reactions

An important source of lost efficiency is due to $\mathrm{CO_2}$ coming in contact with aluminium. It has been suggested that metal droplets can separate from interfacial waves and be suspended in the bath, yielding the back-reaction

$$2\mathrm{Al} + 3\mathrm{CO_2} \rightarrow \mathrm{Al_2O_3} + 3\mathrm{CO}, \tag{5.15}$$

thus lowering the amount of produced aluminium. Assuming that the back reaction is the main contribution to current efficiency loss, the following expression can be obtained for a cell operating at a current efficiency χ_{Al}

$$\frac{\chi_{Al}}{2}\mathrm{Al_2O_3} + \frac{3}{4}\mathrm{C} \rightarrow \chi_{Al}\mathrm{Al} + \frac{3}{4}(2\chi_{Al} - 1)\mathrm{CO_2} + \frac{3}{2}(1 - \chi_{Al})\mathrm{CO}. \tag{5.16}$$

A model allowing for the formation of CO can thus also be used for an estimate of the current efficiency.

5.6 Kinetics

Kinetics deal with the determination of reaction rates for chemical processes. The main factors influencing the reaction rate are the thermodynamical states of the reactants, their concentrations, temperature and whether or not catalysts are present. In general terms, the change in Gibbs potential determines whether or not a reaction is thermodynamically favourable, while the kinetics determines how fast a reaction occurs. In the following a brief review of the kinetics for the relevant reactions presented in the previous chapter is given.

Following Bird et al. [6], two types of reactions are distinguished. For homogeneous reactions, reactions are allowed to take place within the entire system volume, while heterogeneous reactions take place only at surfaces.

For a homogeneous first order reaction, the rate of production of species i , is given by an expression of the form

$$\dot{R}_i = k''' C_i \qquad [\mathrm{kg/m^3 \cdot s}], \tag{5.17}$$

where $\dot{R}_i$ is the volumetric production rate, k''' is a first order reaction rate and C_i is the concentration of the reacting species . For a heterogeneous first order reaction, the rate of production at the reaction surface can be expressed as

$$\dot{\mathcal{M}}_i^M = k'' C_i^M \big|_{surf} \qquad [\mathrm{kg/m^2 \cdot s}], \tag{5.18}$$

where $\dot{\mathcal{M}}_i$ is the mass flux of species i and k'' (m/s) is a first order (mass) transfer coefficient.

As the exact chemistry of the Hall-Héroult process at the present time is unknown, "all kinetic aspects have still to be clarified" (Grjotheim et al. [44]). As a consequence, the kinetic parameters are based on processes *assumed* to take place within the cell. The following data is taken from chapter 7 in Thonstad et al. [116].

5.6.1 Disassociation of cryolite and dissolution of alumina

Considering the homogeneous reaction 5.3, the reaction rate is found to be in the range 2000 - 8000 $\mathrm{s^{-1}}$ (Thonstad et al. [116]).

As the formation of oxyfluoraluminates remains an open question, no data is found for the kinetics of complex formation. However, a great deal of work has been conducted concerning alumina dissolution due to its high impact on cell operation. As pointed out by Kvande and Grjotheim [47], alumina may take three distinct paths when in contact with the bath

1 It rapidly disperses as discrete grains and dissolves easily.

2 It can agglomerate as a clump and freeze bath around it, which can either float or sink.

3 It can sink without dispersing.

If feeding is done in such a way that alumina is dispersed effectively in the bath, the condition for rapid dissolution is very favourable, yielding dissolution times of the order of seconds. As discussed in Kvande and Grjotheim [47], large variations in dissolution times can occur as a consequence of varying operational conditions.

As there are no experimental indications of free aluminium ions in the melt, it is reasonable to believe reaction rate to form complexes is fairly high, whatever the complex is, suggesting that its reaction time can be neglected when compared to the longer dissolution time of alumina.

An extensive study of the dissolution kinetics of alumina has been done by Kobbeltvedt [67], carrying out work on both the kinetics of dissolution and coupling to the bubble driven convection in the cell. Kobbeltvedt [67] concludes that magnetic compensation of the cells weaken the bath flow loops at the expense of alumina transport, possibly influencing the current efficiency in a negative way due to additional sludge formation. As a consequence, the bubble driven flow becomes more important for the dissolution kinetics.

5.6.2 Anode reaction

Due to the large uncertainties in the exact anode process, several kinetic parameters are suggested in the literature. A common feature is however a fairly large dependence of alumina concentration. Kisza et al. [64] and [65] study the kinetics of mechanisms on the form of 5.8 and 5.9 finding rate which point to relatively large Damköhler numbers (cf. Bird et al. [6]), suggesting that the reaction rate can be taken to be instantaneous, compared to the hydrodynamic scales of interest in the present work, which are of the order of 1 second (cf. for instance Keniry et al. [59]).

5.6.3 Cathode reaction

Thonstad et al. [116] give results for the charge transfer reaction of the type sketched in equation 5.13, split into a two-step process. The slower of these two processes is shown to have a relaxation time of a few microseconds, again suggesting a fairly fast reaction comparing to time scales of interest.

Chapter 6

Typical geometry and properties of the Hall-Héroult cell

In order to make realistic predictions for industrial cells, models should incorporate relevant physics within a relevant geometry using relevant parameters. As these factors influence all the phenomena presented previously, this chapter will treat geometry and parameters as a whole.

6.1 Geometry and boundaries of the cell

Although the sketch shown in figure 1.1 is instructive, the geometry of a real cell is somewhat more involved. Whereas figure 1.1 shows only one anode, modern prebaked cells typically have *two* anodes in the cross section. Furthermore, a complete cell consists of 10-20 such anode pairs. A realistic cross section of an industrial Hall-Héroult cell is given in figure 6.1. Based on information provided in Prasad [97] and Paulsen [90], typical cell dimensions are summarized in table 6.1.

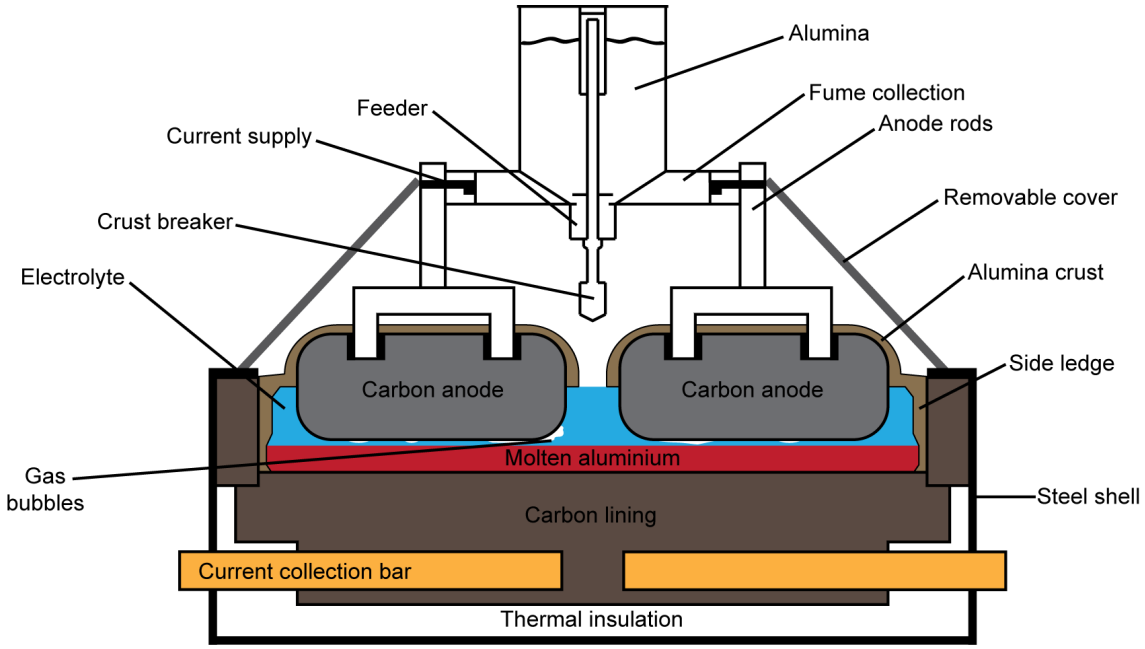

Figure 6.1: Realistic cross section of an industrial Hall-Héroult cell as of Prasad [97].

Table 6.1: Typical cell dimensions as of Prasad [97] and Paulsen [90]

Property	Typical value	Unit	Comments
Anode distance (between rows)	10 to 20	cm	Center channel size
Anode distance (in row)	3 to 18	cm	Side channel size
Anode height	20 to 60	cm	Depending on time
Anode width	70	cm	In paper plane
Anode length	140 to 170	cm	In cross section
Anode to side ledge (end channel)	10 to 40	cm	
Anode to side ledge (side channel)	10 to 30	cm	
Interpolar distance (anode to metal)	2 to 5	cm	
Bath height	15 to 25	cm	
Metal height	10 to 30	cm	Depending on time
Cell length	10 to 20	m	Depending on number of anodes
Cell width	3 to 5	m	Depending on anode length

6.1.1 The side ledge

Considering the phase diagram of the NaF-AlF_3 system (cf. Grjotheim and Kvande [47]), in the operational range of modern cells, one observes that the first solid phase to form is cryolite. The heat loss is significant at the side walls of the system, yielding a freezing of cryolite at this boundary. The exact form of this side ledge will necessarily depend upon the temperature distribution at the side wall as well as the local velocity distribution.

Due to the importance of the overall cell energy balance, the side ledge has been studied extensively using various approaches. Considering the thermal problem alone, a rough shape of the side ledge can be obtained by studying the predicted isotherms of a cell geometry. A sketch of such isotherms is given in figure 6.2.

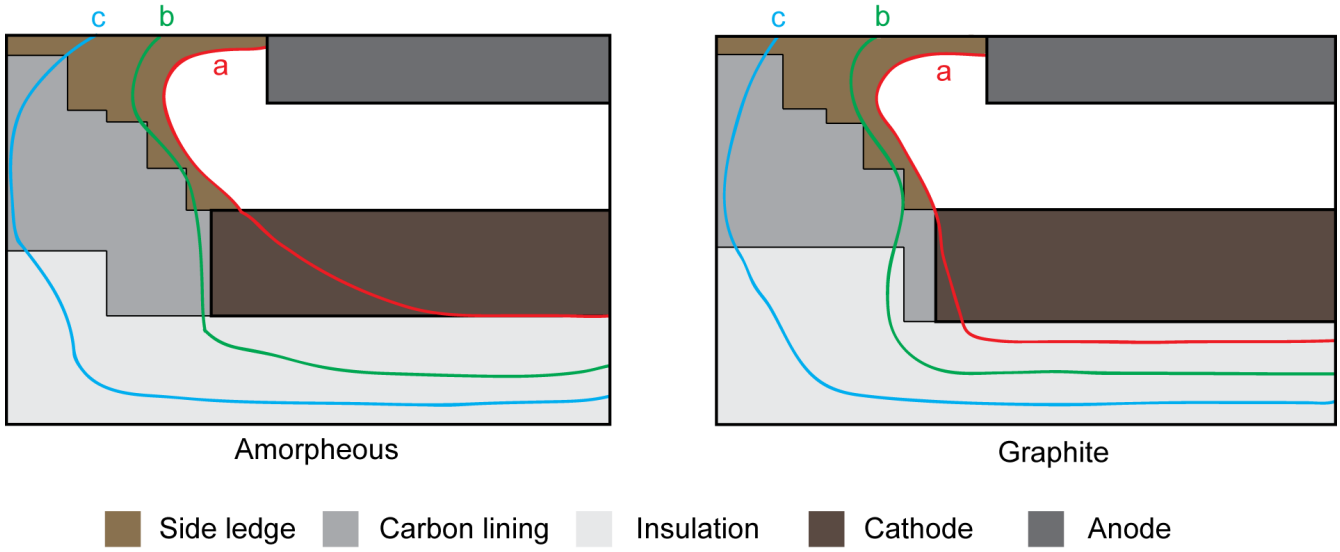

Figure 6.2: Isotherms for different cathode blocks and insulation in the same cell. Inner isotherms (a) are at 950°C, middle ones (b) at 850°C and outer ones (c) at 550°C. The light brown region shows where frozen cryolite is formed. Figure as of Grjotheim and Kvande [47].

As seen from figure 6.2, the 950°C isotherm forms a curved surface above the side insulation. As seen from the phase diagram of the NaF-AlF_3 system (cf. Grjotheim and Kvande [47]), this isotherm is close to the liquidus of the system and one should thus expect that the region between the isotherm and the cell side (light brown region in figure 6.2) is frozen.

6.1.2 The cathode and metal pad

Ideally, the carbon cathode is not consumed during operation. However, due to mechanical wear (erosion) and chemical reactions, the cathode is gradually deteriorated. This process

is however slow, compared to the inner dynamics of the cell, and the expected life time of the cathode is of order of 2000 days (Vasshaug [123]).

During operation molten aluminium is deposited on the cathode and thus acts as an effective cathode for the process (due to its high conductivity). Several elements however produce perturbations of varying magnitude on the metal pad, the most important of these being Lorentz forces arising from uneven current distribution and waves due to bubble and bath motion. In addition, the height of the metal pad varies during operation due to production and tapping of aluminium, the latter having a typical frequency of 24-48 hours (Grjotheim and Kvande [47]).

Though the cathode is "inactive" in the sense of reactions producing aluminium, it is important when determining the current distribution in the molten aluminium. An important factor impeding current transport at the cathode boundary is the formation of sludge, typically consisting of undissolved alumina which sinks to the cathode surface. An uneven current distribution in the molten metal gives rise to additional Lorentz forces that in principle could disrupt the stability of the cell. The formation of sludge is strongly dependent on local thermodynamic properties and its transport is necessarily coupled to the flow field.

6.1.3 The anode

The anode is consumed during operation and is typically exchanged after 22-26 days (Grjotheim and Kvande [47]). Initially, the anode has a rectangular shape with sharp corners, but due to the nonuniformity of the current density the anode corners eventually become rounded. Zoric et al. [149] modelled the evolution of the anode shape, by means of a 2D computation of the current distribution around an anode, as shown in figure 6.3.

In addition, as pointed out by Fortin et al. [38], the anode burns off parallel to the average cathode surface (i.e. the metal-bath interface), resulting in a permanent anode tilt, promoting gas evolution in a preferred direction. To the author's best knowledge, the literature lacks studies on anode shapes leaving the exact geometry of the anode an open question.

The anode is typically made from a petroleum coke aggregate and a pitch binder, resulting in an inhomogeneous porous structure, with a (volumetric) porosity of up to 20% (Grjotheim and Kvande [47]). The irregular porous structure of the anode surface allows for nucleation of gaseous bubbles and possibly diffusion of species on a molecular level. The pore size spans a large range, typically from 1-1000μm, as shown by Rørvik and Øye [102], cf. figure 6.4.

As seen from figure 6.4, although the measured pore radii span a large range, the majority of the pores have a radius in the range of 10-50μm, accounting for approximately half of the total observed porosity.

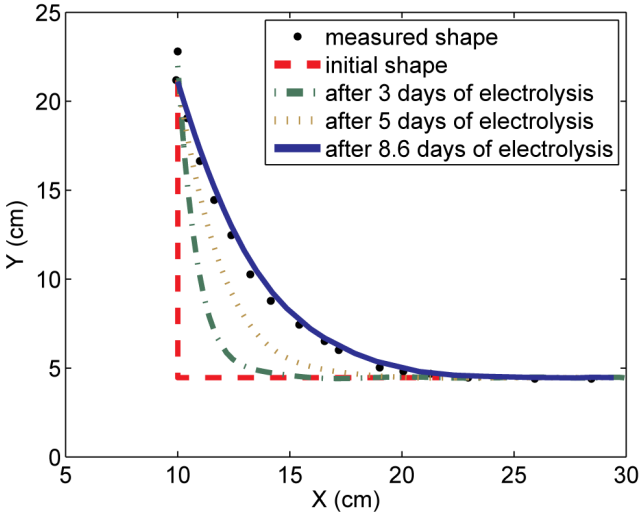

Figure 6.3: Results of the computations of Zoric et al. [149] for the evolution of anode shape over several days of electrolysis.

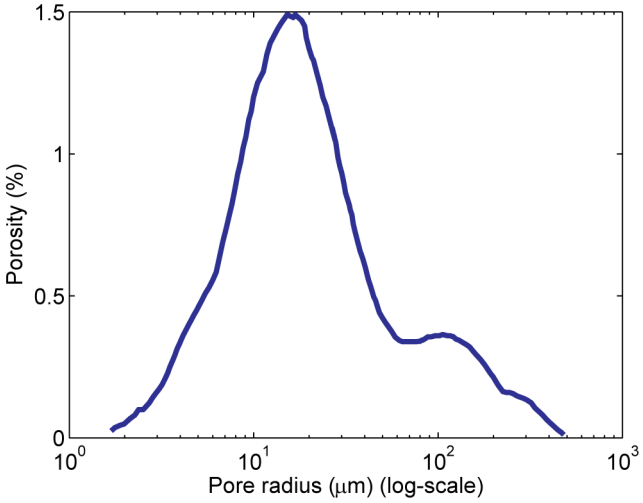

Figure 6.4: Anode pore size distribution as of Rørvik and Øye [102].

6.2 Physical properties

In the following sections a summary of the physical properties of the substances in the Hall-Héroult cell is given. As seen in chapter 5 the composition of the bath is a complicated issue, an issue necessarily transferred to its physical properties. It is thus not expected that the models for physical parameters presented here give an accurate description in *all* conditions and their use should thus be considered with some care.

Density

The density of the phases in the system is important for two reasons, it separates the aluminium from the bath and it allows bubbles to be buoyant. According to Grjotheim et al. [44], the density of molten aluminium can be expressed as

$$\rho_{Al} = 2560.976 - 0.272T, \quad [\mathrm{kg/m^3}] \tag{6.1}$$

where T is the temperature in °C. Thus, for a cell operating at a temperature of 960°C, the density of molten aluminium is typically 2300 kg/m^3.

The density of (pure) cryolite is given as [44]

$$\rho_{cry} = 3032 - 0.937T, \quad [\mathrm{kg/m^3}], \tag{6.2}$$

yielding a density of approximately 2100 kg/m^3 at 960°C. However, as discussed in preceding sections, pure cryolite is not the working substance in a Hall-Héroult cell. For a bath of "general" composition, several models exist in the literature (cf. chapter 5 in Thonstad et al. [116]). One such model, including effects of the most common additives and temperature variations is given by Solheim [110], suggesting a linear temperature dependence of the form

$$\rho_{bath} = \rho_{bath,1000} - (T - 1000)b, \quad [\mathrm{kg/m^3}], \tag{6.3}$$

where the density at 1000°C, $\rho_{bath,1000}$, and b are composition dependent parameters. The most important additive in this context is alumina, which in all cases will *reduce* the density of the bath (Grjotheim et al. [44]).

Little information is found regarding the state of gaseous CO_2 bubbles. According to Moran and Shapiro [83], the critical temperature and pressure of CO_2 is 304 K and 73.9 bar, respectively. Generalized compressibility charts (cf. Moran and Shapiro [83]) show that CO_2 behaves close to ideally during normal cell operation and the density can thus be modelled as

$$\rho_{CO_2} = \frac{p}{\mathcal{R}_{CO_2} T}, \quad [\mathrm{kg/m^3}], \tag{6.4}$$

where $\mathcal{R}_{CO_2}$ is the specific gas constant, 189 J/(kg K). At 960°C, the gas density is 0.435 kg/m^3.

Viscosity

Viscosity is important as it is one of the parameters governing the hydrodynamic processes in the Hall-Héroult cell. In spite of the importance of this parameter, reported data on viscosity is relatively scarce and independent data is often scattered (Grjotheim et al. [44]). The temperature dependent viscosity of liquid aluminium is given by

$$\mu_{Al} = 0.2567 \exp \frac{1527}{T}. \quad [10^{-3}\text{kg}/(\text{m} \cdot \text{s})] \tag{6.5}$$

According to Grjotheim et al. [44], the viscosity is *strongly* influenced by impurities. The extent of this statement is however not quantified.

The temperature dependence of viscosity on cryolite is given by

$$\mu_{cry} = 28.88 - 42.09 \cdot 10^{-3} T + 15.99 \cdot 10^{-6} T^2, \quad [10^{-3}\text{kg}/(\text{m} \cdot \text{s})]. \tag{6.6}$$

As for the density, additives need to be considered for a realistic model, the most important being alumina, shown in figure 6.5.

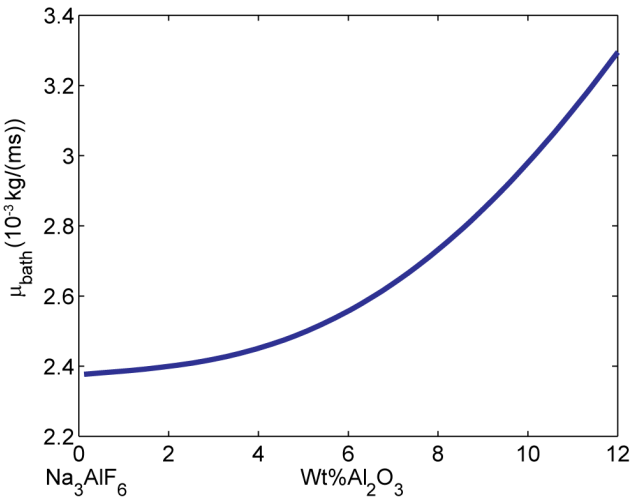

Figure 6.5: The influence of Al_2O_3 on bath viscosity. Solid line shows results as of Tørklep and Øye [120].

As seen in Grjotheim et al. [44], values for the viscosity obtained by Tørklep and Øye [120] are considerably lower (up to 15%) than corresponding measurements performed by other researchers, although the trend is similar; higher concentrations of alumina yielding higher viscosities.

Surface properties

Surface properties of the electrolyte can influence many aspects of the electrolytic process and is important when considering bubbles and deformations of the bath-metal interface. According to Grjotheim et al. [44], the surface tension at the bath-metal interface can be estimated from the corresponding surface tensions to air by

$$\gamma_{bath,Al} = \gamma_{air,bath} - \gamma_{air,Al}, \tag{6.7}$$

This estimate is however rather crude, and one should not expect to obtain results better than correct order of magnitude using this approach.

Grjotheim et al. [44] suggest the following model for the surface tension for air-aluminium

$$\gamma_{air,Al} = 500 - 0.135(T - 660), \quad [10^{-3}\text{N/m}], \tag{6.8}$$

where T is the temperature in °C. Similarly, for molten cryolite, the surface tension is given by

$$\gamma_{air,cry} = 208.63 - 0.108T, \quad [10^{-3}\text{N/m}]. \tag{6.9}$$

Little information is found regarding surface tensions at a bath-CO_2 interface. However, as both air and CO_2 behave approximately as ideal gases, it is plausible that their behaviour at interfaces is similar as well, at least in order of magnitude, i.e. of order 0.1 N/m.

As for the other properties of the bath, the surface tension is strongly dependent on composition, as observed in the number of models presented in Thonstad et al. [116]. Experimentally, it is found that the common additives Al_2O_3, CaF_2 and LiF *increase* the interfacial tension, whereas an increasing bath ratio (NaF to AlF_3 mass ratio) yields a decrease. Based on a regression analysis, the following relation for typical operational temperatures is given by Thonstad et al. [116].

$$\gamma_{bath,Al} = 700 - 88(BR)^2 + 7.3w(Al_2O_3) + 4.6w(\text{LiF}), \quad [10^{-3}\text{N/m}], \tag{6.10}$$

where BR is the bath ratio and $w(Al_2O_3), 4.6w(\text{LiF})$ represent wt % of Al_2O_3 and LiF, respectively.

Based on the above models, the bath-aluminium surface tension is of order 0.5 N/m.

It should be stressed that the above models are based on zero current density. As pointed out by Thonstad et al. [116], experiments show a dependence upon current density, possibly due to the accumulation of ions at interfaces during electrolysis.

Local imbalance of surface tension that may result from surface active agents at the interface can change the heat and mass transfer rates and alter flow patterns. This is the so called Maragoni effect, which causes convection close to the interface, cf. Utigard and Toguri [122].

The wetting or contact angle θ is a measure of the degree of wetting of a solid surface by a liquid phase in contact with a gaseous phase. It is determined by the surface tension of the three phases and defined by

$$\cos\theta = \frac{\gamma_{s,g} - \gamma_{s,l}}{\gamma_{l,g}}, \tag{6.11}$$

Small wetting angles signify that the solid surface is wetted well by the liquid phase. No general model of wetting is found in the literature, though Thonstad et al. [116] present several experimental studies of carbon wetting. Wetting is found to be influenced by several parameters such as carbon type, alumina content, gaseous species and temperature. Typical experimental values for cryolite lie between 140° to 110° for graphite anodes and 130° to 100° for amorphous anodes.

A strong dependency upon alumina is identified by Dorward [27], indicating that the contact angle of cryolite on graphite changes from 115° for pure cryolite to 65° for cryolite saturated with alumina. For typical operating conditions, i.e 5wt% Al_2O_3, the apparent contact angle is found to be approximately 70°, i.e. significantly lower than that identified for pure cryolite.

A summary of the experimental findings related to wetting is shown schematically in figure 6.6.

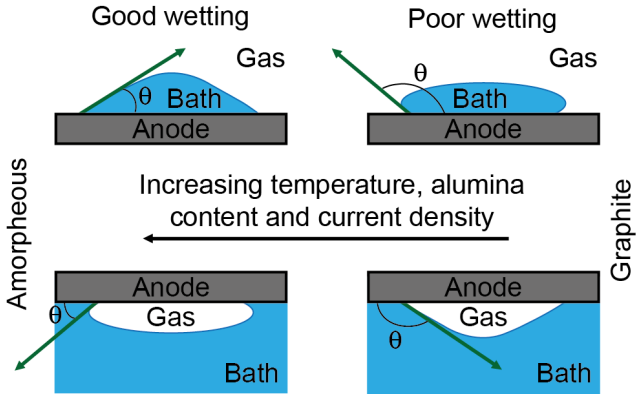

Figure 6.6: Sketch of the influence of parameters on the contact angle.

CO_2 properties

Molecular CO_2 is formed on the bath side of the anode and the transport properties of CO_2, i.e. diffusivity and solubility, are thus of importance for gas evolution. The literature is unfortunately scarce with respect to experiments and measured values span a large range. According to Poncsak et al. [93], the diffusivity of CO_2 is of order $10^{-9} - 10^{-13}$ m^2/s, while

the solubility typically is in the range 0.1-0.2 kg/m^3. As shown by Numata and Bockris [85], the solubility is strongly dependent upon alumina concentrations.

The combination of low diffusivity and solubility indicate that the regions in proximity of the anode are likely to be supersaturated with molecular CO_2, allowing for nucleation of bubbles on the anode surface.

Electrical conductivity

The electrical conductivity of the system is of prime interest as it essentially governs the cell voltage. As a result, a great deal of literature is available on this subject. A review of available data and models is given in Thonstad et al. [116] and Grjotheim et al. [44].

Wang et al. [132] present a model for conductivity in cryolite with additives based on a regression equation from experimental data, given by

$$\begin{aligned} \ln \sigma_{bath} &= 1.9105 + 0.3240BR - \frac{1745.7}{T} - \\ &- (17.38w(Al_2O_3) + 3.955w(CaF_2) + \\ &+ 9.227w(MgF_2) - 21.55w(LiF)) \cdot 10^{-3}, \end{aligned} \tag{6.12}$$

where σ is the electrical conductivity in $\Omega^{-1}\text{cm}^{-1}$, BR is the bath ratio, T is the temperature and w is the wt% of the additives. Thus, for typical operational ranges, the predicted conductivity is in the range of 2 to $3\Omega^{-1}\text{cm}^{-1}$. These values are somewhat lower than the conductivity measured in industrial electrolytes, being in the range of 1.75 to $2.05\Omega^{-1}\text{cm}^{-1}$ (Grjotheim et al. [44]).

Temperature data for the resistance of molten aluminium is provided by Grjotheim et al. [44], indicating a constant value

$$\sigma_{Al} = 33333, \quad \text{if} \quad 930^\circ\text{C} < T, \quad [\Omega^{-1}\text{cm}^{-1}] \tag{6.13}$$

Little information is found concerning the conductivity of CO_2. However, as long as it is non-ionized, the conductivity is expected to be very low and thus negligible compared to the bath and metal.

Chapter 7

Review

Because of the high temperature, highly corrosive and opaque environments of the Hall-Héroult process, quantitative data of phenomena occurring are not easily obtainable. One thus relies on modelling to describe processes in the cell. Due to the complexity of the system, a large amount of literature is available covering various subjects relevant to the process, both from a theoretical and experimental point of view. While the goal of the previous chapters was to describe the theory that in principle could describe the processes in the Hall-Héroult cell, this chapter will review some essential modelling activities over the last decades. The main focus will be on the central node in figure 1.2, i.e. hydrodynamics and its coupling to other phenomena.

In addition to experimental work on physical models of the cell, models can broadly be placed in two categories:

- Fundamental models based on idealized cells.
- Computationally intensive investigations solving the governing equations in realistic geometries.

In the former of these two approaches, it is necessary to make sufficient idealizations of the cell in order to obtain a problem that is simple enough to solve. Even though such models provide valuable qualitative insight, the necessary idealizations may not be applicable to an actual cell. Increased computational capability has made it possible to relax the high degree of idealization, thus favouring the latter approach.

7.1 Experimental work

7.1.1 Physical model experiments

Physical models have been used extensively since the 1970's and have to a large extent been used to validate computational models. The focus of the early studies in physical models was mainly related to gas induced circulation and deformations of the bath-metal interface. Early experiments were carried out by Dernedde and Cambridge [25] in a two-dimensional water-oil model. Waves with wavelengths up to 47 cm, periods up to 3 seconds and amplitudes up to 16 mm were observed on the interfaces. Waves in the side channel are also reported by Chenosis and LaCamera [15], having a period of 0.5-1.0 s. The wave heights were found to depend on the interpolar distance, current densities and the shape of the anode. The bath height was also reported to influence the amplitudes.

A more recent study by Bearne et al. [4] report wavelengths 200-400 mm in the side channels of the cell. These travelling waves were reflected on the side walls allowing for interference, yielding amplitudes up to 50 mm. As the distance between anode and side wall was decreased, the interfacial deformations became less regular, reduced in amplitude and altered in appearance to more irregular localised disturbances, rather than waves.

The work of Fortin et al. [38] was done in a full scale room-temperature water model with a fixed, rigid "cathode" of Plexiglas. The objective of the study was to explore the effects of cell operation conditions and geometrical parameters on the gas layer at the anode. Small bubbles were found to coalesce into large bubble sheets, travelling to the edge of the anode where, when released, induced rigorous mixing in the side channel. The bubble sheets observed are sketched in figure 7.1.

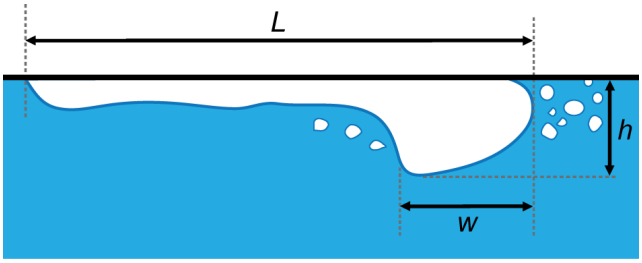

Figure 7.1: Bubble sheets as observed by Fortin et al. [38]. Longitudinal dimensions, L, ranged from 2-128 cm and front widths, w, varying from 0-14.5 cm. Bubbles formed a thick bubble front, h, with dimensions 0.8-2.5 cm, followed by a thin trailing portion of thickness around 5 mm.

Bubbles were found to travel with velocities ranging from 8-40 cm/s, being released at the anode edge with frequencies of 0.2-3 Hz, consistent with findings of Chenosis and LaCamera [15], reporting periodic gas release with a frequency of 1 Hz.

The experiments of Fortin et al. [38] did not allow for deformations of the bath-metal interface, as this was modelled as a fixed boundary. However, it is interesting to note that the authors observed that the detachment of large bubbles from the anode, caused enough disturbances to shake the 9 mm thick Plexiglas sheet representing the cathode. This effect suggests that a significant amount of momentum is transferred to the bath-metal interface due to the detaching bubbles. Fortin et al. [38] noted that the disturbance increased with decreasing interpolar distances.

Solheim et al. [111] used a 2D physical model to investigate the bubble driven convection, concluding that the bubble driven effects were of the same magnitude as those due to magnetohydrodynamics in the bath. The results from the physical model were used to validate a computational model for interfacial deformations. The coupling of bubbles and interfacial deformations was further studied by Einarsrud [30], identifying a distinct (geometry dependent) bubble induced deformation on the interface.

The discrepancies in observed average wave patterns in Dernedde and Cambridge [25], Bearne et al. [4] and Chenosis and LaCamera [15] strengthen the notion that gas induced circulation and interfacial waves are dependent of geometry and flow rates, consistent with the findings of Fortin et al. [38] and Einarsrud [30]. This observation stresses the need of exact knowledge of geometry and flow rates used in experiments, if the results are to be used to validate a computational model.

The various flow regimes of bubbles under anodes has been studied by Perron et al. [91], using a room temperature water model. Two distinct flow regimes were identified and classified as creeping and free motion. The authors argue that bubbles initially move in the creeping regime, where buoyancy and surface forces are in equilibrium. After a certain time (typically 1 second in Perron et al.'s setup) the buoyancy at the nose overcomes the surface forces and causes the nose to "climb" the liquid. In this transition region, the front and rear of the bubble are subject to different forces, causing an elongation of the bubble much like the ones observed by Fortin et al. [38]. Depending on bubble size and velocity, the entire bubble can either detach, and slide along a wetting film to the anode edge, or split into two smaller bubbles, one creeping and one free.

Detailed information on the distribution of velocity and turbulence in physical models can be obtained by means of Particle-Image-Velocimetry (PIV), as shown by for instance Cooksey and Yang [22] and Yang and Cooksey [141]. Yang and Cooksey [141] conclude from their measurements that the flow field is *strongly* dependent upon the cell geometry, confirming the more qualitative observations of previously published material. It is however pointed out that further investigations are needed in order to fully describe the physical phenomena that can be directly applicable to a real aluminium reduction cell.

The above point is of great importance, as traditional physical models have used water and oil to simulate bath and metal. Though water-oil models have several positive features, the obvious drawback is that the materials used in physical models are *not* the same as those encountered in an industrial cell. Despite differences in specific parameters, it is

the *combination* of these parameters that determine whether or not similarity between physical models and a real Hall-Héroult cell can be claimed. Following Zhang et al. [148], the bubble Froude number Fr_{bub} is critical for an accurate representation of the bubbles. Fortunately, the Froude number can be defined from geometrical considerations as

$$Fr_{bub} = \frac{u_g^2}{gL}, \tag{7.1}$$

where u_g is the gas velocity, g is the acceleration of gravity and L is the typical anode size. Hence, by choosing a 1:1 representation of the anode and realistic gas rates, similarity can be claimed for Fr_{bub}. As noted by Zhang et al. [148], the effects of the other non-dimensional groups are of secondary order.

7.1.2 Experiments on actual cells

Although similarity can be claimed for physical model, the possibility for discrepancies advocates the use of experimental data from actual cells in order to validate computational models. The literature is *very* scarce on data from industrial measurements, the reason for this being either that results are unpublished due to industrial secrecy or due to the challenges related to obtaining reliable and accurate data from industrial cells. Some procedures that in principle could yield useful data from industrial cells are however described in the open literature.

In order to visualize the flow in the bath and metal radioactive tracers (cf. Grjotheim et al. [45]) could be used, yielding, at least in principle, velocity data of the same type as that obtained by PIV measurements. The metal motion can furthermore be visualized by means of erosion of iron rods as discussed in Grjotheim et al. [46]. Furthermore, the method proposed by Kobbeltvedt and Moxnes [68], monitoring temperature depression which follows the addition of alumina, could provide further information on the flow field. Finally, the interfacial deformations could in principle be determined by means of the probe presented by Olsen et al. [87].

The control of aluminium reduction cells relies almost exclusively on the continuous sensing of potline current and cell voltage (Keniry et al. [59]). The value of the voltage as well as its changes are the key input to vital cell functions such as alumina feeding, anode positioning and instability control (cf. Grjotheim and Kvande [47]). There are several sources to the voltage variations, both internal (i.e. related to flow phenomena) and external (for instance anode replacement and metal tapping). The three principal internal sources to voltage variations are summarized schematically in figure 7.2.

Keniry et al. [59] identify distinct frequencies credited to the release of gaseous bubbles. The measured voltage signals show a dependence upon anode age; young anodes having a spectrum concentrated around 1Hz, while older anodes have a larger spread over an interval of 1–3 Hz, consistent with typical values obtained in oil-water physical models. As

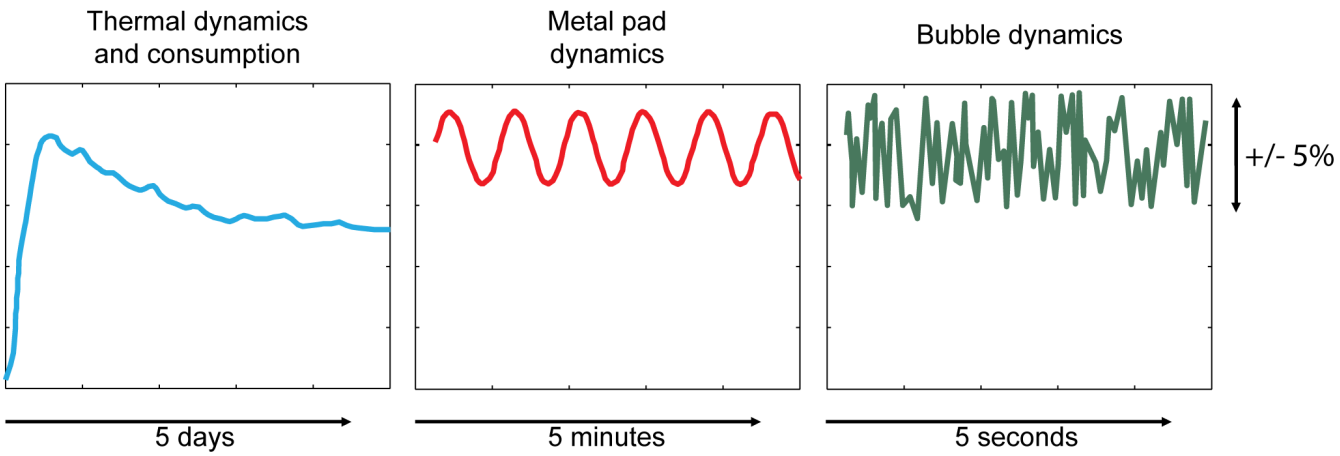

Figure 7.2: Principal internal sources of voltage variations as of Keniry et al. [59].

there exists a correlation between voltage oscillations in the cell and bubble release under the anode (bubble noise), this could in principle be used to map the bubble behaviour in a cell without the need for invasive techniques.

7.1.3 Experiments on bubble evolution

A thorough review of this subject is given by Cooksey et al. [21], and only selected papers are treated here.

Experiments on bubble evolution is traditionally limited to lab-scale cells. Though restricted to (relatively) small geometries, the results obtained are instructive as bubbles are allowed to form within a realistic environment. A detailed description of the growth and evolution of single bubbles is given by Xue and Øye [139], performing experiments on a see-through lab cell with a cylindrical anode with diameter 1 cm. Three distinct stages where identified based on both visual observations and measured voltage signals:

1 Initial stage: Nucleation and growth of spherical or semi spherical bubbles with diameter in the range 0.4-0.6 mm. Bubbles formed predominantly on specific nucleation sites, although some bubbles were found to be detached from the anode. This stage is characterized by a linear growth in voltage, credited to the increasing Ohmic screening with increasing bubble number and size, bubbles growing in a diffusion controlled regime as $D_{bub}(t) \sim \sqrt{t}$.

2 Coalescence and growth stage: Smaller bubbles merge creating larger bubbles while continuing to grow due to mass transport. Bubbles in this stage are no longer spherical, instead forming flattened spheroids. This stage shows random fluctuations in voltage (with small magnitude), although the average behaviour is a linear increase with a

rate slightly lower than that found for stage 1. In parallel to the increasing voltage, the contact angle of the bubbles is found to increase from 30 to 130°.

3 Escape stage: The final stage of the bubble is its detachment and escape from the anode, characterized by a sudden decline in the voltage signal. The detachment was found to be periodic, the period being strongly dependent upon the average current density at the anode. The diameter of the bubble upon escape was found to be comparable to the size of the anode.

Voltage signals obtained by Xue and Øye show similar properties to that found by Keniry et al. [59], albeit a far more regular pattern is observed, due to the more controllable environments on a small anode. Xue and Øye identify frequencies in the range of 0.03 to 0.33Hz, monotonously increasing as the current density is increased from 0.1 to 1.0 A/cm^2.

The influence of various parameters has been studied in detail by Wang and Taberaux [133] on an intermediate size lab scale anode with diameter 15.2 cm. Anode consumption allowed the initially cylindrical anode to evolve to a hemisphere over the time of the experiment, significantly altering the overall voltage pattern as shown in figure 7.3.

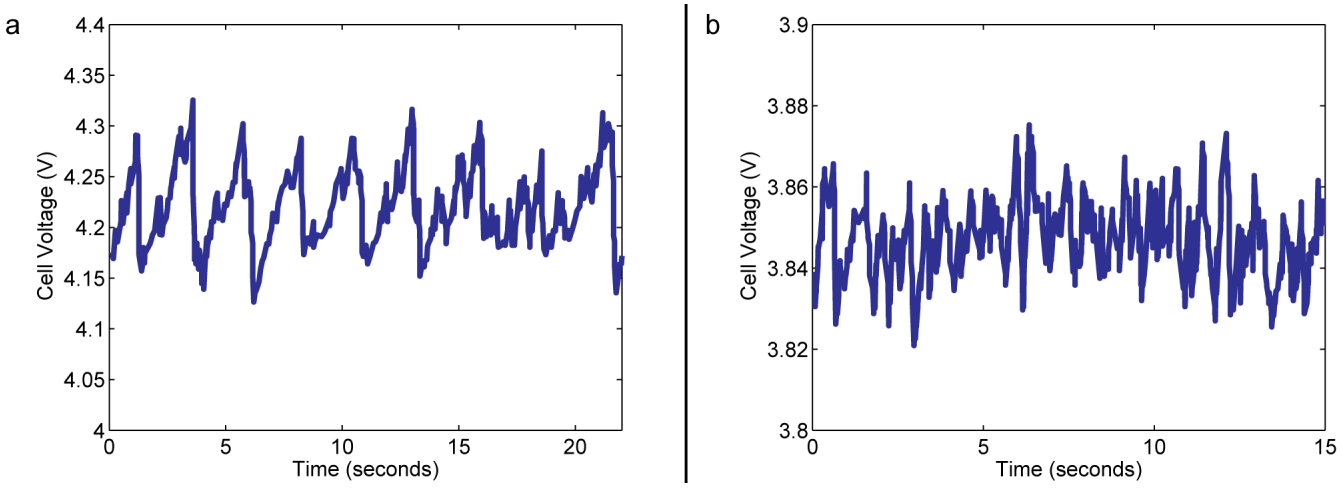

Figure 7.3: Anodic voltage variation as of Wang and Taberaux [133]. Frames *a* and *b* show typical voltage behaviour at 1200 and 12460 amp-hours into the electrolysis, respectively.

Consistent with industrial measurements, Wang and Taberaux [133] show that the (average) frequency increases, while the average magnitude of the fluctuations decreases with increasing anode age, voltage fluctuations being inversely proportional to frequency. As expected from Ohm's law, the cell voltage is found to increase with current density. Frequencies and the average volume of detaching bubbles are however found to both increase and decrease with increasing current density, depending upon the anode age.

The voltage curves for the young anode of Wang and Taberaux [133] (figure 7.3) are less

regular than those obtained on the smaller anode of Xue and Øye [139]. A distinct pattern corresponding to small scale anodes is however visible, an effect not easily observed on the industrial measurements of Keniry et al. [59]. This is believed to be a geometrical effect; larger anodes being able to sustain several large bubbles simultaneously, yielding a regular pattern only if some degree of self-organization is present.

Cassayre et al. [14] set out to compare the gas behaviour between inert and consumable carbon anodes by means of several experimental techniques. Experiments show that several bubbles form underneath the anode, occurring at specific nucleation points. The growth rate, release frequency as well as the number of nucleation sites was found to increase with increasing current density. Regarding bubble evolution, smaller bubbles where found to coalesce into larger bubbles, finally covering a large area of the anode before being released, as expected from Xue and Øye [139]. The rate of coalescence was found to *decrease* with increasing current density, thus yielding a release of smaller bubbles. The results are shown in figure 7.4

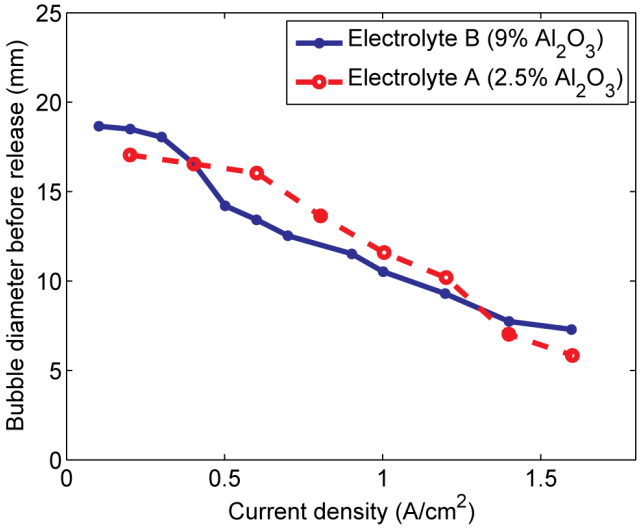

Figure 7.4: The evolution of average bubble diameter before release under graphite anode as of Cassayre et al. [14]

Similar studies by Wang et al. [134] and Gao et al. [40] confirm the dependence of bubble size upon current density, but also provide data showing a dependence upon anode size.

7.1.4 MHD experiments

The literature on physical modelling of MHD phenomena in reduction cells is scarce. This is probably due to the difficulties of obtaining fields as strong as those present in industrial cells, running with currents up to 400 kA (Evans [36]). Some experiments (Banerjee and

Evans [3]) have been performed, using woods metal to simulate molten aluminium. Due to the small scale of the experiment, Lorentz forces were measured to be one order of magnitude less than those expected in industrial cells.

Zhang et al. [144] study the effect of DC magnetic fields on single bubbles moving in a molten metal. Though the experimental set up is different from that of a Hall-Héroult cell, it is worthwhile to note that the magnetic field influences the overall bubble behaviour. For small bubbles, the drag force *increased* with increasing magnetic interaction parameters, the opposite was however observed for larger bubbles. Furthermore, the measurements revealed a distinct damping of the bubble induced velocity in the surrounding liquid as well as a rectification of bubble trajectories. Moreover, significant modifications were found in the wake behind the bubbles, increasing magnetic fields yielding larger eddies. Finally, as shown in Zhang [143] and Zhang et al. [145], MHD effects tend to increase the local Reynolds number, possibly enhancing mass transfer phenomena. As conductivities in the bath are several orders of magnitude smaller than in molten metals, the coupling is however believed to be less pronounced in a Hall-Héroult setting.

7.2 Joint steady state models

Purdie et al. [100] present results from a research programme into reduction cell hydrodynamics, with the aim of developing a three-dimensional computational model of the electrolyte flow field, considering transport of alumina. The model was constructed in a customized version of FLUENT based on a two-fluid model with turbulence treated by means of the $k - \epsilon$ model. Bubbles were modelled as spherical particles of uniform size (1 cm diameter) and were generated at 100 randomly chosen injection sites at a rate equivalent to a current density of 1 A/cm^2, solved as a steady state problem. The model is validated by data obtained in a gas-water model with similar geometry.

Purdie et al. [100] illustrate mechanisms of gas bubble release and show that the electrode inclination angle and current density affect bubble behaviour significantly and indicate that gas evolution is the single most important driver of the electrolyte flow.

Bilek et al. [5] propose the first model simulating the reality of industrial electrolyte flow with combined gas driving and MHD forces, based on the approach of Purdie et al. [100]. The model presented simulates the electrolyte flow field in a full reduction cell, with both gas and MHD driving forces, and predictions for mass transfer at the bath-metal interface. Simulations were carried out for four cases in order to study the physics of each phenomena separately *and* joint. The following main conclusions were drawn from the study:

- The distribution of turbulence is dictated by gas release.
- MHD drives heat transfer at the ends of the cell while gas drives it at the side walls.
- Mixing is determined by the gas driving force, MHD giving rise to an asymmetry.

- Convective transport and turbulent diffusion contribute to current efficiency loss. These processes are dominated by the bubble driving force.
- Design changes which impact the gas driving force, rather than the MHD forces, have a greater impact on the transport processes considered. The design improvement process is however not straightforward due to competing requirements to each process.

A similar (though restricted to two dimensions) recent study by Doheim et al. [26] focuses on the joint effects of gas- and MHD driven flows on mass transfer coefficients, using an Euler-Lagrange model, concluding that the flow in the electrolyte is dominated by the motion of bubbles. The work of Doheim et al. [26] did however not incorporate effects of interface deformations, as only the gas-electrolyte system was considered.

The above modelling approaches allows for insight in the relative importance of the two main driving forces in the Hall-Héroult cell and can at the same time be used to study alternative designs of the cell. If a global approach as the one presented above is to produce realistic output, realistic input must however be provided. Such input is for instance size-distributions of bubbles and bath-metal interface deformation, both depending upon local (transient) factors such as varying current densities and species concentrations. Furthermore, several possibly important phenomena are necessarily neglected, such as the complex bubble sheet topology and coupling to the cell voltage.

These details have received increased attention over the last years and selected contributions are discussed in the following sections.

7.3 Pure MHD models

Early contributions to transient computations in Hall-Héroult cells were related to MHD driven flows. For instance, Wahnsiedler [131], Potocnik [96] and Segatz et al. [107] have all presented three-dimensional transient models, considering the bath and metal flow, in order to predict instabilities on the bath-metal interface.

Different multiphase models have been investigated by Severo et al. [108], providing a benchmark case for the prediction of MHD-related bath-metal deformations using a constant turbulent viscosity turbulence model. Realistic geometries and electromagnetic fields are provided and typical deformations and velocity distributions in the molten aluminium are simulated. Severo et al. [108] predict a (steady) dome-shaped interface, shown schematically in figure 7.5.

As expected from the classical paper of Givry [42], the internal (symmetric) contribution to the Lorentz force yields a quadratic surface, while the inclusion of an external magnetic field results in a asymmetric contribution, highly dependent upon geometrical features such as cell alignment (cf. for instance Grjotheim an Kvande [47]).

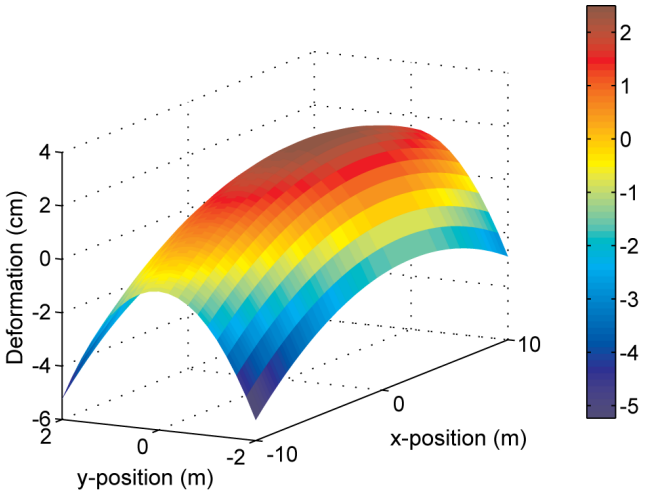

Figure 7.5: Sketch of typical bath-metal interface as of Severo et al. [108].

The bath-metal deformation predicted by Severo et al. [108] has been successfully reproduced by Bojarevics and Pericleous [7], using a shallow water model (Moreau and Ziegler [84]). Bojarevics and Pericleous point that although the electromagnetic fields given are representative when considered alone, they do not appear to be compatible with each other when considering the Maxwell equations. In addition, the accurate prediction of the bath-metal interface is found to be dependent upon several additional features, such as the anode profile being altered corresponding to the local interface deformation, an effect not mentioned by Severo et al. [108].

Further aspects related to modelling of the bath-metal interface can be found in the recent textbook of Gerbeau et al. [41].

7.3.1 Bubble-MHD interactions

The details of MHD interactions with one single bubble have been described in a recent study by Bojarevics and Roy [8], showing that MHD forces become important for a bubble exceeding 2 mm in size, when the fields from the entire cell is considered. The forces identified by Bojarevics and Roy [8] can become sufficiently large to overcome the typical drag forces associated with the electrolyte flow and can thus oppose the buoyant force driving the bubbles. Further studies are however required to quantify the effect of MHD forces on a population of bubbles varying in both size and position.

7.4 Pure gas bubble models

Several important contributions have been made over the last decades by Vogt,[125]–[129], providing analytical models for gas and bubble behaviour in the boundary layer of gas evolving electrodes. The main parameter of Vogt is a *gas evolution efficiency*, defined as the fraction of (molecular) gas produced at the electrode which is *evolved as bubbles*. As shown in [127], less than 30% of the gas produced by Faraday's law is evolved as bubbles at the electrode. The remaining gas is transported to the bulk of the electrolyte in dissolved form, thus supersaturating the surrounding liquid.

A detailed model of the two phase flow and current distribution along a vertical electrode is given by Dahlkild [23]. The two phase model considers transport of species and existing empirical models for particle transport in sheared and sedimenting suspensions are adopted for the bubble mixture to close the two phase equation system. Dahlkild [23] shows that ionic species concentrations are essentially homogenous, due to the mixing effect of bubbles and electrophoresis. Moreover, the effect of non-uniform current density due to non-uniform bubble coverage is captured by the model.

Although the above modelling approaches provide valuable insight in the fundamental processes occurring at the electrode, they fall into the class of fundamental models based on idealized cells, and extensions are thus required in order to treat the complete hydrodynamic picture.

As found in experimental studies (cf. Xue and Øye [139]), gas bubbles pass through several stages, which all need to be captured by a realistic model. The various stages are:

- Nucleation
- Growth
- Detachment
- Motion
- Coalescence

The order of the above stages is not chronological, for instance, two growing bubbles can coalesce and creeping motion can induce detachment as described by Perron et al. [91].

A mathematical framework, based on microscopic modelling of the bubble layer has been developed by Kiss et al. over the last decades [62], [63], [60], [94], following the above sequence with the overall goal of determining the covering factor of the bubbles. The model is motivated by the fact that advanced CFD models such as the VOF, that in principle can yield an exact solution, become exceedingly computationally demanding if a large number of bubbles are to be simulated. While a simpler multiphase model would treat coalescence by means of a kinetic expression for the average rate, the model of Kiss et al. [62] treats each coalescence event individually (i.e. a Euler-Lagrange model). Bubbles are assumed to

have diffusion controlled growth after nucleation, with molecular gas transported through porous structures in the anode rather than through the surrounding electrolyte.

Kiss [60] shows that the nature of the bubble noise is highly dependent on the number of bubbles present. A regular pattern in the bubble covering factor is observed for single bubbles (figure 7.6a), corresponding to its growth. When many bubbles are present, the combined effect of growing, coalescing and detaching bubbles results in random like fluctuations as shown in figure 7.6b. However, under certain conditions, bubbles can manifest a concerted movement due to very big gas pockets 'sweeping' along the anode, engulfing lesser bubbles in its motion. The effect of this self-organisation on bubble coverage is shown in figure 7.6c. .

The model of Kiss et al. [94], shows good agreement with data from air-water experiments. The results indicate that a large number of small bubbles can coexist with a few medium and large gas bubbles. Despite their low numbers, big gas bubbles dominate the bubble layer due to their significant fraction of total gas present.

Besides the limitations of the Lagrangian formalism, the main drawback of the model of Kiss et al. [62] is that the generation of bubbles is essentially decoupled from effects related to local current densities, as only the gas coverage factor is predicted. As shown by Perron et al. [92], the Ohmic resistance in the electrolyte can be found using semi-empirical relations for conductivity and predicted gas coverage fractions as of Kiss et al. [62]. A two way coupled approach, i.e. allowing for bubbles to alter the local current density and thus production, using the above models has however yet to be published.

Recent studies involving the group of Kiss et al. [12] adopt a VOF model to validate single bubble behaviour in new oil-water experiments. As shown also by Einarsrud [30], the VOF model is an adequate approach for treating the complex topology of the (large) anodic bubbles, a feature which is not easily obtained by a more traditional Lagrangian approach.

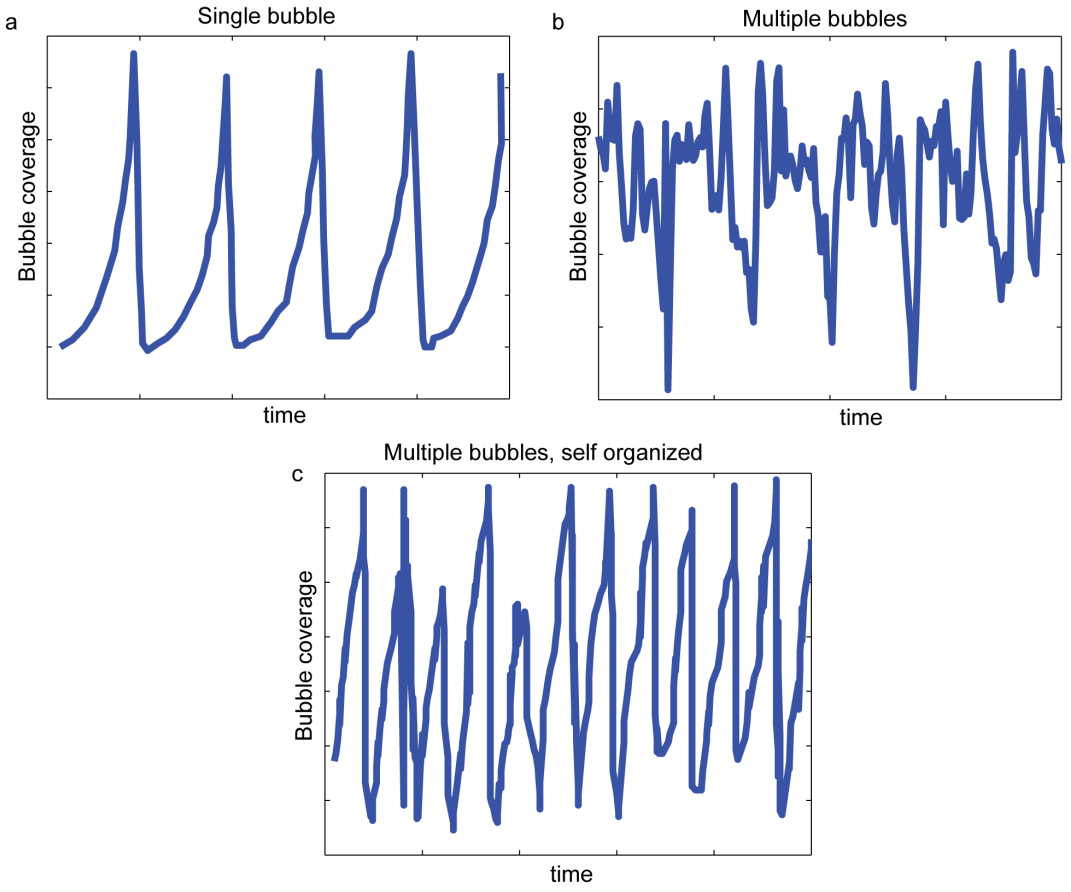

Figure 7.6: Typical time series of gas coverage for each of the bubble flow regimes described by Kiss [60].

7.5 Summary

Modelling tools and experimental work has shown a great advance over the last decades and various phenomena in complex geometries have been studied.

Due to the harsh environments of a Hall-Héroult cell, several experiments have been performed using room temperature physical models. Although instructive, some care should be issued in transferring the results to an actual cell, as similarity cannot always be claimed. Although several experimental procedures have been proposed to obtain quantitative data on industrial cells, the literature is limited to studies of the cell voltage.

Several investigations have been performed on lab-scale electrolysis cells with focus on bubble generation. On small anodes, bubbles are found to follow a sequence of nucleation, growth and coalescence events before departing from the anode, yielding a (quasi) periodic variation in cell voltage. On intermediate sized anodes, the typical behaviour is less periodic, approaching the full complexity found on industrial scales. Although lab scale systems typically are several orders of magnitude smaller, bubble departure rates appear to be similar for a given current density, the typical range being 0.3-3Hz. A common factor for all of the experimental procedures is a strong dependence upon geometry. This observation stresses the need of *detailed* knowledge of the geometry in question, if the results are to be used for a quantitative validation of a computational model.

Computational models are either global models, seeking to describe global properties based upon realistic input, or detailed models seeking to produce the input required in a global approach. Global approaches indicate that convection in the bath mainly is due to bubbles, while MHD forces give a strong contribution to convection in the metal, resulting in deformations of the bath-metal interface.

Bubble-MHD interactions have been considered only recently, indicating that this, under certain conditions, can produce forces comparable to buoyancy; the only force considered in traditional approaches.

Traditional bubble models are almost exclusively based on a Euler-Lagrange formalism in which bubbles have a specified shape, which in turn dictates their interaction with their surroundings. Despite its limitations, Lagrangian models appear to well reproduce experimental data from room temperature models and to some extent also electrolysis cells. However, the Lagrangian models fail to capture the details of large anodic bubble sheets, for which interface tracking and reconstruction is required, a requirement which can be met by for instance the VOF-method.

The open literature appears to lack the description of a fully coupled model for the flow and electromagnetic behaviour in the interpolar region. In particular, the prediction of voltage fluctuations due to the production and evolution of gaseous bubbles does not appear to be fully described, even though this parameter is the prime output from several experimental investigations.

Part II: Experiments

Outline of Part II

Part II describes the procedures and results from experimental studies performed as a part of this thesis. It is divided into two chapters which cover:

- Industrial measurements.
- Lab-scale measurements.

The industrial measurements presented in the following describe the behaviour of bubble related voltage oscillations, with particular attention to the possibility for interanode communication and age dependent effects on the voltage signal. Following the traditional experiments, a novel experimental method combining voltage measurements with high speed video recordings of the bath surface is described, allowing for a detailed interpretation of the voltage signal.

Although industrial measurements provide insight to the actual process at hand, data obtained cannot easily be used for quantitative validation, due to the sheer size of an industrial cell and the multitude of simultaneous phenomena.

In order to obtain data for validation purposes, a set of lab scale experiments are performed, mapping bubble behaviour under various conditions, as described by Eick et al. [29]. The proposed combination of voltage measurements and high speed video recordings of the bath surface identify a strong correlation between the release of anodic bubbles and observed voltage fluctuations, indicating that the voltage fluctuations on the lab scale electrolysis cell are due to single detaching bubbles.

The results from the lab-scale experiments serve as a basis for the validation of the numerical model developed in parts III and IV of this thesis.

Chapter 8

Industrial measurements

As discussed in Part I, the variations in the voltage signal are due to different internal phenomena such as gas bubble release and metal pad instabilities. On small and intermediate lab scale cells, a correlation is found between bubble detachment and peaks in voltage, while the signal originating from an industrial cell is believed to be composed of the collective behaviour of several anodic bubbles. However, as pointed out by Wang and Taberaux [133], no *direct* studies have been reported regarding the bubbling phenomena occurring in commercial cells.

Over the last decades, the control of gas evolution has been enhanced by the introduction of slots on the anode surface, forcing large anodic bubbles to depart from the anode in a preferred direction. As the anode is consumed, the slots decrease in depth before disappearing entirely towards the end of the anode life cycle. The altered anode topology can in principle introduce significant age effects, which are important if industrial measurements are to be used for model validation.

Due to the preferred direction for bubble escape, a large transfer of momentum occurs in the centre channel between the anodes. In water model experiments (cf. Einarsrud [30]), this results in a resonance between centre and side channels, which in principle can trigger a coupled bubble detachment between two anodes facing each other. If such a coupling is present (and strong), the bubble behaviour under an anode can thus not be considered as a local phenomenon; bubble behaviour on surrounding anodes would also contribute.

The above three points motivate the industrial scale experiments described in the following.

8.1 Experimental setup

The following experiments were performed at the Hydro aluminium plant in Årdal, Norway on the 26th - 29th of October, 2009. All measurements presented in the following sections

were done on cells L29 and L32. Each individual anode rod was fitted with two bolts, placed 10 cm from each other (20 cm on L32), with an insulated wire which was stretched alongside the cell to a Faraday cage, where a multilogger was placed. All measurements where done with a CR23X multilogger from Campbell Scientific, UK, and were restricted to ±50mV, with resolution 1.6 μV.

A 50 Hz Low-pass filter was applied in order to remove high frequency noise, while actual measurements were done at a sampling frequency of 10 Hz.

The anode numbering for L29 is sketched in figure 8.1

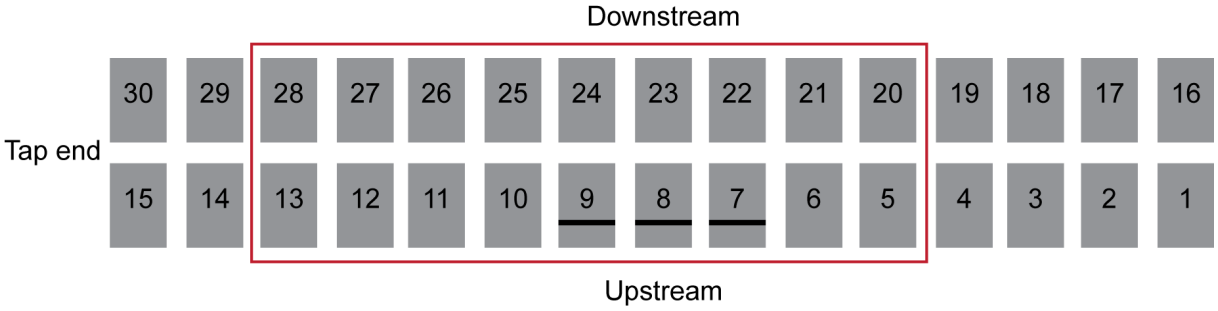

Figure 8.1: Sketch of cell L29. Anodes within the red square were instrumented. Anodes 7,8 and 9 where instrumented first after the anode change on October 27th.

8.1.1 Experiment 1: Voltage measurements

With the introduction of slotted anodes, gaseous bubbles are dominantly transported in the direction of the slots and into the centre channel. In order to identify a possible coupling, various anode configurations were investigated, as sketched in figure 8.2.

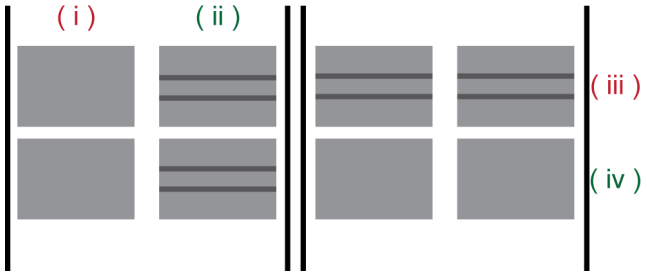

Figure 8.2: Sketch of the four different anode configurations where resonance will be investigated.

Configuration (ii) is expected to give the least correlated signal, as gas bubbles in this case are transported away from the interanode gap. Configurations (i) and (iv) are expected to

behave similarly, as slots are not present (no preferred direction for gas). Anode inclination due to metal heaving could however create some correlation in (iv) as the metal pad is expected to have a parabolic shape in this plane (cf. figure 7.5). Configuration (iii) is expected to have the most dominant correlation, if present, as both slots and metal curvature is believed to drive most of the gas into the centre channel.

The measurements from this experiment will also be used to determine the frequency spectrum of slotted and worn anodes in order to detect any shifts in frequency with increasing anode age.

8.1.2 Experiment 2: Video assisted voltage measurements

With the aid of a high speed camera, bubbles escaping through the bath surface can be counted and a bubble release frequency determined, which should correspond to the frequency spectrum of the measured signal, if the low frequency oscillations in industrial cells indeed are due to anodic bubbles.

The high speed recording of the bath surface was done with a PHOTRON 1024PCI FASTCAM digital camera, controlled by a laptop PC by means of a PCI bus. The camera was supplied with a Nikon 28-85 mm zoom-lens and mounted on a tripod. Due to the risk of damage from the magnetic fields to the laptop, it was placed in a mobile Faraday cage, as shown in figure 8.3.

Figure 8.3: Mobile Faraday cage for transport of computer.

In order to observe escaping anodic bubbles, the bath must necessarily be visible. For the current experiments, the bath was made visible by enlarging the tap hole at the end of the cell (cf. figure 8.1) and the camera was placed so that bubbles in the centre channel between

anodes 15 and 30 could be recorded[1]. The two anodes in question were instrumented as in experiment 1, allowing for simultaneous voltage measurements and bubble observations. The positioning of the camera is shown in figure 8.4.

Figure 8.4: Positioning of camera at L32. The distance from the camera to the cell is 2 meters.

8.1.3 A remark on signal analysis

As seen from figure 7.2 signals from industrial Hall-Héroult cells typically include several long and short term effects. A direct Fast Fourier Transform (FFT) of a raw signal thus includes all these effects. In order to obtain spectral information on anodic bubbles, a "clean" signal with zero mean is sought, which can be achieved by means of smoothing.

The basic idea behind smoothing is to use a moving average along the raw signal to capture the (relatively) long term variations. The smoothened signal is then *subtracted* from the original data, producing a signal which includes only the rapid, bubble related, fluctuations. For the current data, smoothing performed by replacing each point in the raw signal with the average of n adjacent points, where n is a positive (odd) integer called the smoothing width. As an illustration, a three point smooth of the raw signal ϕ at point j is

$$\bar{\phi}_j = \frac{\phi_{j-1} + \phi_j + \phi_{j+1}}{3}. \tag{8.1}$$

Close to the ends of the data set a full n-point smoothing is not possible. In order to deal with this, the number of points are gradually reduced towards the ends, i.e. the first

[1]Recording the bath surface during anode replacement was also considered. This approach was however impractical due to the limited time available during anode replacement and the risk of doing experiments under the cranes transporting heavy and hot material.

and final points of the smooth signal are identical to the points in the raw signal, while the second and second last points are determined by a 3-point smoothing etc. A 21-point smoothing is used for the current data, ensuring a sharp representation, and hence removal, of peaks with period 10 seconds and *larger* (i.e. the low frequency components).

8.2 Results from voltage measurements

The voltage measurements were done on October 27th, from 08:58 to 09:31, and on October 29th, from 09:20 to 09:40. Measurements were done with a 10Hz sampling frequency, over 3 and 4 minute intervals on the respective days.

8.2.1 Anode communication

Due to the anode changing pattern at Årdal, the idealized situations sketched in figure 8.2 were not obtainable. Instead, an attempt was made to combine anodes in such a way that the general features of a typical cell were captured. A summary the various experiments is presented in table 8.1.

Table 8.1: Measured anode configurations

Measurement (#)	Date	Anode 1 (#)	Age (days)	Anode 2 (#)	Age (days)	Comment
1	27.10.09	5	18	6	18	Close to case (ii)
2	27.10.09	20	2	21	2	Case (ii)
3	27.10.09	6	18	21	2	Close to case (iii)
4	27.10.09	6	18	27	9	Opposite anodes
5	27.10.09	12	25	27	9	Between case (iii) and (iv)
6	29.10.09	5	20	6	20	Close to (i)
7	29.10.09	11	12	12	27	Close to case (ii)
8	29.10.09	5	20	20	4	Close to case (iii)
9	29.10.09	6	20	21	4	Close to case (iii)

The correlation coefficient between the signals in each measurement is given in table 8.2.

Considering that the second highest correlation is found in measurement 4, where anodes are situated in opposite sides of the cell, table 8.2 does not give any definite conclusions regarding the correlations between anode pairs. As correlation coefficients at best give a *linear* correlation between two data sets, the analysis is extended to a graphical one, comparing the bubble signals in the measurements.

Table 8.2: Correlation coefficients between anode pairs

Measurement	Anode pair	Correlation coefficient
1	5 and 6	0.4641
2	20 and 21	0.0865
3	6 and 21	0.2587
4	6 and 27	0.3896
5	12 and 27	0.2747
6	5 and 6	-0.0371
7	11 and 12	-0.1408
8	5 and 20	0.0413
9	6 and 21	0.1657

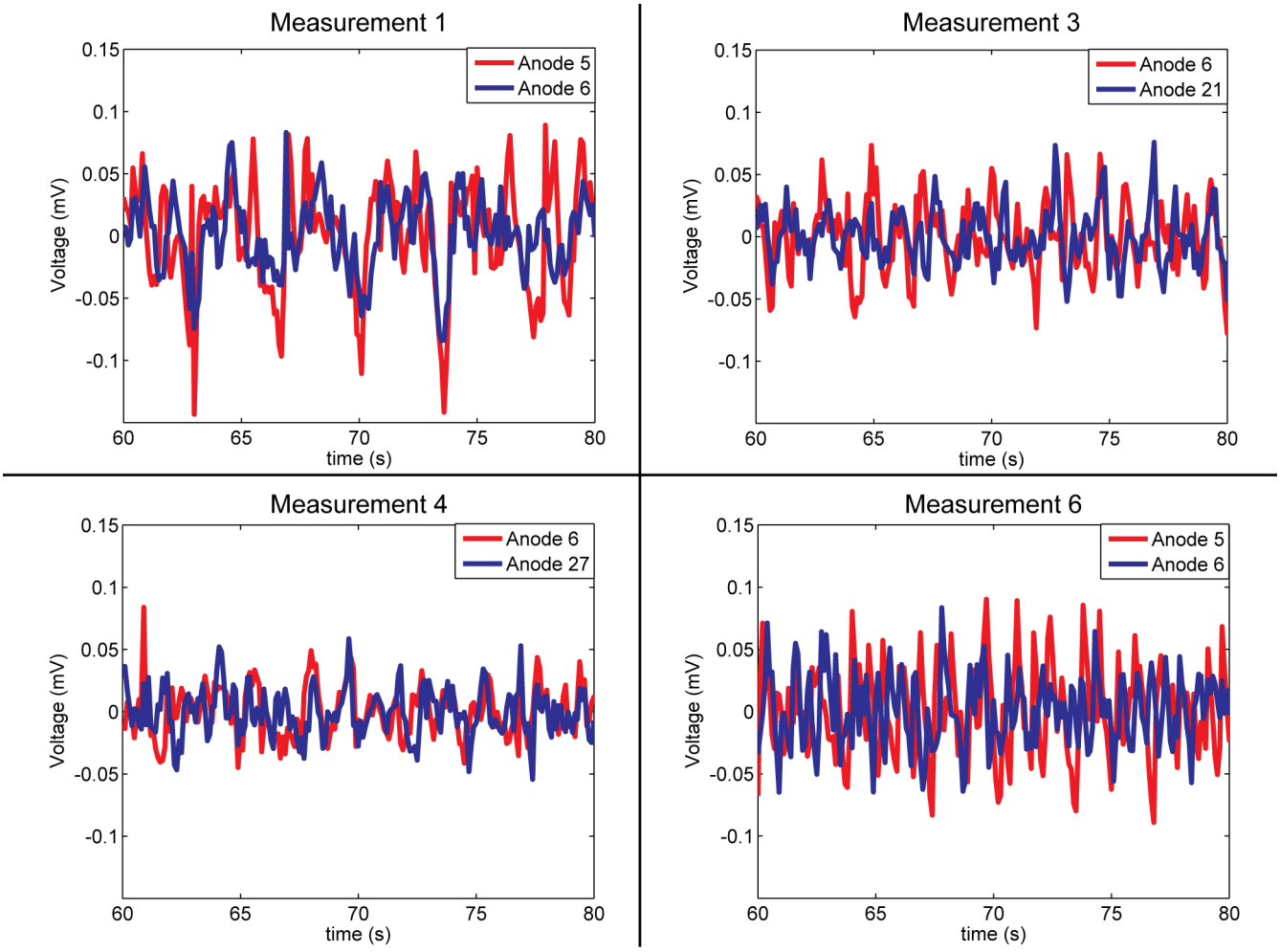

Figure 8.5: Sample bubble related voltage signal from measurements 1, 3, 4 and 6 for each of the anodes considered.

In figure 8.5, sample signals from measurements 1, 3, 4 and 6 are shown. Measurements 1 and 6 are performed on anodes located on the same side (at different times), measurement 3 is on anode pairs which are facing each other(correlation expected), while measurement 4 is on anodes at opposite sides of the cell (reference measurement, no correlation expected).

As seen from figure 8.5 (and table 8.2) the current data does not indicate that any form of correlation between anodes, suggesting that coupling between anode pairs due to bubble detachment is insignificant.

8.2.2 Frequency analysis of data

Sample FFT spectrums are shown in figure 8.6, while a summary of essential results for all the measurements are given in tables 8.3 and 8.4. The signal domain is defined as $4\Sigma_U$, Σ_U being the standard deviation of the voltage signal, representing the typical amplitude of the signal[2].

Table 8.3: Summary of frequency analysis for measurements done on 27.10.09. 1st and 2nd frequency denote the most dominant and second most dominant frequency found in the signal, respectively.

Meas. #	Anode #	Mean Voltage mV	1st frequency Hz	2nd frequency Hz	Signal domain ($4\Sigma_U$) mV
1	5	3.65	0.55	0.65	0.47
1	6	3.92	0.77	0.37	0.23
2	20	2.84	0.81	0.86	0.20
2	21	3.71	0.51	0.54	0.14
3	6	3.82	0.73	0.82	0.23
3	21	3.77	0.67	0.58	0.18
4	6	3.91	0.73	0.84	0.22
4	27	3.46	0.47	0.61	0.35
5	12	3.53	0.71	0.56	0.57
5	27	3.46	0.38	0.77	0.32

Evidently, as seen from the tables and figure 8.6, the measured voltage signal has dominant frequencies in the range 0.5-1.5 Hz.

[2]Thus based on (minimum) 94% of the measured points, assuming a normal distribution around the mean.

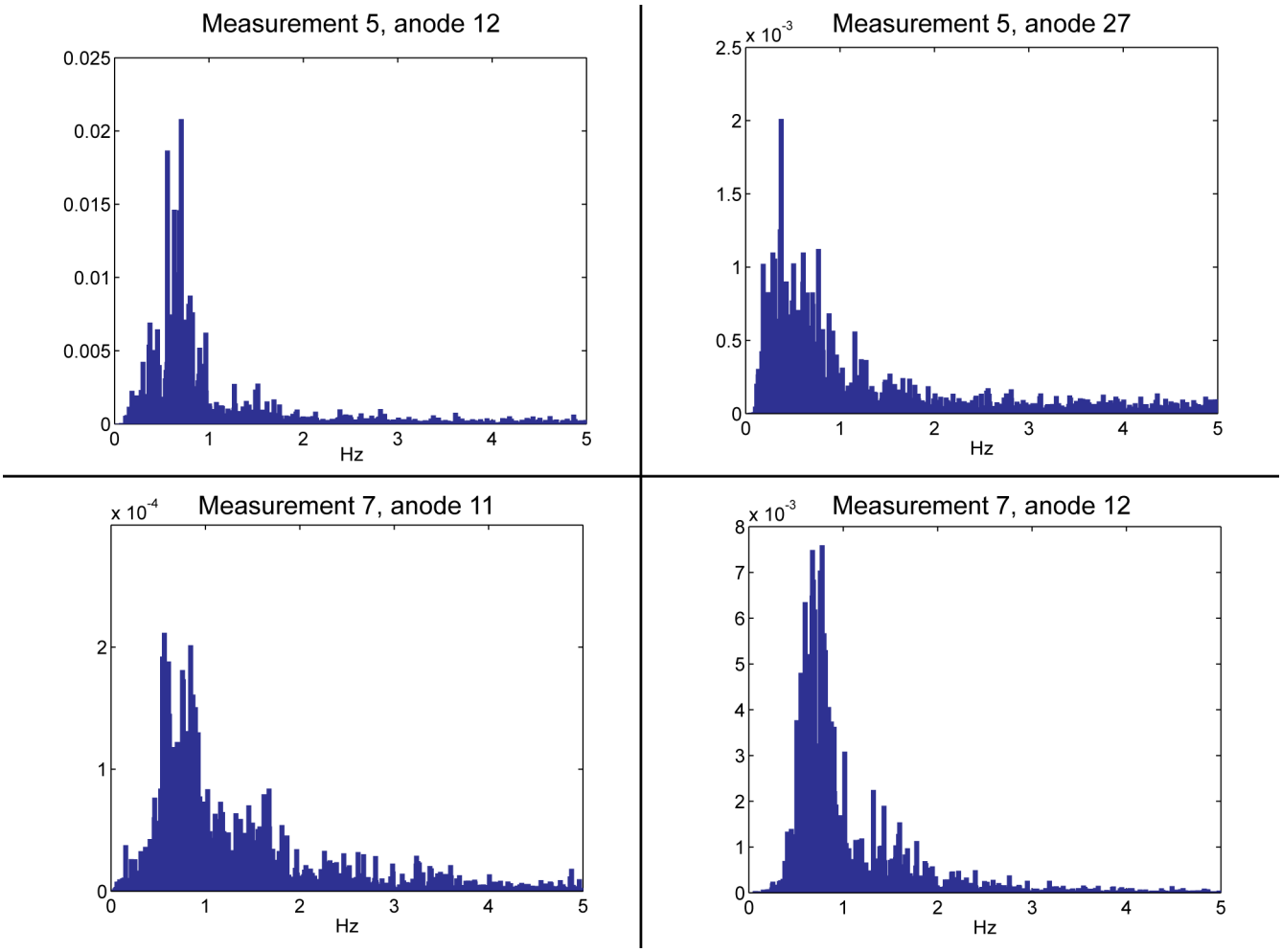

Figure 8.6: Spectra of signals to anodes 12 and 27 (measurement 5, top) and anodes 11 and 12 (measurement 7, bottom).

Table 8.4: Summary of frequency analysis for measurements done on 29.10.09. 1st and 2nd frequency denote the most dominant and second most dominant frequency found in the signal, respectively.

Meas. #	Anode #	Mean Voltage mV	1st frequency Hz	2nd frequency Hz	Signal domain ($4\Sigma_U$) mV
6	5	3.45	1.59	0.76	0.22
6	6	3.83	1.88	1.82	0.17
7	11	3.39	0.57	0.85	0.09
7	12	3.70	0.78	0.67	0.39
8	5	3.45	1.50	1.76	0.26
8	20	3.01	0.64	0.77	0.10
9	6	3.81	1.79	1.98	0.17
9	21	3.56	0.63	0.83	0.10

8.2.3 Age dependent effects

Figure 8.7 shows the mean voltage, signal domain and dominating frequencies plotted against anode age.

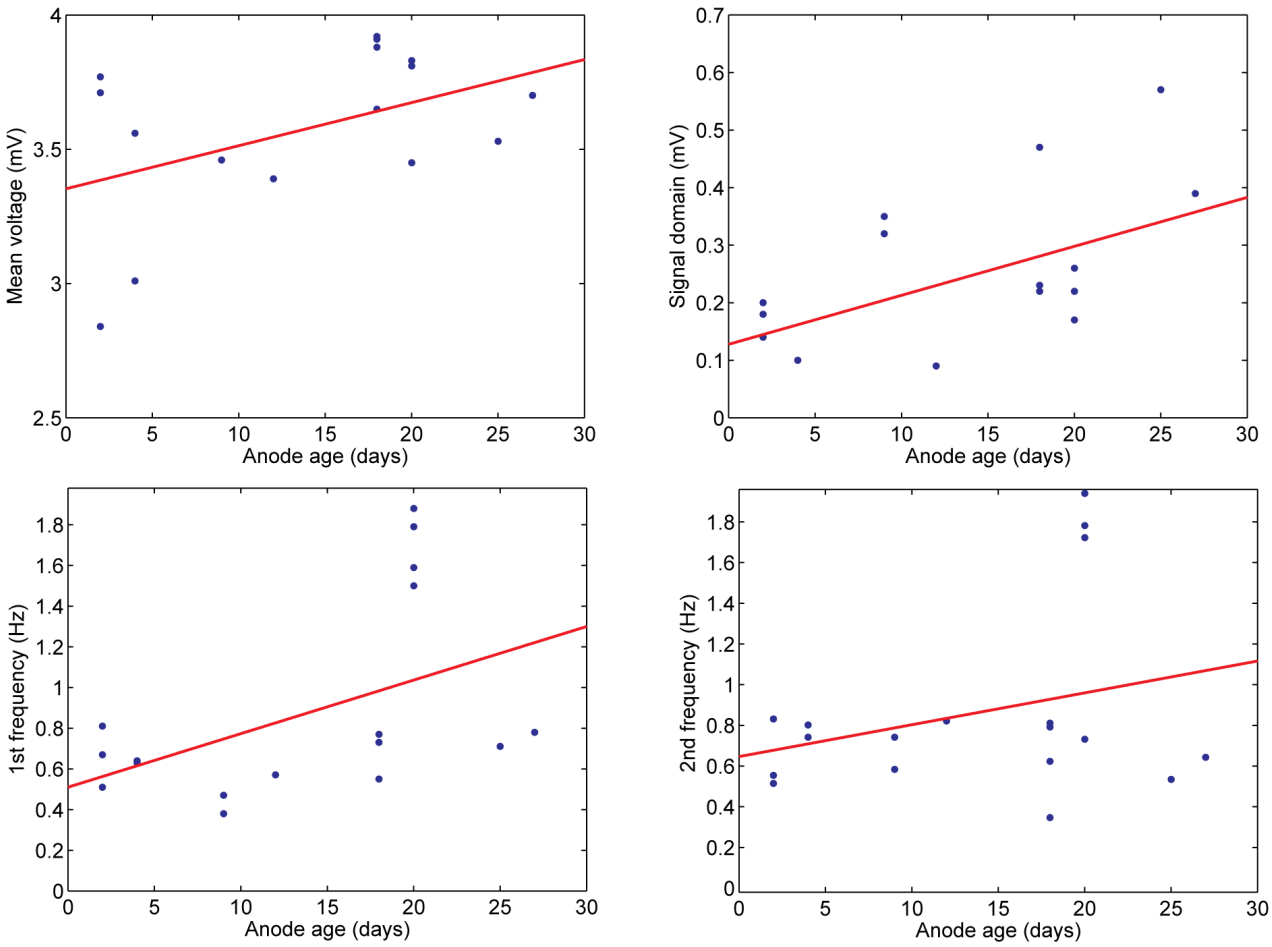

Figure 8.7: Summary of age dependent effects in industrial measurements. The figure shows the evolution of mean voltage (top left), signal domain (top right), 1st frequency (bottom left) and 2nd frequency (bottom right) as a function of anode age. A trend line is given in each plot.

As seen from the above figure, all parameters considered here appear to increase with anode age. The large increase in mean voltage is strongly influenced by the two outliers seen in the lower left corner, which correspond to the measurements on anode 20. The lower voltage suggests that the anode is drawing less current, i.e. it is set too high initially. Omitting these outliers yields a mean voltage which is close to constant, as expected. The influence of these two points on the other graphs shown in figure 8.7 is minimal.

As expected from the findings of Keniry et al. [59], the spread in frequencies appears to increase with anode age, yielding, on average, higher frequencies for older anodes. Opposed to the results of Keniry et al. [59], the signal domain (figure 8.7, top right) *increases* with increasing anode age. This effect is credited to diminishing influence of the slots, allowing for larger projected bubble areas and hence a greater effective resistance as anodes grow older.

8.2.4 Short term variations

The variation in bubble frequency is visible both on a long and short term perspective. As pointed out by Wang and Tabereaux [133]; the bubble release time and magnitude of the voltage oscillation are not constant *even at the constant electrolysis current*, indicating that the frequencies and amplitudes of the voltage signal varies within a certain range. This variation becomes evident when splitting a given signal into segments and analysing each segment individually. Such an analysis is shown in figure 8.8, where the signal from measurement 9, anode 21 is split into 12 segments of 20 seconds.

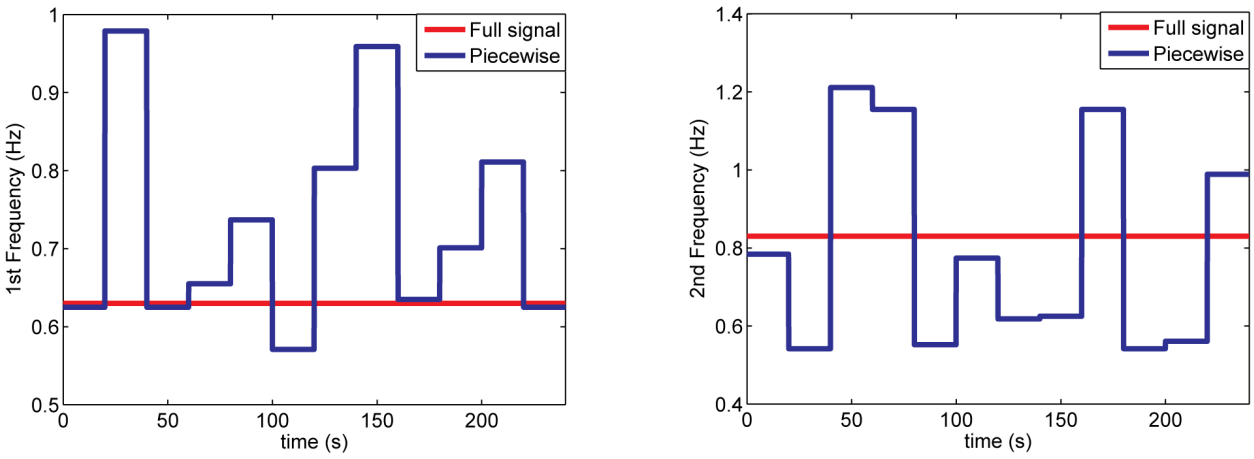

Figure 8.8: Variations in 1st and 2nd most dominating frequencies over segments of 20 seconds for measurement 9, anode 21. Red lines represent frequencies obtained by a FFT of the *complete* signal.

As seen from the above figure, the dominating frequencies vary significantly over the time the voltage signal is measured. Frequencies presented in tables 8.3 and 8.4 should thus be interpreted as representative *mean* frequencies for a given measurement.

8.3 Results from video assisted voltage measurements

The camera was positioned as shown in figure 8.4 at L32, in such a way that anodes 15 and 30 were visible, as shown in figure 8.9. Anode 15 was relatively young, 5 days old, while anode 30 was 22 days old. The slots of anode 30 where not visible above the bath surface, resulting in massive bubble release through the bath in the centre channel. Approximately 5 cm of the slots of anode 15 were visible above the bath.

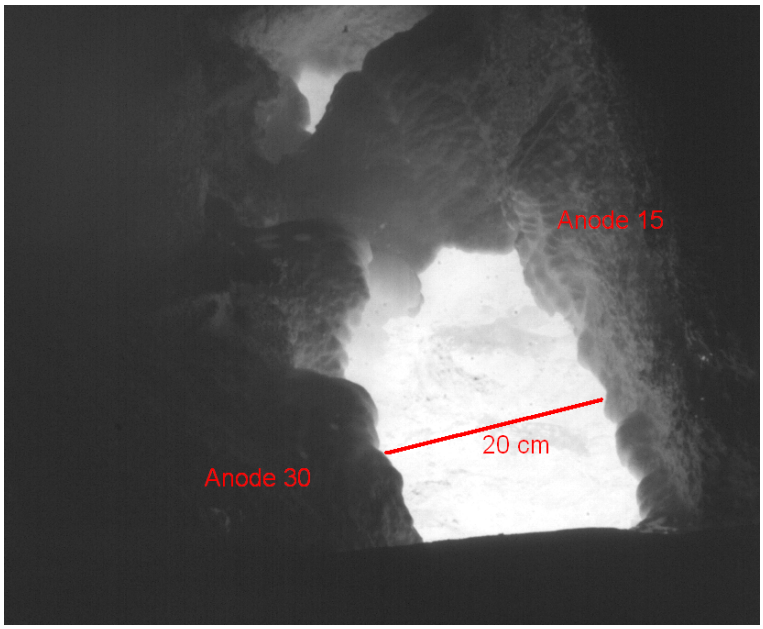

Figure 8.9: View of bath surface through tap hole in L32.

Both of the anodes shown in figure 8.9 were connected to the multilogger, which had the same setup as in experiment 2, allowing voltage to be logged simultaneously to the high speed recording[3]. The camera was set to record at 250 fps, yielding 25.6 seconds of footage (6400 frames). Only two recordings were performed, due to the slow transfer of files from the camera buffer to the laptop.

Essential results from voltage measurements to anodes 15 (two measurements) and 30 (one measurement)[4] are given in table 8.5. Spectra for measurement 11 are shown in figure 8.10.

[3]The higher mean voltage seen in table 8.5 is due to a larger distance between the bolts where the logger was attached.

[4]The reason for having only one measurement to anode 30 is that the contact between the logger and anode 30 unfortunately was broken during the first measurement.

Table 8.5: Summary of frequency analysis for video assisted measurements done on 29.10.09. 1st and 2nd frequency denote the most dominant and second most dominant frequency found in the signal, respectively.

Meas. #	Anode #	Mean Voltage mV	1st frequency Hz	2nd frequency Hz	Signal domain ($4\Sigma_U$) mV
10	15	7.92	0.77	0.69	0.26
11	15	7.64	0.56	0.68	0.28
11	30	6.72	0.56	0.64	0.14

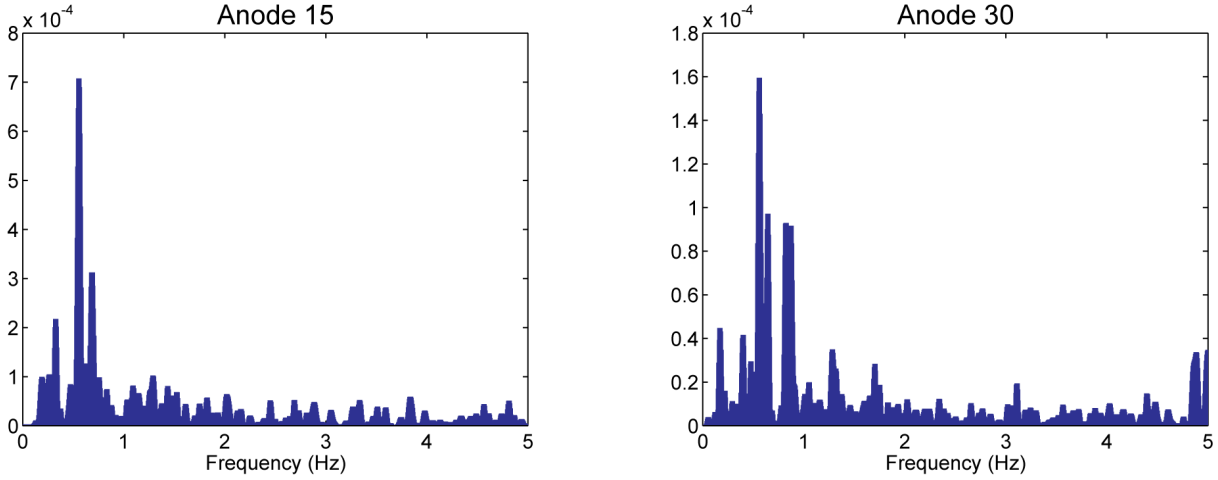

Figure 8.10: Spectra from measurement 11, anodes 15 and 30.

The frequency values obtained from the FFT consistent with measurements from L29, with dominant peaks in the range 0.4-1.0 Hz and lesser peaks in the range 1-2 Hz. Though both signals from measurement 11 show very similar frequencies, there appears to be little correlation between the signals (correlation coefficient of 0.23).

8.3.1 Results from recordings

A detailed analysis of each frame reveals a total of 99 and 110 bubbles for each of the recordings, respectively.

Evidently, the total number of bubbles counted in the centre channel originate from *both* anode 15 *and* 30, while the measured voltage signal is related to each individual anode. Detailed observations of the recordings reveal that escaping bubbles have a tendency to leave the bath in preferred directions as shown in figure 8.11.

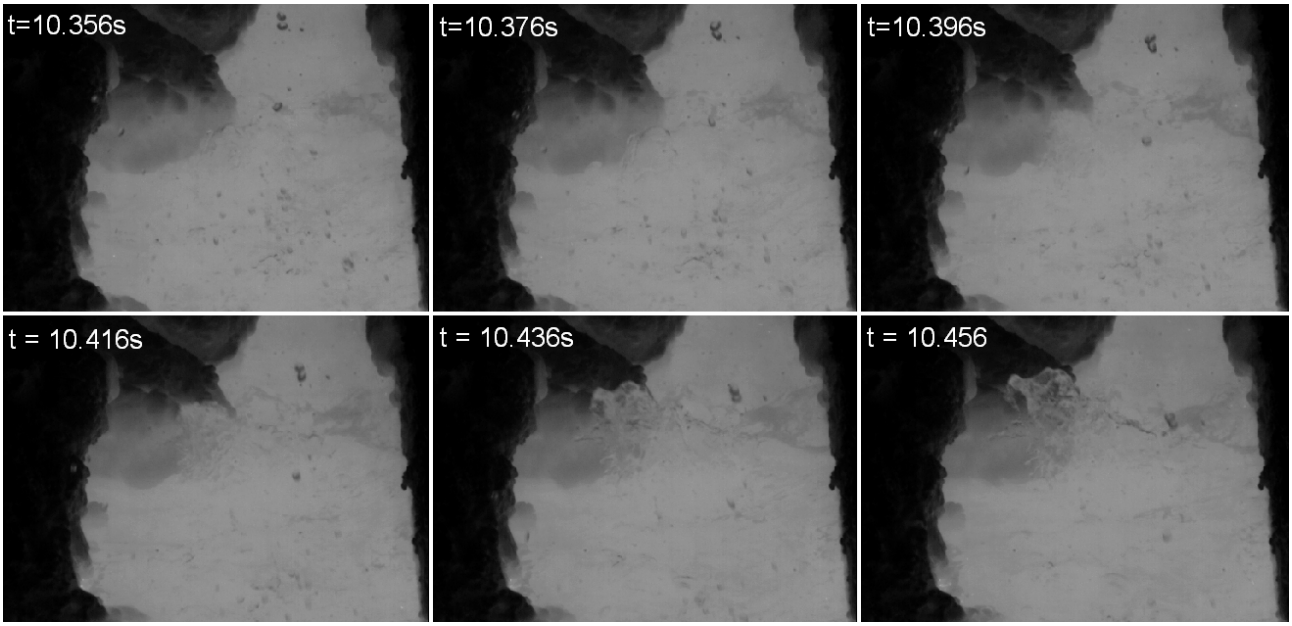

Figure 8.11: Sequence showing bubble leaving bath with dominant left bound motion.

This preferred direction of the escaping bubbles is due to the ("horizontal") momentum accumulated by the bubble during its travel under the anode. This notion is strengthened further by noting that most bubbles escape through the *centre* of the centre channel, suggesting that they move in a diagonal trajectory from the anode edge, rather than creeping alongside the anode. Hence, by observing the preferred direction of the escaping bubbles, it is possible to relate individual bubbles to each individual anode. The bubble distribution for each anode is given in table 8.6. The unaccounted bubbles in table 8.6 (15 for measurement 10 and 10 for measurement 11) did not have any preferred direction and could in principle originate from any of the two anodes.

In addition to the distinction between right bound and left bound bubbles, the influence of the slots was clearly visible as shown in figure 8.12.

As seen from the number of bubbles in table 8.6, typical frequencies are almost a factor 2 higher than those found by a FFT of the corresponding signal. As noted by Kiss and

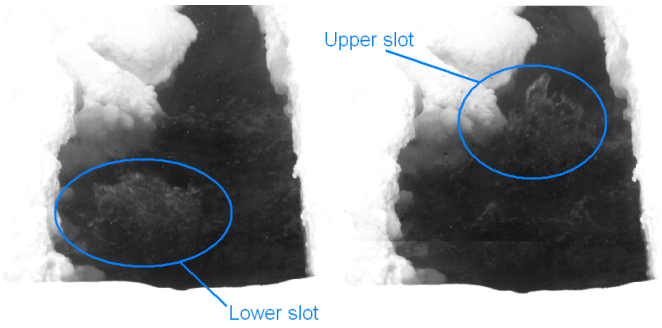

Figure 8.12: Distinction between bubbles originating from lower and upper slots. Colours have been inverted for clarity.

Table 8.6: Distribution of bubbles between individual anodes and slots.

Measurement	Anode	Total number of bubbles	Upper slot	Lower slot
10	15	48	30	18
10	30	36	22	14
11	15	50	27	23
11	30	50	24	26

Poncsak [62], the frequencies of *individual* bubbles are difficult to observe. Besides the influence from their release at the anode edge, interactions between moving bubbles and their coalescence dominate the spectrum of the voltage fluctuations.

Based on these findings, a hypothetical collective bubble signal is reconstructed based on the observed bubble release. The procedure used is as follows:

1 The time from which a bubble appears on the surface to it escapes is registered.

2 The bubble time, combined with the extent of the splashing give an indication of the bubble size, which is divided into three classes (0.25, 0.5 and 1).

3 The residence time under the anode is approximated from the bubble escape time.

4 Based on the approximated residence time and the size class, a time dependent coverage factor is obtained for each individual bubble.

5 The total signal is computed from the sum of each individual bubble.

6 The reconstructed signal is normalized and a FFT is applied in order to determine dominating frequencies.

Figure 8.13a shows the time of escape for bubbles originating from anode 15, measurement 11. The magnitude of the signal is determined from the size of each bubble. The escape time of the bubbles is found to be somewhat irregular, bubbles appearing as bursts, rather

than at a distinct frequency. This is as expected, as measured frequencies also vary with time as shown in figure 8.8. Furthermore, several of the peaks are separated by very small time intervals, close to the sampling time used in the voltage measurements. This overlap becomes even more visible when a linear relation between the first appearance of the bubble and its time of escape is plotted (assuming the appearance of the bubble has zero magnitude), as in figure 8.13b.

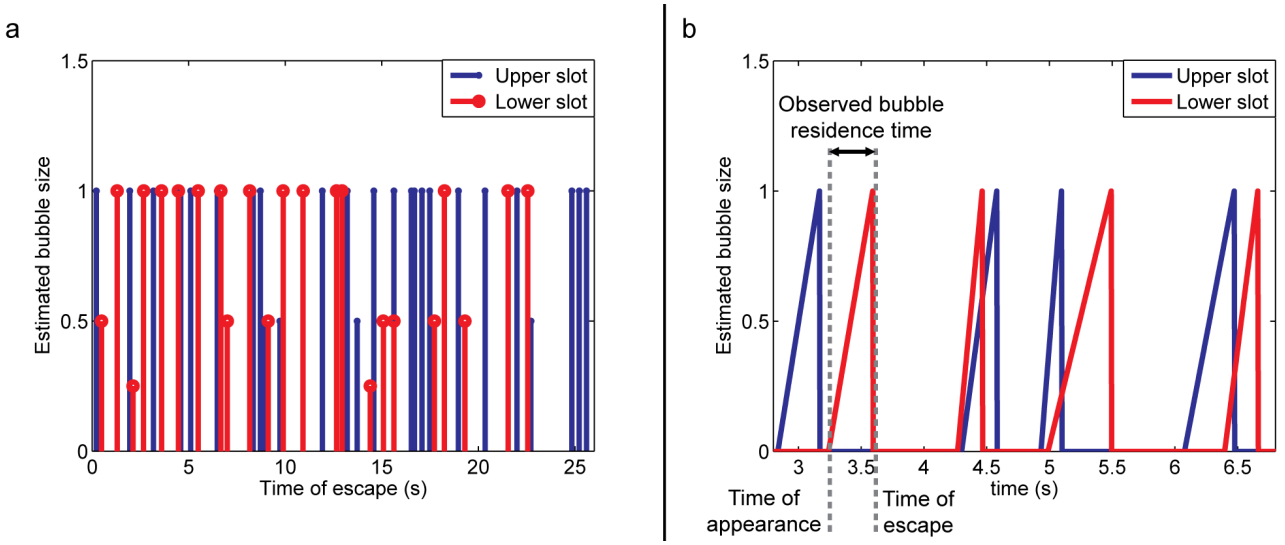

Figure 8.13: Observed time and estimated size for bubbles escaping from anode 15, measurement 11 (a), and observed bubble residence time (b).

As noted by Kiss and Poncsak [62] and observed in water models and simulations (cf. Einarsrud [30]), the nature of the bubble changes dramatically when detaching at the anode edge; from an elongated flat bubble under the anode to a more spherical shape in the center channel. In effect, this *increases* the residence time of the bubble under the anode, compared to its residence time in the centre channel (i.e. the time from its appearance to its escape). The bubble residence time for an equivalent volume bubble under the anode can be approximated by the simple relation

$$t_{anode} = t_{channel} \frac{\bar{U}_{channel}}{\bar{U}_{anode}} \frac{L_{anode}}{L_{channel}}, \tag{8.2}$$

where $\bar{U}_{channel}$ and $\bar{U}_{anode}$ represent average bubble velocities in the channel and under the anode and L_{anode} and $L_{channel}$ represent typical length scales. The velocity in the side channel is comparable to that under the anode, cf. Einarsrud [30], the length scales are, however, significantly different; the typical anode length being of order 100 cm, while the typical bath height is 20 cm. Hence, the approximated bubble residence time under the anode is

$$t_{anode} \approx 5 t_{channel}, \tag{8.3}$$

resulting in reconstructed bubble coverage curves as shown in figure 8.14a. The sum of each individual bubble gives an indication of the bubble coverage under the anode, as shown in figure 8.14b, which in turn should correspond to the observed variations in *voltage*.

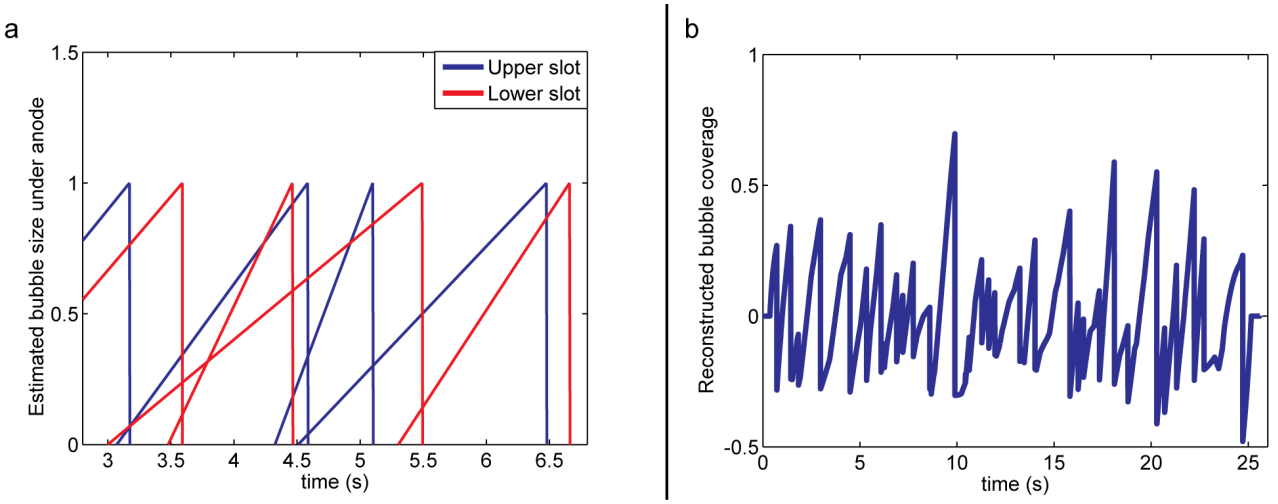

Figure 8.14: Estimated residence time under anode 15, measurement 11 (a), and resulting collective bubble coverage (b).

Comparing the reconstructed signal in figure 8.14b to actual voltage measurements a good qualitative agreement is found. A FFT of the reconstructed signal yields dominating frequencies of 0.47 and 0.70 Hz, which is close to that of the measurements (cf. table 8.5), suggesting that the measured frequency indeed is due to the collective behaviour of the anodic bubbles, although individual bubbles are found to release at significantly higher frequencies.

The influence of bubble residence time

The most critical parameter in the above analysis is without doubt the approximation of the bubble residence time. Figure 8.15 shows the spectrum of the reconstructed signal for three different ratios of $t_{anode}/t_{channel}$.

Evidently, the bubble residence time has a large impact on the resulting spectrum; lower residence times yielding higher frequencies. Recalling how the bubble residence time is defined (equation 8.2), a reduced residence time is equivalent to a shortening of the anode in the bubble flow direction. A similar frequency increase is predicted by Kiss [62], showing an increase in the dominating frequency of a factor 4 when the aspect ratio of the anode is changed correspondingly. This strong influence stresses the need for detailed knowledge of the geometry in question, if experimental results are to be used for validation purposes.

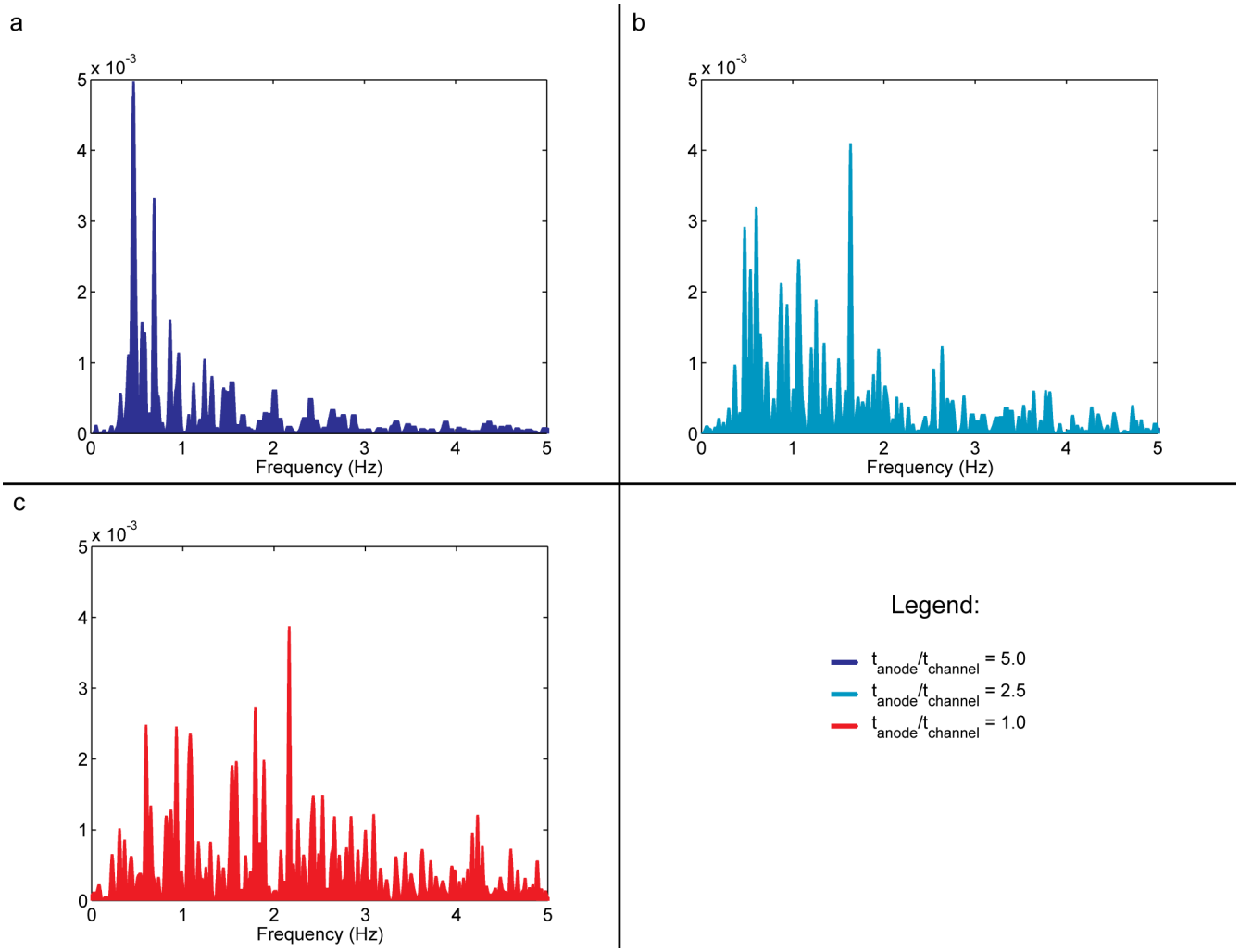

Figure 8.15: Spectrum of reconstructed bubble signal for anode 15, measurement 11. Influence of varying bubble residence time.

8.4 Summary of industrial scale measurements

Experiments have been performed on an industrial cell, identifying bubble related signals with frequencies in the range 0.5 to 2 Hz responsible for as much as ±5% of the voltage variation. Results indicate that the bubble related voltage oscillations increase in both frequency and magnitude with increasing anode age, the latter of which is believed to be due to the diminishing influence of slots as anodes age.

With aid of high speed video recordings of the bath surface, it is shown that the measured voltage signal is due to the collective behaviour of several anodic bubbles, which individually are found to release at frequencies significantly larger than those present in the measured signal.

No significant correlation is found between anode pairs in different configurations, suggesting that interanode communication, if present at all, is a second order effect. This, combined with the observations regarding the huge impact of the collective motion of bubbles suggests that bubble models for individual anodes are meaningful, also with respect to industrial applications, given that the geometry is adequately described.

Chapter 9

Lab scale measurements

As seen from the previous chapter, industrial measurements are challenging due to the inherently complicated processes occurring in a cell. Although quantitative data and interpretations are obtainable, uncertainties related to geometry, localized effects and coupled phenomena makes the use of these data at best suited for only a *qualitative* validation of a numerical model.

In order to obtain data on anodic bubbles under controllable conditions with known geometry, a series of lab-scale experiments were conducted with objective to study bubble release and voltage behaviour under varying current density, anode inclination and anode-cathode distance (ACD), down to very low values.

In the following sections, the setup as of Eick et al. [29] is discussed for reference, followed by an analysis of selected cases. Finally, a detailed analysis of bubble phenomena using high speed video recordings is given.

9.1 Experimental setup

An anode with an active area of 10 by 10 cm was made from industrial carbon and placed in a cylindrical graphite crucible lined with Si_3N_4-SiC with inner diameter 28 cm. The anode was fixed to a steel rod so that the anode-cathode distance could be varied. By means of a jack, the heating furnace containing the graphite crucible could be lifted on one side, allowing for inclination angles up to 10 degrees. The long-sides of the anode where fitted with Si_3N_4-plates in order to force gas bubbles to escape from either of the short sides.

The inclination forces bubbles to be released at a specified side, where a gas collection chamber allowed for analysis of gaseous species.

To avoid phenomena related to the metal pad, a wettable cathode element was used, as proposed by Haarberg et al. [48], allowing for operations at very low ACD without influence of metal droplets on the cathode.

Initially, 6.7 kg of bath (11wt% excess AlF_3, 5wt% CaF_2 and 4wt% Al_2O_3) was melted and standard industrial alumina was added at regular intervals. The typical alumina concentration during operation was in the range of 8–9 wt%.

The anode was connected to a power supply (type LAMBDA ESS) allowing for currents up to 500 A. The cell voltage was logged at 50Hz using a CR23X multilogger from Campbell Scientific, UK, with resolution 1.6 μV. The motion of the bath interface due to escaping bubbles was recorded using a PHOTRON 1024PCI FASTCAM digital camera, controlled by a laptop PC by means of a PCI bus. The camera was supplied with a Nikon 28-85 mm zoom-lens and was mounted on a tripod. The experimental setup is shown schematically in figure 9.1.

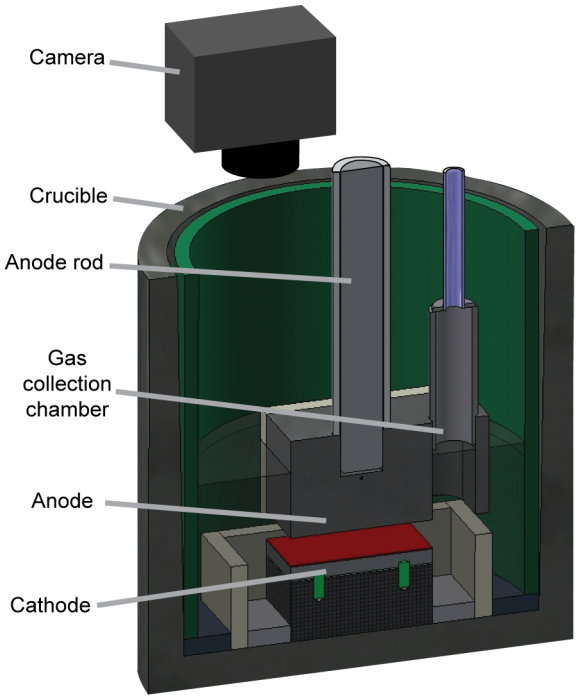

Figure 9.1: Overview of laboratory cell as of Eick et al. [29]

The process parameters were changed in a randomized way during the experiments, following a planned schedule. The range of the parameters were:

- Current density (CD): 0.8, 0.95 and 1.1 A/cm^2.
- ACD: 1.5, 2.0, 3.0 and 4.0 cm.
- Inclination angle (inc): 0, 2, 4 and 10°.

9.2 Selected results on voltage behaviour

Detailed results concerning the influence of the various parameters investigated in the experiments can be found in Eick et al. [29] and only a selected set of data is included here for reference.

A summary of the influence of the various experimental parameters on the frequencies and magnitude of the voltage signal is given in figure 9.2. As seen from the figure, the large span in experimental parameters produce a corresponding span in the output, dominating frequencies varying from 0.2 to 1.0 Hz and signal domain varying from 0.03 to 0.43 V.

Measurements with 4° inclination are omitted from figure 9.2 as these were performed with constant ACD=3cm and CD=0.95 A/m^2, cf. Eick et al. [29].

Both frequencies and amplitudes *increase* with increasing current densities, as expected due to increased gas production rates. No general trend is however identified regarding the ACD and its influence on the voltage oscillations. Considering variations in the inclination angle, the mean current density is constant (CD=0.95 A/m^2) for each set of experiments, thus enabling a direct comparison between mean frequencies and signal domain for each inclination, as shown in figure 9.3. As seen from the figure, increasing inclination angles tends to increase the frequencies of the signal, as buoyancy becomes increasingly important, while the signal domain decreases, indicating changes of the bubble topology.

For validation purposes, a subset of the lab scale experiments are chosen, focusing on selected points. As the main concern of the current thesis is bubble generation and MHD, the current density (CD) is of major interest as it governs the Lorentz forces (as of equation 4.3) and gas generation (as of equation 4.4). All three current densities from the experiments are thus considered. The ACD and anode inclination (inc) are restricted to typical industrial values, i.e. 2-5 cm and 1-4°, respectively.

As noted by Eick et al. [29] (and expected from Wang and Taberaux [133] and Keniry et al. [59]), the voltage behaviour changes with time as the initially sharp corners of the anode become rounded. In order to capture this variation, each selected setup is considered at different times.

Essential results for experiments meeting the above requirements are given in table 9.1, while sample voltage curves are shown in figure 9.4. These data are to be used for validation of the bubble model presented in Part IV.

As seen from table 9.1, the typical frequencies obtained are in the range 0.25-0.6 Hz, lower than that found on industrial scales, but within the range found on other lab scale experiments. As the anode used in the current experiments was unslotted, the expected behaviour of a decreasing *signal domain* with increasing anode age is found (cf. Eick et al. [29] for further details). Results indicate that elevated frequencies are to be expected with increasing anode age, although the trend is not as clear as for the signal domain.

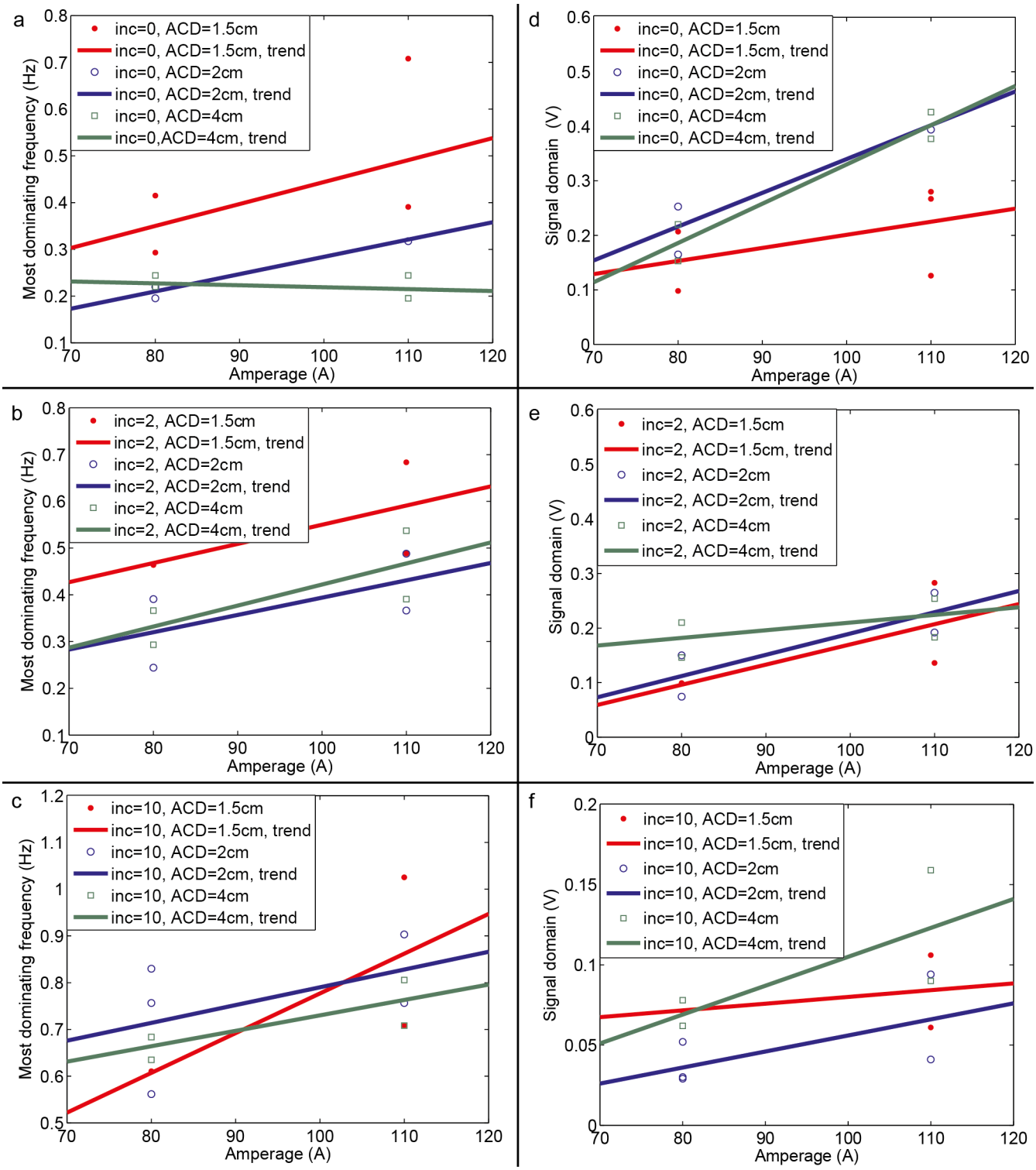

Figure 9.2: Summary of results from laboratory cell described in Eick et al. [29]. Figure shows dominating frequencies (a-c) and signal domain (d-f) (symbols) as a function of amperage for various operating conditions. A trend line (solid lines) is added for each data set.

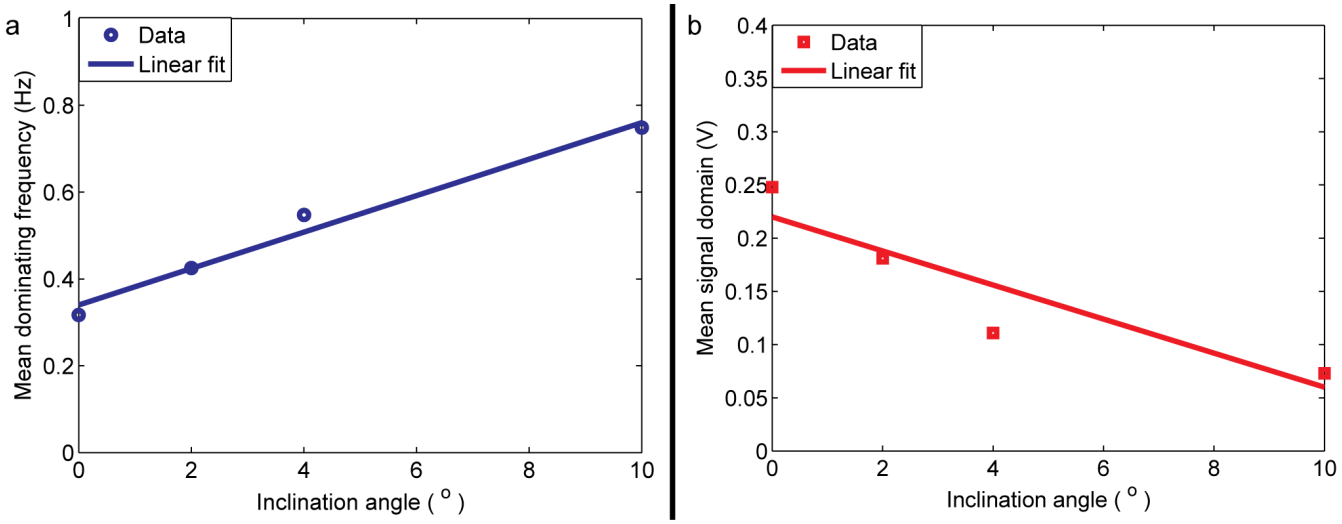

Figure 9.3: Influence of inclination on dominating frequencies (a) and signal domain (b) on laboratory cell described in Eick et al. [29]. The data (symbols) is represented as the average of all values measured at a given inclination.

Table 9.1: Results from selected lab scale experiments. 1st and 2nd frequency denote the most and second most dominant frequency found in the signal, respectively. Results are sorted by replicates.

Exp. (#)	Time (hh:mm)	CD A/cm^2	ACD (cm)	inc (°)	Mean voltage (V)	1st frequency (Hz)	2nd frequency (Hz)	Signal domain ($4\Sigma_U$) (V)
3	10:24	0.95	3	4	3.36	0.42	0.29	0.13
25	14:24	0.95	3	4	3.31	0.49	0.39	0.08
5	10:51	1.10	2	2	3.29	0.37	0.32	0.24
28	14:47	1.10	2	2	3.18	0.49	0.34	0.16
8	11:23	0.80	4	2	3.26	0.29	0.20	0.16
31	15:07	0.80	4	2	3.27	0.29	0.37	0.11
14	12:23	0.80	2	2	2.78	0.34	0.27	0.13
37	16:00	0.80	2	2	2.77	0.24	0.66	0.06
22	13:46	1.10	4	2	3.93	0.39	0.54	0.22
44	16:43	1.10	4	2	4.02	0.61	0.53	0.14

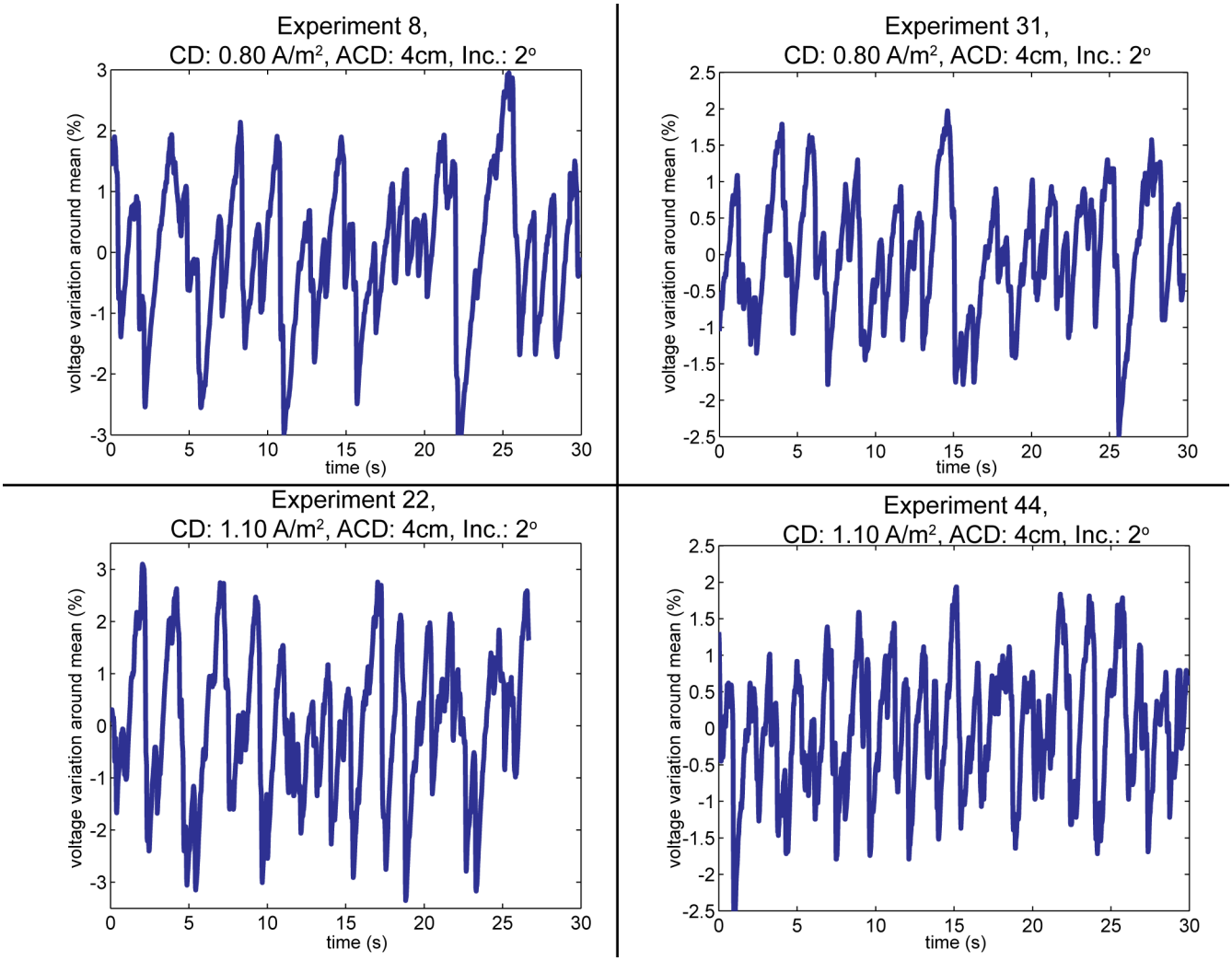

Figure 9.4: Sample voltage variation from lab scale experiments corresponding to table 9.1. Voltage variation defined as $(U - \bar{U})/\bar{U}$, where $\bar{U}$ is the mean voltage.

9.3 Bubble release behaviour

For a horizontal anode (i.e. zero inclination), bubbles could release at either of the short sides of the anode, allowing for their observation with a high speed camera as indicated in figure 9.1. Eight experiments were performed, summarized in table 9.2.

Table 9.2: Summary of conditions for video assisted lab-scale measurements.

Experiment (#)	Time (hh:mm)	CD (A/m^2)	ACD (cm)
1	08:51	0.80	4
2	10:07	0.80	4
19	13:37	1.10	1.5
20	13:46	0.80	4
27	14:48	1.10	4
41	16:23	1.10	1.5
42	16:31	0.80	4
43	16:39	0.80	1.5

As for the inclined experiments presented previously, the cell voltage was monitored during the experiments. In parallel with the voltage measurements, the motion of the bath surface was recorded in order to relate voltage events to escaping bubbles. A typical evolution of the bath surface due to an escaping bubble is shown in figure 9.5.

Two uncertainties exist when comparing observed events (i.e. visual observation of escaping bubble) and events in the measured signal (i.e. a sharp drop in voltage)

- Both the camera and multilogger where started manually at a given time.
- The (size dependent) rise time of the bubble through the side channel results in a mismatch in the times between its detachment from the anode (measured event) and escape-time at the surface (observed event).

Due to the size of the bubbles and the large density difference, the rise time is expected to have little influence compared to the uncertainty due to the manual operation of the equipment, which is estimated to $\pm$ 0.25s.

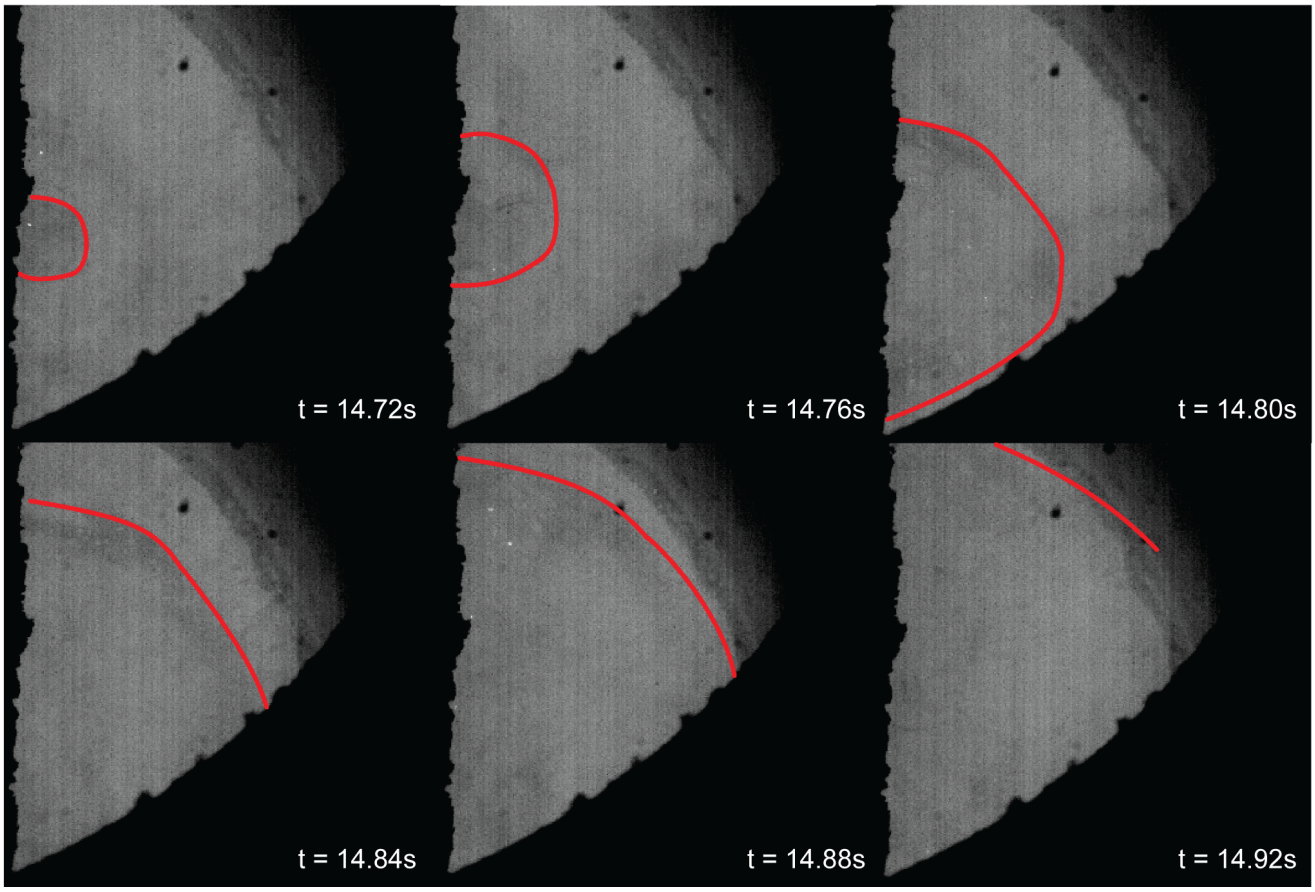

Figure 9.5: Bubble escape during horizontal cell operation, resulting in a perturbation the bath surface. Resulting surface wave is emphasized with solid red line.

The time of observed bubble events are compared to sample measured voltage signals in figure 9.6.

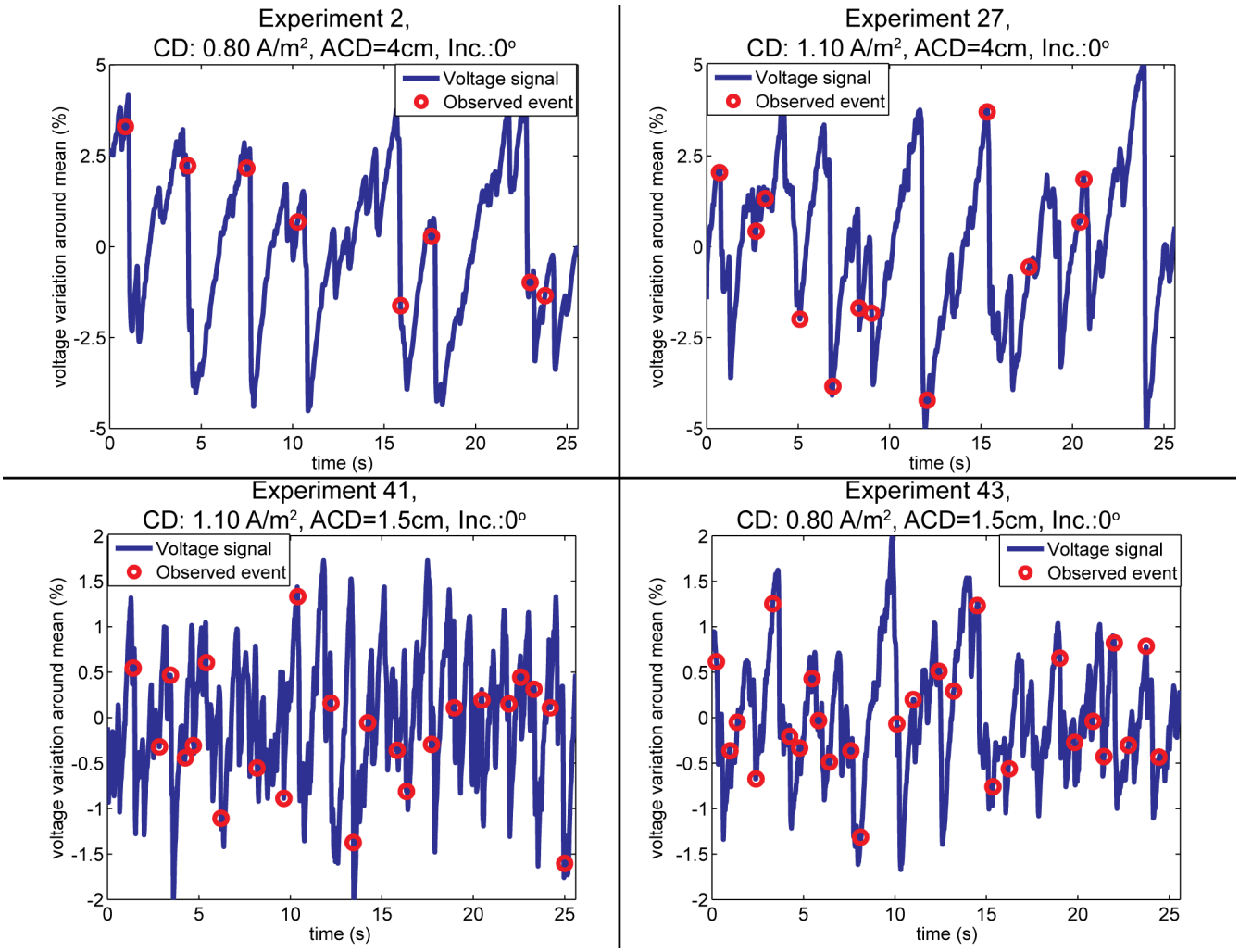

Figure 9.6: Variation in voltage signals (solid lines) and observed bubble events (red circles) for selected experiments. The uncertainty in observed events, ±0.25s is indicated by the size of the red circles. Voltage variation defined as $(U - \bar{U})/\bar{U}$, where $\bar{U}$ is the mean voltage.

As seen from figure 9.6, there is a good correspondence between observed and measured events, observed events accounting for approximately 95% of the fluctuations with amplitude larger than ±0.5% of the average voltage.

9.3.1 Frequency analysis

Essential results from the measured voltage signals and estimated frequencies from observations[1] are given in table 9.3.

Table 9.3: Results from video assisted lab scale experiments. 1st and 2nd frequency denote the most and second most dominant frequencies found in the signal, respectively.

Exp. (#)	Mean voltage (V)	1st frequency (Hz)	2nd frequency (Hz)	Signal domain ($4\Sigma_U$) (V)	Observed frequency (Hz)
1	3.37	0.20	0.29	0.28	0.39
2	3.38	0.15	0.34	0.27	0.31
19	3.15	0.39	0.34	0.22	0.43
20	3.31	0.22	0.17	0.19	0.39
27	4.04	0.24	0.56	0.33	0.47
41	3.03	0.71	0.56	0.09	0.90
42	3.33	0.37	0.24	0.15	0.70
43	3.09	0.55	0.45	0.07	0.66

As seen from table 9.3, there are some discrepancies between observed frequencies and those obtained by a FFT of the signal, although not as large as those found on industrial scale. Due to the smaller size of the lab scale anode, it is unlikely that the influence of overlapping bubbles is as significant as on an industrial scale.

Considering for instance the measurements and observations from experiment 2 (cf. figure 9.6, top left), the average time between each bubble release is 3.1s, with standard deviation 1.7s, signifying a large spread in bubble residence time under the anode. Hence, the signal is *not* truly periodic, thus violating the main purpose of the FFT.

The influence of aperiodicity

Consider two idealized representations of the measured signal from experiment 2, one with a fixed period of 3.1 s and amplitude 0.27 V (corresponding to the mean values of the original signal) and one with fixed amplitude and period corresponding to the original signal, as shown in figure 9.7a and b, respectively.

[1]Frequency estimated as $f_{OB} = N_{OB}/T_{OB}$, N_{OB} being the number of bubbles observed over the measurement time $T_{OB} = 25.6$s.

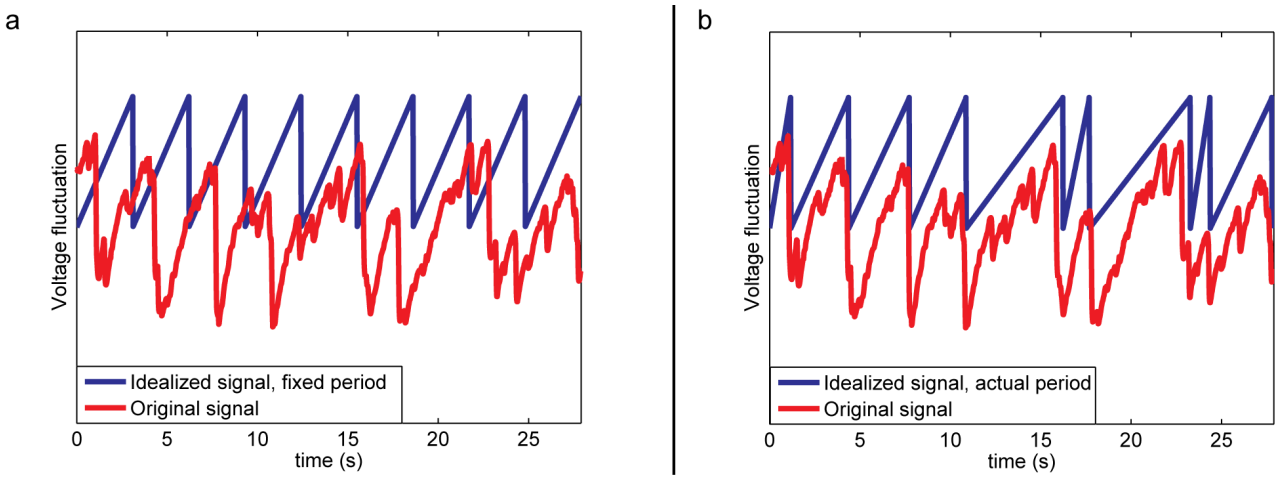

Figure 9.7: Idealized lab scale voltage signals with fixed (a) and actual (b) period.

In the above idealized cases, nine (full) bubble events occur in the time span of the experiment, corresponding to an observed frequency of 0.32 Hz. The resulting FFT spectrum for the idealized cases is shown in figure 9.8.

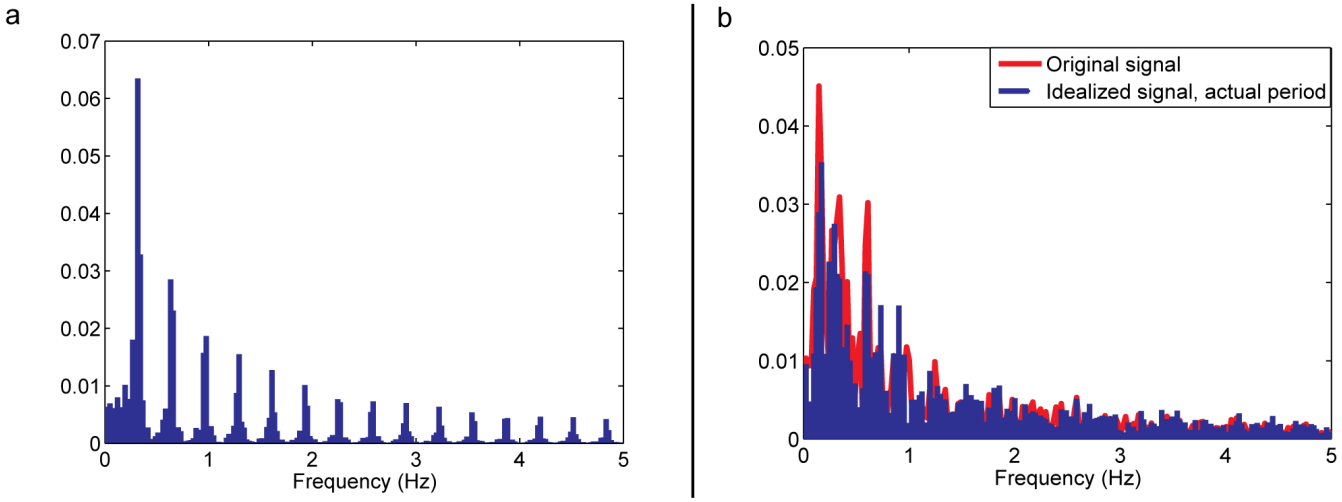

Figure 9.8: Spectra of idealized lab scale voltage signals with fixed (a) and actual (b) period. The spectra of the original signal is shown in red in (b) for comparison.

As expected, the dominating frequency for the idealized case shown in figure 9.7a is 0.32Hz, identical to the observed frequency. The dominating frequency is however reduced to 0.17Hz for the signal shown in figure 9.7b, corresponding well to the frequency of the actual signal (0.15Hz).

Hence, the discrepancy in observed and calculated frequencies is not a physical effect,

rather a question of how frequencies are defined and whether or not a FFT of an aperiodic signal is meaningful.

9.4 Summary of lab scale experiments

A series of lab scale experiments have been performed in order to obtain data for model validation. Experiments were performed with various current densities, interpolar distances and anode inclination in order to cover ranges typically encountered on an industrial scale. Typical bubble frequencies in the signal were found in the range 0.25–0.6 Hz, with corresponding amplitudes as large as ±4% around the mean voltage.

Increasing current densities and inclination angles are found to increase the typical frequencies found in the voltage signal. Increased inclination angles tend to decrease the signal domain, while the opposite behaviour is identified for increasing current densities.

The signal domain is found to decrease with increasing anode age, along with elevated frequencies, although the trend is not as clear as for the signal domain.

With help of high speed video recordings of the bath interface, voltage fluctuations are matched with the departure of anodic bubbles, observed bubbles accounting for 95% of large voltage fluctuations in the corresponding measured signal. The departure of bubbles is found to be (somewhat) irregular, yielding the *physical* information contained in the resulting FFT spectrum questionable. A numerical model being able to reproduce the sought spectrum should thus be closely assessed, in order to ensure that the full complexity of the bubble signal is captured, in addition to the "mean" values obtained from the FFT.

Part III: Electromagnetism

Outline of Part III

This part deals with the development and essential verifications of the primary functions of the electromagnetism model and is divided into four chapters which cover:

- Theory and background
- Verification studies
- MHD forces on single bubbles
- MHD effects in lab scale geometry

Following the (generic) theoretical derivations and verification of essential features (i.e. conservation of electrical current and boundary conditions) presented in the first two chapters, specific cases related to bubble-MHD and MHD effects on a lab scale geometry are investigated.

MHD effects derived in this part are coupled to the anodic bubble flow described in part IV of this thesis.

Chapter 10

Theory and background

Lorentz forces and gas production are two essential features of the Hall-Héroult process, which are governed by electromagnetic fields. In the following, the underlying theory for electromagnetic fields is given and a model is developed from first principles in order to retain control over what physics that are included and excluded as well as allowing for a tailored approach for the physics present in the Hall-Héroult cell, thus ensuring compatibility with other models developed.

10.1 Background and assumptions

In an industrial setting, the current density can be separated into two parts, an internal current density passing through the cell in question and an external, which typically is the current density passing to other cells in the aluminium plant. Letting Λ denote a specific cell, the current density is thus defined as

$$\boldsymbol{j} = \begin{cases} \boldsymbol{j}_{ext} & \text{in } \bar{\Lambda} \\ \boldsymbol{j}_{int} & \text{in } \Lambda \end{cases} \tag{10.1}$$

Electrical charge is assumed to be conserved, leading to the constraint

$$\int_A \boldsymbol{j} \cdot \boldsymbol{n} dA = 0 \quad \Rightarrow \nabla \cdot \boldsymbol{j} = 0, \tag{10.2}$$

which holds both for internal and external currents.

The continuum form of Ohm's law

$$\boldsymbol{j} = \sigma \left(\boldsymbol{E} + \boldsymbol{u} \times \boldsymbol{B} \right) \tag{10.3}$$

and Maxwell's equations

$$(i) \qquad \nabla \cdot \boldsymbol{E} = \frac{1}{\epsilon_0}\varrho_e \qquad (ii) \qquad \nabla \cdot \boldsymbol{B} = 0$$
$$(iii) \qquad \nabla \times \boldsymbol{E} = -\frac{\partial \boldsymbol{B}}{\partial t} \qquad (iv) \qquad \nabla \times \boldsymbol{B} = \mu_0 \boldsymbol{j} + \mu_0 \epsilon_0 \frac{\partial \boldsymbol{E}}{\partial t}$$

are assumed to hold in the entire domain.

The two sources of electrical current density in equation 10.3 are denoted potential and induced currents, i.e.

$$\boldsymbol{j} = \boldsymbol{j}_{pot} + \boldsymbol{j}_{ind}, \tag{10.4}$$

where

$$\boldsymbol{j}_{pot} = \sigma \boldsymbol{E} \quad \text{and} \quad \boldsymbol{j}_{ind} = \sigma \boldsymbol{u} \times \boldsymbol{B}. \tag{10.5}$$

Interpreting Amperes law (iv) as a result of Lenz' law, i.e. a current induces a magnetic field, and assuming negligible displacement currents, we have

$$\nabla \times \boldsymbol{B} = \begin{cases} \nabla \times \boldsymbol{B}_{ext} = \mu_0 \boldsymbol{j}_{ext} & \text{in } \bar{\Lambda} \\ \nabla \times \boldsymbol{B}_{int} = \mu_0 \boldsymbol{j}_{int} & \text{in } \Lambda \end{cases} \tag{10.6}$$

Hence, in Λ, we require

$$\nabla \times \boldsymbol{B}_{ext} = 0 \tag{10.7}$$
$$\nabla \times \boldsymbol{B}_{int} = \mu_0 \boldsymbol{j}, \tag{10.8}$$

that is, the external magnetic field is unaffected by the internal current density. It should be noted, that by addition of equations 10.7 and 10.8, the original form of Amperes law is obtained. Consequently, the *total* magnetic field is given as

$$\boldsymbol{B} = \boldsymbol{B}_{int} + \boldsymbol{B}_{ext}. \tag{10.9}$$

Fluids are assumed to be electrically neutral so that the Lorentz force density term is of the form

$$\boldsymbol{f}_L = \boldsymbol{j} \times \boldsymbol{B}. \tag{10.10}$$

Electromagnetic fields adapt at a timescale which is *much* smaller than the typical time-scales in the system (i.e. inertial time scales) and are thus assumed to be *stationary*.

For the purpose of book-keeping, Ohm's law and the Lorentz force is split into different contributions:

$$\boldsymbol{j} = \underbrace{\sigma \boldsymbol{E}}_{\mathcal{O}(0)} + \underbrace{\sigma \boldsymbol{u} \times \boldsymbol{B}_{ext}}_{\mathcal{O}(1)} + \underbrace{\sigma \boldsymbol{u} \times \boldsymbol{B}_{int}}_{\mathcal{O}(2)}. \tag{10.11}$$

$$\boldsymbol{f}_L = \underbrace{\boldsymbol{j} \times \boldsymbol{B}_{ext}}_{\mathcal{O}(0)} + \underbrace{\boldsymbol{j} \times \boldsymbol{B}_{int}}_{\mathcal{O}(2)} \tag{10.12}$$

10.1.1 Dimensional considerations

Considering the form of Ohm's law (equation 10.3) it is evident that the current arises due to two sources, which may change in different regions of the cell. Due to the large difference in conductivity in bath and molten aluminium (cf. Grjotheim et al. [46]), the potential loss is far greater in the bath than in the molten aluminium. Considering a simplified Ohm's law for the potential drop

$$\Delta U_i = R_i I, \tag{10.13}$$

and assuming a constant current density across the phases, the potential drop in each liquid phase is related by

$$\Delta U_{Al} = \Delta U_b \frac{\sigma_{bath} l_{Al}}{\sigma_{Al} l_{bath}}. \tag{10.14}$$

Inserting typical values for conductivities ($\sigma_{bath} \approx 200\ \Omega^{-1}\mathrm{m}^{-1}$, $\sigma_{Al} \approx 3000000\ \Omega^{-1}\mathrm{m}^{-1}$) as well as for the interpolar distance and metal height (3 cm, 20 cm), one obtains

$$\Delta U_{Al} \approx 10^{-5} \Delta U_{bath}. \tag{10.15}$$

Further, approximating the electrical field as

$$E \approx \frac{\Delta U_i}{l_i}, \tag{10.16}$$

and inserting typical values for ΔU_{bath}, $\boldsymbol{u}$ and $\boldsymbol{B}$ (1.5 V, 0.5 m/s, 0.01T), it is evident that the potential currents dominate in the *bath*, while contributions are of comparable magnitude in the molten metal.

10.2 Modelling approaches

As seen from the discussion in the introductory section, the general MHD system is relatively complex, even at a strictly formal level. It is thus not surprising that several different methods have been developed to model the system, taking into account effects of leading importance. In the following, three different modelling approaches are presented, denoted zero, first and second order models, referring to the separation of terms given in equations 10.11 and 10.12.

10.2.1 Zero order model

The zero-order model is based on the assumption of negligible induced currents, as is the case for the bath. In this case, Ohm's law reads

$$\boldsymbol{j} = \sigma \boldsymbol{E}. \tag{10.17}$$

Assuming steady electromagnetic fields, it is evident from Maxwell equation (*iii*) that the electric field can be expressed as a gradient of a potential, i.e.

$$\boldsymbol{j} = -\sigma \nabla \phi \tag{10.18}$$

Assuming the existence of derivatives of $\boldsymbol{j}$, and that current is conserved, the local form of equation 10.2 is given as

$$\begin{aligned} \nabla \cdot \boldsymbol{j} &= 0 \\ &\Rightarrow \quad \nabla \sigma \nabla \phi = 0, \end{aligned} \tag{10.19}$$

i.e., the electrical potential ϕ is determined by a Laplace equation.

In order to compute the Lorentz force, a magnetic field is needed. Staying with zero order terms, the Lorentz force is given as

$$\boldsymbol{f}_L = \boldsymbol{j} \times \boldsymbol{B}_{ext}, \tag{10.20}$$

where $\boldsymbol{B}_{ext}$ is a *known* external magnetic field.

The zero-order model is, as the name suggests, an approximation of reality, as the assumption of negligible induction currents will not hold in the molten metal. Its simplicity is however its strength as even analytical solutions are obtainable, for reasonable boundaries.

10.2.2 First order model

A natural extension to the zero order model is to include the induction currents arising from external magnetic fields. Equation 10.11 then reads

$$\boldsymbol{j} = -\sigma \nabla \phi + \sigma \boldsymbol{u} \times \boldsymbol{B}_{ext}, \tag{10.21}$$

while the Lorentz force is given as

$$\boldsymbol{f}_L = \boldsymbol{j} \times \boldsymbol{B}_{ext}. \tag{10.22}$$

As current is conserved, the potential equation reads

$$\nabla \sigma \nabla \phi = \nabla \cdot (\sigma \boldsymbol{u} \times \boldsymbol{B}_{ext}), \tag{10.23}$$

where σ and $\boldsymbol{u}$ are determined from the flow equations and $\boldsymbol{B}_{ext}$, again, is a known quantity.

Analytical solutions are in principle obtainable for the first order model as well, given some flow-field and distribution of conductivity.

10.2.3 Second order models

Second order models involve the full complexity of equations 10.11 and 10.12. Assuming that the external magnetic field is known, the challenge of the second order model is to adequately predict the electrical current density and the *internal* magnetic field.

The classical MHD-approach is to develop a transport equation for the magnetic field. Combining the Ohm's law and the Ampere equation

$$\nabla \times \boldsymbol{B} = \mu_0 \boldsymbol{j} = \mu_0 \sigma \left(\boldsymbol{E} + \boldsymbol{u} \times \boldsymbol{B} \right) \tag{10.24}$$

and dividing by $\mu_0 \sigma$ before taking the curl, one obtains

$$\nabla \times \mathcal{D}_{mag} \left(\nabla \times \boldsymbol{B} \right) = \nabla \times \boldsymbol{E} + \nabla \times \left(\boldsymbol{u} \times \boldsymbol{B} \right) = \nabla \times \left(\boldsymbol{u} \times \boldsymbol{B} \right), \tag{10.25}$$

where $\mathcal{D}_{mag} = 1/\mu_0 \sigma$ is the magnetic diffusivity and $\nabla \times \boldsymbol{E}$ term is neglected due to the assumption of stationary fields. Expanding the RHS and using the assumptions of divergence free velocity and magnetic fields, the $\boldsymbol{B}$ transport equation is finally written as

$$\left(\boldsymbol{u} \cdot \nabla \right) \boldsymbol{B} + \nabla \times \mathcal{D}_{mag} \left(\nabla \times \boldsymbol{B} \right) = \left(\boldsymbol{B} \cdot \nabla \right) \boldsymbol{u}. \tag{10.26}$$

With a known magnetic field, the current required to compute the Lorentz force is easily obtained from Ampere's law

$$\nabla \times \boldsymbol{B} = \mu_0 \boldsymbol{j}. \tag{10.27}$$

Boundary conditions are somewhat complicated using this approach, as they are to be provided for $\boldsymbol{B}$, while one in a real case knows only the current and potential distribution. The potential distribution is of practical interest and must be derived by some additional relation, for instance Ohm's law.

The inclusion of an external magnetic field is challenging when a model of this type is used due to the inverse interpretation of Ampere's law; Here, the magnetic field induces *the current*. Hence, for this model to be used in the context of a Hall-Héroult cell, a splitting of the magnetic field must be treated formally.

Retaining the Ohm's law for the description of the current density, i.e.

$$\boldsymbol{j} = -\sigma \nabla \phi + \sigma \boldsymbol{u} \times \boldsymbol{B}, \tag{10.28}$$

the magnetic field must be calculated by an alternative approach. A classical approach in this context is obtained by means of the Biot-Savart law, yielding a magnetic field on the form

$$\boldsymbol{B} = \frac{\mu_0}{4\pi} \int_{\Lambda} \frac{\boldsymbol{j}(\boldsymbol{y}) \times \boldsymbol{r}}{\|\boldsymbol{r}\|^3} d\boldsymbol{y} + \boldsymbol{B}_{ext}, \tag{10.29}$$

where $\boldsymbol{r}$ is the displacement vector from a current element to the point where the field is to be computed.

In this approach, there is no need for boundary conditions for $\boldsymbol{B}$ as it is a quantity derived from the electrical current. Though appealing, the Biot-Savart law is somewhat problematic as it involves an integral over the entire fluid domain, i.e. a sum over all cells in the computational domain. Needless to say, such a procedure could significantly impede computational efficiency in the case of a fine mesh.

An alternative approach is obtained by introducing a magnetic vector potential $\boldsymbol{\mathcal{A}}$, defined by

$$\boldsymbol{B} = \nabla \times \boldsymbol{\mathcal{A}}. \tag{10.30}$$

Introducing the definition in Maxwell equation (iv), yielding

$$\nabla \times \nabla \boldsymbol{\mathcal{A}} = \mu_0 \boldsymbol{j} \tag{10.31}$$

and choosing the Coulomb gauge

$$\nabla \cdot \boldsymbol{\mathcal{A}} = 0, \tag{10.32}$$

(cf. Griffiths [43]), the following simple equation is obtained for $\boldsymbol{\mathcal{A}}$

$$\nabla^2 \boldsymbol{\mathcal{A}} = -\mu_0 \boldsymbol{j}. \tag{10.33}$$

From the above definitions, the complete magnetic field in Λ is

$$\boldsymbol{B} = \nabla \times \boldsymbol{\mathcal{A}} + \boldsymbol{B}_{ext}. \tag{10.34}$$

In total, the above model consists of four transport equations (ϕ and $\boldsymbol{\mathcal{A}}$) and three constitutive relations ($\boldsymbol{j}$), written as

$$\begin{aligned} \nabla \left(\sigma \nabla \phi\right) &= \nabla \cdot \left(\sigma \left[\boldsymbol{u} \times \left(\nabla \times \boldsymbol{\mathcal{A}} + \boldsymbol{B}_{ext}\right)\right]\right) && (10.35)\\ \nabla^2 \boldsymbol{\mathcal{A}} &= -\mu_0 \boldsymbol{j} && (10.36)\\ \boldsymbol{j} &= \sigma \left(-\nabla \phi + \boldsymbol{u} \times \left(\nabla \times \boldsymbol{\mathcal{A}} + \boldsymbol{B}_{ext}\right)\right). && (10.37) \end{aligned}$$

The $\boldsymbol{A}-\phi$ approach incorporates all relevant physics through two simple Poisson equations, which is a clear advantage over the more complex transport equation for $\boldsymbol{B}$. Furthermore, as seen from equation 10.33, the magnetic vector potential is *parallel* to the electrical current making it straightforward to relate conductor/insulator boundaries to the magnetic vector potential. Finally, the $\boldsymbol{A} - \phi$ model yields a direct decoupling of the induced- and external magnetic fields. Consequently, this model is chosen for the current work in cases where full coupling is required.

Chapter 11

Verification studies

As the proposed MHD model is developed from first principles, a verification of its essential features is required, as described in the following sections.

11.1 General properties

For the various simulations, three different fluids are used, which all are assumed to be homogeneous. Properties of relevance are summarized in table 11.1 and are used throughout the following sections, unless otherwise noted.

Table 11.1: Main properties of simulated fluids for MHD cases

Property	Symbol	Cryolite	Gas	Aluminium	Dimension
Phase	#	1	2	3	-
Density	ρ_i	2070	0.435	2270	$\mathrm{kg/m^3}$
Conductivity	σ_i	300	$1 \cdot 10^{-12}$	$3 \cdot 10^{6}$	$(\Omega\ \mathrm{m})^{-1}$

The electromagnetic transport equations are implemented as user defined scalars (UDS) (cf. equation 3.27), with no advection function and transient term due to the assumption of steady fields. For the electrical potential, the diffusivity is taken to be the electrical conductivity, while it is taken to be unity for the magnetic vector potential. As these equations are of a Poisson-Laplace form, the AMG aggregative W-cycle is used for these equations in order to enhance convergence.

Equations are assumed to be converged at an absolute residual of $1 \cdot 10^{-10}$. The strict requirement for the residual of the UDS is due to uncertainties arising in computed electrical currents if residuals are too high. The high degree of convergence is easily obtained by using a W-type AMG cycle.

11.2 Prediction of electrical potential

As the electrical potential ϕ is to be used extensively throughout the case studies presented in the following, its accurate prediction is essential in order to obtain sensible results. Three simple cases are computed in order to validate the compatibility of the FLUENT UDF structure and the Laplace equation obtained from the Maxwell equations. The following calculations are performed with cryolite as working material.

11.2.1 Electrical potential between infinite parallel plates

Figure 11.1 shows two parallel plates with fixed electrical potential (ϕ_1 and ϕ_2 at $y = b$ and $y = 0$, respectively), enclosed by non-conducting walls (at $x = 0$ and $x = b$) yielding zero current across these interfaces.

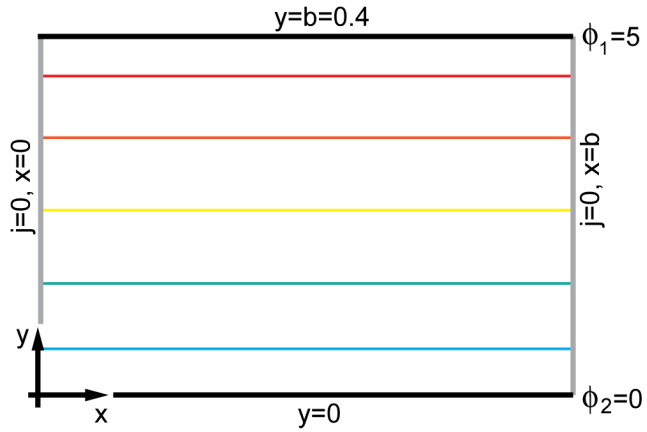

Figure 11.1: Sketch of geometry and solution for electrical potential between infinite parallel plates.

The solution of the Laplace equation

$$\nabla^2 \phi = 0, \tag{11.1}$$

in the geometry sketched above is

$$\phi(x, y) = \phi_1 \frac{y}{b}. \tag{11.2}$$

Evidently, the equipotential lines are horizontal. Figures 11.2 a and b show the solution obtained by FLUENT on a 60 by 60 Cartesian mesh and comparison with the analytical solution in a corresponding geometry.

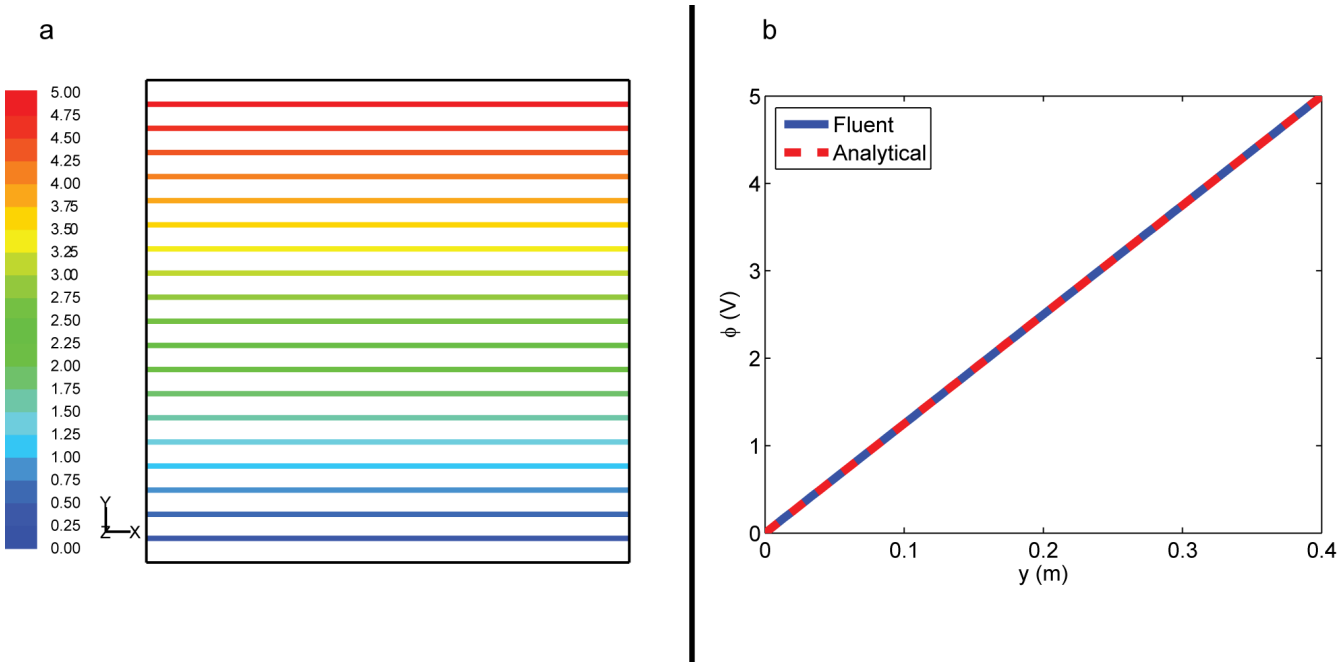

Figure 11.2: FLUENT solution for electrical potential (a) and comparison to analytical solution (b).

An important result of the linear electrical potential is that its gradient (i.e. the current) is *constant* and equal to

$$\frac{\partial \phi}{\partial y} = \frac{\phi_2 - \phi_1}{\Delta y} = \frac{\phi_1}{b}. \tag{11.3}$$

For the geometry used in figure 11.1, the gradient is 12.5 V/m, which as seen from figure 11.2 is accurately predicted by FLUENT.

11.2.2 Electrical potential for given current distribution

In order to determine if FLUENT is able to handle Neumann boundary conditions and still predict the correct electrical potential, the above case is modified so that current density is known at $y = b$. The chosen current distribution is

$$j_y = -\sigma \frac{\partial \phi}{\partial y}_{y=b} = -x, \tag{11.4}$$

i.e. a linearly growing current *entering* the domain through the upper surface. Retaining all other properties, the resulting electrical potential is

$$\phi(x, y) = \frac{a}{2} y - \sum_{n=1}^{\infty} \frac{10a^3}{n^3 \pi^3} \frac{\sinh \frac{n\pi y}{a}}{\cosh \frac{n\pi b}{a}} \cos \frac{n\pi x}{a}. \tag{11.5}$$

Figure 11.3 shows the predicted electrical potential for various heights, compared to the analytical solution.

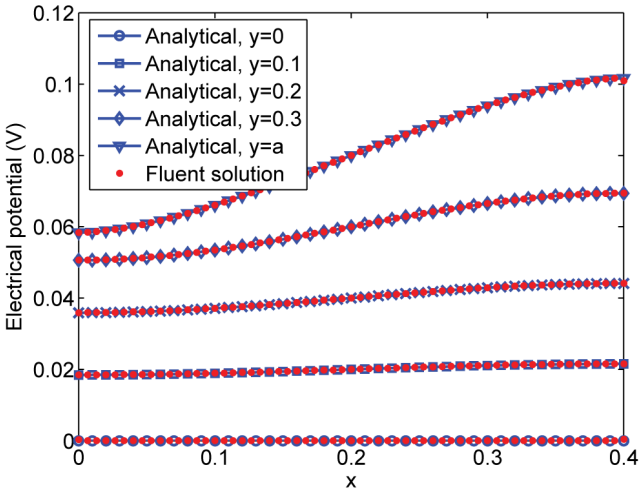

Figure 11.3: Comparison of FLUENT and analytical solution for parallel plates with Neumann boundary conditions.

As for the infinite parallel plates, the difference between the two solutions is negligible.

11.2.3 Electrical potential between finite parallel plates

The final case related to the electrical potential is a combination of the two previous, which is boundaries with combined Dirichlet and Neumann boundary conditions. A sketch of the problem domain is shown in figure 11.4.

As no known analytical solution is found to this problem, the solution obtained by FLUENT is compared to the solution obtained by the PDEtools package in MATLAB (based on FEM).

As seen from figure 11.5, the two solutions are in good agreement, although some minor discrepancies exist between the two solutions. These discrepancies are due to different meshing techniques (PDEtools using a trigonal mesh, while the FLUENT solution is obtained on a Cartesian mesh) and different procedures for interpolating the solution. The two procedures predict the same electrical potential with an average absolute error of less than 5%.

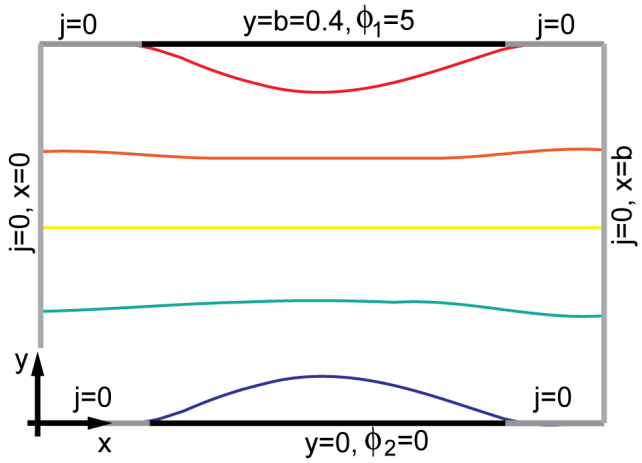

Figure 11.4: Sketch of geometry and equipotential lines between finite parallel plates modelled by a mixture of Neumann and Dirichlet boundary conditions.

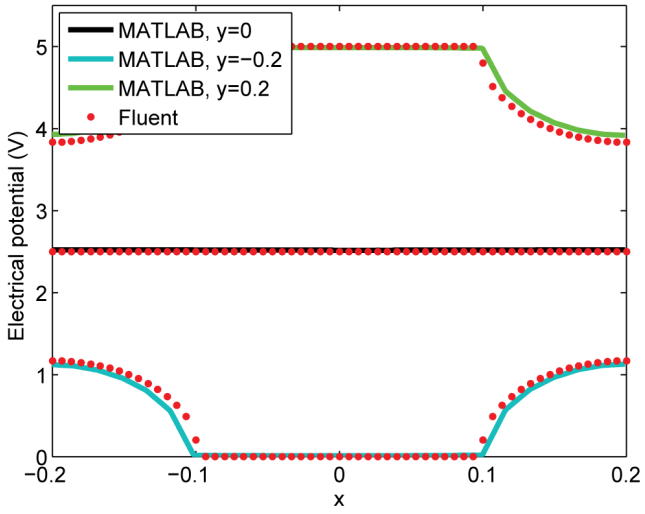

Figure 11.5: Comparison of solutions to the finite plate problem obtained by MATLAB and FLUENT.

11.3 Current across sharp interfaces

As seen from table 11.1, the value of the electrical conductivity σ_i varies with several orders of magnitude within the system considered. This is particularly problematic with the (sharp interface) VOF-model, as properties then are discontinuous across interfaces, possibly resulting in a wrong representation of transported properties (i.e. the electrical potential and current).

Consider the zero order model, summarized as

$$\nabla \cdot \sigma \nabla \phi = 0 \tag{11.6}$$

$$\boldsymbol{j} = -\sigma \nabla \phi, \tag{11.7}$$

where σ represents the electrical conductivity of the *mixture*. By default, the mixture conductivity in a given computational cell is given as

$$\sigma = \sum_i \alpha_i \sigma_i, \tag{11.8}$$

where i represents the phase index.

A subtle problem arises from the way gradients are calculated in a finite volume code. Considering the gradient of the scalar field ϕ and using the divergence theorem, we obtain

$$\int \nabla \phi dV = \int \phi \boldsymbol{n} dA, \tag{11.9}$$

where A is the area with normal vector $\boldsymbol{n}$ enclosing the volume dV. Assuming that the variation of $\nabla\phi$ is small over dV, the gradient can be approximated as

$$\nabla \phi \approx \frac{1}{\Delta V} \sum_f \phi_f \boldsymbol{n}_f A_f, \tag{11.10}$$

i.e. a flux of ϕ across the faces f enclosing the control volume ΔV[1]. A problem arises here due to the cell based structure of UDS equations in FLUENT, that is, only cell centred values are accessible to users. Hence, in order to compute the gradient of the electrical potential by equation 11.10, the face values of the scalar field must be found by means of some interpolation scheme.

The default scheme used to find the face value ϕ_f is a distance weighted interpolation, written as

$$\phi_f = \frac{\phi_0 d_1 + \phi_1 d_0}{d_0 + d_1}, \tag{11.11}$$

[1]This approximation of the gradient is commonly denoted as the reconstruction gradient

where d_0 and d_1 are the distances from the center of cells with values ϕ_1 and ϕ_2, to the face f between them. For an equidistant grid, the face value is simply the average value

$$\phi_f = \frac{\phi_0 + \phi_1}{2}, \tag{11.12}$$

which is easily verified by setting $d_0 = d_1$ in equation 11.11. The concept is further illustrated in figure 11.6.

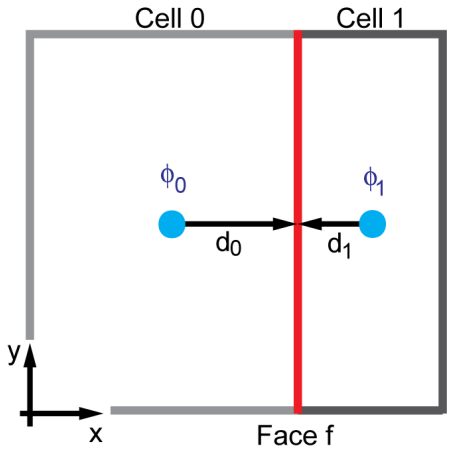

Figure 11.6: Geometry used to define reconstruction gradient.

As will be shown, the distance based gradient yields faulty results when computing a current across a sharp interface. The alternative to this scheme is a conductivity weighted interpolation defined as

$$\phi_f = \frac{\phi_0\sigma_0 d_1 + \phi_1\sigma_1 d_0}{\sigma_0 d_1 + \sigma_1 d_0}. \tag{11.13}$$

In the following, the influence of these schemes will be investigated for two distinct scenarios of practical importance, namely a non-conducting bubble in a conducting fluid (cryolite) and a stratified system of two conducting fluids (cryolite and aluminium). The initial setup for the two scenarios is shown in figure 11.7.

Figure 11.8 shows the magnitude of current density along the center line calculated with default and conductivity weighted gradients for the two cases shown in figure 11.7. As seen from the figure 11.8, although currents far from the interface are consistent, the default distance based gradient yields large and unphysical current densities close to the interface. Hence, the conductivity weighted gradients are used for current density calculations in all simulations.

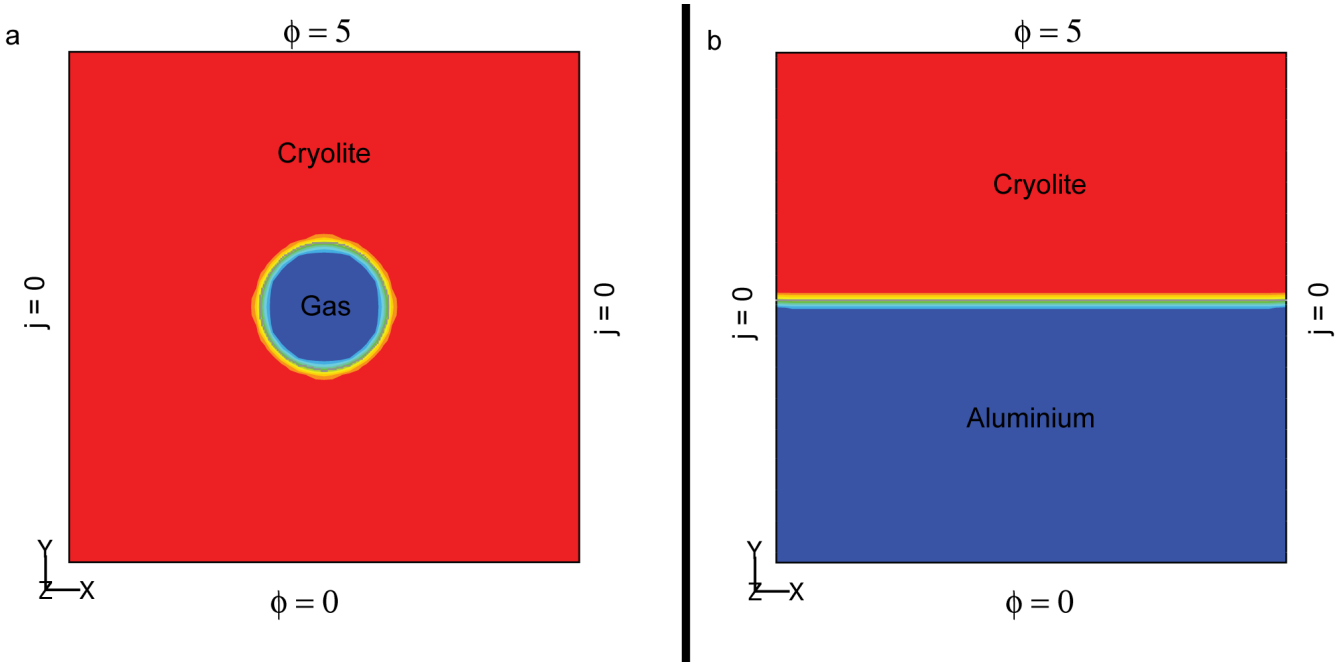

Figure 11.7: Setup for non-conducting bubble in cryolite (a) and stratified cryolite-aluminium system (b). Figure is coloured by phase fraction. Geometry consists of 60x60 quadrilateral cells.

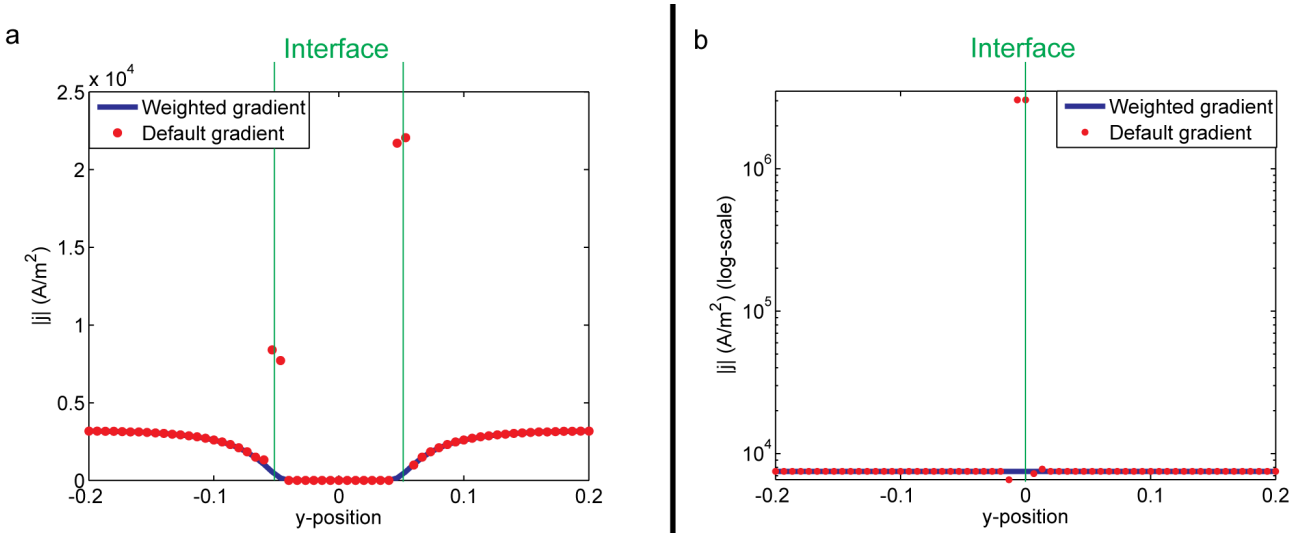

Figure 11.8: Influence of gradients for currents across sharp interfaces for non-conducting bubble in electrolyte (a) and stratified electrolyte-aluminium system (b). Position of interface is shown with green line.

11.4 Magnetic boundary conditions

Consider the magnetic field arising from a uniform, circular conductor with infinite length, as sketched below.

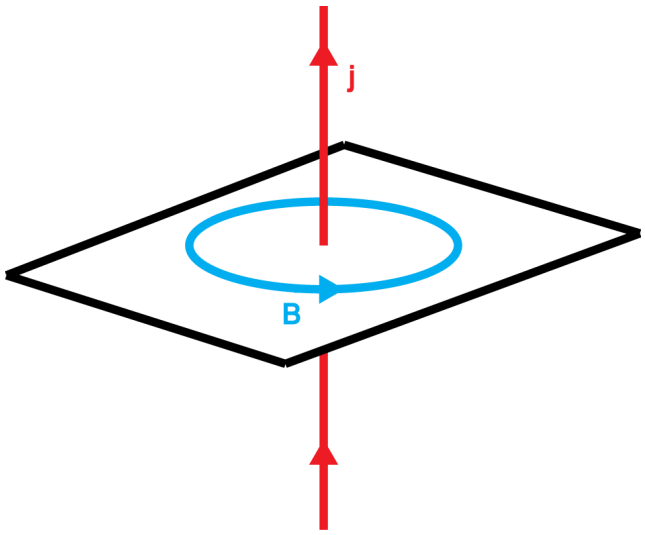

Figure 11.9: Sketch of current carrying conductor and resulting magnetic field.

Assuming that the current density is in the z-direction ($\boldsymbol{j} = j\hat{\boldsymbol{z}}, \quad j = j(x, y)$), the induced magnetic field is restricted to the x, y-plane, i.e. $\boldsymbol{B}_{ind} = B_x(x, y)\hat{\boldsymbol{x}} + B_y(x, y)\hat{\boldsymbol{y}}$. Using the (general) integral form of Ampere's law, the magnetic field is given as

$$\boldsymbol{B}_{ind} = \begin{cases} \frac{\mu_0 j}{2}(x\hat{\boldsymbol{y}} - y\hat{\boldsymbol{x}}) & \text{if} \quad \sqrt{x^2+y^2} < r_0 \\ \frac{\mu_0 j r_0^2}{2(x^2+y^2)}(x\hat{\boldsymbol{y}} - y\hat{\boldsymbol{x}}) & \text{if} \quad \sqrt{x^2+y^2} \geq r_0 \end{cases} \tag{11.14}$$

where r_0 is the radius of the conductor, assumed to carry a uniform current distribution j.

Given a magnetic vector potential model and the current distribution, one essentially has the choice between Dirichlet or Neumann boundary conditions, i.e.

$$\boldsymbol{A} \quad \text{is known} \quad \text{or} \quad \frac{\partial}{\partial n}\boldsymbol{A} \quad \text{is known}, \tag{11.15}$$

where the Neumann condition can determine the solution up to some constant. With correct boundary values, both of the above boundary conditions should result in a vector potential which curl is identical to the magnetic field given by equation 11.14.

As the analytical magnetic field is known, the magnetic vector potential and hence the exact boundary conditions can be determined. From definition, the Neumann boundary condition is given as

$$\frac{\partial A_z}{\partial n} = [-B_y, B_x] \cdot \boldsymbol{n}, \tag{11.16}$$

where $\boldsymbol{n}$ is the normal vector of the boundary.

For the Dirichlet boundary condition, assuming continuity across the conductor boundary, the magnetic vector potential is given (up to an additive constant) as

$$A_z = \begin{cases} -\frac{\mu_0 j}{4}\left(x^2+y^2\right) & \text{if} \quad \sqrt{x^2+y^2} < r_0 \\ \frac{\mu_0 j r_0^2}{4}\left(\ln\frac{r_0^2}{x^2+y^2} - 1\right) & \text{if} \quad \sqrt{x^2+y^2} \geq r_0 \end{cases} \tag{11.17}$$

Clearly, the exact boundary conditions given by equations 11.16 and 11.17 are significantly different from the commonly encountered academic boundary conditions, where constant values are chosen at the boundaries. The influence of the different choices for boundary conditions on the predicted magnetic field is studied in the following.

11.4.1 Planar 2D-system

Assume that the current is *known* and uniform within the conductor as for the analytical case. As $\boldsymbol{A}||\boldsymbol{j}$, equation 10.33 reduces to

$$-\nabla^2 A_z(x,y) = \mu_0 j_z(x,y), \tag{11.18}$$

which can be solved through the UDS-framework in FLUENT with $\mu j_z(x,y)$ as a source term.

The computational domain is made up by 100x100 quadrilateral cells and only the UDS equation is solved. For simplicity, the parameter $\mu_0 j$ is given a value of unity.

In order to test the possible cases encountered in a realistic situation, the following three cases are simulated:

1 The boundaries are "far" from the conductor periphery.

2 The boundaries are close to the conductor periphery.

3 The boundaries are within the conductor, i.e. the entire computational domain has a finite current density.

Boundaries far from conductor

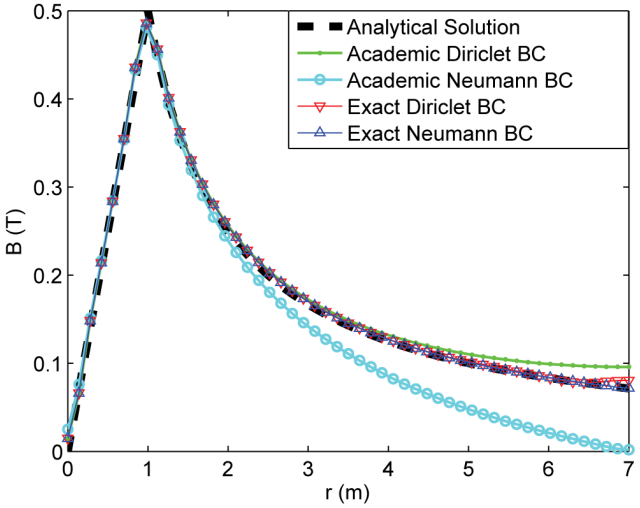

Figure 11.10: Magnitude of magnetic field in radial direction r for various boundary conditions (symbols), compared to analytical solution (dashed line). Conductor is given a radius $r_0 = 1$ m, while the distance from the center of the conductor to the boundary is 7 m.

Figure 11.10 shows that all four boundary conditions give reasonable results up to $r \sim 3$ m. This is as expected, as the boundaries are relatively far from the conductor and the solution thus depends more on the source term rather than the boundary condition. Closer to the boundary, the academic Neumann boundary condition enforces a zero magnetic field which yields a large error, while the corresponding Dirichlet boundary condition appears to asymptotically approach some constant value, approximately 20% larger than the analytical result. The exact boundary conditions reproduce the analytical result with a maximal error of 3%.

Boundaries close to conductor

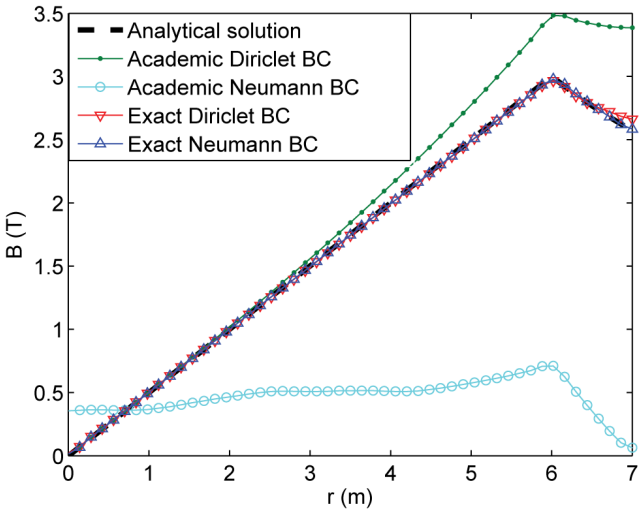

Figure 11.11: Magnitude of magnetic field in radial direction r for various boundary conditions (symbols), compared to analytical solution (dashed line). Conductor is given a radius $r_0 = 6$ m, while the distance from the center of the conductor to the boundary is 7 m.

As seen from figure 11.11, the academic Dirichlet boundary condition behaves physically reasonable and is able to accurately predict the magnetic field up to some limit from which it over predicts the field by as much as 30 %. The Neumann solution however poorly represents the actual field, which is as expected as we enforce a zero (tangential) magnetic field at the boundaries which now are very close to the conductor. The exact boundary conditions predict the analytical result with a maximal error of 3%.

Observing the vector plots shown in figure 11.12 reveals another problem with the academic Neumann boundary condition, namely a *radial* component of the magnetic field. Furthermore, the expected circulating field around the origin appears to be off-centre. This is possibly due to inaccuracies in the undetermined constant in the magnetic vector potential, originating from the inadequate choice of the boundary value. The predicted field from the academic Dirichlet boundary conditions on the other hand appear to behave in a more physically sensible way, at least considering the field in the wall-normal direction.

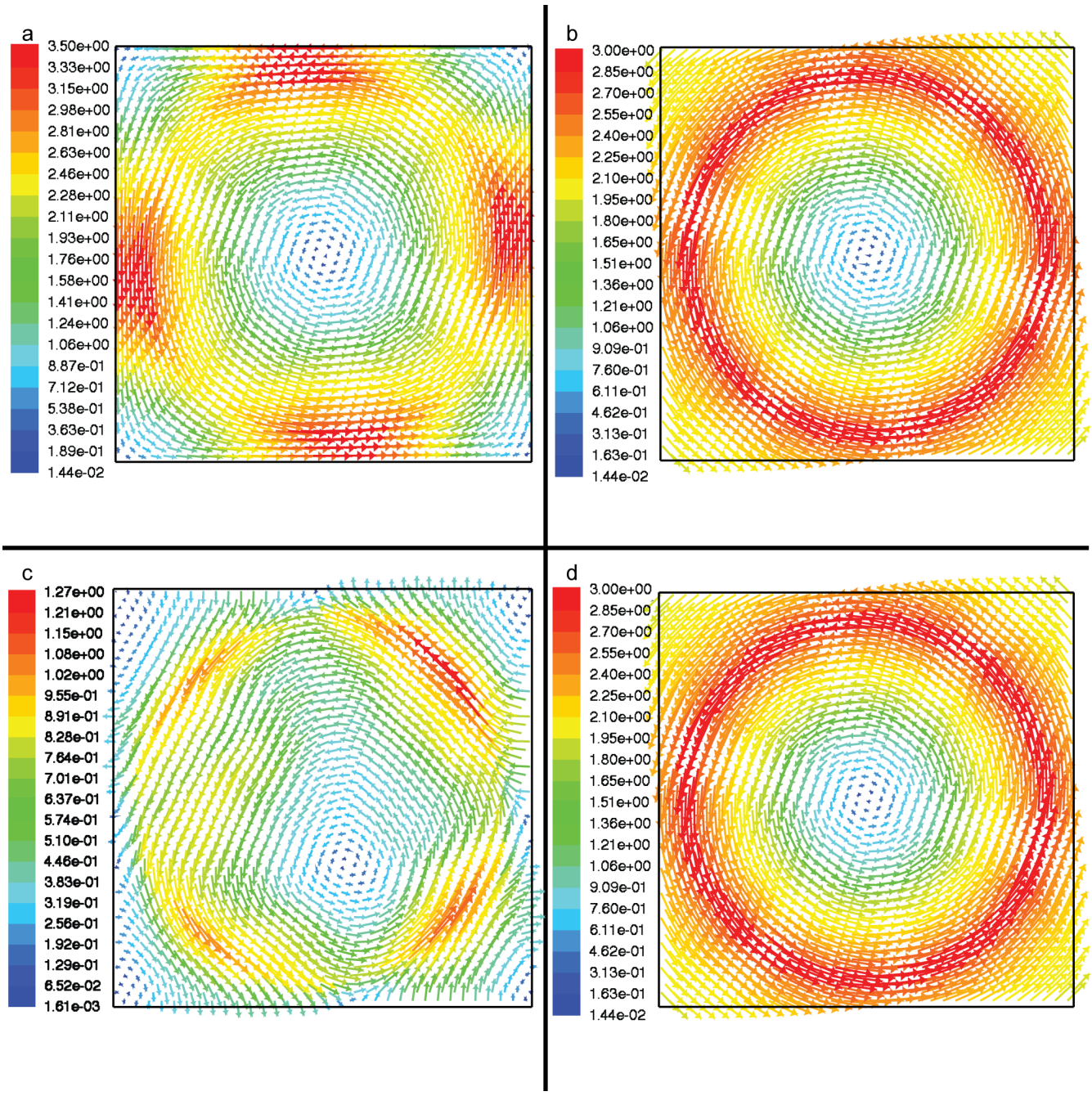

Figure 11.12: Predicted magnetic field with academic (a) and exact (b) Dirichlet and academic (c) and exact (d) Neumann boundary conditions. The direction of the current is out of the paper plane, with centred origin. Vectors coloured by the magnitude of the magnetic field.

Boundaries within conductor

Figure 11.13 shows the final case where the entire computational domain carries a current. As expected, the academic Neumann condition fails completely in this situation. However, the academic Dirichlet condition yields a surprisingly good prediction, at least for the (far) interior of the domain. As for the two previous cases, the academic Dirichlet solution over predicts the value of the magnetic field with as much as 30%, while analytical boundary conditions yield a maximal error of less than 3%.

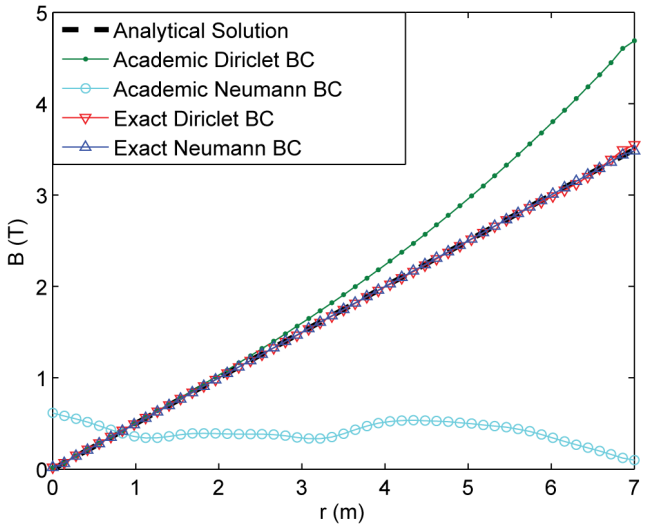

Figure 11.13: Magnitude of magnetic field in radial direction r for various boundary conditions (symbols), compared to analytical solution (dashed line). Conductor is given a radius $r_0 = 10$ m, while the distance from the center of the conductor to the boundary is 7 m.

11.4.2 Planar magnetic field due to 3D current tube

Consider a generalization of the planar case to a quasi-3D problem, meaning that the current and magnetic vector potential still are restricted by $\boldsymbol{j} = j(x, y)\hat{\boldsymbol{z}}$ and $\boldsymbol{A} = A(x, y)\hat{\boldsymbol{z}}$, but the problem is solved in a 3D geometry as sketched in figure 11.14.

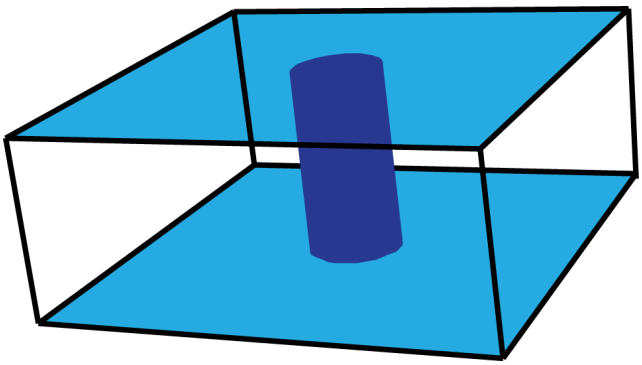

Figure 11.14: Current tube in 3D, shaded in dark blue. Geometry consists of 60x60x24 cells and the size of the box is 1x1x0.4 m. The central current tube has a radius of 0.1 m.

The main difference between the quasi-3D and the planar case is the presence of surfaces through which current passes. As these boundaries are of practical importance (as this would be typical behaviour at the electrodes), any differences in the boundary conditions should be identified.

In this specific case the academic and exact Neumann boundary conditions are identical on the horizontal surfaces, i.e.

$$\frac{\partial \boldsymbol{A}}{\partial z} = 0, \tag{11.19}$$

as $A = A(x, y)$. The exact Dirichlet boundary condition for the conducting surfaces is identical to that of the parallel walls, which differs significantly from the academic Dirichlet boundary condition, imposing a "no slip" condition on the magnetic vector potential along horizontal surfaces. The influence of the six different combinations of boundary conditions on the magnetic field *parallel* to the conductor is shown in figures 11.15 and 11.16.

As seen from figure 11.15a, academic Dirichlet boundary conditions on all surfaces grossly under predicts the magnetic field even in close proximity of the current tube. This effect is most visible close to the conducting surfaces (z=0 and z=0.4) and is due to the "no slip" condition imposed on the magnetic vector potential. The academic Neumann boundary conditions behave similarly to the plane case, somewhat under predicting the magnetic field far from the conductor (cf. figure 11.10). As expected, the exact boundary conditions reproduce the analytical magnetic field with good accuracy.

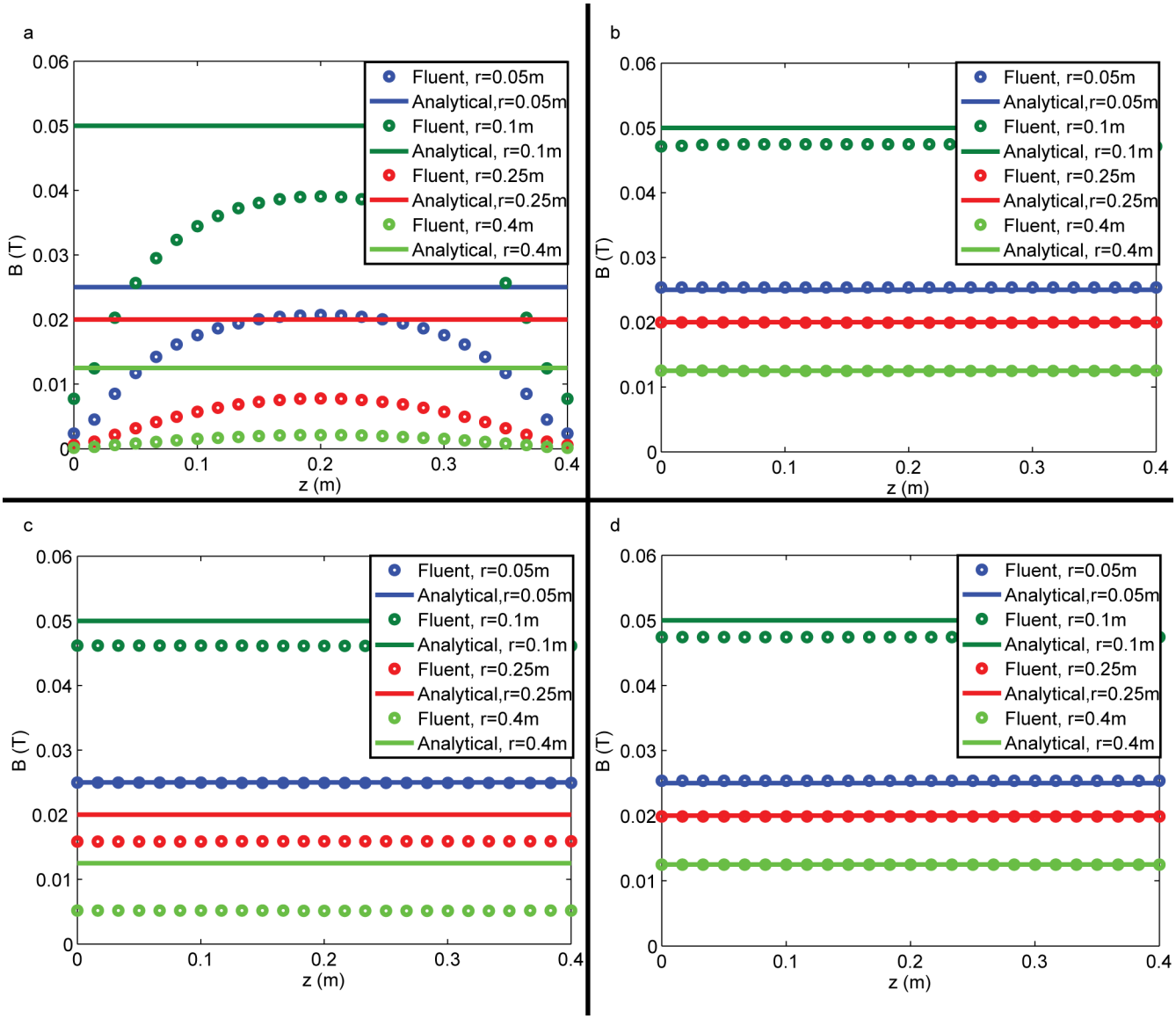

Figure 11.15: Computed magnetic field (circles) as a function of height (z) for various radial distances r from the current tube, compared to the analytical result (solid lines), with academic (a) and exact (b) Dirichlet and academic (c) and exact (d) Neumann boundary conditions on all surfaces.

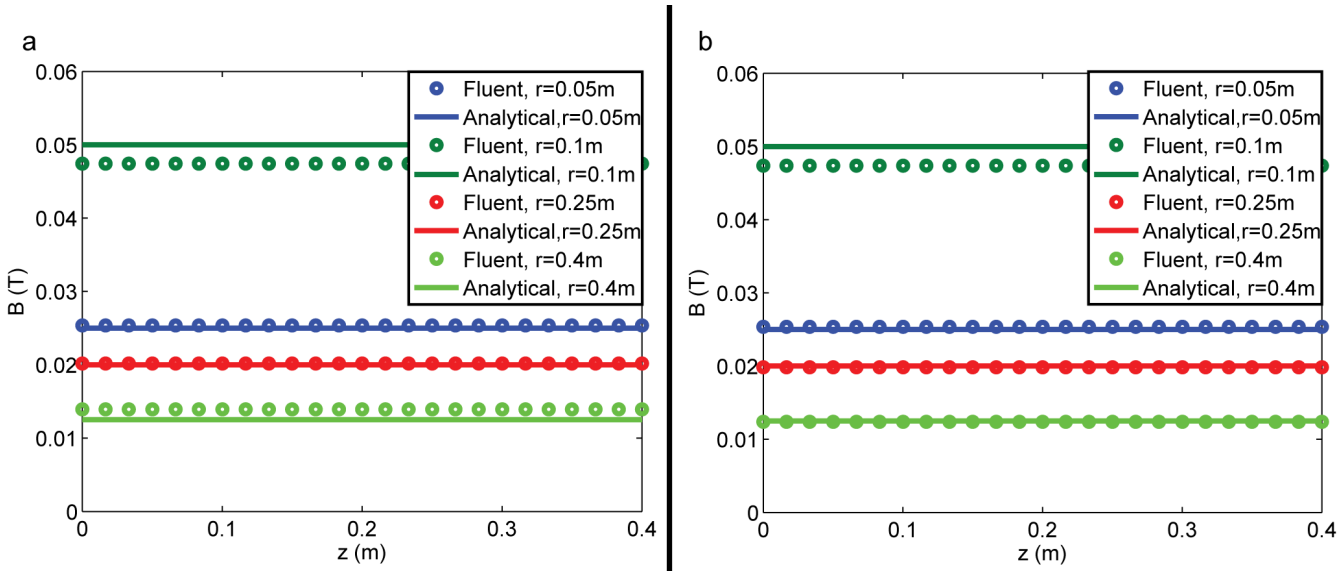

Figure 11.16: Computed magnetic field (circles) as a function of height (z) for various radial distances r from the current tube, compared to the analytical result (solid lines), with academic (a) and exact (b) boundary conditions. Dirichlet and Neumann conditions are applied to insulating and conducting surfaces, respectively.

Figure 11.16 shows the effect of combining Dirichlet and Neumann boundary conditions. As clearly seen from figure 11.16a, the predicted magnetic field from the academic boundary conditions is *significantly* improved when using this combination, the difference when compared to the analytical result being less than 15%. The result using the mixed exact boundary conditions does not change the result as the two formulations are equivalent.

Numerical remark

Although the exact Dirichlet and Neumann boundary conditions have similar predictive power, the computational time varies *significantly*. On average, the magnetic field using Neumann boundary conditions converged in an average of 500 iterations, while the Dirichlet boundary conditions converged in only 5 iterations. The same tendency is found when using academic boundary conditions. Usage of the mixed boundary conditions (as seen in figure 11.16) reduced the number of iterations to an average of 10. This slow convergence is due to the undetermined constant arising from the pure Neumann boundary condition, impeding convergence as there is no reference point for the magnetic vector potential.

11.5 Magnetostatic pressure

The final verification of the basic MHD functionality of the proposed model is related to the Lorentz force,

$$\boldsymbol{f}_L = \boldsymbol{j} \times \boldsymbol{B} \tag{11.20}$$

which is coupled to the Navier-Stokes equation. The Lorentz force can be Hodge decomposed, i.e. split into a irrotational and divergence free part. If known prior to a calculation, the irrotational part is commonly combined with the (irrotational) pressure gradient, resulting in the magnetostatic pressure

$$-\nabla\tilde{p} = -\nabla p + (\boldsymbol{j} \times \boldsymbol{B})_{irrotational}\,. \tag{11.21}$$

Assuming a stationary fluid and a purely irrotational Lorentz force, a pressure gradient will form exactly balancing the Lorentz force, i.e.

$$\nabla p = (\boldsymbol{j} \times \boldsymbol{B})_{irrotational}\,. \tag{11.22}$$

Assuming, for simplicity, $\boldsymbol{j} = j_0\hat{\boldsymbol{y}}$ and $\boldsymbol{B} = B_0\hat{\boldsymbol{z}}$, the resulting pressure is

$$\begin{aligned} \frac{\partial p}{\partial x} &= j_0 B_0 \\ &\rightarrow \quad p = j_0 B_0 x + C. \end{aligned} \tag{11.23}$$

Figure 11.17 shows a comparison between the analytical result (equation 11.23) and the result obtained by FLUENT for a stationary liquid, on a 60 by 60 computational mesh.

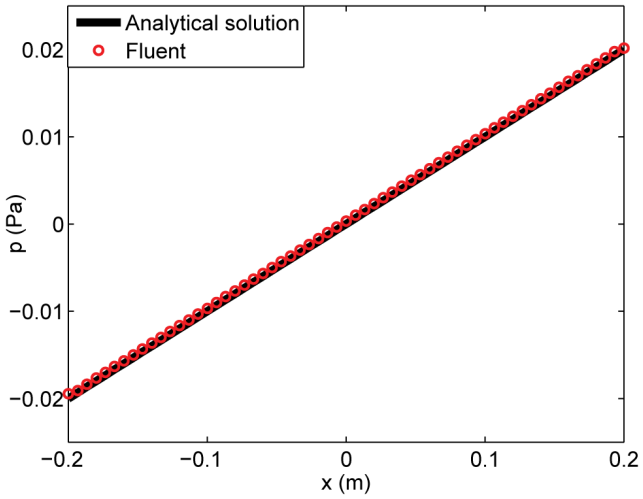

Figure 11.17: Computed magnetostatic pressure (circles) compared to analytical solution (solid line).

Chapter 12

MHD forces on a single bubble

Due to the negligible conductivity of CO_2, electrical currents passing in a conducting medium surrounding a bubble will become deflected, resulting in a force distribution along the bubble surface. In the following the effect of this is studied, first for a non-conducting solid sphere, as the analytical solution for this problem known, and then for a deformable object, i.e. a bubble.

12.1 Forces on a non-conducting solid sphere

Consider a non-conducting sphere suspended in a conducting fluid, carrying a uniform charge density $\boldsymbol{j}_0$ as sketched in figure 12.1, together with definitions for the chosen spherical coordinates.

The boundary conditions for the problem are that the electrical current is tangential to the surface of the sphere while it remains unchanged at large distances. As the sphere is non-conducting, the normal current on the sphere surface is zero. This is equivalent to solving the problem of a uniform, incompressible and inviscid fluid flow past a sphere, provided that induced currents can be neglected.

From the above observation, it is clear that there exists a current stream function Ψ_j, relating to the current density by

$$\begin{aligned} j_r &= -\frac{1}{r^2 \sin\phi}\frac{\partial \Psi_j}{\partial \phi}, \quad j_z = \frac{1}{r\sin\phi}\frac{\partial \Psi_j}{\partial r} \\ &\Rightarrow \quad \boldsymbol{j} = \frac{1}{r\sin\phi}\left[-\frac{1}{r}\frac{\partial}{\partial\phi}, \frac{\partial}{\partial r}, 0\right]\Psi_j. \end{aligned} \tag{12.1}$$

The current stream function is obtained by a superposition of a uniform current $-j_0\hat{\boldsymbol{z}}$ and

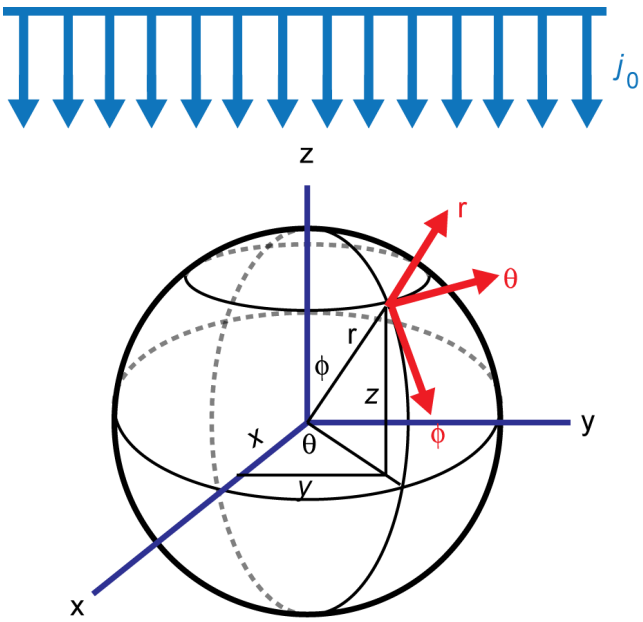

Figure 12.1: Sketch of the problem geometry and definition of coordinate axes.

a doublet at the origin, yielding

$$\Psi_j = \frac{1}{2} j_0 r^2 \sin^2\phi \left(1 - \frac{R^3}{r^3}\right), \tag{12.2}$$

where j_0 is the free current density and R is the radius of the sphere.

Using equation 10.8 and the above relations, the magnetic field is easily identified as

$$\boldsymbol{B} = -\mu_0 \frac{\Psi_j}{r \sin\phi} \hat{\boldsymbol{\theta}}, \tag{12.3}$$

yielding a Lorentz force contribution of the form

$$\boldsymbol{j} \times \boldsymbol{B} = -\mu_0 \frac{\Psi_j}{r^2 \sin^2\phi} \nabla \Psi_j. \tag{12.4}$$

Assuming non-zero, but sufficiently small velocities so that the assumption of a negligible magnetic Reynolds number still holds, the momentum equation to leading order in velocity reads

$$\begin{aligned} \nabla p &= \mu \nabla^2 \boldsymbol{u} + \boldsymbol{j} \times \boldsymbol{B}_{ind} \\ \Rightarrow \nabla p &= -\mu \nabla \times \nabla \times \boldsymbol{u} + \boldsymbol{j} \times \boldsymbol{B}_{ind}, \end{aligned} \tag{12.5}$$

where the assumption of an incompressible fluid has been used to express the Laplacian as a curl. Equation 12.5 resembles a fluid undergoing creeping Stokes motion under the

influence of an electromagnetic field. As noted in section 11.5, the Lorentz force in general consists both rotational and irrotational parts, the former resulting in a flow field, the latter in a pressure gradient. The contribution from the rotational part of the Lorentz force is found by taking the curl of equation 12.5, yielding

$$\mu\nabla\times\nabla\times\nabla\times\boldsymbol{u}=\nabla\times(\boldsymbol{j}\times\boldsymbol{B}_{ind})=-\frac{3}{2}\mu_0 j_0^2\sin\phi\cos\phi\frac{R^3}{r^3}\left(1-\frac{R^3}{r^3}\right)\hat{\boldsymbol{\theta}} \tag{12.6}$$

Assuming that the fluid velocity has the same symmetry properties as the electromagnetic fields, together with the assumption of incompressibility, the fluid velocity can be derived from a stream function for the fluid flow:

$$\boldsymbol{u}=\frac{1}{r\sin\phi}\left[-\frac{1}{r}\frac{\partial}{\partial\phi},\frac{\partial}{\partial r},0\right]\Psi_f. \tag{12.7}$$

The triple curl of equation 12.6 can, after some tedious algebra, be expressed as

$$\mu\nabla\times\nabla\times\nabla\times\boldsymbol{u}=\frac{\mu}{r\sin\phi}\left[\frac{\partial^2}{\partial r^2}+\frac{\sin\phi}{r^2}\frac{\partial}{\partial\phi}\left(\frac{1}{\sin\phi}\frac{\partial}{\partial\phi}\right)\right]^2\Psi_f\hat{\boldsymbol{\theta}}, \tag{12.8}$$

i.e. a fourth order, inhomogeneous PDE for the fluid stream function. Following the ansatz of Chow [17], the stream function describing the *fluid* flow can be written as

$$\Psi_f=R(r)\sin^2\phi\cos\phi, \tag{12.9}$$

resulting upon substitution in equation 12.6 in an ODE for the radial function, with solution easily obtained by power series:

$$\Psi_f=\frac{\mu_0 j_0^2 R^5}{16\mu}\left[c_1\left(\frac{r}{R}\right)^5+c_2\left(\frac{r}{R}\right)^3+\left(\frac{r}{R}\right)^2+c_3\left(\frac{R}{r}\right)^2+\frac{R}{r}+c_4\right]\sin^2\phi\cos\phi. \tag{12.10}$$

The constants c_i are determined from the requirement of physical velocities when r is large and zero velocities on the surface of the sphere (i.e. a no-slip condition is imposed), yielding

$$c_1=0 \qquad c_2=0 \tag{12.11}$$

$$c_3=\frac{1}{2} \qquad c_4=-\frac{5}{2} \tag{12.12}$$

It should be noted that this yields *finite* velocities at large r, resulting from the neglected inertia term in the Navier-Stokes equations. It is suggested by Chow [17] that this could be corrected by using an Oseen approach, as done by Chow and Billings [18]. Nevertheless, the Stokes approximation should hold within the vicinity of the sphere.

Given Ψ_f, the expression can be substituted in equation 12.5 to find the pressure field. On the surface of the sphere, the pressure is

$$p_{surf}=p_0-\frac{9}{16}\mu_0 j_0^2\sin^2\phi R^2, \tag{12.13}$$

i.e. it has its minimum along the equator of the sphere. Considering a sphere of radius 1 cm situated in a fluid carrying $10^4 \mathrm{A/m}^2$, the pressure difference between the top and equator is 0.0071 Pa.

Figure 12.2 shows the steady state pressure distribution and velocity field along the sphere obtained by FLUENT as well as a comparison to the analytical solution. For simplicity, the magnetic field is specified directly as of equation 12.3. Geometry and boundary conditions are as in figure 12.3, except for the sphere which, necessarily, is treated as a no-slip solid surface.

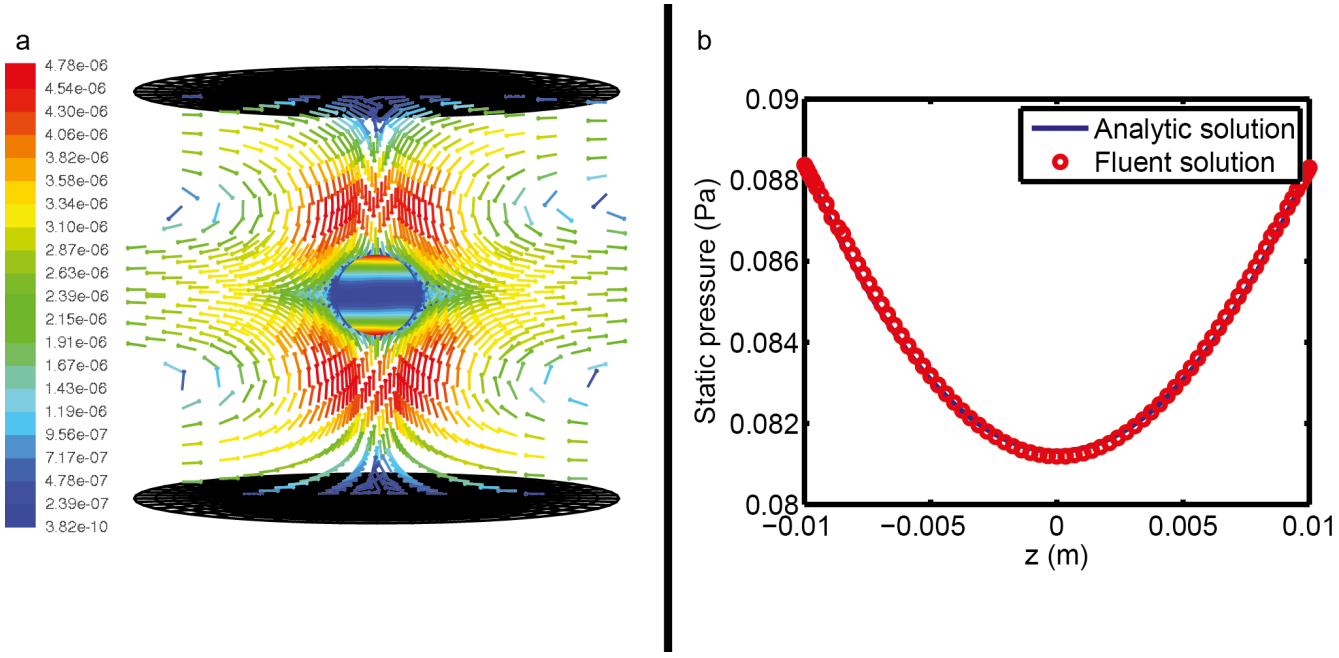

Figure 12.2: Flow field coloured by velocity magnitude and pressure on sphere surface (a) and comparison with analytical solution (b).

The FLUENT solution yields a pressure difference of 0.0072 Pa between the top and equator of the sphere, i.e. an absolute error of 1.4%.

12.2 Forces on a non-conducting bubble

Consider an initially spherical bubble of non-conducting gas placed in a medium carrying an electrical current. As shown in the analysis of a solid sphere, the current deflection of current around a non-conducting sphere yields a pressure field which is minimal along the equator of the sphere. For a deformable object, such as a gaseous bubble, this pressure field results in a compression of the bubble in the direction parallel to the current.

The problem is set up in FLUENT as a two-phase VOF problem, using the full $\boldsymbol{A} - \phi$ model for MHD in a cylindrical geometry (cf. figure 12.3). The bubble is assumed to have an initial radius of 1 cm and situated in cryolite, carrying a uniform current density of 10^4 A/m^2. A constant current density is specified at the bottom of the system, while the reference potential is given at the top.

The top and bottom surfaces are treated as solid walls, while the outer cylinder in treated as a zero gauge pressure outlet. Pressure is discretized by the PISO scheme, while the equations for momentum and UDS equations are discretized using the QUICK scheme. Transient behaviour is treated by the first order implicit method with a constant time step of $1 \cdot 10^{-4}$ s. The mesh, consisting of 568512 quadrilateral cells is shown in figure 12.3.

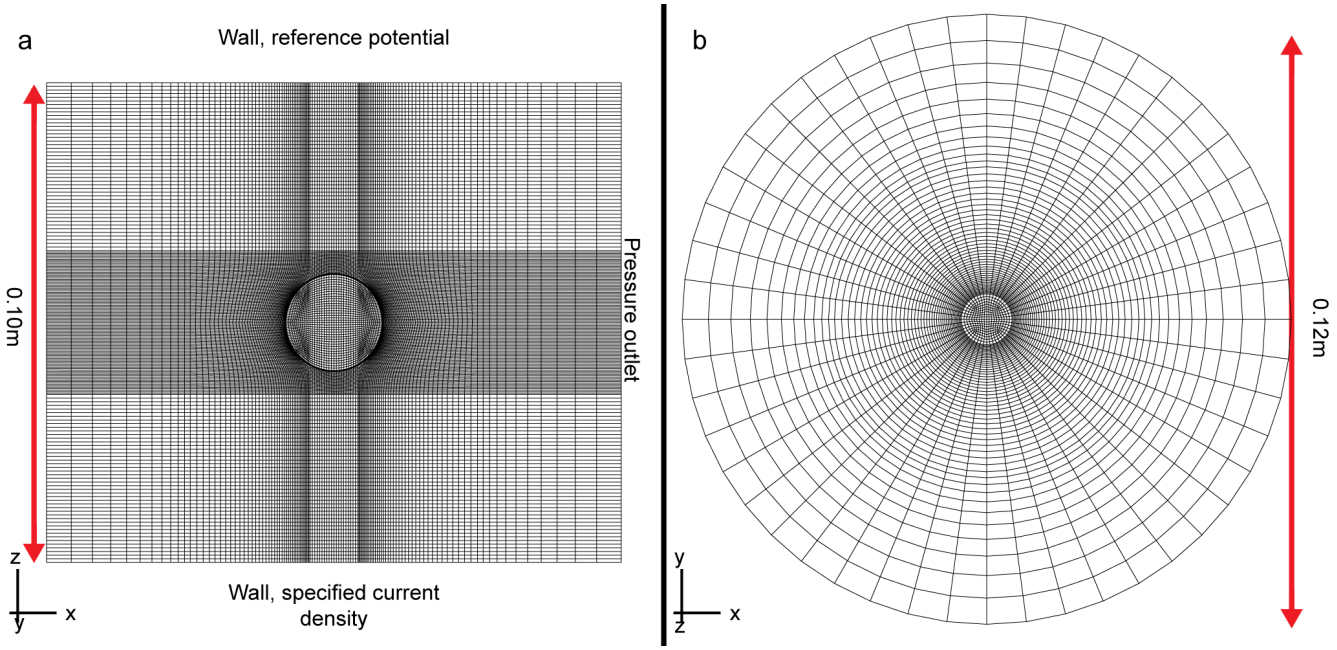

Figure 12.3: Computational mesh, geometry and boundary conditions for non-conducting bubble.

Considering a point far from the bubble (i.e. the outer surfaces), the current field can be approximated by $-j_0\hat{z}$, which is identical to that of section 11.4.2. Hence, the boundary

conditions for A_z can be approximated by equation 11.17. The deflected current along the bubble surface yields a source for the remaining components of the magnetic vector potential. The influence of these components on the outer surfaces can however be considered as a perturbation, so that academic boundary conditions can be used as a first approximation. As all fields are *shared* in the VOF formulation, no boundary conditions are needed for the bubble-cryolite interface.

Figure 12.4 shows the converged current and resulting magnetic field for a bubble with no deformation.

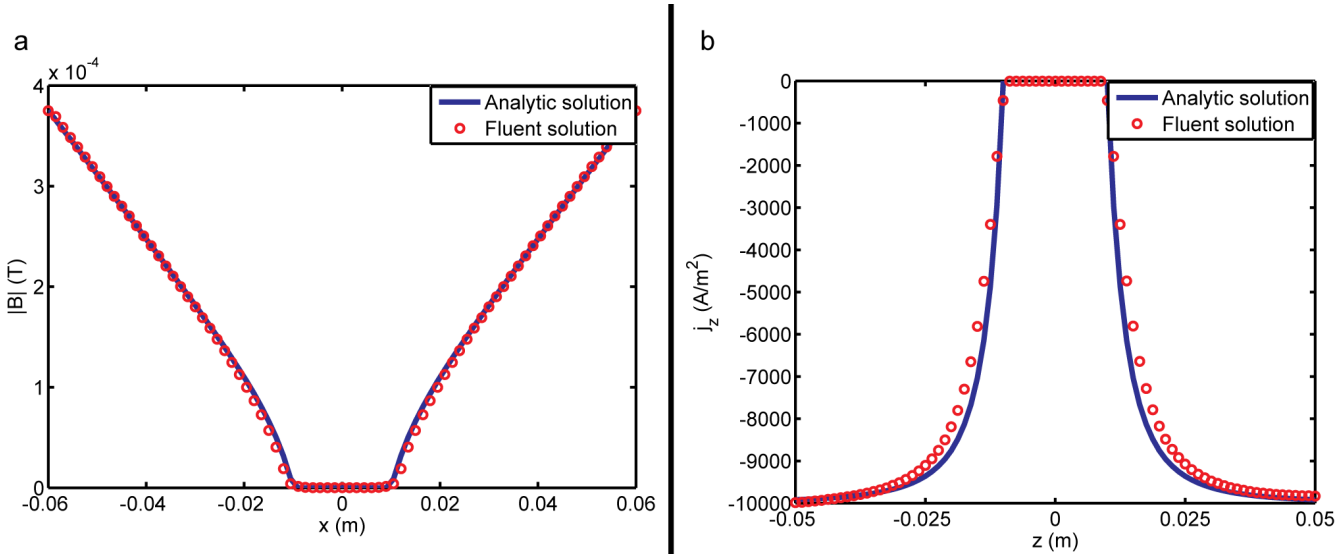

Figure 12.4: Comparison of analytical solution for solid sphere (solid line) and FLUENT solution for non-deformed bubble (circles) for magnetic field (a) in zx-plane along x-axis and electrical current (b) in zx-plane along z-axis.

As seen from figure 12.4, both the electrical current and resulting magnetic field correspond well to the expected analytical behaviour of a solid non-conducting sphere, the average absolute error being less than 5%. Figure 12.5 shows the evolution of a 1 cm bubble over 5 seconds flowtime under the influence of the resulting MHD-forces.

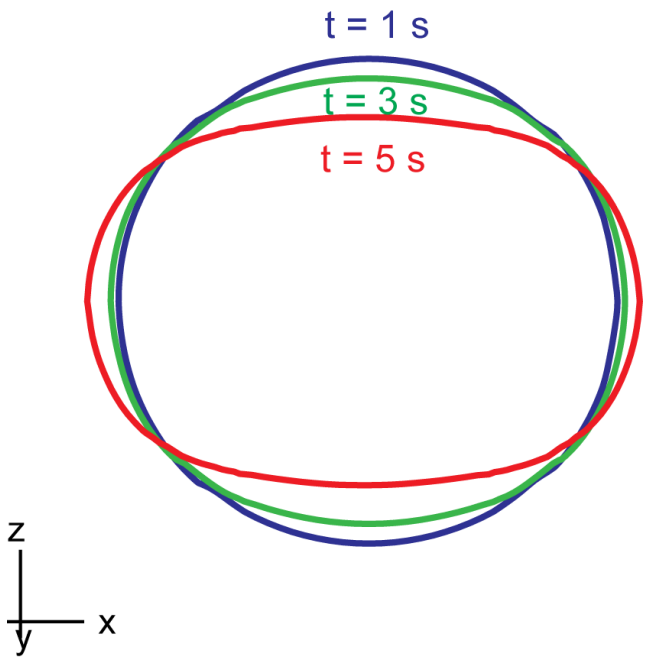

Figure 12.5: Evolution of bubble surface under influence of MHD-forces. Surface shown at 1, 3 and 5 seconds flowtime.

As expected, the bubble is flattened due to the pressure imbalance along its surface.

The resulting pressure due to the deflecting currents is of order 10 mPa, which is small compared to other forces present. For instance, the overpressure in a gaseous CO_2 bubble in cryolite of radius 0.01m due to surface tension is approximately 10 Pa; four orders of magnitude larger. The case with surface tension is not treated here due to the (inadequate for this case) CSF-treatment of surface tension (cf. Appendix A), yielding spurious velocities along the bubble surface effectively screening out effects of the (low magnetic Reynolds number) physical velocity field.

Disregarding surface tension effects, the time scales required to obtain a noticeable deformation are of the same order as a full bubble cycle. Hence, the *local* MHD effects, that is, effects owing to fields produced by a single bubble, discussed in this chapter are not expected to have a significant influence on the overall bubble behaviour.

Chapter 13

MHD effects in a lab scale cell

Results from the previous chapter indicate that local MHD effects are small when compared to other forces acting on a bubble. Global MHD effects can however, under certain conditions, be significant, as proposed by Bojarevics and Roy [8]. As the principal validations on the bubble model of this thesis are performed on a lab-scale electrolysis cell (Eick et al. [29]), which magnetic fields are unknown, these are estimated in the following sections using the proposed $\boldsymbol{\mathcal{A}} - \phi$ model.

13.1 Geometry and setup

In order to simplify meshing, the laboratory cell of Eick et al. [29] is represented by cubes with dimensions corresponding to that of the real cell, as shown in figure 13.1. The essential features of the anode and cathode are well represented by this simplification, but the outer *cylindrical* casing is not. This is however not a critical issue, as the electrical current is nonzero only in the proximity of the interpolar region. Hence, outside this region the magnetic field will decrease in magnitude, rendering MHD effects in this region insignificant.

In essence, the system considered is similar to that studied in section 11.4.2 (with inverted direction), provided that the influence of horizontal currents is small. Hence, in the interpolar region, the dominating contribution to the Lorentz force is expected to be of the form

$$\boldsymbol{f}_L = -\frac{\mu_0 j_0^2}{2} \left(x\hat{\boldsymbol{x}} + y\hat{\boldsymbol{y}} \right), \tag{13.1}$$

i.e. directed towards the center of the interpolar region, with resulting magnetostatic pressure

$$p = p_0 - \frac{\mu_0 j_0^2}{4} \left(x^2 + y^2 \right). \tag{13.2}$$

For the following simulations, cryolite is assumed to be the working material. Simulations are performed with the steady state solver in FLUENT. User defined scalars are discretized using a Power Law scheme and are solved using a W-cycle for increased convergence rate. All other solver settings are kept at default values. Academic boundary conditions as of section 11.4.2, i.e. Dirichlet and Neumann conditions to insulating and conducting surfaces, respectively, are applied to the magnetic vector potential on all internal surfaces, while exact Dirichlet boundary conditions as of equation 11.17 are used for $\mathcal{A}_z$ on the *outer* boundaries.

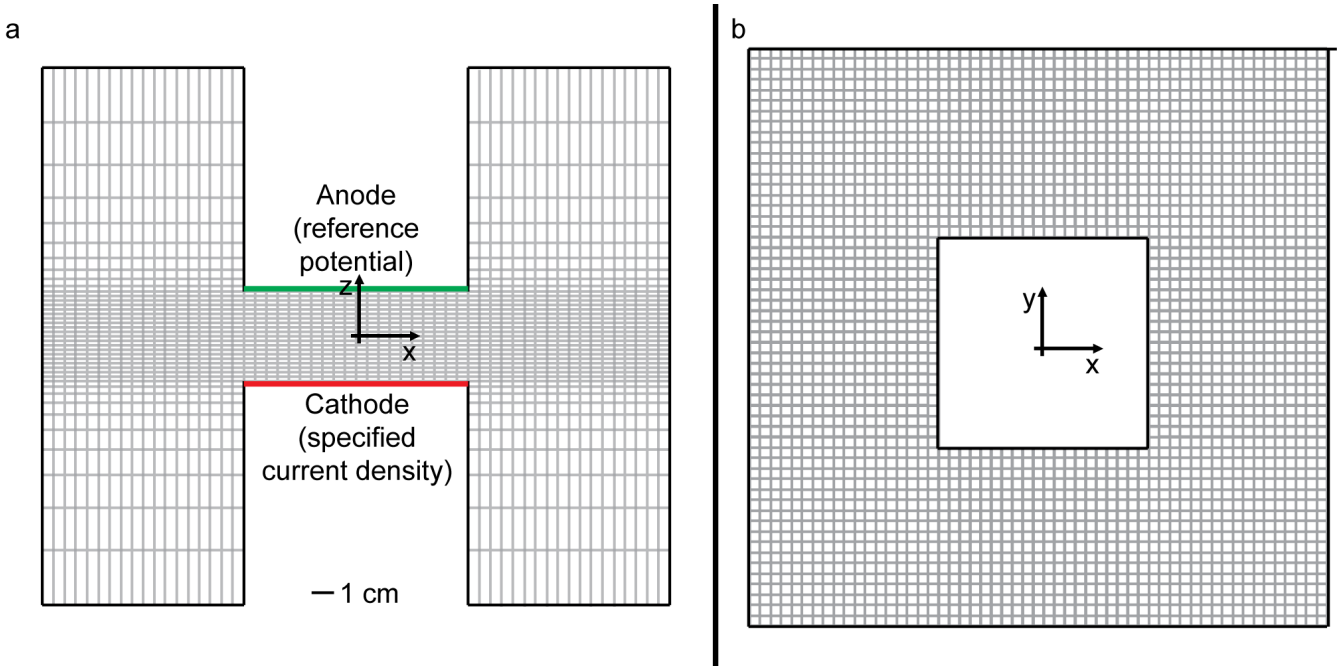

Figure 13.1: Side (a) and top (b) view of geometry and mesh used for lab-cell MHD simulations. The anode potential is fixed while the cathode carries a uniform current density. All other walls (black lines) are considered to be non-conductive. Geometry consists of 117440 cells.

13.2 Electric and magnetic fields

Figure 13.2 shows the converged current density field in the $y = 0$-plane and the magnitude of current density along the line $z = y = 0$ compared to the ideal case of uniform current density, with a prescribed current density of 8000 A/m^2 at the cathode.

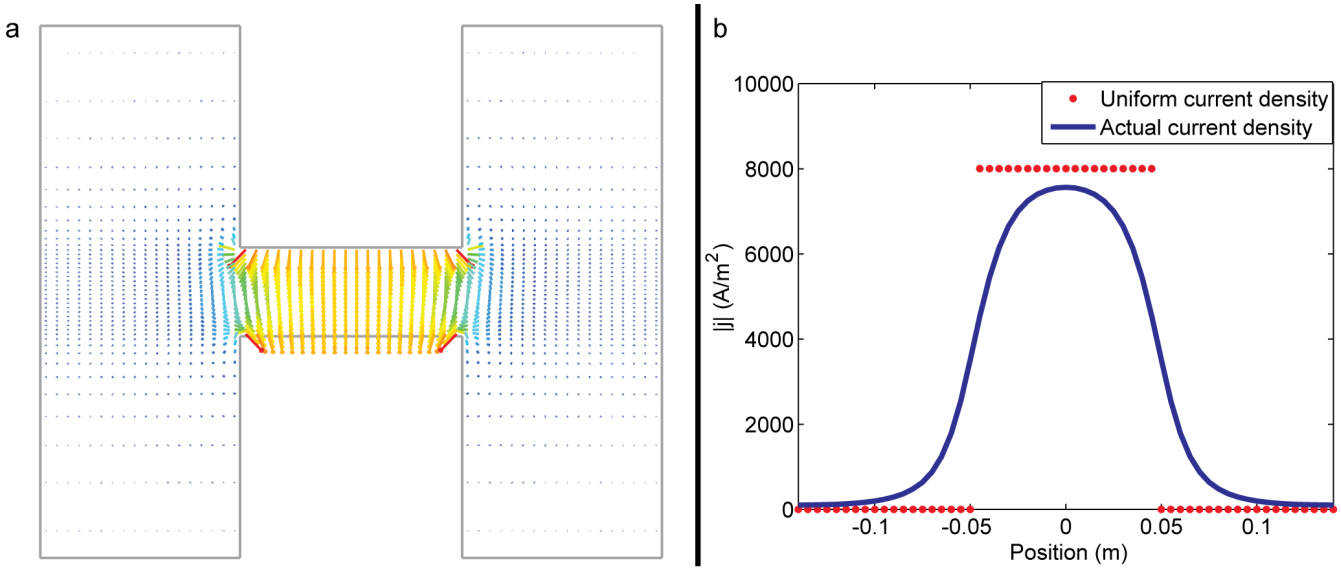

Figure 13.2: Predicted current density field in the $y = 0$-plane (a) and magnitude (solid line) compared to uniform current density (circles) (b).

As seen from the above figure, the actual current density is smeared outside the interpolar region compared to the idealized case. Hence, given a loop with area corresponding to the electrode, *less* current will pass through it than in the uniform case, resulting in smaller magnetic fields along the periphery of the loop. Due to the smearing of the electrical field, the resulting magnetic field outside of the interpolar region is expected to decline at a lower rate than in the idealized case.

Figure 13.3 shows the predicted magnetic field in the $z = 0$-plane and its magnitude along the line $z = y = 0$ compared to the field obtained from a uniform current density.

The calculated magnetic field in the interpolar region (cf. figure 13.3b) is on average 5% lower than that found in the idealized case.

As for the idealized case, the main contribution to the Lorentz force is radial and directed towards the centre of the interpolar region. The resulting (gauge) pressure in the $z = 0$-plane and along the line $z = y = 0$ compared to that obtained by equation 13.2 is shown in figure 13.4.

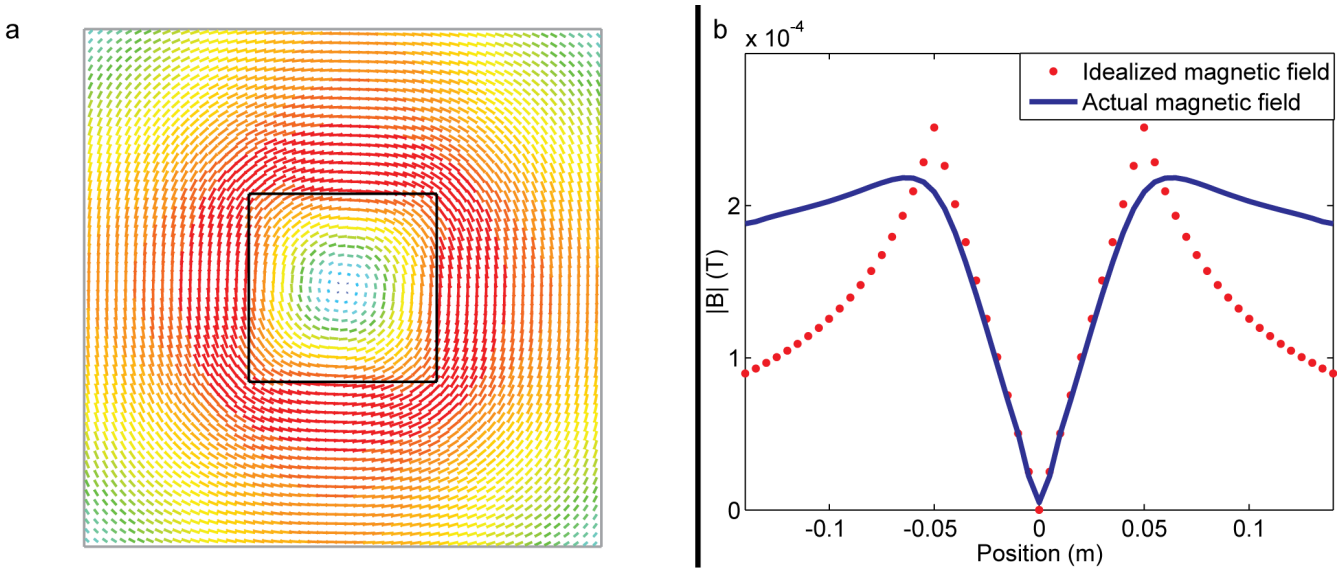

Figure 13.3: Predicted magnetic field in the $z = 0$-plane (a) and magnitude (solid line) compared to field from uniform current density (circles) (b).

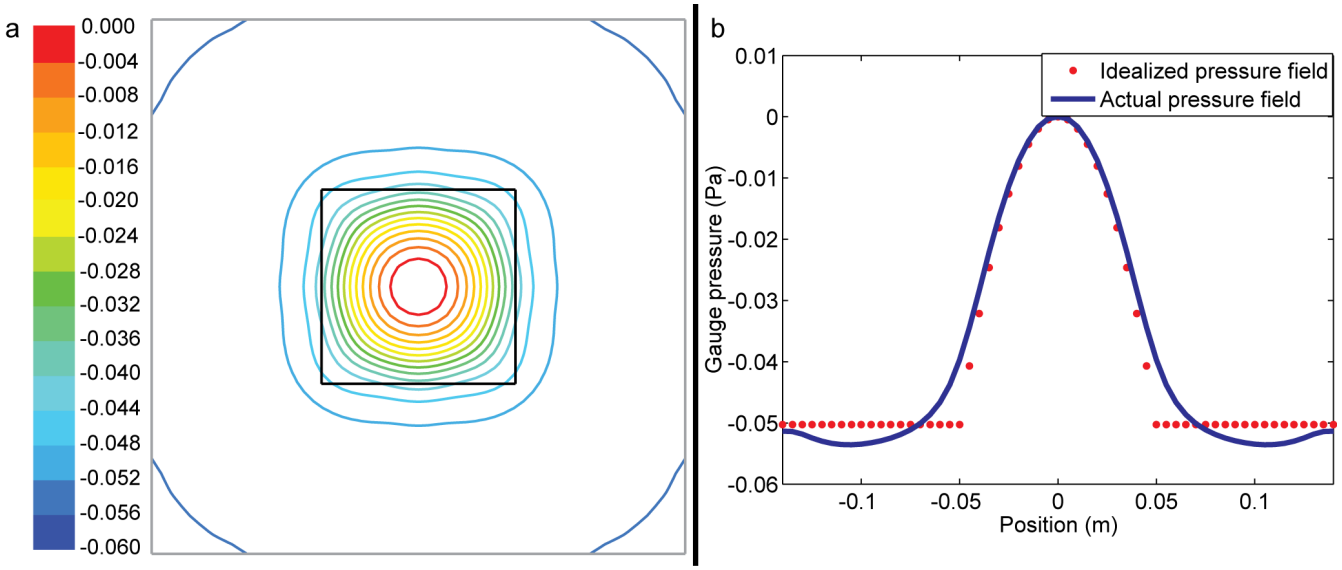

Figure 13.4: Contours of predicted magnetostatic pressure field in the $z = 0$-plane (a) and along line $z = y = 0$ (solid line) compared to field from uniform current density (circles) (b).

The imbalance of pressure between the interpolar region and the outer regions of the cell necessarily results in a motion of the bath. The steady state solution of this motion is shown in figure 13.5.

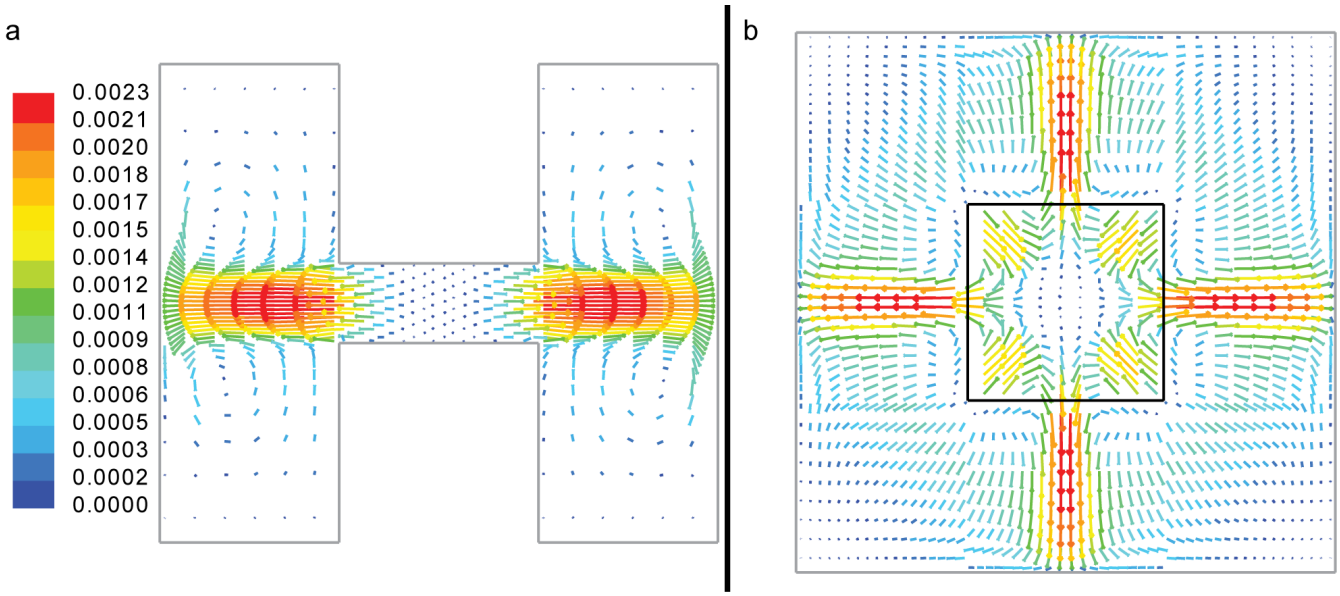

Figure 13.5: Steady state velocity field in $y = 0$- (a) and $z = 0$-plane (b). Vectors are coloured by velocity magnitude.

As seen from the above figure, the MHD-induced pressure field results in a jet-like motion of bath across the sides of the interpolar region, with velocities in the order of 1 mm/s.

Although the resulting pressure and velocity fields are small in magnitude, their direction is such that they lead to enhanced transport to either of the anode edges. The significance of this enhanced transport is studied further in connection with the full bubble model, treated in Part IV of this thesis.

13.3 Bubble-current interactions

The previous section describes the behaviour of the electromagnetic fields in the lab scale cell of Eick et al. [29] without any bubbles present. As seen from figure 11.7, the presence of a non-conductive bubble significantly alters the distribution of electrical current, thus increasing the cell voltage for a given current density.

For simplicity, consider a cylindrical bubble with diameter D_{bub} and thickness h placed on the centre of the anode, as shown in figure 13.6.

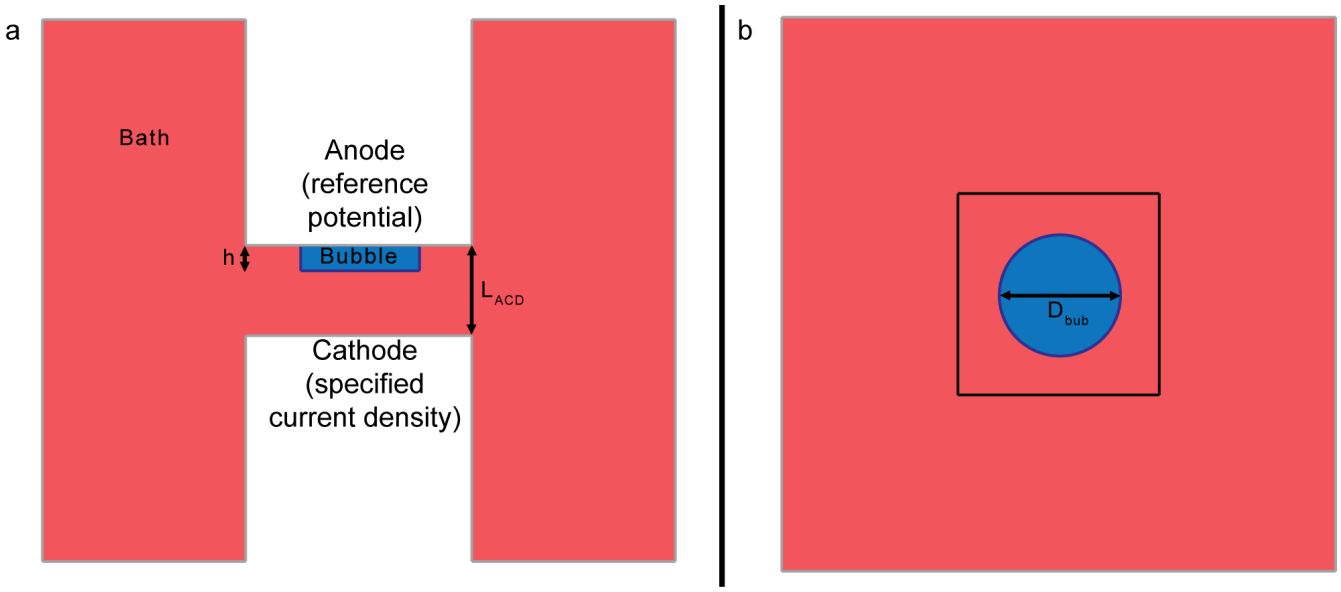

Figure 13.6: Side (a) and top (b) view of geometry for bubble-current interactions. A cylindrical bubble with diameter D_{bub} and thickness h is placed in the interpolar region with length L_{ACD}. Mesh is identical to that shown in figure 13.1.

The classical view of bubble resistance (cf. Hyde and Welch [53]) is that bubbles contribute to the electrical resistance through a reduced interpolar space $(L_{ACD} - h)$ and a coverage factor

$$\theta_{cov} = \frac{A_{bub}}{A_{anode}}, \tag{13.3}$$

where A_{bub} is the projected bubble area on an anode with surface A_{anode}. Detailed calculations by Zoric and Solheim [150] and Thonstad et al. [117] show that the influence of current deflection can be as large as 30% of the total resistance, thus extending the classical view. The total resistance of the cell is as of Thonstad et al. [116] given as

$$\frac{R_T}{R_0} = 1 + \left(\frac{1}{1-\theta_{cov}} - 1\right)\left(\frac{h}{L_{ACD}} + \frac{1 - \frac{h}{L_{ACD}}}{1 + \frac{10(L_{ACD}-h)}{D_{bub}}\sqrt{\theta_{cov}}}\right), \tag{13.4}$$

where R_0 is the electrical resistance when no bubbles are present. Figure 13.7 shows a comparison between the above equation and the cell voltage predicted by FLUENT for $L_{ACD} = 4$cm for various values of D_{bub} and h, at a current density of 8000 A/m^2.

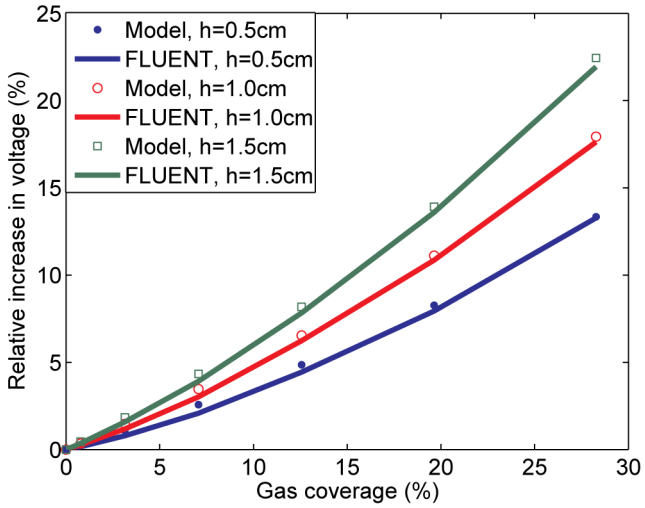

Figure 13.7: Predicted cell voltage (solid lines) compared to equation 13.4 (symbols) for various bubble sizes.

The average difference between simulated voltage and that obtained by equation 13.4 is less than 10% for the cases considered.

As shown by Zoric and Solheim [150], the presence of a bubble results in a local maxima of current density close to the bubble edge, while the local current density in the bubble should be zero. In addition, a local minima in current density occurs in the shadow of the bubble. As seen from figure 13.8, the proposed model reproduces the expected behaviour.

As a result of the altered current density, the distribution of magnetic fields and the resulting Lorentz forces necessarily change. As seen from figure 13.9, this is indeed the case; the magnetic field is effectively suppressed within the bubble, as no current density passes through this region. The far-field is however identical, as the *total* current density is the same for both cases considered.

The inclusion of bubbles thus introduces localized, temporal, MHD effects which in principle can alter global bubble behaviour, the dynamics of which will be treated in Part IV of this thesis.

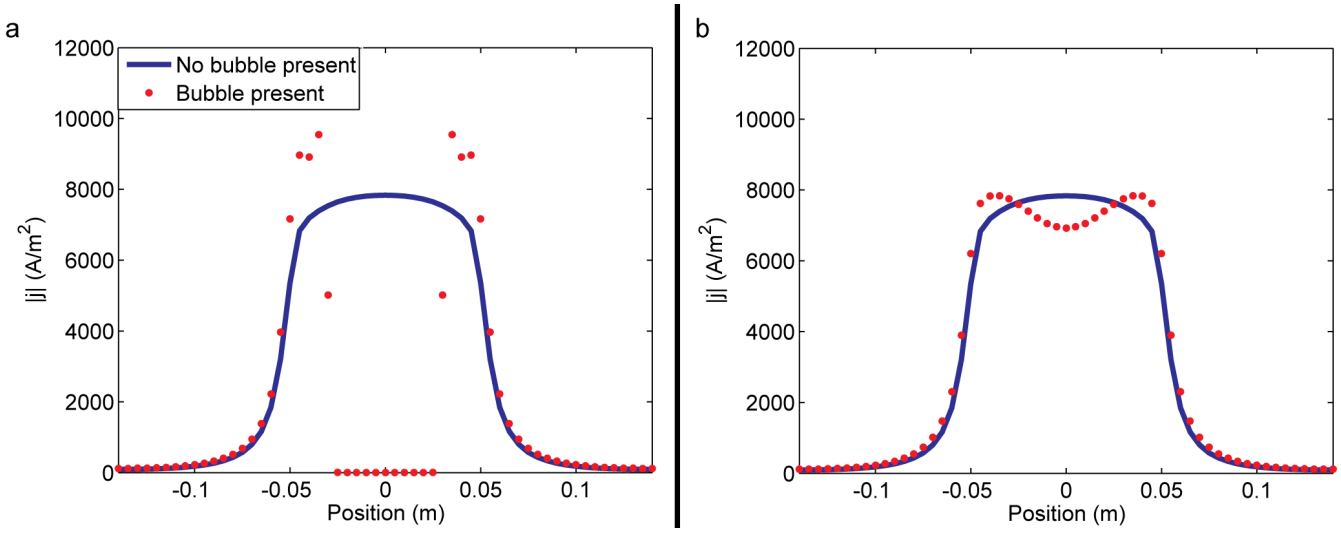

Figure 13.8: Distribution of current density with bubble present (symbols) compared to case without bubble (solid line) along lines passing through bubble $y = 0, z = 1.5$ (a) and close to cathode $y = 0, z = -1.5$ (b), for j=8000 A/m^2, D_{bub}=3 cm, h=1 cm and L_{ACD}=4 cm.

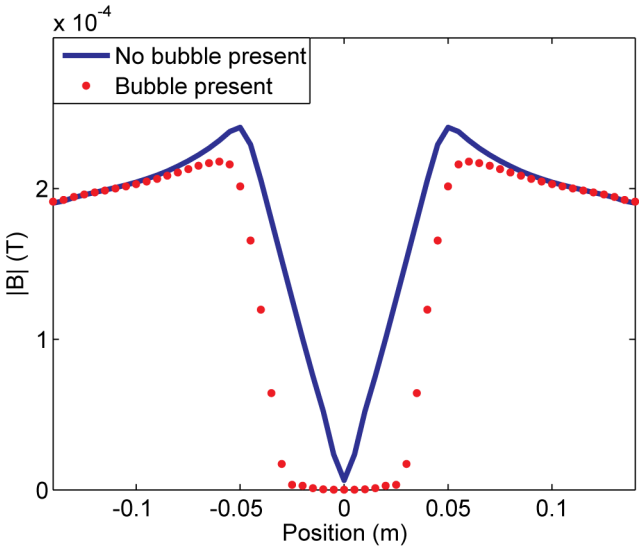

Figure 13.9: Prediction of magnetic field bubble present (symbols) compared to case without bubble (solid line) along lines passing through bubble $y = 0, z = 1.5$ for j=8000 A/m^2, D_{bub}=3 cm, h=1 cm and L_{ACD}=4 cm.

Part IV: Gas generation and bubble evolution

Outline of Part IV

Part IV describes a phenomenological model for the creation and transport of anodic gas bubbles. It is divided into four chapters which cover:

- Theory and background
- Verification studies
- Validation studies
- 3D case study

Following the derivation of the proposed model and essential verification studies, the model is validated against the lab scale experiments described in part II of this thesis.

The proposed model is a *new* multiscale approach in which molecular species are produced and transported through a supersaturated electrolyte. Sub grid bubbles are allowed to form through nucleation and the resulting bubble population evolves through mass transfer and coalescence. As sub grid bubbles reach a certain size they are transferred to a macroscopic phase which evolution is governed by the VOF method.

Chapter 14

Theory and background

A realistic model of gas evolving anodes in a Hall-Héroult cell should treat the following issues:

- Generation and transport of molecular CO_2.
- Nucleation of gaseous bubbles.
- Growth and coalescence of bubbles.
- Dynamic evolution of the bubbly flow and coupling to flow- and MHD fields.

The final stage, termed the macroscopic stage, is treated by means of the VOF model and MHD effects are governed by the models presented in Part III of this thesis. In the following sections, a formalism treating each of the remaining above issues is developed.

14.1 Microscopic gas generation and transport

14.1.1 Generation of microscopic gas fractions

It is an undisputed experimental fact that small gaseous bubbles predominantly form on specific nucleation sites, a phenomena which relies upon the presence of CO_2, which is formed on the anode surface by some chemical reaction. Considering the following, simplified, half reaction on the anode

$$\frac{3}{2}O^{2-} + \frac{3}{4}C \rightarrow \frac{3}{4}CO_2 + 3e^-, \tag{14.1}$$

where oxygen is supplied from the raw material (alumina), carbon is supplied from the anode and electrons are supplied from the imposed external current (passing through the carbon anode). Although reaction 14.1 is the most simple form of the anode reaction, it introduces four effects which influence the overall picture;

1 The anode is consumed during operation.

2 Oxygen (in some form) must be present in order to produce CO_2.

3 The reaction rate can be a limiting step.

4 Electrons must reach the specified reaction site (i.e. a site with non-zero local current density) in order to produce CO_2.

As the anode is consumed, the (average) anode-cathode distance (ACD) is adjusted so that it is constant in order maintain stable operational conditions (cf. Grjotheim and Kvande [47]). Furthermore, the anode consumption rate is small compared to typical bubble time scales, typically on the order of 1–2 cm per 24 hours. Hence, the anode consumption can as a first approximation be neglected.

The presence of oxygen containing species depends upon the dissolution and transport of Al_2O_3. Throughout operation, alumina is fed from specific sites to the cell at regular intervals in order to keep the concentration within a given band (cf. Grjotheim and Kvande [47]). Hence, the concentration of oxygen containing species in the bath can be assumed to be close to the sought operational concentration band. Furthermore, as shown by Dahlkild [23], concentrations of *ionic* species are essentially homogeneous close to the electrodes due to the mixing effect of bubbles and electrophoresis. Based on these arguments, it can thus be assumed that the concentration of oxygen containing species is homogeneous and constant.

The consequences of the two above assumptions is that

a Anode properties such as pore-distribution and local height remain constant.

b The anode effect (cf. Grjotheim and Kvande [47]) cannot be handled.

c The dynamics of alumina dependent properties cannot be treated.

Regarding the reaction rate, several kinetic parameters are suggested in the literature due to the large uncertainties in the exact anode process. A common feature is, necessarily, a fairly large dependence of alumina concentration. Kisza et al. [64] and [65] study plausible reactions and find reaction rates pointing to relatively large Damköler numbers (cf. Bird et al. [6]), suggesting that the reaction rate can be taken to be instantaneous, compared to time scales of interest, as a first approximation.

Neglecting the influence of the first three issues presented above leads to the readily encountered assumption that the generation of CO_2 is dependent only upon local current density. That is, the CO_2 production (kg / s) on the anode surface is given by Faraday's law

$$\dot{m}_{CO_2,d} = \frac{M_{CO_2} I}{\nu_e F}. \tag{14.2}$$

14.1.2 Transport of molecular gas species

The produced CO_2 is transported away from the anode surface by molecular diffusion and superimposed advection. As described by Vogt [126]; *If the interfacial concentration exceeds a certain value (depending on the properties of the electrolyte, the gas and the surface morphology of the electrode) nuclei at the electrode surface become active and molecular gas is transformed into a gaseous phase. The electrode starts working as a gas evolving electrode.* Hence, the distribution of molecular CO_2 is governed by two processes;

a Convective and diffusive transport of CO_2.

b Mass transfer of molecular CO_2 to nuclei and growing bubbles.

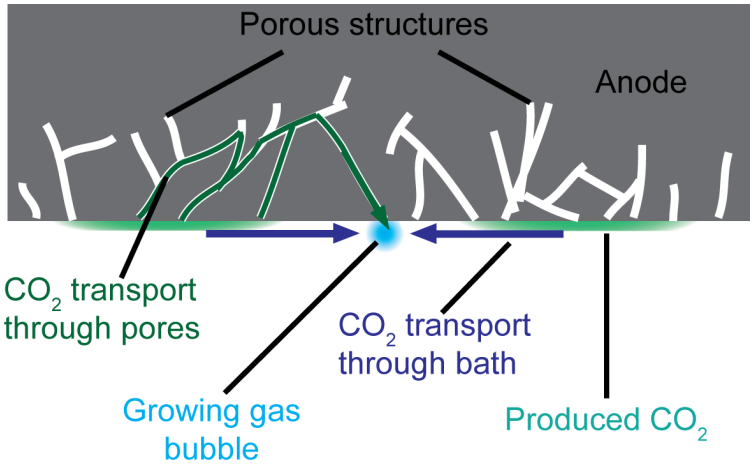

Figure 14.1: Sketch of the two possibilities for transport of molecular CO_2.

Although the literature agrees upon that molecular CO_2 is produced on the anode surface, the path taken by gaseous species following production is somewhat disputed. As sketched in figure 14.1, two possibilities exist:

- CO_2 is transported through pores in *the anode*.
- CO_2 is transported through *the bath*.

Both processes rely on the fact that either the anode or the bath operates as a gas reservoir. Although both transport mechanisms have been used for general electrolysis applications, it appears as though the anode transport scenario has become the most common approach when it comes to the Hall-Héroult process, possibly due to the conclusion of Poncsák et al. [93] stating that storage and diffusion of gas through the electrolyte plays a negligible role in the aluminium reduction cell. This conclusion is based upon the fact that CO_2 has a relatively low solubility in the bath, ranging from 1 to 5 mol/m^3 (depending upon alumina concentrations, Numata and Bockris [85]), and low diffusivities, ranging from 10^{-9}-10^{-5} cm^{-2}/s (Poncsák et al. [93]).

The anode commonly used in the Hall-Héroult process is known to have a volumetric porosity of 10-30% (Grjotheim and Kvande [47]), suggesting that it can contain a corresponding amount of gas. Poncsák et al. [93] estimate the molecular diffusivity of CO_2 in the carbon anode to be $1.5{\cdot}10^{-2}$ cm^2/s; significantly higher than in the bath. An analysis based exclusively on a comparison of the diffusivities of (pure) CO_2 clearly favours the anode transport model, as this mode will allow for faster evolution of bubbles. However, considering the broader picture, effects reported in the literature indicate that this transport mechanism has some shortcomings.

First and foremost, a direct consequence of the anode transport model is that a non-porous anode cannot develop into a gas evolving electrode. Nevertheless, successful electrolysis experiments have been performed using so-called glassy anodes (cf. for instance Leistra and Sides [73]). Secondly, no plausible mechanism explaining the physics resulting in a saturated anode is given, i.e. by which physical principles the gas moves through the anode and back to bubble nuclei, rather than leaving the anode altogether. In addition, the mass transfer coefficient from the anode to bubble nuclei is unknown and must be estimated. Poncsák et al. [93] determine the mass transfer coefficient by means of a parametric study in order to match the model to experimental values[1].

The low diffusivity and resulting slow mass transfer pointed out by Poncsák et al. [93] is not necessarily as important as it at first might appear, as this, in combination with the low saturation concentration, indicates that the bath in proximity of the anode rapidly becomes *supersaturated*, thus allowing for bubble nucleation and further mass transfer. Although the low diffusivity would suggest that mass transfer would be slow, high levels of supersaturations could in principle compensate for this, thus evolving bubbles at rates comparable to the anode transport mode.

Due to the large uncertainty in factors influencing the mass transfer, both transport modes are left with the same degree of uncertainty. In a real process (excluding glassy anodes), both bath and anodic gas transport are most certainly present and the dominating mode will vary depending upon operational parameters and local hydro- and thermodynamical conditions. From a modelling perspective one mode can be included in the other by adjusting the mass transfer parameters accordingly, yielding the two transport mechanisms equivalent. The choice of model thus becomes of a practical nature based on predictive power, numerical stability, compatibility with other models and computational cost.

As the main goal of the present work is to describe transport phenomena in the interpolar region (i.e. the bath) and due to a somewhat higher predictive power (possibility to treat glassy anodes), the bath transport model is chosen. In this case, the mass fraction of dissolved (molecular) CO_2 is governed by the following advection-diffusion equation

$$\frac{\partial \rho X_{CO_2}}{\partial t} + \nabla \cdot (\boldsymbol{u}\rho X_{CO_2} - \rho \mathcal{D}_{eff} \nabla X_{CO_2}) = S^p_{CO_2} - S^n_{CO_2} - S^{dmt}_{CO_2}, \tag{14.3}$$

[1] Which results in a somewhat unfair comparison to the bath transport model

where X_{CO_2} is the local mass fraction of CO_2, ρ is the local fluid density, $\boldsymbol{u}$ is the bath velocity and $\mathcal{D}_{eff}$ is the effective diffusivity. The source- and sink terms on the right hand side represent production (as of equation 14.2), nucleation of gaseous bubbles and direct mass transfer to existing bubbles, respectively. The corresponding local *concentration* of CO_2 is given as $C_{CO_2} = \rho X_{CO_2}$.

14.2 Nucleation of gaseous bubbles

Nucleation is a broad term covering the generation of particles, for instance bubbles or crystals, from supersaturated and/or superheated fluids. As expected from the broad definition, nucleation processes occur in numerous applications ranging from carbonated beverages to cavitation on a propeller of a submarine. Somewhat related to the first example is nucleation in electrolysis cells, where chemical reactions produce a supersaturated state from which bubbles are created. Hence, in order for nucleation to proceed, the local species molar fraction Y_i (or concentration) must exceed the (local) saturation molar fraction (solubility) Y_s. That is,

$$\mathcal{S} = \frac{Y_i}{Y_s} - 1 > 0, \tag{14.4}$$

where $\mathcal{S}$ is the supersaturation, must be fulfilled.

A classical estimate of the degree of supersaturation needed is obtained from Henry's law, relating pressure to molar fractions through a linear relation. Using Henry's law, the pressure elevation due to supersaturation is given as

$$\Delta p = p_i - p_s = H\left(Y_i - Y_s\right) = p_s \mathcal{S}, \tag{14.5}$$

where H is Henry's constant for this particular system. From a mechanic perspective the pressure elevation Δp is due to surface tension, σ acting in the (curved) surface of the bubble and is given by

$$\Delta p = \frac{\gamma}{D_{bub}}, \tag{14.6}$$

where D_{bub} is the diameter of the bubble. Evidently, the required supersaturation can be significant if nucleated bubbles are small, which typically is the case.

As argued by Jones et al. [57], the nucleation events observed in most instances occur at low to moderate degrees of supersaturation, leading to a new classification of different modes of nucleation.

14.2.1 Nucleation modes of Jones et al.

Jones et al. [57] use the term nucleation to *generically denote any process that leads autogenously to the formation of a bubble*. Due to the generic nature of the term and confusion in the literature, the authors make an effort to mechanistically define *four* types of nucleation, described in the following sections, thus extending the classical picture based on homogeneous and heterogeneous nucleation.

Bubble generation by classical homogeneous nucleation (type I)

Classical homogeneous nucleation involves nucleation of bubbles in the liquid bulk of a homogeneous solution. Prior to the nucleation event, there are no gas cavities present, meaning that bubbles are created at seemingly random places as sketched in figure 14.2.

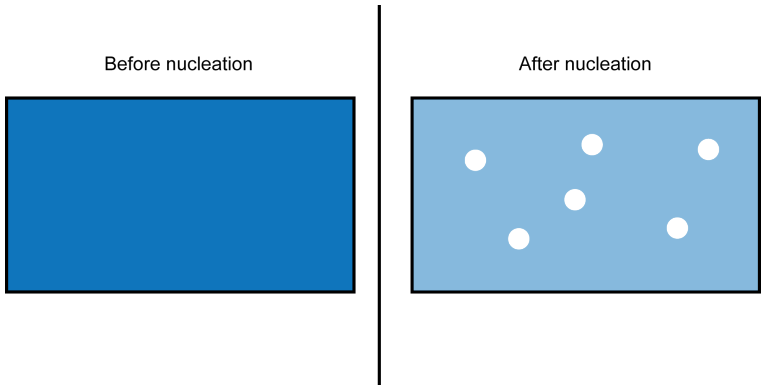

Figure 14.2: Classical homogeneous nucleation where bubbles are nucleated in the bulk of a liquid.

For a classical nucleation event to occur, a (bubble) surface must be formed in a region where no gas was present, thus "tearing apart" the surrounding fluid. This motion of the surrounding fluid requires a significant amount of energy, available only at high partial pressures, i.e. high levels of supersaturation. As shown by Jones et al. [57], homogeneous nucleation requires supersaturation levels of 100 or more and nucleation of an additional bubble at the same site (after bubble departure) is highly unlikely.

Bubble generation by classical heterogeneous nucleation (type II)

Heterogeneous nucleation is similar to the homogeneous case, except that nucleation occurs on some irregularity in the system, for instance a crevice on a surface as shown in figure 14.3.

As for type I nucleation, no gas is present in the system prior to the nucleation event, suggesting that the level of supersaturation required is comparable in the two cases. Upon departure of the bubble, a small portion of gas may remain at the surface enabling nucleation of type III and IV, as described in the following.

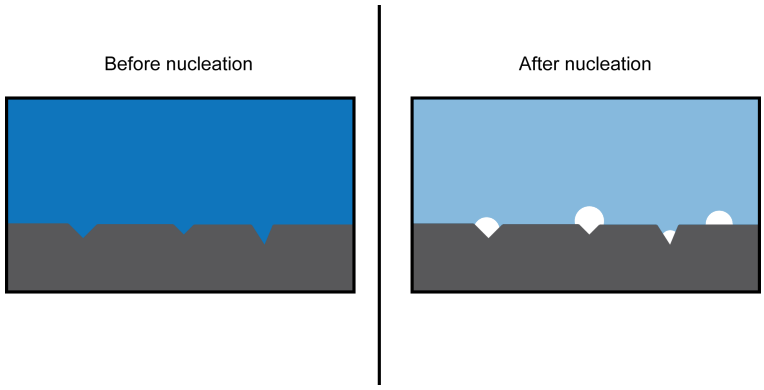

Figure 14.3: Classical heterogeneous nucleation where bubbles are nucleated on imperfections of a surface.

Bubble generation by pseudo-classical nucleation (type III)

Pseudo classical nucleation involves the generation of bubbles at *pre-existing* gas cavities in the system, as shown in figure 14.4.

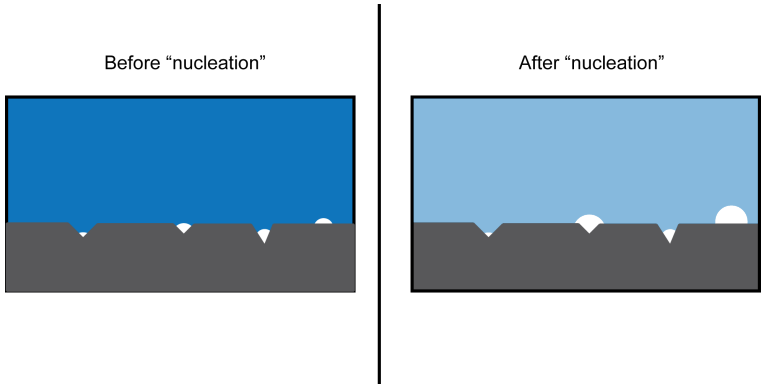

Figure 14.4: Pseudo-classical nucleation where bubbles are generated on pre-existing gas cavities with curvature less than the classical stable radius.

The pre-existing cavities are metastable in the sense that their curvature is less than the stable radius predicted by the classical theory (equation 14.6). Hence, there exists a finite energy barrier that must be overcome in order for further growth (nucleation) to occur. According to Jones et al. [57], local fluctuations in supersaturation are responsible for bringing nucleation sites to life. This is similar to the classical nucleation theory, although much lower levels of supersaturation are needed as a surface already is present.

Bubble generation by non-classical nucleation (type IV)

Type IV nucleation is denoted non-classical by Jones et al. [57] because there is no nucleation energy barrier to overcome. Such a process is possible on pre-existing gas cavities with curvature *larger* than the classical stable radius, as shown in figure 14.5. Hence, this mode is entirely different from the *classical* notion of nucleation.

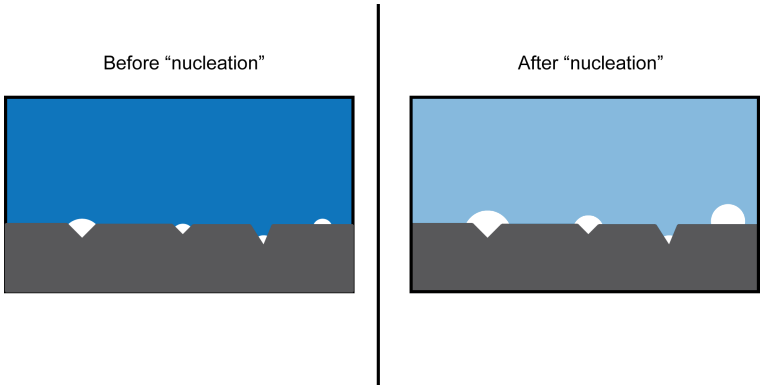

Figure 14.5: Non-classical nucleation where bubbles are generated on pre-existing gas cavities with curvature larger than the classical stable radius.

The pre-existing gas cavities are present from prior nucleation events (type II or III) or as residues from the preparation of the system. As no energy barrier is present, type IV nucleation is essentially equivalent to bubble *growth* in a supersaturated solution, i.e. mass transfer driven by a concentration difference between the bulk fluid and bubble surface. As the supersaturation decreases, the critical radius of a given cavity increases until bubble production ceases. In this case, a new type III nucleation event is required before bubble generation by type IV nucleation continues.

The quasi-steady state picture of a bubble evolving system is thus an alternation between pseudo- and non-classical nucleation. However, the observed steady cycle of bubble production in for instance carbonated beverages is, as postulated by Jones et al. [57], accounted for by the non-classical nucleation theory. As shown in the following, this theory can also serve as a basis for treating bubble generation in Hall-Héroult cells.

14.2.2 Bubble generation in Hall-Héroult cells

On a fundamental level, little is known regarding generation of bubbles in Hall-Héroult cells. A phenomenological description can however be extracted from the overall information found in the literature. Experimental observations indicate that large to moderate voltage oscillations are due to a (quasi) periodic release of *large* bubbles. Large bubbles are created in a semi-continuous fashion through the successive coalescence and growth of smaller bubbles down to some minimal bubble size (typical diameter of 0.4-0.6 mm) found to originate *from the anode surface* in a steady manner (cf. Xue and Øye [139]). The formation of these microbubbles is in the following denoted as *nucleation*, following the general definition of Jones et al. [57].

Xue and Øye [139] find a linear relation between voltage and time during the initial growth of bubbles (before coalescence occurs), which corresponds to a linear increase in the projected bubble area, as of equation 13.4 for small values of θ_{cov}. This suggests that the bubble diameter, D_{bub} should follow a growth-law of the form

$$D_{bub} \propto \sqrt{t}, \tag{14.7}$$

which essentially is the classical result of Scriven [106], describing the *growth* of bubbles in supersaturated solutions, analogous to the model adopted by Jones et al. [58], to describe type IV nucleation.

As shown in figure 14.6, the linear voltage regime starts shortly after the release of a (large) bubble.

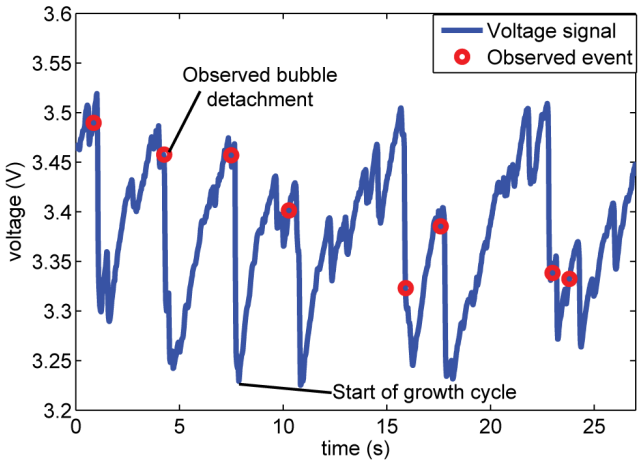

Figure 14.6: Measured voltage signal (solid line) and observed escaping bubbles (circles) for lab scale experiments described by Eick et al. [29].

The short time between release and generation of new bubbles suggests that low to moderate levels of supersaturation are sufficient to initiate bubble nucleation. Furthermore,

the characteristic growth curves indicate a smooth increase in bubble coverage following a release event.

The above observations indicate that nucleation in Hall-Héroult cells relies upon a steady production of gas, rather than an abrupt flashing of bubbles requiring high levels of supersaturation. That is, non-classical nucleation appears to phenomenologically describe steady state bubble generation in Hall-Héroult cells.

The main requirement for bubble generation by type IV nucleation is that gas cavities exist prior to the nucleation event. Considering the porosity of industrial anodes (Grjotheim and Kvande [47]), the surface roughness is expected to be significant. Measurements of the surface roughness reveal large variations in pore size, the majority of the measurements yield pore diameters in the range of 20 to 100 μm (cf. for instance Rørvik and Øye [102]). This results in a high density of sites where gas in principle could be trapped.

A detailed review of mechanisms leading to gas entrapment in cavities is given by Jones et al. [57]. In general, the literature agrees that gas entrapment depends upon the geometry of the crevice and the contact angle between fluid and gas. Specifically, the requirement

$$\theta > 2\beta, \tag{14.8}$$

where θ is the contact angle and β is the half angle of the crevice, is needed for gas to remain trapped in the pore. That is, the depth h_p of a pore with diameter D_p must be such that

$$h_p > \frac{D_p}{2\tan\frac{\theta}{2}}. \tag{14.9}$$

Considering typical contact angles of 100 to 140° (cf. Grjotheim et al. [46]), the depth of the pore should be of order 10% or greater than the corresponding pore diameter, if gas is to remain trapped in it. Typically, as seen from the permeability studies of Rørvik and Øye [102], the pores present on the anode surface appear to meet this requirement.

14.2.3 A simple model for pore distribution

As the typical pore diameter is the μm-range, it is evident that in a practical calculation of even a lab scale anode (10 by 10 cm), the detailed porous structure cannot be resolved by the computational mesh. Hence, the current section sets out to describe a model which transforms the essence of the sub-grid porosity to a macroscopic property, namely the effective pore density.

As a simplified model, the following is assumed

a Only one pore diameter is present (the mean pore diameter).

b The effective pore density ($\rho_{pore} = A_{pore}/A_{tot}$) is given by a random distribution.

As a basis for the effective pore density, consider figure 14.7, showing the surface of a 5 by 5 cm piece of anodic material.

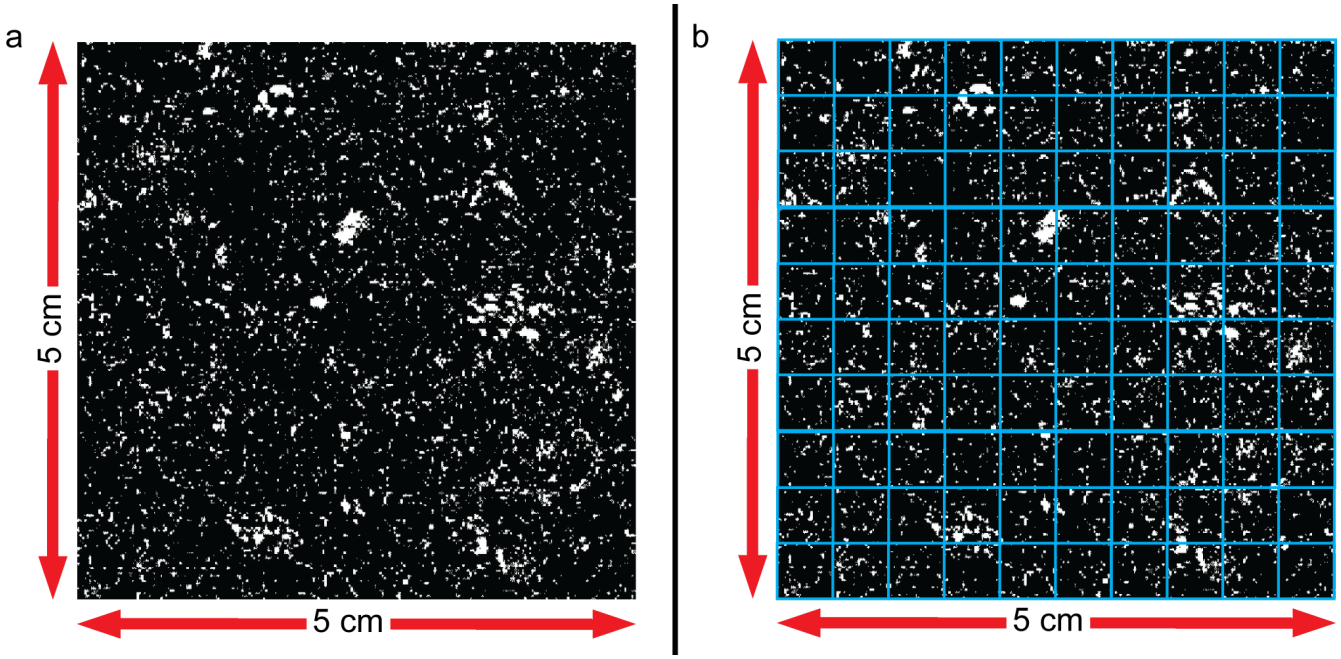

Figure 14.7: Segment of anode surface (a) divided into 100 cells (b). White regions represent pores and cavities. Image courtesy of Lorentz Petter Lossius [78]

Considering figure 14.7, it is evident that the anode surface has a significant microstructure. In order to transfer the above detailed information to a macroscopic pore density, the given anode surface is divided into 100 cells, each with area 5 by 5 mm^2, as shown in figure 14.7b. The division into 100 cells is used in order to obtain a dataset of sufficiently large size and corresponds roughly to the finest resolution used in practical calculations.

The (total) pore density (i.e. white area divided by total area) in each of the cells depicted in figure 14.7, results in the distribution shown in figure 14.8.

As seen from figure 14.8, the distribution of the porosity is clearly biased towards the low porosity regions. For the given sample (and resolution), all cells are found to have a porosity between 2 and 25%. In order to simulate the observed properties, the pore distribution is for simplicity modelled as a linear distribution on the form

$$\rho_{pore} = (1 - \sqrt{1 - \vartheta})(\rho_{p,max} - \rho_{p,min}) + \rho_{p,min}, \tag{14.10}$$

where ϑ is a uniformly distributed random number between 0 and 1, and $\rho_{p,min}$ and $\rho_{p,max}$ respectively represent the lower and upper bands of the distribution. Figure 14.8 shows the resulting pore density distribution using equation 14.10 with $\rho_{p,min} = 2\%$ and $\rho_{p,max} = 24\%$.

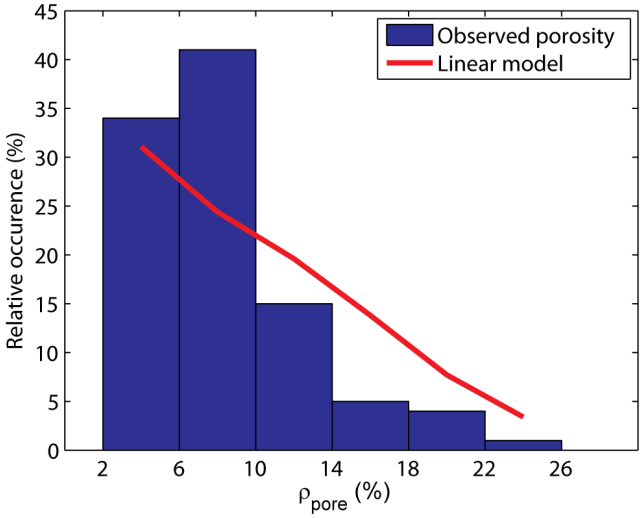

Figure 14.8: Distribution of porosity from anode sample (histogram) and reconstructed linear distribution (solid red line).

Given the pore distribution, the number of active pores in one unit area, A, is given as

$$N_{pore} = \gamma_a \rho_{pore} \frac{A}{A_{p0}}, \tag{14.11}$$

where A_{p0} is the area of one single pore (assumed to be given by the mean pore diameter) and γ_a is an activation parameter, defined by equation 14.91.

14.3 Mass transfer to bubbles

Mass transfer can essentially occur by means of two modes: diffusion and advection. The term advection is here used broadly to describe all flow related modes of mass transfer, i.e. mass transfer which is not based on pure diffusion. Mass transfer is formally analogous to heat transfer, where heat conduction and convection correspond to the two modes treated here. In practical applications, both modes may occur simultaneously.

14.3.1 General treatment of mass transfer

In the following the essential features of mass transfer are described, based on a corresponding discussion related to heat transfer found in chapter 7 of Johansen et al. [56].

Mass transfer by diffusion

The phenomenological law for diffusive mass transfer, Fick's law, gives the mass flux for a species i as

$$\dot{\boldsymbol{\mathcal{M}}}_i = -\mathcal{D}_i \nabla C_i, \tag{14.12}$$

where $\mathcal{D}_i$ is the diffusivity of the species in question. For non-stationary cases, the concentration of species is governed by Fick's 2nd law,

$$\frac{\partial C_i}{\partial t} = \nabla \cdot (\mathcal{D}_i \nabla C_i) \tag{14.13}$$

Mass transfer by advection

For mass transfer by advection, the transfer rate is proportional to the concentration difference between the surface and the bulk of the surrounding fluid. The constant of proportionality is the mass transfer coefficient, k_i', defined by

$$\dot{\mathcal{M}}_i = k_i'(C_{i,b} - C_{i,s}). \tag{14.14}$$

The physical justification for applying the mass transfer concept is that the fluid is well mixed with a uniform bulk concentration, except for within a concentration boundary layer with thickness δ surrounding the particle where diffusion occurs, that is

$$\dot{\mathcal{M}}_i = -\mathcal{D}_i \left(\frac{\partial C_i}{\partial n} \right) \approx \frac{\mathcal{D}_i}{\delta} \left(C_{i,b} - C_{i,s} \right). \tag{14.15}$$

Since the boundary layer thickness in the general case is unknown, it is common practice to use equation 14.14 instead of 14.15. Unlike the diffusivity, the mass transfer coefficient

is merely given by the definition and depends upon flow conditions such as average fluid velocity and in particular whether the flow is turbulent or laminar. As for convective heat transfer, the complexity of most situations precludes an exact analysis and semi-empirical correlations must be used in engineering applications. In practice, the correlations are given by the Sherwood number (Sh), which acts as a dimensionless mass transfer coefficient, corresponding to the Nusselt number in heat-transfer problems.

Quasi-steady mass transfer to a particle

Consider an instantaneously rigid particle with diameter D_p at rest in a quiescent fluid which is supersaturated with concentration $C_{i,b}$ outside the concentration boundary layer. The particle surface is in equilibrium, having concentration equal to the saturation concentration, $C_{i,s}$, as sketched in figure 14.9. Assuming quasi-steady state, that is considering

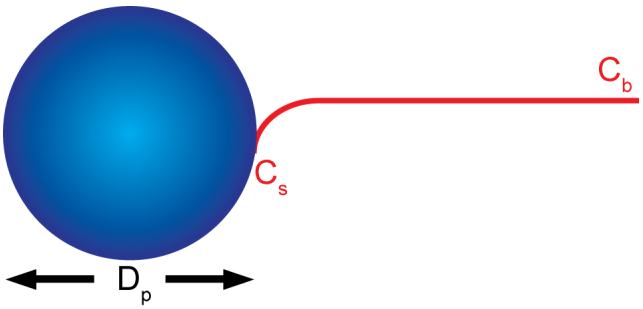

Figure 14.9: Concentration distribution outside particle at rest.

only the instantaneous conditions, the transient term in Fick's second law is dropped, resulting in

$$\frac{1}{r^2}\frac{\partial}{\partial r}\left(r^2\mathcal{D}\frac{\partial C_i}{\partial r}\right) = 0, \tag{14.16}$$

in spherical coordinates. With the boundary conditions

$$\begin{aligned} C_i &= C_{i,s}, \quad r = \frac{D_p}{2} \\ C_i &\to C_{i,b}, \quad r \to \infty, \end{aligned} \tag{14.17}$$

the resulting concentration field is given as

$$C_i = \frac{D_p}{2r}\left(C_{i,s} - C_{i,b}\right) + C_{i,b}. \tag{14.18}$$

From the above concentration distribution, the mass flux at the particle surface is obtained from Fick's law

$$-\mathcal{D}\left.\frac{\partial C_i}{\partial r}\right|_{r=\frac{D_p}{2}} = \frac{2\mathcal{D}}{D_p}\left(C_{i,s} - C_{i,b}\right), \tag{14.19}$$

which describes the mass transfer from the particle to the fluid. In most cases, the flux in the opposite direction is of primary interest and the mass flux to the particle is thus defined as

$$\dot{\mathcal{M}} = \frac{2\mathcal{D}}{D_p}\left(C_{i,b} - C_{i,s}\right). \tag{14.20}$$

Comparing to equation 14.14, it is evident that a mass transfer coefficient

$$k' = \frac{2\mathcal{D}}{D_p}, \tag{14.21}$$

can be defined also in the case of pure diffusion. Introducing the Sherwood number, defined as

$$Sh = \frac{k' D_p}{\mathcal{D}}, \tag{14.22}$$

the final form of equation 14.20 is

$$\dot{\mathcal{M}} = \frac{\mathcal{D}}{D_p} Sh \left(C_b - C_s\right), \tag{14.23}$$

where $Sh = 2$ for the case of diffusive mass transfer in a quiescent fluid. Equation 14.23 is the general result for combined modes of mass transfer as the Sherwood number can incorporate advective effects through dependence on the Reynolds number. Typically, as seen in chapter 12 of Kolev [69], the Sherwood number is given as a relation of the form

$$Sh = a + bRe^c Sc^d, \tag{14.24}$$

where Sc is the Schmidt number, defined as

$$Sc = \frac{\mu_i}{\rho_i \mathcal{D}_i}, \tag{14.25}$$

which typically is of the order of 10^3 to 10^7 in a Hall-Héroult cell depending on the value of the diffusivity of CO_2 in the bath. The various models presented in the literature provide significantly different values for the exponent of the Schmidt number, ranging from 0.3 to 1, resulting in large variations in the corresponding Sherwood number. Vogt [127], [128] indicates that $d = 1/2$ (i.e. Boussinesq) overpredicts mass transfer, while $d = 1/3$ (i.e. Ranz-Marshall) adequately represents mass transfer to adhering bubbles, typically encountered in the current application.

In addition to the uncertainties related to the diffusivity and large variations in semi-empirical models, the presence of other phenomena influencing the advection and concentration boundary layer complicates the matter further. For instance, the Marangoni effect, MHD-induced flow and thermo-, turbo- and electrophoresis are all examples of phenomena which could have significant effect on mass transfer, but which are not considered directly in conventional models.

14.3.2 Bubble growth

The classical description of spherically symmetric bubble growth in a supersaturated solution is due to Scriven [106], describing the bubble radius as

$$D_{bub}(t) = 4\beta\sqrt{\mathcal{D}t}, \tag{14.26}$$

where the growth factor β is defined implicitly by

$$\frac{\rho_b\left(C_{i,b} - C_{i,s}\right)}{\rho_g\left(\rho_b - C_{i,s}\right)} = \phi\left(\beta, \epsilon\right) \equiv 2\beta^3 \exp\left(\beta^2 + 2\epsilon\beta^2\right) \int_\beta^\infty x^{-2} \exp\left(-x^2 - 2\epsilon\beta^3 x^{-1}\right) dx, \tag{14.27}$$

where $\epsilon = 1 - \rho_g/\rho_l$. Equation 14.26 is valid for bubble growth in an infinite medium where the bulk concentration C_b is constant and incorporates the enhanced mass transfer due to the moving bubble interface.

A corresponding growth law can be obtained by considering an isobaric expansion of an ideal gas, as shown by Jones et al. [58]. Considering a bubble with surface area $A_{bub} = f_1 D_{bub}^2$, the rate of mass transfer is given by

$$\dot{m} = f_1 D_{bub}^2 k'\left(C_{i,b} - C_{i,s}\right) = f_1 D_{bub} Sh\mathcal{D}\left(C_{i,b} - C_{i,s}\right) = f_1 D_{bub} Sh\mathcal{D}\Delta C_i. \tag{14.28}$$

From the isobaric expansion of a bubble with volume $V_{bub} = f_2 D_{bub}^3$, the rate of mass transfer can also be written as

$$\dot{m} = \rho_g \frac{dV_{bub}}{dt} = 3\rho_g f_2 D_{bub}^2 \frac{dD_{bub}}{dt}. \tag{14.29}$$

Combining equations 14.28 and 14.29, the bubble diameter is described by

$$D_{bub}(t) = \sqrt{K\Delta C_i t} + D_{bub,0}, \tag{14.30}$$

where

$$K = \frac{2}{3}\frac{Sh\mathcal{D}}{\rho_g}\frac{f_1}{f_2}, \tag{14.31}$$

which corresponds to the results of Scriven [106] if the Sherwood number is defined as

$$Sh_S = 2.0 + \sqrt{2.0 ReSc}, \tag{14.32}$$

where the velocity in the Reynolds number is dD_{bub}/dt, that is, the only source for advection is due to the expanding bubble.

Relation to non-classical nucleation

As indicated in section 14.2.1, non-classical nucleation is essentially equivalent to bubble growth in a supersaturated solution. This analogy is used by Jones et al. [58] to predict the nucleation time for a bubble of a given diameter. Considering a bubble growing from initial diameter $D_{bub,0} = 0$, the time required to reach a detachment diameter $D_{bub,d}$ is given by equation 14.30 as

$$t_d = \frac{D_{bub,d}^2}{K\Delta C_i}. \tag{14.33}$$

Qualitatively equation 14.33 contains the required effects, that is; large bubbles require longer times to form than smaller ones and enhanced mass transfer or increased supersaturation reduces the overall time required. As noted by Jones et al. [58], the bulk concentration C_b and the Sherwood number can change significantly over time. However, for the brief period of time required to produce one single bubble, Jones et al. [58] consider the values as being constant. The same assumption is made in the current model due to a significant numerical advantage; the update of relevant properties is needed only at the beginning of each time-step.

The typical detachment diameter depends upon the forces acting on the growing bubble. Jones et al. [57] perform an analysis for a bubble growing from a crevice on an otherwise flat surface whose normal vector is antiparallel to gravity. From this assumption, the detachment condition is obtained from a balance of the two most dominating forces; buoyancy and contact forces.

For anodic bubbles in a Hall-Héroult cell, the picture is somewhat more complicated. Considering a flat anode, gravity is parallel to the anode normal vector resulting in bubbles being forced towards the anode. In reality, the anode is inclined due to uneven consumption and local irregularities, promoting bubble detachment. These are however transient phenomena from which general properties are challenging to extract. The same is the case for momentum exchange with the surrounding bath flow (i.e. drag forces), which is highly dependent upon local, a-priori unknown parameters.

Considering experimental observations, the term bubble detachment appears to be used both for nucleation events and for macroscopic bubbles departing from the anode. The latter case appears to be well documented (cf. for instance Wang and Tabereaux [133]) due to its relation to global voltage fluctuations. The former is described, to the author's best knowledge, only briefly by Xue and Øye [139] as detached (but not departing) microbubbles moving randomly in the immediate neighbourhood of the anode, with typical size 0.4-0.6 mm. The presence of detached bubbles are accredited to the combination of buoyancy, reaction forces, surface tension, bath flow and turbulence. No attempt is however made to quantify the relative importance of each of the suggested phenomena.

Jones et al. [58] argue that the *nucleation time*, t_n, is proportional to the detachment time,

described by equation 14.33. That is;

$$t_n = \frac{\mathcal{N} D_{bub,d}^2}{K\left(C_b - C_s\right)}, \tag{14.34}$$

where $\mathcal{N}$ is a unknown factor of proportionality. The factor $\mathcal{N}$ is included to account for the fact that a region partially depleted of dissolved gas exists in the surroundings of the cavity after bubble detachment. For the system studied by Jones et al. [58], the factor is approximated to

$$\mathcal{N} \approx \frac{10h}{D_{bub,d}}, \tag{14.35}$$

where h is the distance from the solid surface to the position of the bubble in the crevice. The derivation of equation 14.35 depends upon knowing the typical boundary layer thickness as well as the partial gas pressure in the cavity; information which is not easily obtainable for anode cavities. Assuming that the approximation of Jones et al. [58] is valid and that h is of the same magnitude as the pore diameter, $\mathcal{N}$ is of order unity.

The inclusion of the factor $\mathcal{N}$ is crucial in the analysis of Jones et al. [58], as the bulk concentration C_b is assumed to be constant. In the current model, however, the bulk concentration is governed by equation 14.3 meaning that the effect of gas depletion is treated implicitly, updating the (local) bulk concentration field at each time step. Thus, $\mathcal{N}$ is taken to be unity and the nucleation time for a single bubble is identical to its detachment time, t_d.

The nucleation time combined with the number of active pores (equation 14.11) yields the nucleation frequency

$$f_{nuc} = \frac{N_p}{t_n} = \frac{N_p K \Delta C_i}{D_{bub,d}^2}. \tag{14.36}$$

Challenges related to resolved bubbles

The preceding phenomenological description of bubble growth is a global treatment (as seen from the bubble), as the mass transfer relies entirely on the assumption that the macroscopic properties of the bubble (i.e. its diameter) and representative averages of surrounding fields are known. Consequently, this description is primarily used for dispersed type flows with a known size distribution or single bubbles with special symmetry properties.

In the general case of a large, non-spherical bubble, a detailed *local* description of mass transfer is required. From a numerical perspective, a local description requires that the scales involved (that is the bubble and its surrounding boundary layer) are sufficiently *resolved*.

Assuming that no nucleation sites are present and that production is negligible, initially supersaturated gas can be freed only at the interface of an already existing bubble. In this case, the transport equation for dissolved gas reads

$$\frac{\partial C_{CO_2}}{\partial t} + \nabla \cdot (\boldsymbol{u} C_{CO_2} - \mathcal{D}_{eff} \nabla C_{CO_2}) = -S^{dmt}_{CO_2}. \tag{14.37}$$

The source term on the right hand side is recovered in the continuity equation for the (continuous) gas phase

$$\frac{\partial \alpha_g \rho_g}{\partial t} + \nabla \cdot (\alpha_g \rho_g \boldsymbol{u}_g) = S^{dmt}_{CO_2}, \tag{14.38}$$

ensuring mass conservation of CO_2. The challenge is thus to transfer the phenomenological global laws described in the previous section to local (volumetric) mass-sources. Consider a resolved bubble in a supersaturated solution as sketched in figure 14.10.

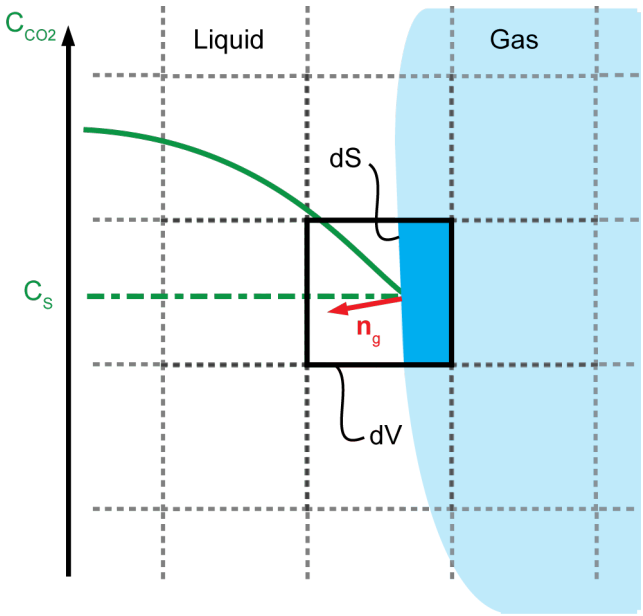

Figure 14.10: Resolved bubble (blue) in supersaturated solution (sketched by green line). Given a small volume dV, the gas surface enclosed within the volume, dS, has a normal vector $\boldsymbol{n}_g$.

Assuming that concentration boundary layer is stagnant, i.e. mass transfer is diffusion based[2], Fick's law describes the mass flux (in kg/m^{2}s) as

$$\dot{\mathcal{M}} = -\mathcal{D}_{eff} \left(\boldsymbol{n} \cdot \nabla C_{CO_2} \right), \tag{14.39}$$

[2]This is easily extended to a general mass flux by extending equation 14.39 so that sought phenomena are included.

where $\boldsymbol{n}$ is the (unit) normal of the surface element, dS, on which the transition occurs. Using equation 14.39, the (volumetric) source term in equation 14.38 can be written as

$$S_{CO_2}^{dmt} = \frac{\dot{\mathcal{M}} dS}{d\mathcal{V}}, \tag{14.40}$$

where $d\mathcal{V}$ is the volume element in which the transition occurs. From the Slattery-Whitaker theorem, the unit normal vector of the surface is given as

$$\boldsymbol{n}_g = -\frac{\nabla \alpha_g}{|\nabla \alpha_g|}. \tag{14.41}$$

Furthermore, the gradient in phase fraction is related to the surface by

$$|\nabla \alpha_g| d\mathcal{V} = dS. \tag{14.42}$$

By substitution, the volumetric source term is finally written as

$$S_{CO_2}^{dmt} = \mathcal{D}_{eff} \left(\nabla \alpha_g \cdot \nabla C_{CO_2} \right), \tag{14.43}$$

which is nonzero only in regions that contain an interface.

A source term of the form of equation 14.43 provides a formidable numerical challenge. First and foremost, the challenge is related to accurately predicting the relevant gradients in the immediate neighbourhood of the interface. As the shape and extent of a macroscopic bubble is time dependent and highly variable, a (non-adaptive) mesh capable of resolving all involved scales would have to be exceedingly fine.

An additional challenge is related to the nature of equation 14.43, resulting in a source term distribution localized in a narrow region at the interface. As shown by Hardt and Wondra [49], this can lead to instabilities.

Returning to the detailed description of Xue and Øye, it is evident that the relative importance of bubble growth by means of mass transfer declines as bubbles grow in size, resulting in a coalescence dominated regime. That a regime transition occurs is based upon the observation that the average voltage rate decreases past some point prior to macroscopic bubble departure, as shown in figure 14.11.

Due to the apparent presence of two different regimes as well as the challenges related to growing macroscopic bubbles, mass transfer is treated only for sub-grid spherical particles (described in the following chapter), while macroscopic bubbles are allowed to grow only by interaction with sub-grid entities. The advantage of such a division is that the essentials of the governing phenomena are included, but only on the scale at which they are relevant.

14.4 Sub-grid treatment of bubbles

All scales related to bubble dynamics cannot be resolved in a practical calculation, as this will involve at least 7 orders of magnitude; ranging from microscopic bubble nuclei to large

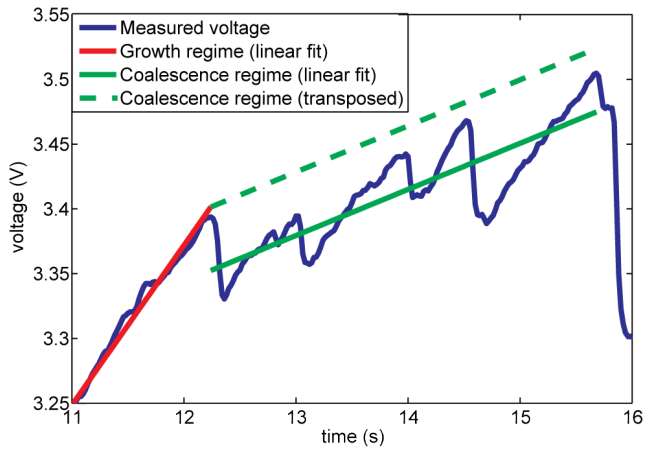

Figure 14.11: Measured voltage signal (blue) and linear fit to the growth regime (red) and coalescence regime (green). Data from lab scale experiments described by Eick et al. [29].

scale bubbles covering the whole anode surface. Hence, a model is needed to treat sub-grid phenomena as well as a transfer mechanism to resolved scales. Two approaches appear as viable candidates, the first being a discrete particle model (DPM), the second a population balance model (PBM). To the author's best knowledge, neither of the two models have previously been adopted in a coupled multiscale manner, as simulations traditionally have focused on either a pure particle type of approach (cf. Solheim et al. [111]) or a pure interface tracking approach (cf. Einarsrud [30]).

Both the DPM and PBM are implemented in ANSYS FLUENT. Unfortunately, neither of the two implementations are adequate for the current application, primarily due to excessive computational time and incompatibility to the VOF-method. Due to this, a tailored sub-grid model based on the PBM is developed, described in the following sections.

14.4.1 Basics of the PBM

A population balance model is, as the name suggests, a model which deals with the interaction of entities forming a population. For instance, the population can represent a dispersed bubbly flow, in which case the entities represent distinct bubble classes, for instance based on volume or diameter. Assuming that N_i bubbles of class i are present in a volume $\mathcal{V}$, the conservation of the i-th bubble number density reads

$$\frac{1}{\mathcal{V}}\frac{dN_i}{dt} = \frac{dn_i}{dt} = b_i - d_i, \tag{14.44}$$

where b_i and d_i respectively represent birth- and death rates for the i-th bubble class. The birth and death of bubbles are coupled in the sense that an event in one class has

consequences for another. For instance, a collision between two bubbles of classes i and j can result in the birth of a bubble in class k, while bubbles in classes i and j are removed. Determining the birth- and death rates and how these influence the population as a total is the core of any PBM.

An additional factor defining the PBM is the discretization chosen for the entities of the population, that is, how classes are defined and related. In order to span a large number of bubble sizes without solving an exceeding amount of equations, an exponential discretization of volume is chosen. The choice of volume as internal coordinate rather than diameter is made as it is easily related to the large scale bubbles through a volume fraction.

In the exponential discretization, neighbouring classes are related by a constant factor,

$$V_{i+1} = qV_i, \tag{14.45}$$

where $q > 1$, as shown in figure 14.12.

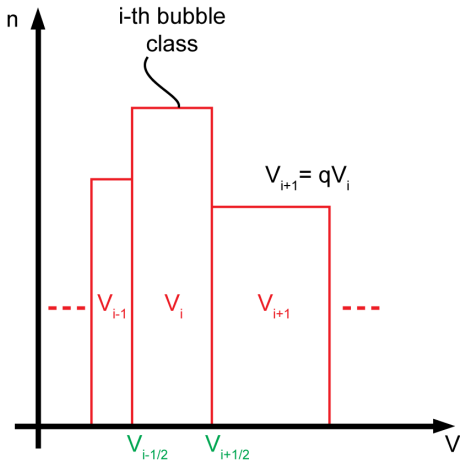

Figure 14.12: Sketch of discrete PBM distribution.

As seen from figure 14.12, the i-th bubble class represents all bubbles with volume $V_{i-\frac{1}{2}} \leq V < V_{i+\frac{1}{2}}$. Within the i-th class, all bubbles are however considered to have volume V_i, that is, the bubbles can only take on discrete volumes, given as the arithmetic mean of the bounding values of the class in question. A large value of q allows for a large range of classes at the expense of accuracy, as unresolved bubble classes and their interactions are lost. Considering a population of M bubbles in the range V_0 to $64V_0$, the population can be described by 7, 4 or 3 classes if q=2, 4 or 8, respectively, as shown in figure 14.13.

Evidently, the coarse discretization results in fewer classes and hence fewer possible interactions[3].

[3]As shown by Outsuki et al. [89], this results in an accelerated growth of the population towards larger classes, as accumulation in intermediate classes is absent, as discussed in appendix B

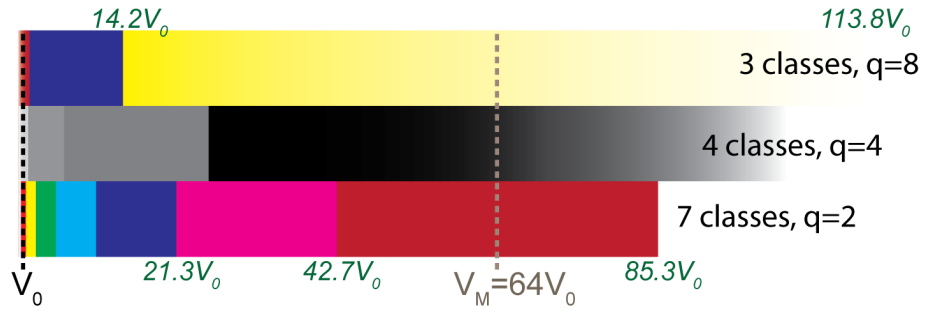

Figure 14.13: Bubble classes for three different discretizations, q=2, 4 and 8. All discretizations have the same mean minimal and maximal volume (V_0 and $V_M = 64V_0$), but the range of each class (indicated in green) varies significantly.

14.4.2 Bubble birth and death due to coalescence

The net evolution of the bubbly flow in a Hall-Héroult cell can in essence be described as a one way process; lesser bubbles coalescing and growing to form larger ones. Hence, a simplification can be made for the population balance, assuming that effects due bubble breakup (on the subgrid level) is negligible. Following Hounslow et al. [51], the birth and death rates are, considering only binary interactions, under this assumption given as

$$b_i \equiv b(V_i) = \frac{1}{2}\int_0^{V_i} \Gamma(V_i - \Omega, \Omega) n(V_i - \Omega) n(\Omega) d\Omega \tag{14.46}$$

$$d_i \equiv d(V_i) = n(V_i) \int_0^{\infty} \Gamma(V_i, \Omega) n(\Omega) d\Omega, \tag{14.47}$$

where $\Gamma(V_i, \Omega)$, the coalescence kernel, is a measure of the frequency of collisions between bubbles of volume V_i and Ω which successfully results in a bubble of volume $V_i + \Omega$. In discrete form for a finite number M of bubble classes ($i = M$ signifying the largest class) equation 14.44 takes the form

$$\frac{dn_i}{dt} = \frac{1}{2}\sum_j^M \sum_k^M \Gamma_{kj} n_k n_j \xi'_{ijk} - n_i(1 - \delta_{iM}) \sum_j \Gamma_{ij} n_j, \tag{14.48}$$

where Γ_{ij} is the discrete coalescence kernel and ξ'_{ijk}, defined as

$$\xi'_{ijk} = \begin{cases} 1 & \text{if} \quad V_{i-\frac{1}{2}} \leq V_k + V_j < V_{i+\frac{1}{2}} \\ 0 & \text{otherwise,} \end{cases} \tag{14.49}$$

assures that colliding bubbles result in the creation of a new bubble in the correct class. The factor 1/2 in the birth term is included to counter the effect of counting each collision twice, while $1 - \delta_{iM}$, δ_{iM} being the Kronecker delta function, ensures conservation of the largest bubble class.

The interaction between two arbitrary bubbles j and k does not necessarily result in a bubble volume which is present in the discrete distribution, as shown in figure 14.14. As a consequence, equation 14.48 does not ensure mass conservation.

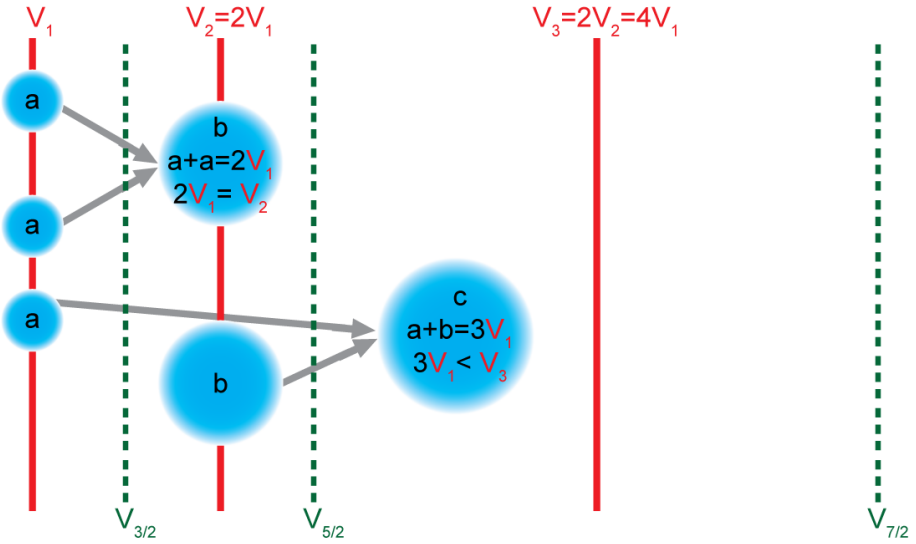

Figure 14.14: Bubble-bubble collision with discretization $V_{i+1} = 2V_i$. A collision between two bubbles a with volume V_1 results in an existing bubble class, but an interaction between bubbles a and b with volumes V_1 and V_2 does not. Transferring the volume of the resulting bubble c to class V_3 does not conserve mass.

Mass conservation is obtained by appropriate weighting of the birth term. As shown by Suttner and Yorke [113], the appropriate weighting is obtained by substituting ξ'_{ijk} with

$$\xi_{ijk} = \begin{cases} \frac{V_k+V_j}{V_i} & \text{if} \quad V_{i-\frac{1}{2}} \leq V_k + V_j < V_{i+\frac{1}{2}} \\ 0 & \text{otherwise.} \end{cases} \tag{14.50}$$

Considering the example sketched in figure 14.14, the corrected weighting coefficient for collisions between particles a and b is $\xi_{312} = 3/4$. As a more extensive example, consider a population of four bubble classes with $q = 2$. The population balance reads:

$$\begin{aligned}
\frac{dn_1}{dt} &= -\Gamma_{11}n_1^2 - \Gamma_{12}n_1n_2 - \Gamma_{13}n_1n_3 - \Gamma_{14}n_1n_4 \\
\frac{dn_2}{dt} &= \frac{1}{2}\Gamma_{11}n_1^2 - \Gamma_{12}n_1n_2 - \Gamma_{22}n_2^2 - \Gamma_{23}n_2n_3 - \Gamma_{24}n_2n_4 \\
\frac{dn_3}{dt} &= \frac{3}{4}\Gamma_{12}n_1n_2 + \frac{1}{2}\Gamma_{22}n_2^2 + \frac{1}{4}\Gamma_{13}n_1n_3 - \Gamma_{23}n_2n_3 - \Gamma_{33}n_3^2 - \Gamma_{34}n_3n_4 \\
\frac{dn_4}{dt} &= \frac{1}{2}\Gamma_{33}n_3n_3 + \frac{3}{4}\Gamma_{23}n_2n_3 + \frac{1}{8}\Gamma_{14}n_1n_4 + \frac{1}{4}\Gamma_{24}n_2n_4 + \frac{1}{2}\Gamma_{34}n_3n_4
\end{aligned}$$

The resulting population, initialized with $\boldsymbol{n} = [0.5, 0, 0, 0]$ and kernel $\Gamma_{ij} = 0.5(1 + \delta_{ij})$, is shown in figure 14.15, as obtained by the ODE45 solver in MATLAB.

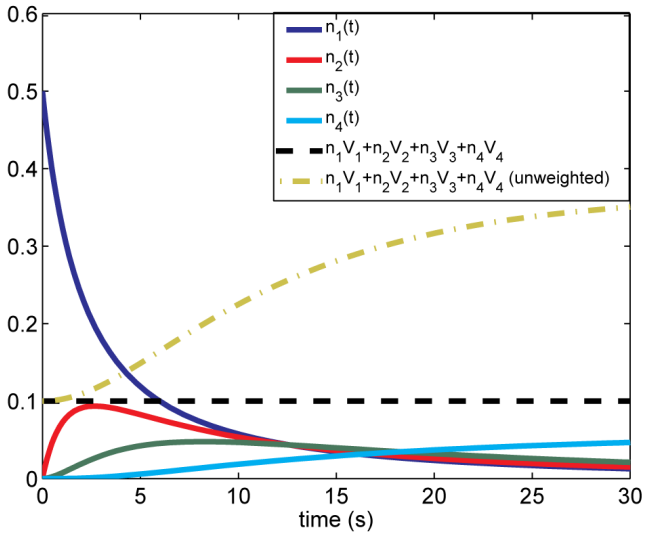

Figure 14.15: Evolution of number densities for four bubble classes (solid lines) and total volume fraction (black dashed line) using equation 14.50. The green dash-dot line shows the predicted volume fraction using equation 14.49.

Clearly, as seen from figure 14.15 the total volume fraction is conserved throughout the calculation, showing that the overall mass is conserved, opposed to the unweighted expression (using equation 14.49).

Coalescence kernel

According to Luo [79], bubble coalescence can be considered as a three step process. First, bubbles collide, trapping a small amount of liquid between them. The trapped liquid drains until the liquid film separating the bubbles reaches a critical thickness at which it ruptures, allowing for coalescence. Hence, the coalescence kernel will depend upon the frequency of collisions and the probability for collision resulting in coalescence, i.e.

$$\Gamma_{ij} = \Omega_{ij} P_{ij}^{C}, \tag{14.51}$$

where Ω and P^C are the collision frequencies and coalescence probabilities, respectively. Following Chesters [16], the collision frequency can be expressed as

$$\Omega_{ij} = k v_{ij} b_{ij}^2, \tag{14.52}$$

where v_{ij} is a characteristic, relative velocity between two points a distance b_{ij} apart.

As an example, consider two spherical particles with diameter D_i and D_j and relative velocity v_{rel} as sketched in figure 14.16. For this situation, all incoming particles contained

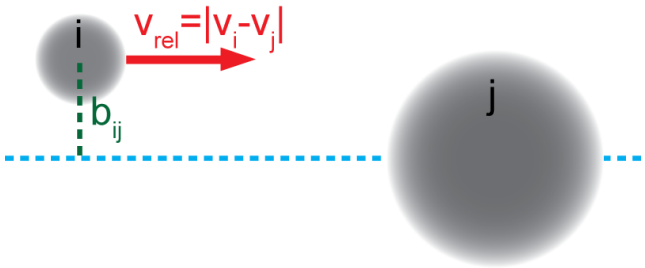

Figure 14.16: Path of collision between two particles.

in the collisional cross section $A_c = \pi b_{ij}^2$ will collide with particle j. Hence, the collision frequency is in this case given as the relative flux of incoming particles, i.e.

$$\Omega_{ij} = \pi v_{rel} b_{ij}^2, \tag{14.53}$$

from which the interpretation of the terms in equation 14.52 is evident.

The value of k as well as the interpretation of the typical velocity depends upon the features which are believed to be characteristic for the flow in question. A common assumption made is that the coalescence process is driven by turbulence in the carrier fluid. In essence, the literature differentiates between two cases; microscopic bubbles interacting with fine scale turbulence and micro- to moderate sized bubbles interacting with inertial subrange turbulence.

The first case, introduced by Saffman and Turner [103], assumes a particle velocity given by

$$v_i = D_i \sqrt{\frac{\epsilon_t}{\nu_f}} \tag{14.54}$$

where ϵ_t is the turbulent dissipation rate and ν_f is the kinematic viscosity of the carrier fluid. Assuming that the characteristic velocity between particles i and j is given by the RMS velocity, i.e.

$$v_{rel} = \sqrt{v_i^2 + v_j^2} = \sqrt{\frac{\epsilon_t}{\nu_f}}\sqrt{D_i^2 + D_j^2}, \tag{14.55}$$

the collision frequency is given as (cf. Chesters [16])

$$\Omega_{ij}^{FST} = \sqrt{\frac{\pi}{15}\frac{\epsilon_t}{\nu_f}} b_{ij}^2 \sqrt{D_i^2 + D_j^2}. \tag{14.56}$$

The case dealing with inertial subrange turbulence, introduced by Kuboi et al. [70] and later extended by Prince and Blanch [99] and Luo [79], assumes a particle velocity on the form

$$v_i = 1.43\left(\epsilon_t D_i\right)^{\frac{1}{3}}. \tag{14.57}$$

Again assuming that the RMS velocity is representative, the collision frequency for inertial subrange turbulence is

$$\Omega_{ij}^{IST} = 1.43\frac{\pi}{4}\epsilon_t^{\frac{1}{3}} b_{ij}^2 \sqrt{D_i^{\frac{2}{3}} + D_j^{\frac{2}{3}}}. \tag{14.58}$$

Although turbulence without doubt has a significant influence upon bubble collisions, large scale effects such as MHD and buoyancy could also contribute. Considering buoyancy and assuming Stokes-flow for the bubbles, the terminal velocity of a bubble with diameter D_i is

$$v_i = \frac{1}{18}\frac{\rho_g g D_i^2}{\mu_f}\left(\frac{\rho_f}{\rho_g} - 1\right). \tag{14.59}$$

Hence, the relative velocity between bubbles i and j is

$$\begin{aligned} v_{rel} &= \frac{1}{18}\frac{\rho_g g D_i^2}{\mu_f}\left(\frac{\rho_f}{\rho_g} - 1\right)\left|D_i^2 - D_j^2\right| \\ &\approx \frac{1}{18}\frac{g}{\nu_f}\left|D_i^2 - D_j^2\right|, \end{aligned} \tag{14.60}$$

with resulting collision frequency

$$\Omega_{ij}^{B} = \frac{\pi}{18}\frac{g}{\nu_f} b_{ij}^2 \left|D_i^2 - D_j^2\right|. \tag{14.61}$$

The distance b_{ij} is chosen to be the mean diameter

$$b_{ij} = \frac{D_i + D_j}{2}, \tag{14.62}$$

as shown in figure 14.16. This serves as a maximal estimate of the collisional cross section as particle trajectories in reality can deviate significantly from the streamlines of the basic fluid flow. However, as a first approximation, the above formulation is retained.

Table 14.1: Maximal and minimal collision frequencies obtained from different models. ϵ_t is assumed to be unity where applicable and viscosity is set to 1.3 mm^2/s.

Model	Minimum (m^3/s)	Min. interaction	Maximum (m^3/s)	Max. interaction
Ω_{ij}^{FST}	$7.1{\cdot}10^{-8}$	(D_{min}, D_{min})	$7.1{\cdot}10^{-5}$	(D_{max}, D_{max})
Ω_{ij}^{IST}	$6.5{\cdot}10^{-8}$	(D_{min}, D_{min})	$1.3{\cdot}10^{-5}$	(D_{max}, D_{max})
Ω_{ij}^{B}	0.0	(D_i, D_i)	$2.5{\cdot}10^{-4}$	$(0.5D_{max}, D_{max})$

For a bubble population in the range of 0.5-5 mm, the maximal and minimal collision frequencies for each of the above models are given in table 14.1.

As seen from table 14.1, all three models predict collision frequencies with approximately the same order of magnitude. The path taken is however different for the buoyancy driven model as bubbles of equal size cannot collide. From a practical point of view, this means that an initially monodispersed population will remain in its initial state, which is clearly unphysical. In a realistic setting, the actual collision frequency is likely to be a combination of the above models.

The coalescence probability

According to Chesters [16], coalescence will follow a collision event if the interaction time, t_I, of two bubbles exceeds the coalescence time, t_C, required for the liquid film between them to drain and rupture. The function describing the coalescence probability is unity for small ratios of these two times and goes to zero in the opposite case. A simple model with these features is suggested by Chesters [16], reading

$$P^C = \exp\left(-\frac{t_C}{t_I}\right). \tag{14.63}$$

Using an analogy to parallel films, Luo [79] suggests a coalescence probability on the form

$$P_{ij}^C = \exp\left\{-c_1 \frac{\sqrt{0.75\left(1+\left(\frac{D_i}{D_j}\right)^2\right)\left(1+\left(\frac{D_i}{D_j}\right)^3\right)}}{\left(1+\frac{D_i}{D_j}\right)^3\sqrt{\frac{\rho_g}{\rho_f}+\vartheta}}\sqrt{We_{ij}}\right\}, \tag{14.64}$$

where c_1 is a positive constant of order unity and ϑ is a virtual mass coefficient, for inertial subrange turbulence. The Weber number, We_{ij}, is defined as

$$We_{ij} = \frac{\rho_f D_i v_{rel}^2}{\gamma}, \tag{14.65}$$

where γ is the gas-fluid surface tension and v_{rel} is the relative velocity introduced earlier.

Using the suggested coalescence probability and collision frequencies of table 14.1, the maximal and minimal coalescence kernels are

$$\begin{aligned} \Gamma_{max}^{IST} &= 4.60 \cdot 10^{-6} \mathrm{m}^3/\mathrm{s} \\ \Gamma_{min}^{IST} &= 2.75 \cdot 10^{-10} \mathrm{m}^3/\mathrm{s}, \end{aligned}$$

for a bubble population with diameters in the range of 0.5-5 mm, coalescing due to inertial subrange turbulence, with corresponding reductions for the other collision modes. Hence, in all cases, the coalescence kernel is expected to be lower than the ideal collision frequency.

14.4.3 Bubble birth and death due to mass transfer

The above discussion relies upon the assumption that sufficient amounts of bubbles are present so that collisions and coalescence can occur. Early in the bubble-cycle, this is however unlikely as individual bubbles nucleate at specific sites which in principle can be separated by distances far greater than typical bubble radii. As described by Xue and Øye [139], single bubbles grow individually until reaching a size at which collisions and coalescence occur.

The initial growth of bubbles following nucleation can only be explained by mass transfer from a reservoir, either the anode or the bath. Following the discretization of Hounslow et al. [51],

$$\frac{\partial n_i}{\partial V_i} \approx \frac{n_i}{V_{i+1} - V_i}, \tag{14.66}$$

a growing population can be described as

$$\frac{dn_i}{dt} = \frac{G_V^{i-1} n_{i-1}}{V_i - V_{i-1}} - \frac{G_V^i n_i}{V_{i+1} - V_i}, \tag{14.67}$$

where the first term represents growth into- and the second term represents growth out of the i-th bubble class and G_V^i is the corresponding growth rate. Assuming an isobaric expansion of an ideal gas, the growth rate can be expressed as

$$G_V^i = \frac{dV_i}{dt} = \frac{\dot{m}_i}{\rho_g} = K_2 \Delta C_{CO_2} V_i^{\frac{1}{3}}, \tag{14.68}$$

where the rate of mass transfer is given by equation 14.28 and the prefactor K_2 is defined as

$$K_2 = \frac{f_1}{f_2^{\frac{1}{3}}} Sh \frac{\mathcal{D}}{\rho_g} = \frac{3}{2} f_2^{\frac{2}{3}} K, \tag{14.69}$$

for a bubble with area $f_1 D_{bub}^2$ and volume $f_2 D_{bub}^3$. Hence a discrete population undergoing growth is described by

$$\frac{dn_i}{dt} = K_2 \Delta C_{CO_2} \left[n_{i-1} \left(\frac{V_{i-1}^{\frac{1}{3}}}{V_i - V_{i-1}} \right) - n_i \left(\frac{V_i^{\frac{1}{3}}}{V_{i+1} - V_i} \right) \right]. \tag{14.70}$$

14.5 Coupling to macroscopic bubbles

Macroscopic (resolved) bubbles are in the present work treated directly by means of the VOF model, to which the above models for coalescence and phase growth do not apply directly. From a PBM point of view, macroscopic bubbles can be created by two processes, namely coalescence or growth of microscopic bubbles into the resolved continious gas phase. From a coupled point of view, the continous gas phase can grow by engulfing lesser bubbles (cf. Fortin et al. [38]), a process similar to that of coalescence between discrete entities.

Hence, as the *formation* of resolved bubbles, at least in principle, does not differ from the formation of a population balance bubble, the PBM formalism described above is used to couple the two models involved.

Considering a population of M bubble classes, the transition to the continuous phase can be treated by extending the population with an additional bubble class, which represents the smallest possible concentration of the continuous phase. As the additional bubble class is not a true entity of the population it is denoted a ghost class, with subscript G. The volume of a ghost bubble is determined by the PBM as

$$V_G = qV_M = V_{M+1}. \tag{14.71}$$

The number density of ghost bubbles is not determined (directly) by a transport equation, but from the volume fraction of the continuous phase, i.e.

$$n_G = \frac{\alpha_g}{V_G}. \tag{14.72}$$

From the above two definitions, the hybrid nature of the ghost class is evident. Its rate of change is analogous to that of the PBM, and is given as

$$\dot{n}_G = K_2 \Delta C_{CO_2} n_M \left(\frac{V_M^{\frac{1}{3}}}{V_G - V_M} \right) + \frac{1}{2} \sum_j^M \sum_k^G \Gamma_{kj} n_k n_j \xi_{Gjk}, \tag{14.73}$$

where the first term is due to mass transfer and the second is due to coalescence and engulfment, including both bubble-bubble- and bubble-continous phase interactions.

The growth term in equation 14.73 is identical to the positive term in equation 14.70, i.e. pure growth from bubble class M to the ghost class G. The coalescence kernel, however, consists of two different phenomena, depending on the nature of the interaction. Considering bubble-bubble interactions, for instance the interaction between two bubbles of class M, the resulting source term is of the form

$$\dot{n}_G^{MM} = \frac{1}{2}\Gamma_{MM} n_M n_M, \tag{14.74}$$

where Γ_{MM} is given by one of the models given in section 14.4.2. The remaining source terms in equation 14.73 are due to interactions between discrete (PBM) bubbles and the continous bubble phase and are of the form

$$\dot{n}_G^{Gi} = \Gamma_{Gi} n_i n_G \xi_{GGi}, \tag{14.75}$$

where the index i is on the interval $[1, \ldots, M]$, which is analogous to the overall PBM treatment. Experiments show, however, that the coalescence kernel is not.

Considering water model experiments (cf. Fortin et al. [38] and Einarsrud [30]), the lab scale experiments of Xue and Øye [139] and numerical experiments by Kiss [60] it is clear that there is a significant difference in the behaviour of micro- and macroscopic bubbles. While small bubbles remain close to stationary in the immediate neighbourhood of the anode surface (moving randomly due to coalescence and secondary fluid flow), large bubbles sweep alongside the anode with velocities in the order of 0.3 m/s, engulfing smaller bubbles as they move, as sketched in figure 14.17.

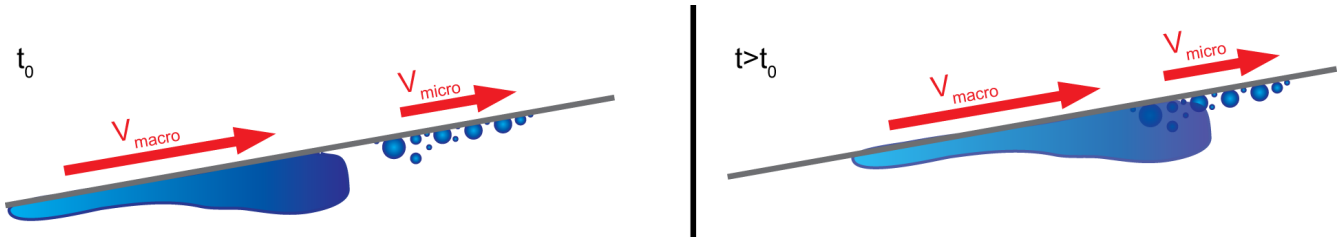

Figure 14.17: Sketch of typical behaviour for microscopic and macroscopic bubbles. The macroscopic bubble typically has a larger velocity, engulfing smaller bubbles in its path.

An additional feature increasing the relative velocities further is the presence of a (turbulent) boundary layer on the anode. Assuming that the anode can be approximated by a flat plate, the turbulent boundary layer thickness is given as (cf. White [135], pp. 466)

$$\delta \approx \frac{0.16x}{Re_x^{1/7}}, \tag{14.76}$$

where x is the distance parallel to the flow. Assuming a typical velocity of 0.3 m/s, the average boundary layer thickness on a 1 m long anode is 1.5 cm, significantly larger than

the typical microbubble diameter. Hence, it is reasonable to assume that microbubbles reside deep within the boundary layer, as illustrated in figure 14.18, and thus have a *lower* velocity than the *resolved* velocity in the proximity of the anode.

As for conventional coalescence, the coalescence kernel between PBM and ghost bubbles is assumed to be of the form

$$\Gamma_{Gj} = \pi v_{rel} b_{Gj}^2 P_{Gj}^C, \tag{14.77}$$

with the distance b_{Gj} chosen as in equation 14.62. Based on the above arguments, the collision velocity is as a first approximation taken to be equal to the velocity of the continous phase.

Observations from water models indicate that macroscopic bubbles are efficient at engulfing smaller ones, leaving a clean surface after passing along it. This suggests that the coalescence probability is large. For simplicity, P_{Gj}^C is thus set to unity.

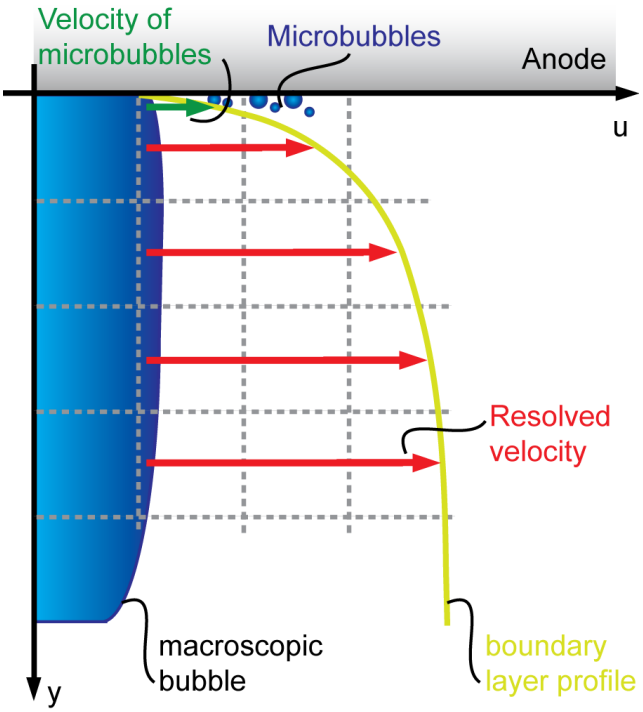

Figure 14.18: Boundary layer profile, resolved velocity and typical velocity where microbubbles are present.

The rate of change for the ghost class serves as a mass source for the continous gas phase, defined as

$$S_g^{PBM} = \rho_g V_G \dot{n}_G. \tag{14.78}$$

Thus, once an entity of the population has evolved to the ghost class, it is transferred to the continous gas phase from which the VOF model handles further evolution.

14.6 Coupling to external fluid flow

Equation 14.44 describes the population balance as a standalone model, that is, there is no explicit coupling to external features. Considering coupling to the surrounding flow field, the most simple approach is the so called one-way coupling, meaning that the fluid influences the motion of the bubbles, but the bubbles' explicit effect on the fluid *flow* may be neglected. In this case, equation 14.44 is generalized to a advection-diffusion equation of the form

$$\frac{\partial n_i}{\partial t} + \nabla \cdot \left(f\left(\boldsymbol{u}\right) n_i - \mathcal{D}_{PBM,i} \nabla n_i \right) = b_i - d_i, \tag{14.79}$$

where $f\left(\boldsymbol{u}\right)$ is an advection function and $\mathcal{D}_{PBM,i}$ is a diffusion tensor. The advection function serves as the principal mode of coupling to fluid flow, simply by transport, while the diffusion tensor will serve as a secondary source of bubble motion, preventing unphysical local accumulation of several bubbles.

The scalar form of equation 14.79 is a significant numerical advantage compared to a two-way coupling approach, in which the velocity field of each bubble class must be solved for, thus involving three times more equations compared to the scalar approach.

14.7 Complete model

In the preceding sections a comprehensive introduction to the underlying principles for three principle parts of the complete model is given, namely dissolved CO_2, microscopic bubbles and their coupling to macroscopic ones. In addition to these three features, the fluid flow and evolution of electromagnetic fields must be treated. As illustrated in figure 14.19 all phenomena are to some extent coupled, mainly through the principal node denoted as flow fields. In the following, the governing equations are presented in a coupled form for reference.

14.7.1 Governing equations

The evolution of macroscopic fluid-fields is governed by the VOF model, where (macroscopic) phase fractions α_k are determined by a transport equation of the form

$$\frac{\partial}{\partial t}\left(\alpha_k \rho_k\right) + \nabla \cdot \left(\alpha_k \rho_k \boldsymbol{u}\right) = S_k, \tag{14.80}$$

for the k-th phase, where S_k is a source term (with units kg/(m^{3}s)). The source term is non-zero for the (continous) gaseous phase and given by

$$S_g = S_g^{PBM} = \rho_g V_G \dot{n}_G. \tag{14.81}$$

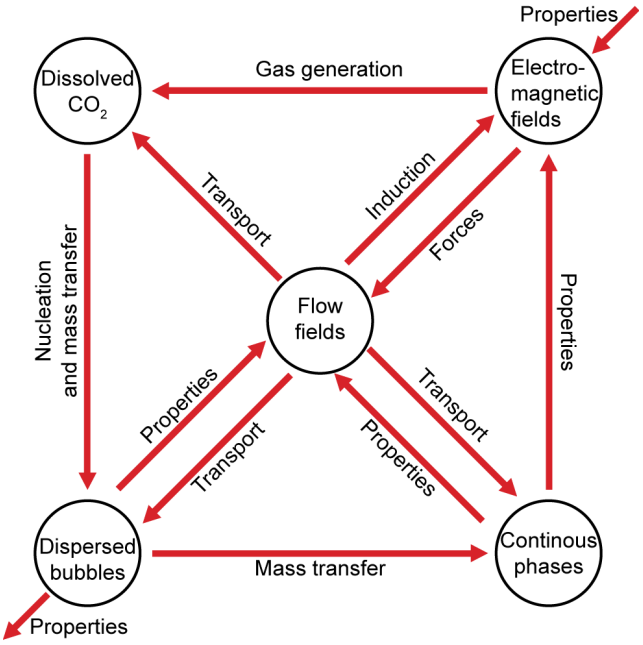

Figure 14.19: Specific coupling diagram. Figure shows the elements of the complete model and their interaction. Continuous fields are treated by the VOF method while remaining outer nodes are treated as scalar fields. Dissolved and dispersed (microscopic bubbles) gas evolves in the electrolyte and transfer to the continuous gas field occurs through ghost-bubbles.

The source term depends upon the rate of change of the ghost class (cf. section 14.5) and thus to the PBM. The rate of change for the ghost class is given by equation 14.73.

In the VOF model a single momentum equation is solved for a mixture fluid, with properties given by appropriate weighting (section 14.7.2). Assuming that the mixed flow field is incompressible, the resulting momentum equation is on the form

$$\frac{\partial}{\partial t}\left(\rho u_i\right) + \frac{\partial}{\partial x_j}\left(\rho u_j u_i\right) = -\frac{\partial}{\partial x_i}p + \frac{\partial}{\partial x_j}\left(\mu\frac{\partial u_i}{\partial x_j}\right) + \beta_i. \tag{14.82}$$

The above equation is equivalent to the single phase Navier-Stokes equation, with velocity and pressure fields ($\boldsymbol{u}$ and p) and properties (density ρ and viscosity μ) equal to the mixture in question. The final term, β_i, represents volumetric body forces. In the present case, the body forces are buoyancy (due to density differences) and Lorentz-forces (due to electromagnetic fields, where applicable). The body force is thus written as

$$\beta_i = \rho g_i + \left(\boldsymbol{j} \times \boldsymbol{B}\right)_i, \tag{14.83}$$

where g_i is the gravitational acceleration, $\boldsymbol{j}$ is the local current density and $\boldsymbol{B}$ is the local magnetic field. The current density is given by Ohm's law

$$\boldsymbol{j} = \sigma\left(\boldsymbol{u} \times \boldsymbol{B} - \nabla\phi\right) \approx -\sigma\nabla\phi, \tag{14.84}$$

assuming negligible induction currents in the bath, where σ is the electrical conductivity of the mixture and ϕ is the electrical potential. The electrical potential is determined from conservation of electrical charge, which under the above assumption reads

$$\nabla\sigma\nabla\phi = 0, \tag{14.85}$$

while the magnetic field is given by the magnetic vector potential

$$\boldsymbol{B} = \nabla \times \boldsymbol{\mathcal{A}}, \tag{14.86}$$

or specified as an external field. The magnetic vector potential is obtained by solving equation 10.33, where applicable.

As shown in section 14.1.2, the transport and evolution of dissolved CO_2 is given as

$$\frac{\partial \rho X_{CO_2}}{\partial t} + \nabla\cdot\left(\boldsymbol{u}\rho X_{CO_2} - \rho\mathcal{D}_{eff}\nabla X_{CO_2}\right) = S^p_{CO_2} - S^n_{CO_2} - S^{dmt}_{CO_2}. \tag{14.87}$$

The source term is the volumetric form of equation 14.2, i.e.

$$S^p_{CO_2} = \frac{M_{CO_2}\boldsymbol{j}\cdot\Delta\boldsymbol{A}}{\nu_e F \Delta V}, \tag{14.88}$$

where $\Delta\boldsymbol{A}$ and ΔV respectively are the surface and volume in which gas is being produced. If the bath is supersaturated, bubbles can be nucleated as described in section 14.2, resulting in a sink term written as

$$S^n_{CO_2} = \frac{N_p K\left(C_{b,CO_2} - C_{s,CO_2}\right)}{D_1^2}\frac{\rho_g V_1}{\Delta V} = \frac{N_p K \Delta C_{CO_2}}{D_1^2}\frac{\rho_g V_1}{\Delta V}, \tag{14.89}$$

where $\Delta C_{CO_2} = C_{b,CO_2} - C_{s,CO_2} = \rho X_{CO_2} - C_{s,CO_2}$, with a corresponding term present in the population balance equation for the smallest bubble class, $i = 1$. The number of active pores, N_p is given by equation 14.11 as

$$N_{pore} = \gamma_a \rho_{pore} \frac{\Delta A}{A_{pore,0}}, \tag{14.90}$$

where the activation parameter is given as

$$\gamma_a = \begin{cases} \left(1 - \frac{n_1 \Delta V A_{pore,0}}{\rho_{pore} \Delta A}\right) & \text{if} \quad n_1 \Delta V < \rho_{pore} \frac{\Delta A}{A_{pore,0}} \\ 0 & \text{otherwise,} \end{cases} \tag{14.91}$$

that is, nucleation stops if all pores have a microbubble attached to it.

For convenience, equations 14.88 and 14.89 are implemented as volumetric sources present *only* in the computational cells adjacent to the anode. This is equivalent to a flux boundary condition on the anode surface, but allows for 2D-planar studies as performed in chapter 15.

The final term in equation 14.87, also coupled to the PBM, is the sink term due to direct mass transfer, provided that the bath is supersaturated. Considering the theory of section 14.4.3, it is clear that the total mass transferred from the dissolved phase should be proportional to the sum of either negative *or* positive terms in equation 14.70. Choosing the negative terms for convenience, the final source term in equation 14.87 is written as

$$S^{dmt}_{CO_2} = \sum_{i=1}^{M} K_{2,i} \Delta C_{CO_2} n_i \left(\frac{V_i^{1/3}}{V_{i+1} - V_i} \right) \rho_g \left(V_{i+1} - V_i \right), \tag{14.92}$$

where $K_{2,i}$ is the mass transfer factor defined in equation 14.69 and indices i refer to one class of the PBM.

The PBM consists of M bubble classes and one ghost class (index $i = M + 1$) responsible for the coupling to macroscopic gas bubbles. The bubble classes are described by an exponential discretization in volume,

$$V_{i+1} = q V_i. \tag{14.93}$$

For bubble classes $i = 1 \ldots M$, the number density of bubbles is governed by the general advection-diffusion equation

$$\frac{\partial n_i}{\partial t} + \nabla \cdot \left(f\left(\boldsymbol{u}\right) n_i - \mathcal{D}_{PBM,i} \nabla n_i \right) = b_i - d_i, \tag{14.94}$$

where b_i and d_i are birth and death rates for the i-th bubble class. For bubble classes $i = 2 \ldots M$, the birth and death rates are due to coalescence (equation 14.48) and mass

transfer (equation 14.70) and are given as

$$\begin{aligned} b_i - d_i &= \underbrace{\frac{1}{2}\sum_j^M \sum_k^M \Gamma_{kj} n_k n_j \xi'_{ijk} - n_i \sum_j^G \Gamma_{ij} n_j}_{\text{coalescence}} \\ &+ \underbrace{K_2 \Delta C_{CO_2} \left[n_{i-1} \left(\frac{V_{i-1}^{\frac{1}{3}}}{V_i - V_{i-1}} \right) - n_i \left(\frac{V_i^{\frac{1}{3}}}{V_{i+1} - V_i} \right) \right]}_{\text{mass transfer}}, \end{aligned} \tag{14.95}$$

where Γ_{kj} is a coalescence kernel (cf. sections 14.4.2 and 14.5).

The smallest bubble class ($i = 1$) differs from equation 14.89 as bubbles are created only by nucleation. In this case, the birth and death rates are given as

$$\begin{aligned} b_1 - d_1 &= \frac{S_{CO_2}^n}{\rho_g V_1} - n_1 \sum_j^G \Gamma_{1j} n_j - K_2 \Delta C_{CO_2} n_1 \left(\frac{V_1^{\frac{1}{3}}}{V_2 - V_1} \right) \\ &= \frac{N_p K \Delta C_{CO_2}}{D_1^2 \Delta V_{cell}} - n_1 \sum_j^G \Gamma_{1j} n_j - \\ &- K_2 \Delta C_{CO_2} n_1 \left(\frac{V_1^{\frac{1}{3}}}{V_2 - V_1} \right). \end{aligned} \tag{14.96}$$

The bubble population evolves according to equation 14.94 until reaching the ghost class (see section 14.5) with number density

$$n_G = \frac{\alpha_G}{V_G}. \tag{14.97}$$

A PBM equation is not solved for the ghost class, but its rate of change is computed as

$$\dot{n}_G = K_2 \Delta C_{CO_2} n_M \left(\frac{V_M^{\frac{1}{3}}}{V_G - V_M} \right) + \frac{1}{2} \sum_j^M \sum_k^G \Gamma_{kj} n_k n_j \xi_{Gjk}, \tag{14.98}$$

which serves as the source term in equation 14.80 for the continous gaseous phase and thus closes the system.

14.7.2 Fluid properties

The material properties of the pure VOF model are shared through a mixture phase. The properties of the mixture phase are obtained through an appropriate weighting by the local

volume fraction of the k-th phase. Density and viscosity are calculated using an arithmetic mean

$$\rho = \rho_{gas}\alpha_{gas} + \rho_{bath}\alpha_{bath} = \rho_{gas}\alpha_{gas} + \rho_{bath}\left(1 - \alpha_{gas}\right), \tag{14.99}$$

where subscripts *gas* and *bath* refer to macroscopic gas and bath phases, respectively. Correspondingly, the electrical conductivity of the mixture, i.e. a computational cell partially filled with bath (with or without microscopic bubbles) and resolved gas, is given as

$$\sigma = \sigma_{gas}\alpha_{gas} + \bar{\sigma}_{bath}\left(1 - \alpha_{gas}\right), \tag{14.100}$$

where $\bar{\sigma}_{bath}$ is the mean bath conductivity, which in the present case is allowed to depend upon the local concentration of microscopic bubbles. As shown by Cooksey et al. [21], several models exist for calculating the electrical conductivity of the bath. Defining the phase fraction of sub-grid bubbles as

$$\alpha_{PBM} = \sum_{i=1}^{M} n_i V_i, \tag{14.101}$$

the theoretical maximum in conductivity is obtained by the arithmetic mean, i.e.

$$\bar{\sigma}_{bath} = \sigma_{gas}\alpha_{PBM} + \sigma_{bath}\left(1 - \alpha_{PBM}\right), \tag{14.102}$$

which corresponds to the case in which the bubbles are arranged in a homogeneous column parallel to the direction of the current (Cooksey et al. [21]). A lower estimate is obtained by Maxwell [81]

$$\bar{\sigma}_{bath} = \sigma_{gas}\alpha_{PBM} + \sigma_{bath}\frac{1 - \alpha_{PBM}}{1 + \frac{\alpha_{PBM}}{2}} \tag{14.103}$$

for a uniform dispersion of spherical bubbles and the Bruggeman equation [11]

$$\bar{\sigma}_{bath} = \sigma_{gas}\alpha_{PBM} + \sigma_{bath}\left(1 - \alpha_{PBM}\right)^{\frac{3}{2}} \tag{14.104}$$

for spheres of unequal size. The mean conductivity calculated by each of the above models is shown in figure 14.20. As seen from figure 14.20, each of the above models predict similar behaviour for the mixture conductivity, a gas phase fraction of 50% resulting in at least a 50% increase in resistivity. The literature is inconclusive on which model yields the best results, other than the statement that all the proposed models yield *reasonable* results for bubbles attached to an electrode (Cooksey et al. [21]). Due to the polydisperse nature of the system at hand, equation 14.104 is used in the following chapters.

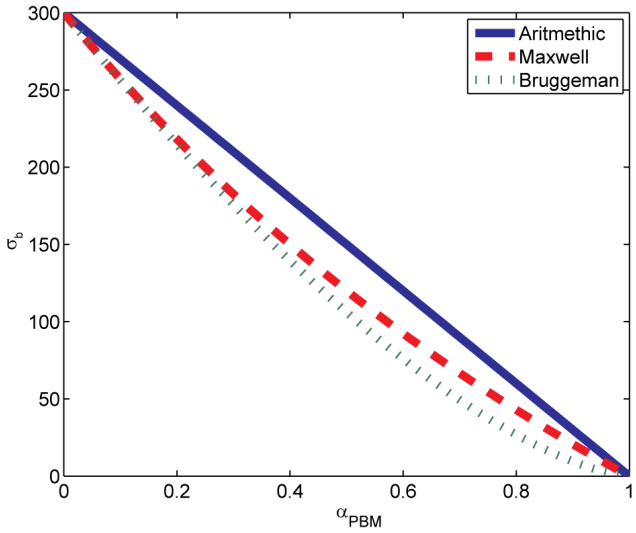

Figure 14.20: Mixture conductivity as a function of gas phase fraction.

14.8 Treatment in FLUENT

Each of the necessary additional equations are solved as user defined scalars (UDS) in FLUENT, while their coupling and the determination of properties is performed by means of a library of user defined functions (UDF). The flow is initialized by means of the `DEFINE_INIT()`-macro, where all initial parameters and anode properties are fixed.

Source terms are updated either at the end of each iteration using the `DEFINE_ADJUST()`-macro or at the end of each time step (for increased stability and convergence rate) using the `DEFINE_EXECUTE_AT_END()`-macro. Properties are updated in the following order

1 Update phase fractions stored in memory.

2 Calculate electromagnetic fields.

3 Calculate gas sources due to nucleation.

4 Calculate source and sink terms due to mass transfer.

5 Calculate source and sink terms due to coalescence.

Calculated source and sink terms are passed to the governing equations through the `DEFINE_SOURCE()`-macro, while fluid properties are updated by `DEFINE_DIFFUSIVITY()`- and `DEFINE_PROPERTY()`- macros, based on stored phase fractions.

By default, FLUENT solves the following equation for an arbitrary scalar ψ

$$\frac{\partial \rho\psi}{\partial t} + \frac{\partial}{\partial x_i}\left(\rho u_i \psi - \Gamma_k \frac{\partial \psi}{\partial x_i}\right) = S_\psi. \tag{14.105}$$

As density does not enter in the scalar equations for the PBM, the default equation is modified by the `DEFINE_UDS_FLUX()`- and `DEFINE_UDS_UNSTEADY()`-macros to the form

$$\frac{\partial \psi}{\partial t} + \frac{\partial}{\partial x_i}\left(f(u_i)\psi - \Gamma_k \frac{\partial \psi}{\partial x_i}\right) = S_\psi. \tag{14.106}$$

14.9 Parameters of the model

Three classes of parameters are introduced in the proposed model, each related to a specific phenomenon but at the same time strongly coupled to the overall picture. The three classes are

1. The number of *active* pores (i.e. mean pore density and -diameter).

2. Bath properties (i.e. diffusivities, saturation concentration, contact angle, viscosity).

3. Transfer properties (i.e. Sherwood number, coalescence kernel and detachment diameter of the smallest bubbles).

The above parameters can in principle be measured for a given setup, although non-equilibrium properties would be highly challenging to quantify. As seen from part I of this thesis, this is also true for the bath properties, being highly dependent upon local properties such as species concentration. Finally, as seen by Rørvik et al. [102], the pore diameter of a given anode sample spans two orders of magnitude.

Evidently, the mean (constant) values required for the proposed model, although not entirely free, are allowed to span a large set of possible values. The parameters are all to some degree coupled and two different sets of parameters can thus in principle result in qualitatively similar global behaviour, with subtle local differences. These differences as well as the overall influence of each of the above parameters can be determined only by comparison with experimental data, as performed in chapter 16.

The first class is believed to be critical as it governs the nucleation of microscopic bubbles and is thus to a great extent responsible for the overall future bubble distribution. A large number of active pores will allow the anode to become flooded with gas, thus impeding the passage of electrical current and thus increasing the cell voltage. Hence, the number of active pores should be such that both the average voltage and bubble generation rate fall within reasonable values.

Nucleation is also related to the diffusivity of CO_2 in the bath and the local Sherwood number, the latter of which also governs bubble growth. Small values for the diffusivity will retard nucleation and growth of bubbles, resulting in a slow evolution of macroscopic bubbles, if the overall number density of microscopic bubbles is small. If the number densities are large, mass transfer will be critical only for the formation of the smallest bubble class as the overall evolution is handled by coalescence. In a real case, coalescence and mass transfer will compete in the creation of macroscopic bubbles and the choice of the respective parameters will determine which part of the cell is governed by each of the phenomena.

Chapter 15

Verification studies

The proposed gas generation and evolution model is fairly complex and involves intricate coupling between several sub-models. Hence, as for the MHD mode, a verification of its essential features is required, as performed in the following sections.

15.1 Setup for verification studies

The first three verification cases deal with issues related to the PBM alone and are performed in a 2D geometry with dimensions 1 by 1 meter and a resolution of 1 cm.

Up to five bubble classes are used, treated as user defined scalars as described in section 14.8, which are discretized using a first order upwind scheme. PBM variables are given a convergence criterion of 10^{-6} on corresponding residuals. Gradients are computed with a Green-Gauss cell based method and pressure velocity coupling (where applicable) is performed by the PISO algorithm with default correction factors for neighbour-skewness. In the final verification case, the multiphase nature of the flow is treated by means of the explicit VOF model, discretized using the PLIC-scheme. For increased stability, the flexible cycle is used for the pressure AMG cycle.

Time advancement is in all cases performed using a first order implicit scheme, with constant time step 0.01s. All other settings are kept at their default values.

Values for the various parameters used in the simulations, unless otherwise noted, are given in table 15.1. The discretizaton factor is given the value $q = 2$, in order to simplify the terms coalescence kernel and to allow for a relatively large span in bubble classes without the need for excessively large values of M, while the detachment diameter D_1 is the mean diameter observed experimentally by Xue and Øye [139]. The mass transfer factor K is given a constant value based on preliminary calculations. It should be noted that the exact

values of the parameters in the following *verification* study is not critical, as the goal is to confirm that the "equations are solved right" (cf. section 3.8).

Table 15.1: Values for various parameters used in verification studies

Parameter	Unit	Value
ρ_{gas}	kg/m^3	1.2
ρ_{bath}	kg/m^3	2070
A_{p0}	m^2	$2.25{\cdot}10^{-8}$
V_{cell}	m^3	$1{\cdot}10^{-6}$
A_{cell}	m^2	$1{\cdot}10^{-4}$
j	A/m^2	$1{\cdot}10^{4}$
D_1	m	$5{\cdot}10^{-4}$
q	-	2
K	m^5/kg·s	$1.1{\cdot}10^{-6}$
C_{s,CO_2}	kg/m^3	0.1

Simulated properties are compared based on their mean relative difference to either an analytical- or numerical solution obtained by MATLAB. The relative difference for a property φ is defined as

$$\varepsilon = \frac{|\varphi_f - \varphi_a|}{|\varphi_a|}, \tag{15.1}$$

where φ_f and φ_a represent FLUENT and alternative solutions, respectively.

15.2 Case 1: Supersaturation and nucleation

The first case deals with supersaturation of the bath and nucleation of the smallest bubble class (index 1), in absence of any other phenomena. In this case, assuming that the bath is supersaturated, the CO_2 concentration is governed by

$$\begin{aligned} \frac{\partial C_{CO_2}}{\partial t} &= S^p_{CO_2} - S^n_{CO_2} \\ &= \frac{M_{CO_2} j A_{cell}}{\nu_e F \Delta V_{cell}} - \frac{N_p K \Delta C_{CO_2}}{D_1^2} \frac{\rho_g V_1}{\Delta V_{cell}}, \end{aligned} \tag{15.2}$$

where the first term represents production as of Faraday's law (equation 14.2) and the second term represents transfer to the smallest bubble class through nucleation as of equation 14.36.

For convenience, equation 15.2 is written on the form

$$\frac{\partial C_{CO_2}}{\partial t} = \eta - \kappa_1 C_{CO_2}, \tag{15.3}$$

with analytical solution

$$C_{CO_2}(t) = \frac{\eta}{\kappa_1}\left[1 - \exp\left(-\kappa_1 t\right)\right] + C_{CO_2}(0)\exp\left(-\kappa_1 t\right), \tag{15.4}$$

$C_{CO_2}(0)$ being the initial (dissolved) CO_2 concentration.

The smallest bubble class is governed by nucleation alone:

$$\frac{\partial n_1}{\partial t} = \frac{S^n_{CO_2}}{\rho_g V_1} = \frac{\kappa_1}{\rho_g V_1}\Delta C_{CO_2} \tag{15.5}$$

with analytical solution

$$\rho_g V_1 n_1(t) = \left[\frac{\eta}{\kappa_1}\left(\kappa_1 t + \exp\left(-\kappa_1 t\right)\right) - C_{CO_2}(0)\exp\left(-\kappa_1 t\right)\right] - C_s\kappa_1 t + \frac{\kappa_1 C_{CO_2}(0) - \eta}{\kappa_1}, \tag{15.6}$$

again, provided the bath is supersaturated and that no bubbles exist initially.

15.2.1 Case 1a: Uniform production and nucleation

Assuming that production and nucleation is uniform and homogeneous, the behaviour in each computational cell is given by equations 15.4 and 15.6. Figure 15.1 shows a comparison between the dissolved gas concentration and the number density of bubbles obtained by FLUENT and the above analytical solutions for a system at initial supersaturation $C_{CO_2}(0) = 0.1$ kg/m^3 and initial number density of bubbles $n_1(0) = 0$ #/m^3.

The *mean* absolute error for each of the cases in figure 15.1 is 0.3% and 3.3%, respectively. The relatively large error is due to the first order time formulation and relatively large time-steps. Reducing the time step to 0.005 s, the error is in each case reduced to $1.5 \cdot 10^{-4}$ and 0.9%, respectively. Compared to results obtained by the ODE45 solver in Matlab (which is 4th order in time) the corresponding error is $1 \cdot 10^{-9}$ and 1.9%, that is, from a numerical point of view, the error in the FLUENT solution is acceptable and as expected.

The total mass in the system should, in this case, at all times correspond to the mass being produced by Faraday's law, that is a straight line with a slope equal to the first term in equation 15.2. Figure 15.2 shows the total gas mass in the system (i.e. dissolved gas and bubbles), compared to that predicted by Faraday's law.

The mean absolute error for the total system mass is 0.4% (with the large time step), which is as expected from the above error estimates.

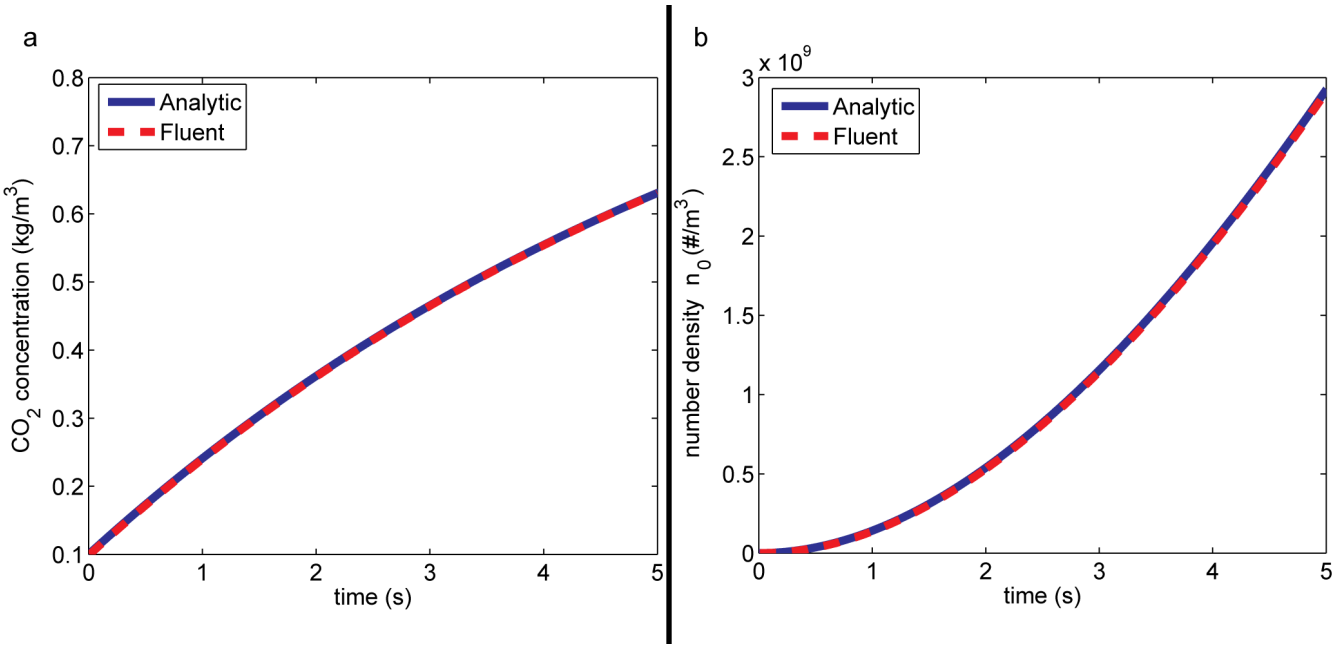

Figure 15.1: Comparison of analytical- (solid line) with numerical solution (dashed line) for dissolved gas concentration (a) and bubble number density (b).

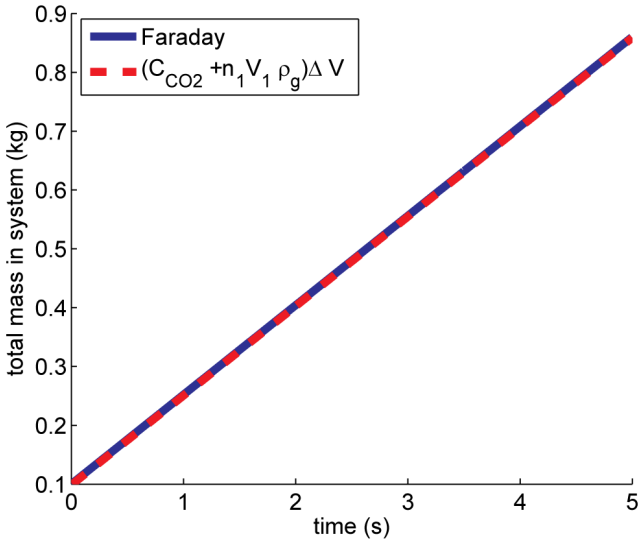

Figure 15.2: Comparison of analytical- (solid line) with numerical solution (dashed line) for total mass in system.

15.2.2 Case 1b: Non-uniform nucleation from supersaturated solution

In the case of no gas production on an inhomogeneous anode, nucleation will proceed only as long as the bath is supersaturated and only at active pores. For a system with pore distribution given by equation 14.10 with $\rho_{max} = 0.35$ at initial supersaturation $C_{CO_2}(0) = 0.11$ kg/m^3 and initial number density of bubbles $n_1(0) = 0$ #/m^3, the evolution of CO_2, n_1 and total mass is shown in figure 15.3.

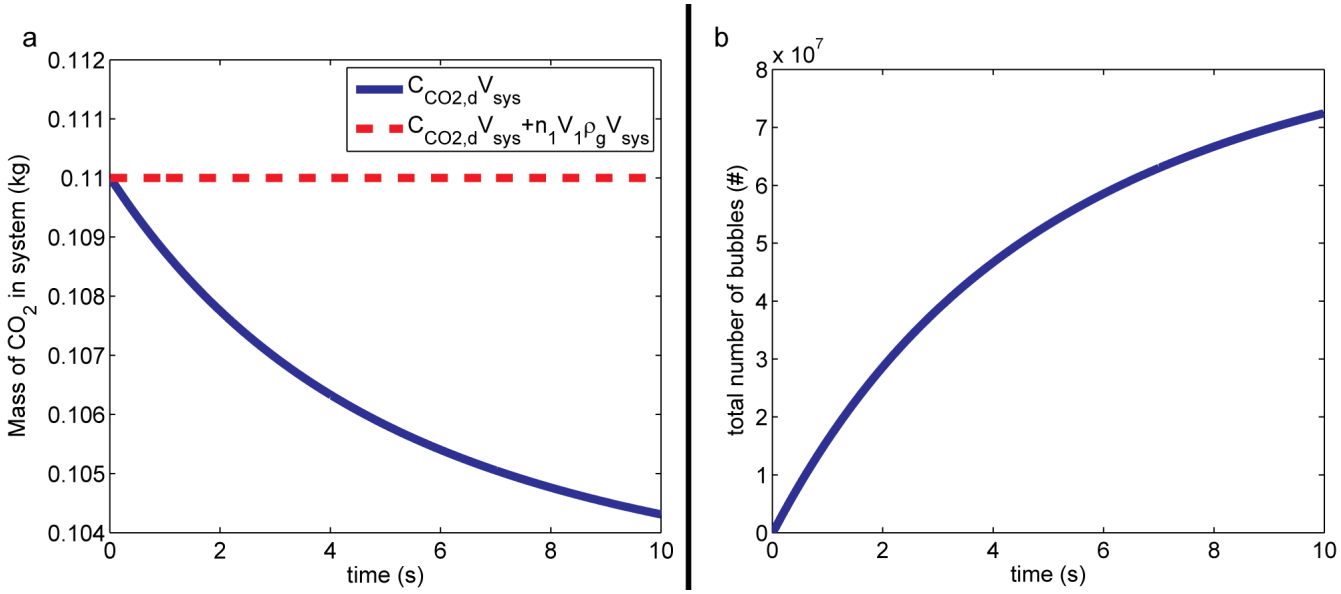

Figure 15.3: Evolution of dissolved CO_2 mass (solid line) and total mass of gas (dashed line) in system (a) and number density of bubbles (b).

As seen from figure 15.3, the total mass of gas in the system is constant, as expected. Figure 15.4 shows the local CO_2 concentration and local number of bubbles at $t = 10$ s. Evidently, the two are strongly correlated.

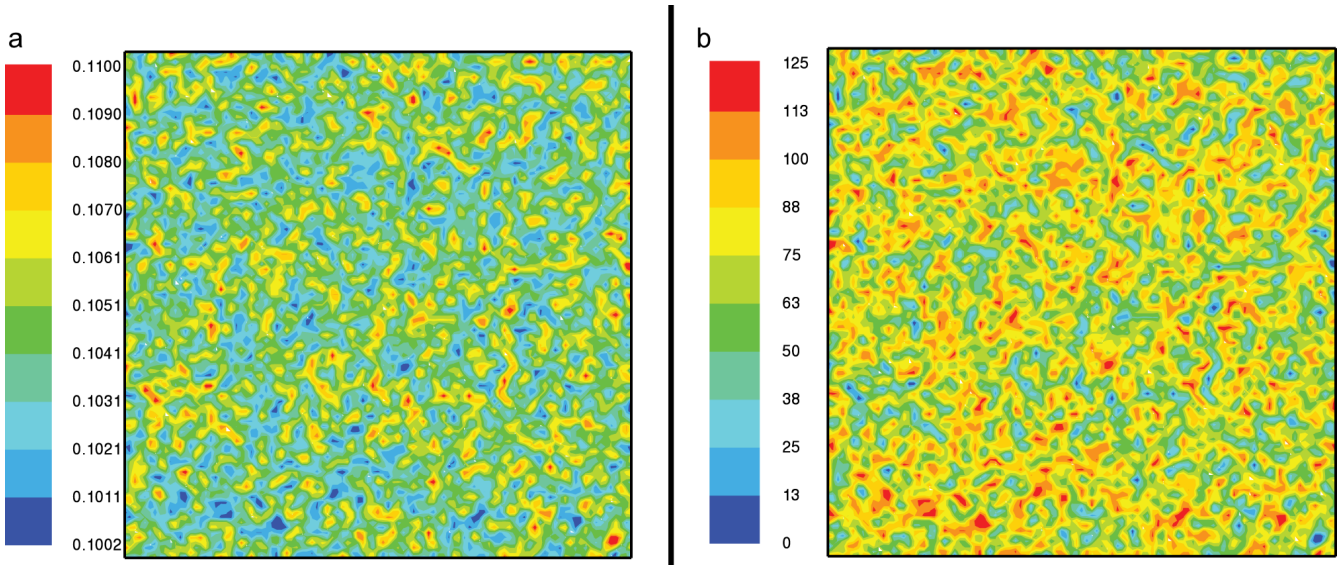

Figure 15.4: Local CO_2 concentration, kg/m^3, (a) and local number of bubbles, #, (b).

15.3 Case 2: Growth model

The second case deals with the growth of bubbles in a supersaturated solution, in absence of other phenomena. In this case, each of the bubble classes is governed by equation 14.70, which in the case of two bubble classes results in the system

$$\frac{\partial n_1}{\partial t} = -K_2 \Delta C_{CO_2} n_1 \left(\frac{V_1^{1/3}}{V_2 - V_1} \right) = -\kappa_2 (C_b - C_s) n_1 \tag{15.7}$$

$$\frac{\partial n_2}{\partial t} = K_2 \Delta C_{CO_2} n_1 \left(\frac{V_1^{1/3}}{V_2 - V_1} \right) = \kappa_2 (C_b - C_s) n_1 \tag{15.8}$$

The mass of dissolved CO_2 declines with rate

$$\frac{\partial C_{CO_2}}{\partial t} = -\sum_{i=1}^{M-1} K_2 \Delta C_{CO_2} n_i \left(\frac{V_i^{1/3}}{V_{i+1} - V_i} \right) \rho_g \left(V_{i+1} - V_i \right) = -\sum_{i=1}^{M-1} \kappa_{i,i+1} \Delta V_{i,i+1} n_i, \tag{15.9}$$

as mass gradually is transferred to the bubbles. In the case of two bubble classes, the rate of CO_2 removal is simply

$$\frac{\partial C_{CO_2}}{\partial t} = -\kappa_2 \Delta C_{CO_2} n_1 \rho_g \left(V_2 - V_1 \right) \tag{15.10}$$

No analytical solution is found for the above system of equations and results are thus compared to solutions obtained by the ODE45 solver in MATLAB and known global parameters.

Consider two bubble classes in an initially supersaturated system with homogeneous concentration $C_{CO_2}(0) = 0.11\text{kg/m}^3$. No gas production is present. Initially, the number density of the smallest bubble class is homogeneous and equal to $1{\cdot}10^9$ $\#/\text{m}^3$, while no bubbles are present in the second class.

The growth process requires that the total number of bubbles is conserved and that mass removed from the dissolved phase is gained in the largest bubble class. Figure 15.5 shows a comparison between the evolution of the two bubble classes and the mass in the system obtained by MATLAB and FLUENT. The mean relative differences between the two so-

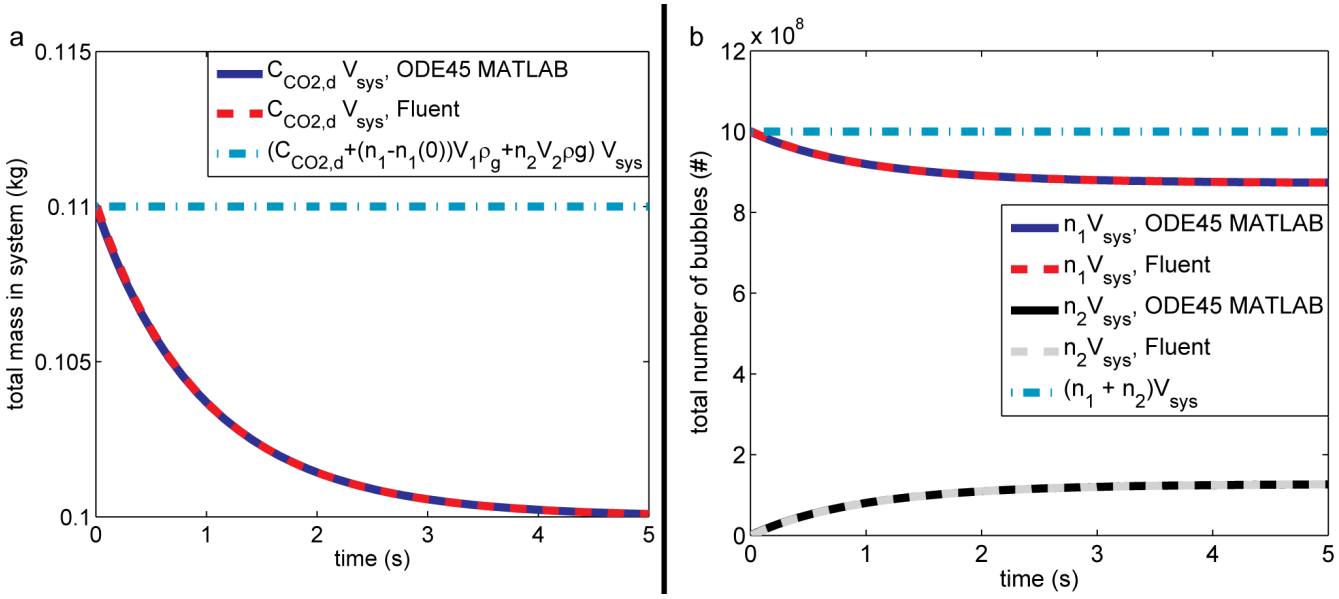

Figure 15.5: Mass in system (a) and total number of bubbles (b). Solid lines show solutions obtained by MATLAB while dashed lines show solutions obtained by FLUENT. The dash-dot line shows the total mass (minus the initial bubble mass) in the system and the total number of bubbles in figures (a) and (b), respectively.

lution methods are $1.1 \cdot 10^{-4}$, $1.6 \cdot 10^{-4}$ and 0.9%, for each of the fields C_{CO_2}, n_1 and n_2, respectively. The differences are comparable to those found for case 1 and is due to the different numerical scheme used for each of the solution methods.

15.4 Case 3: Coalescence model

The third case deals with coalescence of bubbles, in absence of other phenomena. In this case, each of the bubble classes is governed by equation 14.48, i.e.

$$\frac{dn_i}{dt} = \frac{1}{2}\sum_{j}^{M}\sum_{k}^{M}\Gamma_{kj}n_k n_j \xi'_{ijk} - n_i(1-\delta_{iM})\sum_{j}\Gamma_{ij}n_j. \tag{15.11}$$

As for the growth-case, the solution obtained by FLUENT is compared to solutions obtained by the ODE45 solver in MATLAB.

Consider a system in which the initial number density of the smallest bubble class is homogeneous and equal to $1{\cdot}10^9$ $\#/\mathrm{m}^3$, while no bubbles are present in the remaining four classes (i.e. $M = 5$). Assuming (for simplicity) that the coalescence probability is unity and that the collision frequency is given by equation 14.58, multiplied with a factor 10^5 in order to achieve sensible results within reasonable time scales. In absence of other phenomena, the total *mass* of bubbles is conserved throughout the calculation, while the total number density declines. Figure 15.6a shows a comparison between the evolution of bubble classes 1,3 and 5 obtained by MATLAB and FLUENT, while figure 15.6b shows the total system mass and number of bubbles.

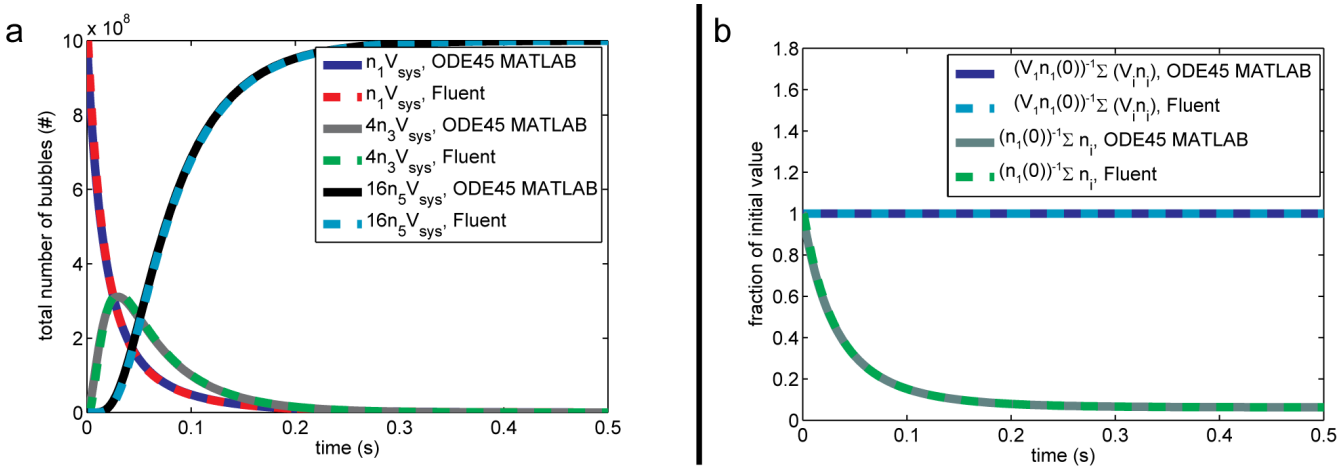

Figure 15.6: Selected population curves (a) and total system mass (blue) and bubble count (green) (b). Solid lines show solutions obtained by MATLAB while dashed lines show solutions obtained by FLUENT. Population lines (a) are normalized for visibility and global values are normalized to initial values.

As seen from figure 15.6b, the total number of bubbles declines and approaches the value $n_1(0)/8$ as expected. The mean relative difference for each of the respective population bins shown in figure 15.6a is 1.4, 3.6 and 6.5%, while the mean relative difference for the

total number density (figure 15.6b) is 0.3%. The somewhat large differences in individual particle bins is mainly due to points where one of the two methods reaches zero, resulting in a large relative difference. Considering only nonzero values, the mean relative difference is less than 1% for each of the cases.

15.5 Case 4: Macro to micro coupling

The final verification case deals with coupling to and generation of macroscopic bubbles with special attention to mass conservation. The two modes of gas generation, i.e. coalescence and mass transfer, are considered separately for clarity. A special 2D-geometry, as shown in figure 15.7, consisting of 6000 cells with a uniform resolution of 5 mm is used for the simulations.

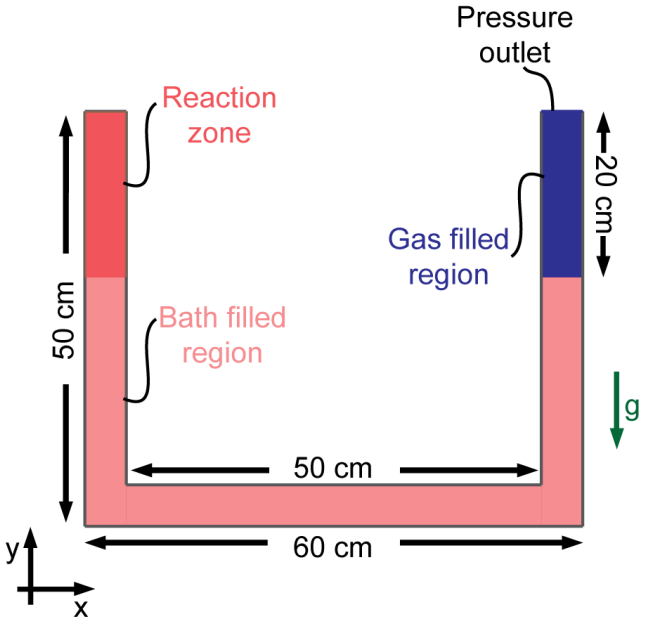

Figure 15.7: 2D geometry used for phase transfer verification. The system is bounded by solid walls except for the upper right horizontal surface which is a pressure outlet. Gravity is set to work in the $-y$-direction. The system is assumed to have unit length in the z direction for volume calculations.

As shown in figure 15.7, the system is initialized to consist entirely of bath, except for a 20 cm region in the upper part of the right leg which is filled with (macroscopic) gas. A corresponding region in the left leg is initialized to have a large quantity of *dissolved* gas, while all other regions are depleted. The rationale for the proposed geometry is that (macroscopic) gas generated in the reaction zone will be trapped (due to gravity), thus

moving the bath up in the right leg. As both phases are considered to be incompressible, the conservation of bath mass is verified by a height difference.

Five bubble classes (in addition to the ghost class) are used for the following simulations. The fluid flow is assumed to be laminar as flow features are of no interest for the current case.

15.5.1 Case 4a: Coupling by mass transfer

Consider 10^9 bubbles with diameter $D_1 = 0.5 \cdot 10^{-4}$ m located in the reaction zone, which in addition has 1.5 kg/m^3 dissolved CO_2. Thus, $2.63 \cdot 10^{-2}$ m^3 of sub-grid gas is available for transfer, corresponding to a macroscopic gas height of 0.263 m in the left leg of the system (if transfer is complete). Growth is assumed to be described by equation 14.70 and transfer to the macroscopic phase is treated as of section 14.5.

A time step of 0.001 s is used and simulations are run for 5 s flowtime. Figure 15.8 shows the initial and final distribution of macroscopic phases. The average height difference Δh

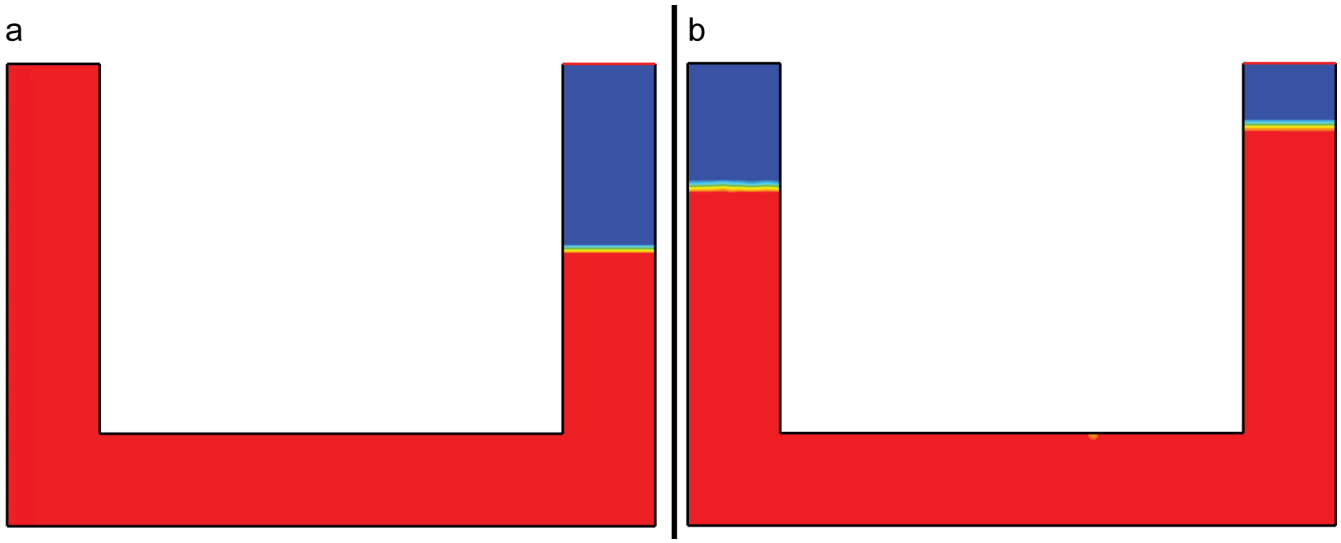

Figure 15.8: Initial (a) and final (5 s flowtime) (b) phase distribution for growth model. Red signifies the bath phase.

is 0.133 m on both sides, showing that the bath-mass is conserved during the process. Comparing to the maximal height, $\Delta h = 0.263$m, the obtained value suggests that some sub-grid gas is still present in the system. Table 15.2 shows the volume integral and corresponding (total) volume of sub grid properties at $t = 5$ s.

As $1.33 \cdot 10^{-2}$ m^3 gas has been evolved, the final result is a total of $2.60 \cdot 10^{-2}$ m^3 of gas in the system; 1% lower than the mass available. This is however expected from the

Table 15.2: Integral values of sub grid properties

Property	Volume integral	Corresponding volume (m^3)
C_{CO2}	$2.39{\cdot}10^{-3}$ kg	$1.99{\cdot}10^{-3}$
n_1	$1.26{\cdot}10^{3}$	$8.25{\cdot}10^{-8}$
n_2	$6.58{\cdot}10^{4}$	$8.62{\cdot}10^{-6}$
n_3	$1.07{\cdot}10^{6}$	$2.80{\cdot}10^{-4}$
n_4	$4.82{\cdot}10^{6}$	$2.52{\cdot}10^{-3}$
n_5	$7.55{\cdot}10^{6}$	$7.91{\cdot}10^{-3}$
sum	-	$1.27{\cdot}10^{-2}$

uncertainty of the VOF model where the uncertainty in the interface position is at least one computational cell, i.e. 5 mm for the current case.

Case 4b: Coupling by coalescence

Consider $1 \cdot 10^9$ bubbles with diameter $D_1 = 5 \cdot 10^{-4}$ m and $1 \cdot 10^8$ bubbles with diameter $D_2 = 6.3 \cdot 10^{-4}$ m located in the reaction zone. Thus, $1.57 \cdot 10^{-3}$ m^3 of sub-grid gas is available, corresponding to a macroscopic gas height of 0.0157 m in the left leg of the system (if transfer is complete). For this simulation, coalescence is assumed to be governed by the coalescence kernel of Luo [79], i.e. collision frequencies given by equation 14.58 and collision probabilities by equation 14.64. The turbulent dissipation rate ϵ is assumed to be 0.1 m^2/s^3.

The simulations are performed with a time step of 0.002 s and simulations are run for 5 s flowtime. Figure 15.9 shows the initial and final distribution of phases.

The height difference Δh is 0.0153 m in both legs, showing that the bath mass is conserved.

Comparing to the maximal height, $\Delta h = 0.0157$m, the obtained value suggests that only small amounts of sub-grid gas is still present in the system. Table 15.3 shows the volume integral and corresponding (total) volume of sub grid properties at $t = 5$ s, confirming that the transfer is almost complete.

Table 15.3: Integral values of sub grid properties

Property	Volume integral	Corresponding volume (m^3)
n_1	$3.94{\cdot}10^{3}$	$2.58{\cdot}10^{-7}$
n_2	$1.48{\cdot}10^{3}$	$1.94{\cdot}10^{-7}$
n_3	$1.87{\cdot}10^{3}$	$4.88{\cdot}10^{-7}$
n_4	$1.36{\cdot}10^{3}$	$7.13{\cdot}10^{-7}$
n_5	$1.79{\cdot}10^{3}$	$1.88{\cdot}10^{-6}$
sum	-	$3.53{\cdot}10^{-6}$

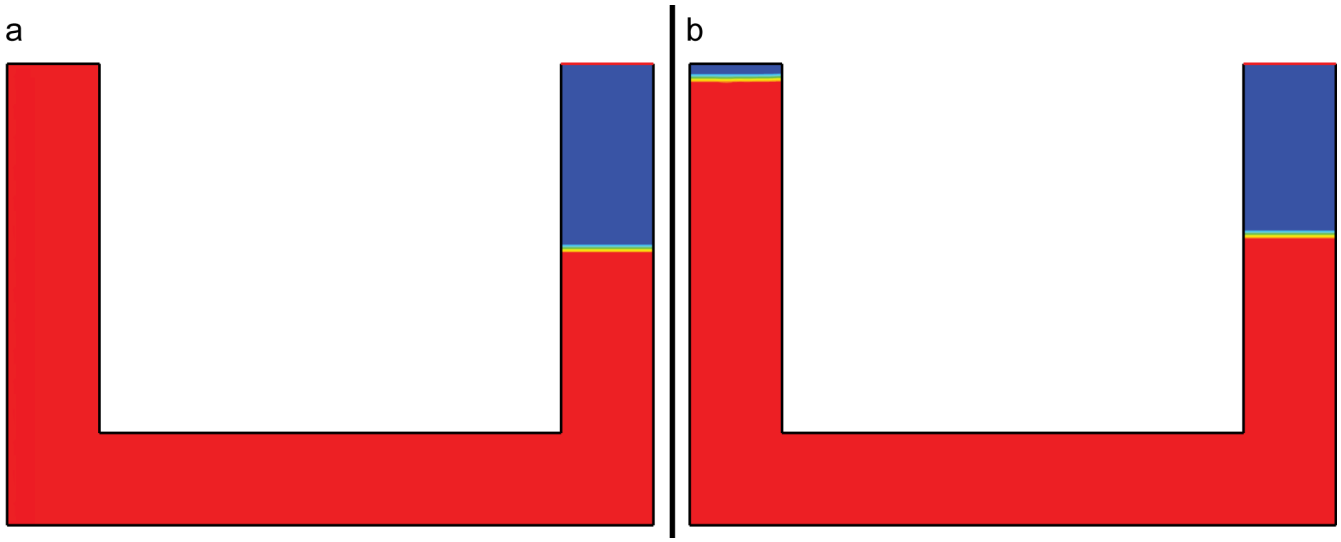

Figure 15.9: Initial (a) and final (5 s flowtime) (b) phase distribution for coalescence model. Red signifies the bath phase.

The predicted interface height (taken to be at $\alpha_{gas} = 0.5$) is lower than the maximal value, suggesting a mass loss of approximately 2%, which is consistent with the uncertainty of the interface position due to the coarse mesh.

Chapter 16

Parametric validation studies

The previous chapter indicates that the constituents of the proposed model behave as expected, and the model can thus be assumed to be verified. In the following sections, the complete model is analysed further and validated against the experimental data given in chapter 9. The validation study is performed in conjecture with a parametric, factorial design study (cf. Montgomery [82]) in order to determine a set of realistic parameters which adequately describe observed phenomena, in addition to provide insight into how strongly simulated results depend upon the choice of these parameters.

Following the preliminary parametric study, the influence of MHD-forces is investigated. Finally, given a set of viable parameters, simulations are performed on various configurations of the lab cell (cf. table 9.1) in order to verify that the obtained parameters are valid over a wide range of cases.

The goal of the current validation study is to reproduce the experimentally measured voltage fluctuations (i.e. frequencies and amplitude). It should however be noted that there are variations in measured results, even with identical (controllable) experimental configurations (cf. table 9.1) and results should thus be considered as being *typical*, rather than exact for the given setup, i.e. the following validation will attempt to reproduce the *range* of the given experiments, rather than the absolute numbers.

In order to handle this vast set of numerical experiments, all simulations presented in this chapter are performed in a *simplified* 2D geometry.

16.1 Computational domain and mesh

The proposed model is applied to the lab scale electrolysis cell described in chapter 9. A sketch of a 2D cross section of the experimental setup is shown in figure 16.1 for reference.

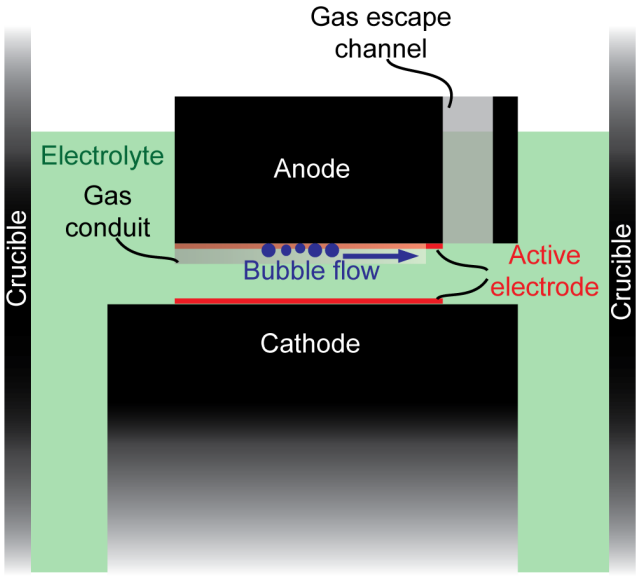

Figure 16.1: Sketch of experimental cell. A gas conduit forces bubbles to escape through a designated gas escape channel. The active electrode regions with dimensions 100 by 100 mm is shown in red.

A simplified representation of the above geometry is shown in figure 16.2. The 2D geometry is simplified compared to the full cross section shown in figure 16.1. In particular, a large portion of the regions of electrolyte surrounding the electrodes is neglected as this region is not electrochemically active. This restricts the bath flow somewhat, as the bath is forced to recirculate into the interpolar region after bubble detachment, but is not believed to be essential for the current validation. In addition, only the anode part to the left of the gas escape channel is assumed to carry an electrical current as this is the part to which the anode rod is connected (green line shown in figure 16.2). Furthermore, the part of the anode to the right of the gas channel is (relatively) far from the cathode, suggesting that only a small part of the electrical current would pass through this region, if it were active.

In order to facilitate meshing, the corners of the anode are assumed to be sharp, thus simulating a new anode.

The mesh used is shown in figure 16.3, consisting of 7700 quadrilateral cells.

This resolution results in a phase fraction of 0.23 for *one* ghost bubble and 0.12 for a bubble of class M, provided $D_1 = 0.5$mm, q=2 and M=5, as in the verification studies.

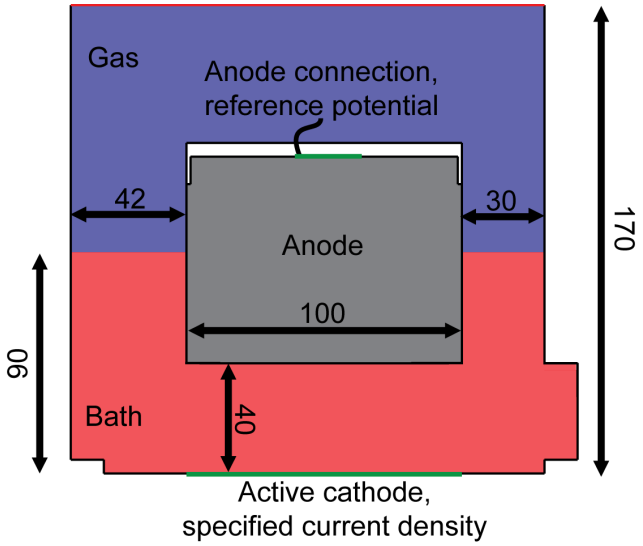

Figure 16.2: Simplified 2D geometry for preliminary analysis with dimensions given in mm. Initial gas and bath distribution is shown in blue and red, respectively.

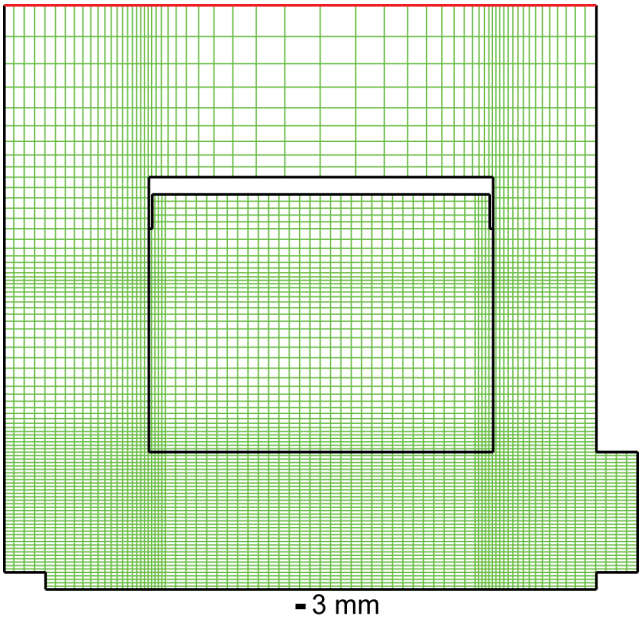

Figure 16.3: 2D mesh used for preliminary study. Geometry is enclosed by solid walls (coupled boundaries where applicable) and one single pressure outlet (red upper line). The resolution on the flat part of the anode is Δx=3mm, Δy=1mm.

16.2 Setup for validation studies

16.2.1 Fluid properties and model parameters

Default values for the various parameters used in the simulations are given in table 16.1, with default bath properties reflecting elevated alumina content, cf. Eick et al. [29].

Table 16.1: Values for various parameters used in simulations

Parameter	Unit	Value
ρ_{gas}	kg/m^3	0.435
ρ_{bath}	kg/m^3	2070
μ_{gas}	kg/m·s	$6.43 \cdot 10^{-5}$
μ_{bath}	kg/m·s	$3.30 \cdot 10^{-3}$
σ_{gas}	$\Omega^{-1}m^{-1}$	$1 \cdot 10^{-12}$
σ_{bath}	$\Omega^{-1}m^{-1}$	200
σ_{anode}	$\Omega^{-1}m^{-1}$	$3 \cdot 10^{6}$
$\mathcal{D}_i$	m^2/s	$5 \cdot 10^{-10}$
$\gamma_{gas,bath}$	N/m	0.1
$\theta_{gas,bath}$	^{o}	110
C_{s,CO_2}	kg/m^3	0.4
A_{p0}	m^2	$5.03 \cdot 10^{-9}$
$\rho_{p,max}$	%	22
$\rho_{p,min}$	%	2
j	A/m^2	8000
D_1	m	$5 \cdot 10^{-4}$
q	-	2
M	-	5
γ_a	-	1
ACD	m	0.04
g_x	m/s^2	-0.3424
g_y	m/s^2	-9.8040
p_{gauge}	atm	0

The default choices for the current density, ACD and inclination correspond to experiments 8 and 31 as of table 9.1.

The effective diffusivity of CO_2 (cf. equation 14.3) is assumed to be given as

$$\mathcal{D}_{eff} = \mathcal{D}_{CO2} + \frac{\nu_t}{Sc_t}, \tag{16.1}$$

where $\mathcal{D}_{CO2}$ is the molecular diffusivity, ν_t is the turbulent viscosity and $Sc_t = 0.90$ is a turbulent Schmidt-number.

For mass transfer, a Ranz-Marshall type correlation is used (cf. Kolev [69] chapter 12 and Vogt [127], [128]), given as

$$Sh = 2.0 + 0.6\sqrt{Re}Sc^{1/3}, \tag{16.2}$$

with Schmidt and Reynolds numbers defined as

$$Sc = \frac{\mu_b}{\rho_b \mathcal{D}_{CO2}} \qquad Re = \frac{\rho_b \left|\boldsymbol{u}\right| \bar{D}_{bub}}{\mu_b}, \tag{16.3}$$

where $\bar{D}_{bub}$ is the *mean* bubble diameter in the cell in question, and $\boldsymbol{u}$ is the local fluid velocity. For nucleation, the Reynolds number is based on the diameter of the smallest bubble class, i.e. D_1.

As the turbulent dissipation rate for the system considered typically is of the order 0.05 $\mathrm{m}^2/\mathrm{s}^3$, microbubbles considered here are typically larger than the resulting fine scale turbulence, scaling as $(\nu_b^3/\epsilon)^{1/4}$. Hence, coalescence is assumed to be governed by inertial subrange turbulence, i.e. coalescence is assumed be given by the coalescence kernel of Luo [79], collision frequencies given by equation 14.58 and collision probabilities by equation 14.64.

As a computational cell becomes filled with microbubbles, the molecular CO_2 sees a smaller effective volume in which it can be dissolved. In order to model this behaviour, the (effective) bulk concentration C_{b,CO_2} is written as

$$C_{b,CO_2} = \frac{C_{CO_2}}{1 - \alpha_{PBM}}, \tag{16.4}$$

where $C_{CO_2} = \rho X_{CO_2}$ is the concentration of dissolved CO_2 (governed by equation 14.87) and α_{PBM} is the local volume fraction of microscopic bubbles.

As seen in Appendix A, the default CSF-formulation for surface tension has considerable numerical challenges, especially for under-resolved bubbles, typically arising in the current model as microbubbles transition to macroscopic ones. One possible improvement is the continuum surface stress model (CSS) introduced in FLUENT 14 (released Q1-2012), which does not require an explicit calculation of surface curvature. It is thus expected to perform *more* physically in under-resolved regions [2]. Hence, the CSS-model is used for the following simulations.

Although improving results (and allowing for variable surface tension), the CSS-model is still prone to spurious velocities on (under-resolved) interfaces, resulting in an unphysical detachment of isolated, under-resolved, bubbles. In order to avoid unphysical detachment, a limiter of the form

$$\gamma_{bath,gas}\,(\mathrm{N/m}) = \begin{cases} 0.1 & \text{if} \quad \alpha_{gas}\,(x) \quad \text{and} \quad \alpha_{gas}\,(x \pm \Delta x) > 0.01 \\ 0.1\alpha_{gas}\,(x) & \text{otherwise,} \end{cases} \tag{16.5}$$

is introduced, where $\alpha_{gas}\,(x)$ is the local phase fraction of resolved (macroscopic) gas and $\alpha_{gas}\,(x \pm \Delta x)$ is the phase fraction of (any) neighbouring cell, i.e., the full value of the

surface tension is applied only for pairs of (neighbouring) cells with phase fractions above 0.01, that is, the interface must span at least two computational cells, as sketched in figure 16.4.

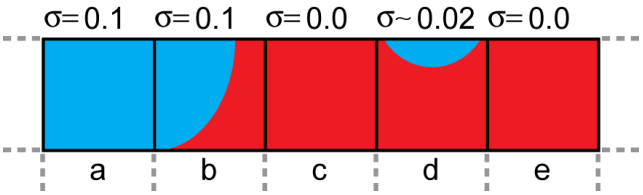

Figure 16.4: Sketch of surface tension limiter. Cells a and b not limited as they both have a neighbouring cell with finite phase fraction, while cell d has no neighbours, resulting in a lower (numerical) surface tension. Cells c and d contain no interface and thus have no surface tension.

Due to the wettable properties of the cathode (cf. Part II, section 9.1) and the resulting lack of a (significant) bath-metal interface in the interpolar region, phenomena related to the metal pad are neglected in all of the following simulations.

16.2.2 Solver settings

All of the following simulations are performed using the 2D, double precision, pressure based, transient solver. The five microbubble classes, discretized using the QUICK scheme, and the electrical potential, discretized by a Power-law scheme, are treated as UDS-equations (cf. section 14.8). Momentum equations are discretized using the QUICK scheme, while the PRESTO!-scheme is used for pressure. Turbulence is discretized using a first order upwind-scheme. Pressure-velocity coupling is performed using the PISO-scheme, with default corrections for skewness-neighbour coupling. Gradients are calculated based on a Green-Gauss cell based scheme and the transient formulation is first order implicit, with a constant time step of 0.002 s, in order to keep the global Courant number below unity thoughout the simulation.

The macroscopic multiphase flow is treated with an explicit two-phase VOF method, with an implicit body force formulation for enhanced convergence, discretized using the PLIC (GEO-reconstruct)-scheme. Turbulence is modelled with the realizable k-ϵ-model with enhanced wall functions.

The flexible AMG-cycle is employed for the pressure correction for increased stability and the V-cycle is used for the UDS equations for increased convergence rate. All other cycles are left at default values.

Residuals and under-relaxation factors are summarized in table 16.2

Table 16.2: Under-relaxation factors and residuals for validation studies

URF		Residual	
Equation	Value	Equation	Value
p	0.3	Continuity	$1 \cdot 10^{-4}$
ρ	0.5		
$\lvert \boldsymbol{f}_b \rvert$	0.5		
ρu	0.5	u	$1 \cdot 10^{-3}$
ρv	0.5	v	$1 \cdot 10^{-3}$
k	0.5	k	$1 \cdot 10^{-3}$
ϵ	0.5	ϵ	$1 \cdot 10^{-3}$
μ_t	0.7		
X_{CO_2}	0.8	X_{CO_2}	$1 \cdot 10^{-6}$
n_1	0.8	n_1	$1 \cdot 10^{-6}$
n_2	0.8	n_2	$1 \cdot 10^{-6}$
n_3	0.8	n_3	$1 \cdot 10^{-6}$
n_4	0.8	n_4	$1 \cdot 10^{-6}$
n_5	0.8	n_5	$1 \cdot 10^{-6}$
ϕ	1.0	ϕ	$1 \cdot 10^{-12}$
γ_{bg}	0.7		

16.2.3 Boundary and initial conditions

The boundary conditions applied to the system considered are shown in figure 16.5.

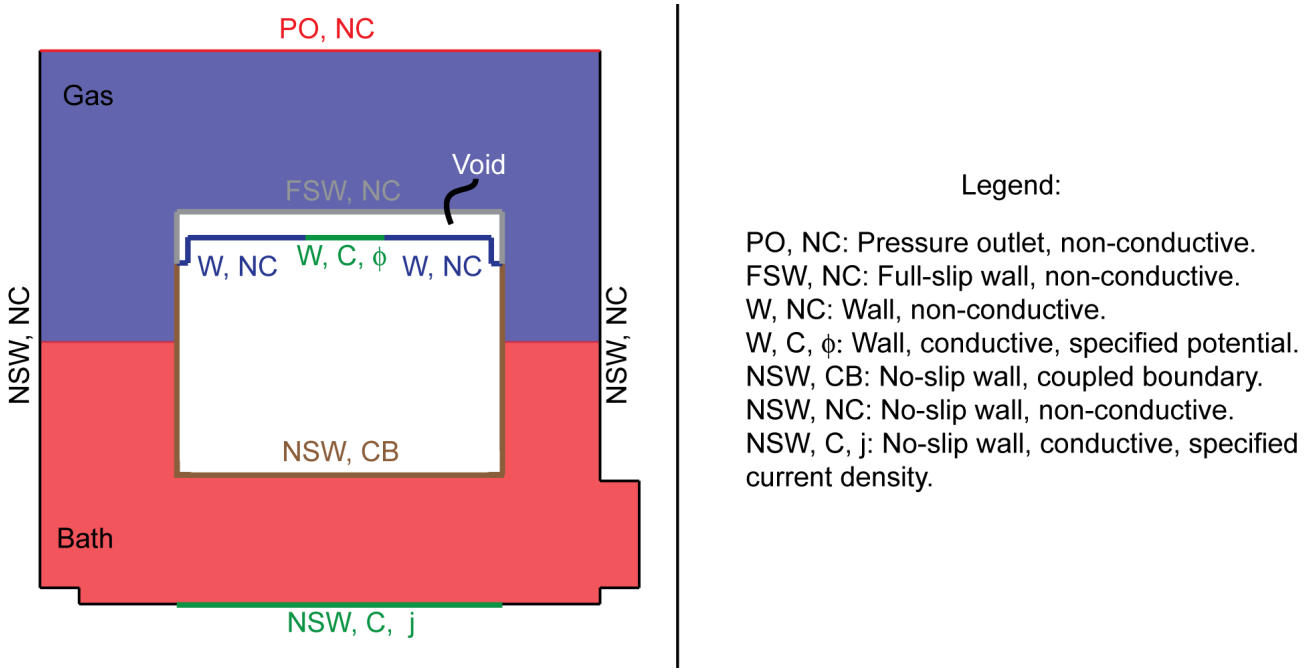

Figure 16.5: Schematic of boundary conditions used for preliminary 2D studies.

A zero reference potential is specified to the anode connection (W,C,ϕ in the above figure), whereas a *uniform* current density corresponding to experimental settings is specified to the active cathode region (surface denoted NSW,C,j in figure 16.5). A zero flux boundary condition for the remaining UDS equations is used on all surfaces, for simplicity, as generation and evolution is handled by means of volumetric source and sink terms.

The pressure outlet is set to zero gauge, with a backflow volume fraction of gas equal to unity.

Initial simulations, cf. [33], indicate that significant amounts of CO_2 can be dissolved in the bath. Consequently, long simulation times (t>200 s) are required in order to achieve steady bubble production, if the system is initialized from zero. Hence, in order to enable steady bubble production within reasonable simulation times, the concentration field is initialized to $10C_{s,CO_2}$ for all of the following simulations. Remaining UDS and flow fields are initialized to zero. Initial bath and gas volume fractions (cf. figure 16.2) are specified using the patching command in ANSYS FLUENT, with 6 cm initial bath height, relative to the anode bottom. Finally, the tilting of the system is simulated by specifying the components of $\boldsymbol{g}$ accordingly.

16.3 Factorial design and results

As seen in section 14.9, the proposed model involves several classes of parameters which exact value are unknown. Hence a parametric study must be performed in order to determine a *set* of parameters which adequately reproduce the experimental data given in Part II of this thesis, while at the same time being within the expected ranges presented in Part I. In addition to determining a set of adequate parameters, the sensitivity of a given parameter is of interest, as this gives an indication of how robust the proposed model is.

In the following, the parametric study and sensitivity analysis is combined through a factorial design, as described by Montgomery [82]. In a factorial design, each of the m parameters considered are investigated at n-levels, resulting in a set of n^m experiments (or simulations in this case) from which the influence of each parameter as well as their joint effect can be determined. For simplicity, the parameters in the following factorial design are restricted to two levels, designated "+" and "-", i.e. each parameter is allowed to take a high and a low level. Results are thus restricted to a linear response to a given factor.

As an example, assume that two factors, A and B, are considered. In order to span all combinations, a total of 2^2 experiments are required. The setup and response for each of the experiments is given in table 16.3.

Table 16.3: Summary of factors and results for factorial design example. The response is in this case the outcome of the given experiment.

Experiment	Factor		Response
(#)	A	B	(-)
1	-	-	20
2	+	-	35
3	-	+	17
4	+	+	29

Using the methodology described in Montgomery [82], chapter 6, the magnitude (% contribution) and direction (sign) of each of the factors can be computed. For the responses given in table 16.3, the result of the factorial design is given in table 16.4.

Table 16.4: Sign and percent contribution for the factors shown in table 16.3.

Factor	A	B	AB
Sign	+	-	-
%	89.0	10.0	1.0

As seen from table 16.4, factor A has the strongest influence on the response. The *positive* sign indicates that an increase in factor A, increases the response, as expected when

comparing experiments 1 and 2 in table 16.3. Correspondingly, the influence of factor B is *negative*, indicating that an increase in B decreases the response, although to a smaller extent than factor A. The small contribution from AB suggests that the interaction between A and B is negligible compared to the influence of the main factors, i.e. A and B alone.

The analysis presented in the following sections will be based upon the three main features of the global voltage fluctuations, namely the frequency, signal domain and mean voltage. In order to capture the spread in frequencies, both 1st and 2nd most dominating frequencies of the signal, f_v^i, are considered. In addition, due to the close correlation between gas coverage and voltage fluctuations, the 1st and 2nd most dominating frequencies in the gas coverage fraction, f_g^i are included in the analysis. Hence, a full factorial design for a given set of properties will consist of four frequency- and one amplitude and mean voltage replicate.

In order to ensure that results are representative, simulations are run for 120 s flowtime, where the first 80 s are rejected in order to avoid any start-up effects. Thus 20 full bubble cycles are analysed for each case, assuming a frequency of 0.5Hz. As for the lab-scale experiments, the signal domain, ΔU, is calculated as $\Delta U = 4\Sigma_U$, while frequencies are calculated based on a FFT of the signal segment considered. Finally, the mean voltage is calculated as the arithmetic mean over the given segment.

The high and low levels of the factors used in the following simulations are chosen based on the corresponding ranges of values reported in the literature (cf. Part I), and thus reflect the level of uncertainty related to this parameter.

16.3.1 Class 1: Pore properties

Factors related to pore properties as well as levels considered are summarized in table 16.5. The levels of the pore area chosen assuming a mean pore diameter of 80 μm (low) and 120 μm (high), while the high level of $\rho_{p,max}$ corresponds to the typical porosity given in Grjotheim et al. [46]. The low estimate of the minimum pore density corresponds to the lowest value obtained from figure 14.8, i.e. 2%.

Table 16.5: Factors and levels related to pore properties.

Factor	Coded name	High level	Low level	Unit
Minimum pore density, $\rho_{p,min}$	A	0.07	0.02	-
Maximum pore density, $\rho_{p,max}$	B	0.22	0.17	-
Pore area, A_{p0}	C	$1.13{\cdot}10^{-8}$	$5.03{\cdot}10^{-9}$	m^2

A summary of the factor levels as well as the resulting signal properties obtained from each of the eight cases simulated in this 2^3 experiment are given in table 16.6.

The estimated effect of each of the factors are shown in tables 16.7, 16.8 and 16.9.

Table 16.6: Summary of factors, frequencies, signal domain and mean voltage obtained when varying pore-properties.

Name	Factor			Frequency replicate				Signal domain	Mean voltage
	A	B	C	f_v^1 (Hz)	f_v^2 (Hz)	f_g^1 (Hz)	f_g^2 (Hz)	ΔU (V)	$\bar{U}$ (V)
Case 1	-	-	-	0.49	0.51	0.49	0.51	0.24	1.37
Case 2	+	-	-	0.47	0.57	0.47	0.61	0.27	1.38
Case 3	-	+	-	0.47	0.41	0.41	0.47	0.22	1.37
Case 4	+	+	-	0.70	0.61	0.70	0.74	0.28	1.39
Case 5	-	-	+	0.25	0.20	0.20	0.23	0.16	1.34
Case 6	+	-	+	0.27	0.31	0.28	0.31	0.22	1.35
Case 7	-	+	+	0.27	0.33	0.27	0.33	0.18	1.35
Case 8	+	+	+	0.33	0.43	0.33	0.25	0.18	1.36

Table 16.7: Sign and percent contribution on frequencies for each of the factors shown in table 16.5.

Factor	A	B	C	AB	AC	BC	ABC
Sign	+	+	-	+	-	+	-
%	11.22	3.93	75.15	2.43	2.17	0.04	5.05

Table 16.8: Sign and percent contribution on amplitudes for each of the factors shown in table 16.5.

Factor	A	B	C	AB	AC	BC	ABC
Sign	+	-	-	-	-	-	-
%	21.14	0.80	68.97	0.33	0.32	0.26	8.18

Table 16.9: Sign and percent contribution on mean voltage for each of the factors shown in table 16.5.

Factor	A	B	C	AB	AC	BC	ABC
Sign	+	+	-	+	+	+	+
%	16.71	1.45	80.95	0.00	0.87	0.01	0.01

Discussion

As seen from table 16.6, calculated frequencies correspond well to that obtained in the corresponding experiments, $f^1_{v,exp} = 0.29$. As expected from the nature of the voltage fluctuations, there is a close correspondence to simulated variations in gas coverage. Figure 16.6 shows sample voltage and gas coverage curves for cases 2 and 6, as well of the resulting FFT spectra for each of the cases.

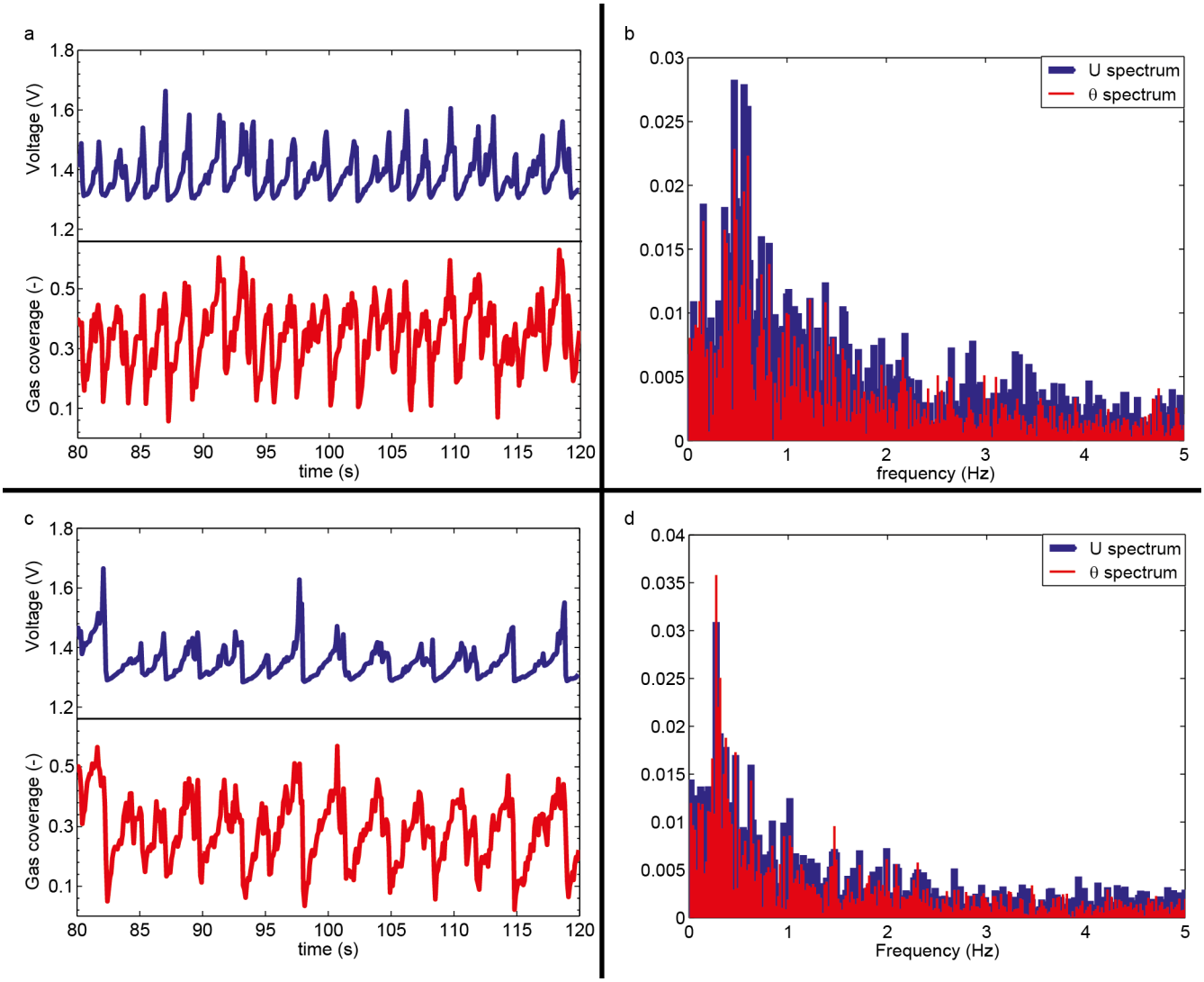

Figure 16.6: Voltage, U, (blue) and gas coverage (of anode bottom), θ_{cov}, (red) variations for different pore properties, case 2 (a) and case 6 (c) and corresponding spectra (b) and (d).

Figure 16.8 shows the evolution of anodic bubbles and resulting redistribution of current

density for a single voltage cycle shown in figure 16.7.

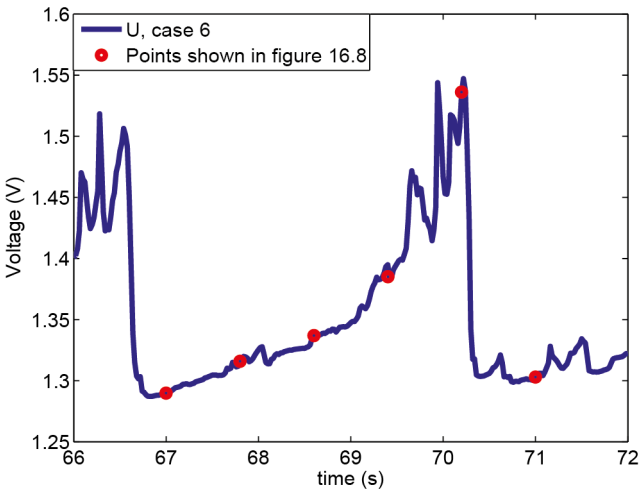

Figure 16.7: Details of single voltage cycle, case 6. Red circles indicate times depicted in figure 16.8.

Figure 16.8 confirms the close relation between high voltages and large gas coverage fractions. As seen from the figure, macroscopic bubbles form at certain cites and block the current density in this region. The local current density *around* the bubbles is however significant, up to three times greater than the nominal current density of 8000 A/m^2 (frame t=70.20 s).

The behaviour depicted in figure 16.8 is typical for all simulations; macroscopic bubbles form at regions where the local concentration of microscopic bubbles is high (due to local flow and pore conditions) and grow by engulfing microbubbles in their proximity. Once macroscopic bubbles have reached a sufficient size, they are set in motion by buoyancy, growing further by means of coalescence, before being released at the anode edge. As the creation of a macroscopic bubble and the following motion of the bath alters the local flow conditions beneath the anode, the next bubble cycle can be initiated at different positions, cf. figure 16.8 frames t=67.00 s and t=71.00 s, thus allowing for shorter or longer paths required for a bubble to escape, resulting in variable bubble residence times under the anode, as seen in figure 16.6 and observed in experiments (cf. figure 9.7).

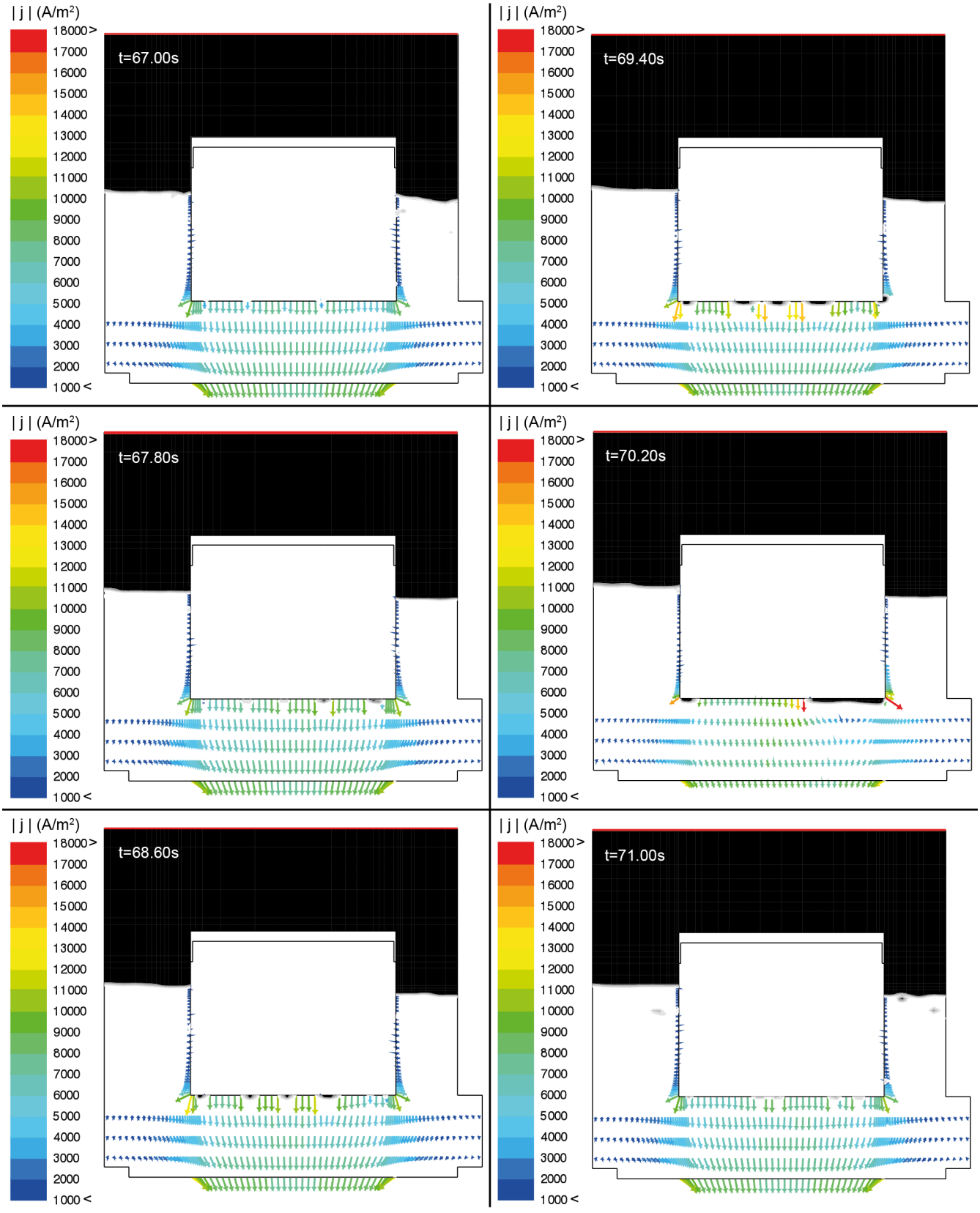

Figure 16.8: Sample evolution of anodic bubbles (greyscale) and redistribution of current density, coloured by magnitude, for voltage cycle shown in figure 16.7.

Table 16.6 indicates that the signal domain is slightly higher than that obtained in experiments, $\Delta U_{exp} = 0.11 - 0.16$ V. The discrepancy between simulations and experiments is believed to be a 2D-effect, arising due to the large redistribution of current required as the bubble rounds the anode corner, where the current density is high. Furthermore, 2D bubbles necessarily span (infinitely) into the paper plane, thus yielding larger regions inactive than that expected in 3D. Finally, as the anode is modelled with sharp corners, this is expected to increase the bandwidth compared to experiments, where anode corners were (gradually) rounded.

As seen from table 16.6, it is evident that the mean voltage predicted by the simulations is significantly lower than that measured in experiments, $\bar{U}_{exp} = 3.26$ V. This is however as expected, as the current simulations consider only voltage losses within the anode and the bubble containing bath, while the voltage obtained in the experiments was measured between the anode connector rod and the current collector at the cathode and thus includes additional sources of electrical resistance not considered in the simulations. Considering the main contributions for the given setup, i.e. the reversible voltage (approximately 1.2 V, constant), anodic activation potential (approximately 0.5 V, close to constant) and cathodic losses (approximately 0.3 V, Ohmic), the total mean simulated voltage is of order 3.4V, which is close to that measured.

Evidently, the distribution of pores alters the detachment behaviour of the bubbles. The largest variation is found in frequencies and amplitudes, while the mean voltage is relatively insensitive to the pore properties, as expected, as the main contribution to the *mean* voltage is due to the conductivity of the (bubble free) bath. Frequencies show a positive response to increasing porosities (factors A and B), as this increases the number of active pores and thus potential nucleation sites. Similarly, increasing the mean pore diameter (factor C) *reduces* the overall frequencies in the signal, as this yields *less* active pores for a given porosity. For the simulations presented in table 16.6, the pore diameter has the strongest influence on the results. The strong influence of the pore diameter is partially due to the (relatively) large difference between high and low levels. The pore diameter also has the strongest influence upon the domain of the signal, for the same reasons as for the frequencies.

16.3.2 Class 2: Bath properties

Following the experiments described in Part II, the spent bath was analysed, showing that it was saturated with alumina. As seen in Thonstad et al. [116], this influences the properties of the bath, in particular viscosity (increased by increased alumina content) and wetting properties (increased wetting with increased alumina content). In addition, as shown by Numata and Bockris [85], the solubility of CO_2 increases with increasing alumina content. Although knowledge of alumina levels *during* the electrolysis experiments is unknown, the possibility of alumina saturation and its influence on the global flow features should be considered. Factors related to bath properties as well as levels considered are summarized in table 16.10. High (default) values are chosen in such a way that properties reflect elevated alumina content, while low values correspond to low alumina content.

Table 16.10: Factors and levels related to bath properties.

Factor	Coded name	High level	Low level	Unit
Bath viscosity, μ_{bath}	A	$3.30{\cdot}10^{-3}$	$2.69{\cdot}10^{-3}$	kg/m·s
Contact angle, $\theta_{gas,bath}$	B	110	90	$^\circ$
CO_2 saturation conc., C_{s,CO_2}	C	0.4	0.2	kg/m^3
CO_2 diffusivity, $\mathcal{D}_{CO2}$	D	$5 \cdot 10^{-10}$	$1 \cdot 10^{-10}$	m^2/s

A summary of the factor levels as well as the frequencies, signal domain and mean voltages obtained from each of the four cases simulated in this 2^4 experiment are given in table 16.11.

The estimated effect of each of the factors are shown in tables 16.12, 16.13 and 16.14.

Table 16.11: Summary of factors, frequencies, the signal domain and mean voltage obtained when varying bath properties.

Name	Factor				Frequency replicate				Signal domain	Mean voltage
	A	B	C	D	f_v^1 (Hz)	f_v^2 (Hz)	f_g^1 (Hz)	f_g^2 (Hz)	ΔU (V)	$\bar{U}$ (V)
Case 1	-	-	-	-	0.25	0.33	0.25	0.33	0.16	1.34
Case 2	+	-	-	-	0.27	0.14	0.14	0.27	0.15	1.33
Case 3	-	+	-	-	0.18	0.20	0.18	0.20	0.16	1.34
Case 4	+	+	-	-	0.20	0.18	0.20	0.16	0.23	1.35
Case 5	-	-	+	-	0.16	0.27	0.27	0.25	0.22	1.33
Case 6	+	-	+	-	0.25	0.16	0.25	0.16	0.14	1.33
Case 7	-	+	+	-	0.20	0.14	0.20	0.14	0.15	1.33
Case 8	+	+	+	-	0.20	0.18	0.20	0.18	0.20	1.34
Case 9	-	-	-	+	0.76	0.35	0.76	0.82	0.22	1.37
Case 10	+	-	-	+	0.68	0.72	0.59	0.68	0.22	1.37
Case 11	-	+	-	+	0.53	0.57	0.57	0.59	0.22	1.37
Case 12	+	+	-	+	0.47	0.61	0.61	0.49	0.24	1.37
Case 13	-	-	+	+	0.64	0.76	0.64	0.57	0.20	1.37
Case 14	+	-	+	+	0.61	0.59	0.61	0.59	0.22	1.37
Case 15	-	+	+	+	0.53	0.63	0.53	0.41	0.22	1.37
Case 16	+	+	+	+	0.47	0.41	0.41	0.47	0.22	1.37

Table 16.12: Sign and percent contribution on frequencies for each of the factors shown in table 16.10.

Factor	A	B	AB	C	AC	BC	ABC	D
Sign	-	-	+	-	+	+	+	+
%	0.75	5.69	0.10	0.92	0.02	0.00	0.02	90.50
Factor	AD	BD	ABD	CD	ACD	BCD	ABCD	
Sign	-	-	-	-	-	-	+	
%	0.03	0.92	0.31	0.28	0.38	0.08	0.00	

Table 16.13: Sign and percent contribution on amplitudes for each of the factors shown in table 16.10.

Factor	A	B	AB	C	AC	BC	ABC	D
Sign	+	+	+	-	-	-	+	+
%	2.03	3.47	16.63	0.94	2.78	3.85	0.04	47.93
Factor	AD	BD	ABD	CD	ACD	BCD	ABCD	
Sign	+	-	-	-	+	+	-	
%	0.11	0.40	13.45	0.51	2.63	2.36	2.87	

Table 16.14: Sign and percent contribution on mean voltage for each of the factors shown in table 16.10.

Factor	A	B	AB	C	AC	BC	ABC	D
Sign	+	+	+	-	+	+	+	+
%	0.72	0.96	0.81	2.11	0.06	0.01	0.00	92.82
Factor	AD	BD	ABD	CD	ACD	BCD	ABCD	
Sign	+	+	-	+	+	-	+	
%	0.04	1.56	0.58	0.15	0.00	0.00	0.17	

Discussion

The properties listed in table 16.11 are comparable to those given in table 16.6, although greater variations are observed, in particular with respect to frequencies, with a factor of six when comparing the smallest and largest calculated values. This is mainly due to the large influence of the diffusivity of CO_2, factor D, which is closely coupled to nucleation and mass transfer rates and thus to the following formation and evolution of macroscopic bubbles. As seen from table 16.11, increasing diffusivities yield higher bubble departure rates.

Both the bath viscosity (factor A) and saturation concentration (factor C) have a negative influence upon the frequencies, as these factors decrease the driving force for mass transfer through the Sherwood number (scaling as $\mu_b^{-1/6}$) and the concentration difference ΔC_{CO_2}, respectively. Furthermore, increased bath viscosity increases the viscous drag on macroscopic bubbles, thus reducing the departure rates and corresponding frequencies in voltage and gas coverage.

In addition to the diffusivity, the contact angle (factor B), has a significant influence upon the resulting frequencies[1]. Table 16.11 shows that increasing contact angles (measured in the *gas* phase), i.e. increased bath wetting, *decreases* the overall frequencies. Although increased wetting by the bath is expected to facilitate bubble detachment, the simulations shown in table 16.11 indicate that the dynamic setting is different. Figure 16.9 shows the mean velocity of a 20ml gas bubble rising in the bath under an inclined surface (cf. Zhang et al. [147] for corresponding setup) as in the preceding simulations, for various values of the contact angle. It should be noted that data shown in figure 16.9 is for a pure bubble rising from rest due to gravity, and no additional phenomena (i.e. mass transfer, PBM, etc.) are included in order to isolate the effect of the contact angle. Evidently, increasing contact angles yield lower bubble velocities, thus resulting in a negative influence as of table 16.12.

Equivalently to the frequencies, increased diffusivities increase the bandwidth of the signal. Significant coupling between the various factors is however observed, indicating that the

[1] In particular considering the (relatively) small difference between high and low levels

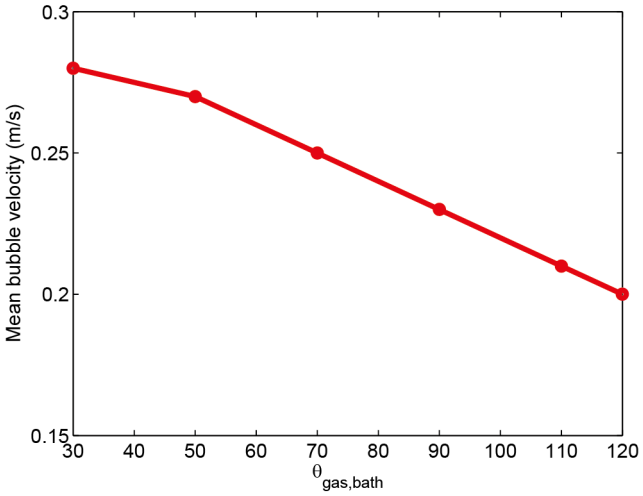

Figure 16.9: Influence of contact angle, $\theta_{gas,bath}$, (measured in gas phase) on bubble velocity.

nature of the amplitudes of the signal is more complex than that of the frequencies, which is fully dominated by the main factors.

16.3.3 Class 3: Transfer properties

The final class of free parameters is related to the transfer properties of the proposed model, i.e. mass transfer and the coalescence kernel. Mass transfer is likely to be over predicted in the current model as the Reynolds number is based on the local (mixture) velocity, thus assuming that microbubbles are at rest in the fluid. Although this is close to what expected from experiments (cf. Xue and Øye [139]), the cell averaged velocity used to determine the local Reynolds number is higher than the typical velocities experienced by the bubbles, which typically reside deep within the boundary layer, cf. figure 14.18. In addition, local (unphysical) velocities arising due to surface tension (cf. Appendix A) contribute to further over prediction of local velocities. For simplicity, the flow dependent part of the Sherwood number is considered at a level corresponding to a twofold reduction, compared to the default case, thus simulating a fourfold reduction of the local Reynolds number.

The coalescence kernel is also likely to be over predicted by the default kernel as bubble streamlines can deviate significantly from those of the fluid. In addition, breakup of microbubbles is neglected in the current study. Again, for simplicity, the low value of the coalescence kernel is taken to be half of the default kernel, corresponding to a reduction of approximately 30% of the default collision cross section.

Another factor which is of importance is the detachment diameter of nucleated bubbles (cf. Jones et al. [58], Kloucek and Romerio [66] and Kiss et al. [61]), D_1, here treated as

a constant based on the experimental observations of Xue and Øye [139]. The detachment diameter enters in the nucleation frequency analogously to the pore density and saturation concentration. Hence, its influence is expected to be of the same order as these parameters. Furthermore, the detachment diameter determines the size distribution of the PBM, thus altering coalescence and growth rates accordingly. The low value of D_1 is taken to be the lower band of that which was observed by Xue and Øye, 0.4 mm, while the high value is the default, mean, value, i.e. 0.5 mm.

Factors related to transport properties as well as levels considered are summarized in table 16.15.

Table 16.15: Factors and levels related to transfer properties.

Factor	Coded name	High level	Low level	Unit
Mass transfer, Sh	A	$2.0 + 0.6\sqrt{Re}Sc^{1/3}$	$2.0 + 0.3\sqrt{Re}Sc^{1/3}$	-
Coalesence kernel, Γ_{ij}	B	Γ^{IST}	$0.5\Gamma^{IST}$	m^3/s
Detachment diameter, D_1	C	$0.5{\cdot}10^{-3}$	$0.4{\cdot}10^{-3}$	m

A summary of the factor levels and resulting properties are given in table 16.16. The estimated effect of each of the factors on frequencies and amplitudes are shown in tables 16.17, 16.18 and 16.19.

Table 16.16: Summary of factors, frequencies, signal domain and amplitudes obtained when varying transfer properties.

Name	Factor			Frequency replicate				Signal domain	Mean voltage
	A	B	C	f_v^1 (Hz)	f_v^2 (Hz)	f_g^1 (Hz)	f_g^2 (Hz)	ΔU (V)	$\bar{U}$ (V)
Case 1	-	-	-	0.27	0.14	0.27	0.33	0.27	1.35
Case 2	+	-	-	0.57	0.53	0.57	0.53	0.23	1.37
Case 3	-	+	-	0.20	0.21	0.25	0.20	0.19	1.34
Case 4	+	+	-	0.45	0.43	0.45	0.43	0.21	1.36
Case 5	-	-	+	0.29	0.35	0.29	0.35	0.19	1.36
Case 6	+	-	+	0.53	0.49	0.49	0.53	0.21	1.38
Case 7	-	+	+	0.29	0.31	0.29	0.31	0.21	1.35
Case 8	+	+	+	0.47	0.41	0.41	0.47	0.22	1.37

Table 16.17: Sign and percent contribution on frequencies for factors shown in table 16.15.

Factor	A	B	C	AB	AC	BC	ABC
Sign	+	-	+	-	-	+	+
%	85.01	6.62	1.66	1.65	4.60	0.41	0.05

Table 16.18: Sign and percent contribution on amplitudes for factors shown in table 16.15.

Factor	A	B	C	AB	AC	BC	ABC
Sign	+	-	-	+	+	+	-
%	0.65	10.57	12.01	8.13	7.80	41.46	19.37

Table 16.19: Sign and percent contribution on mean voltage for factors shown in table 16.15.

Factor	A	B	C	AB	AC	BC	ABC
Sign	+	-	+	+	+	+	+
%	48.97	22.65	26.69	0.09	0.54	0.92	0.12

Discussion

Simulated values obtained for different transfer properties correspond to those obtained for pore- and bath properties. As seen from table 16.17, the frequencies are most strongly influenced by the Sherwood number, comparable to the influence of the diffusivity of CO_2, as expected, as both factors contribute to the same physical process. The value of the detachment diameter propagates throughout the whole PBM, finally resulting in the ghost class, and thus determines the smallest possible volume fraction of macroscopic gas. Larger detachment diameters thus result in larger (initial) macroscopic phase fractions and thus initially greater buoyancy and increased departure rates.

The negative influence of the coalescence kernel appears counter intuitive, as one would expect increased coalescence rates to enhance the production of macroscopic bubbles and thus increase the corresponding frequencies. In this case, however, coalescence cannot be considered alone, as the evolution of bubbles in addition is strongly coupled to growth due to mass transfer. Consider two bubbles of volume V_i. If coalescence dominates, the two bubbles will coalesce into a single bubble of volume $2V_i$ before any (significant) mass transfer occurs. On the other hand, if mass transfer dominates, and sufficient amounts of supersaturated gas exists in the proximity of the bubbles, both bubbles will grow so that *each* attains a volume $2V_i$. As collision frequencies increase with increasing particle size (cf. table 14.1), a coalescence event now becomes more likely, now resulting in a single bubble with volume $4V_i$. Hence, reducing the coalescence kernel allows for additional mass transfer for the smallest microbubbles and thus a faster evolution towards the macroscopic phase, thus increasing the overall frequencies. Consequently, simulations with large coalescence

kernels should, on average, show elevated concentrations of dissolved CO_2, as less gas is being transferred to the microbubbles. Figure 16.10 confirms that this indeed is the case.

The amplitude of the signal is not dominated by a single factor. In fact, the two largest influences are due to coupled effects, again illustrating the complexity behind the amplitude of the voltage fluctuations.

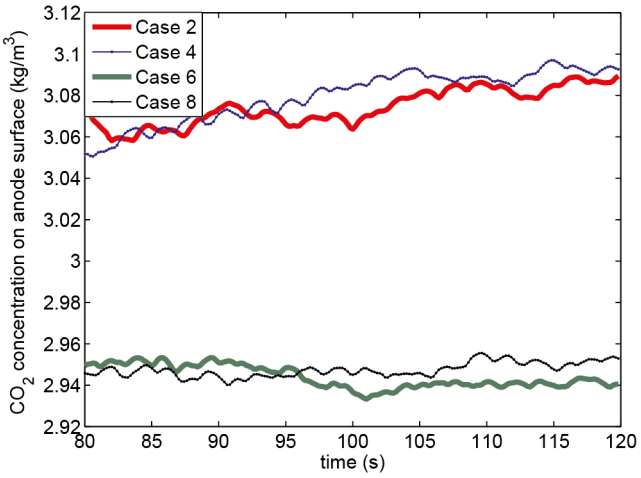

Figure 16.10: Influence of coalescence kernel on concentration levels. Thick lines (red and green) show mean CO_2 concentrations on anode surface for low values of the coalescence kernel, while thin lines (blue and black) indicate levels at high values of the kernel. Case names correspond to those given in table 16.16.

16.3.4 Time dependence

A statistically steady state is (approximately) obtained for all of the current simulations, based on integral mean values of selected parameters,

$$\bar{\psi} = \frac{1}{T}\int_0^T \psi(t)dt, \tag{16.6}$$

i.e. the time average of the quantity ψ over the simulation time T. Four properties are considered; velocities in right, v_r, and left, v_l, channels (at position $x = \pm 60$mm and $y = 35$ mm), the concentration of dissolved CO_2 *on the anode surface*, C_{CO2}, and the cell voltage U. Figure 16.11 shows the integral mean and arithmetic averages[2], of these parameters for case 7 for each of the previous factorial designs.

As seen from figure 16.11, a statistically steady state is reached after approximately 80 s when considering voltage variations and velocities. Mean concentrations on the anode

[2]As the integral mean value approaches this value at a statistically steady state.

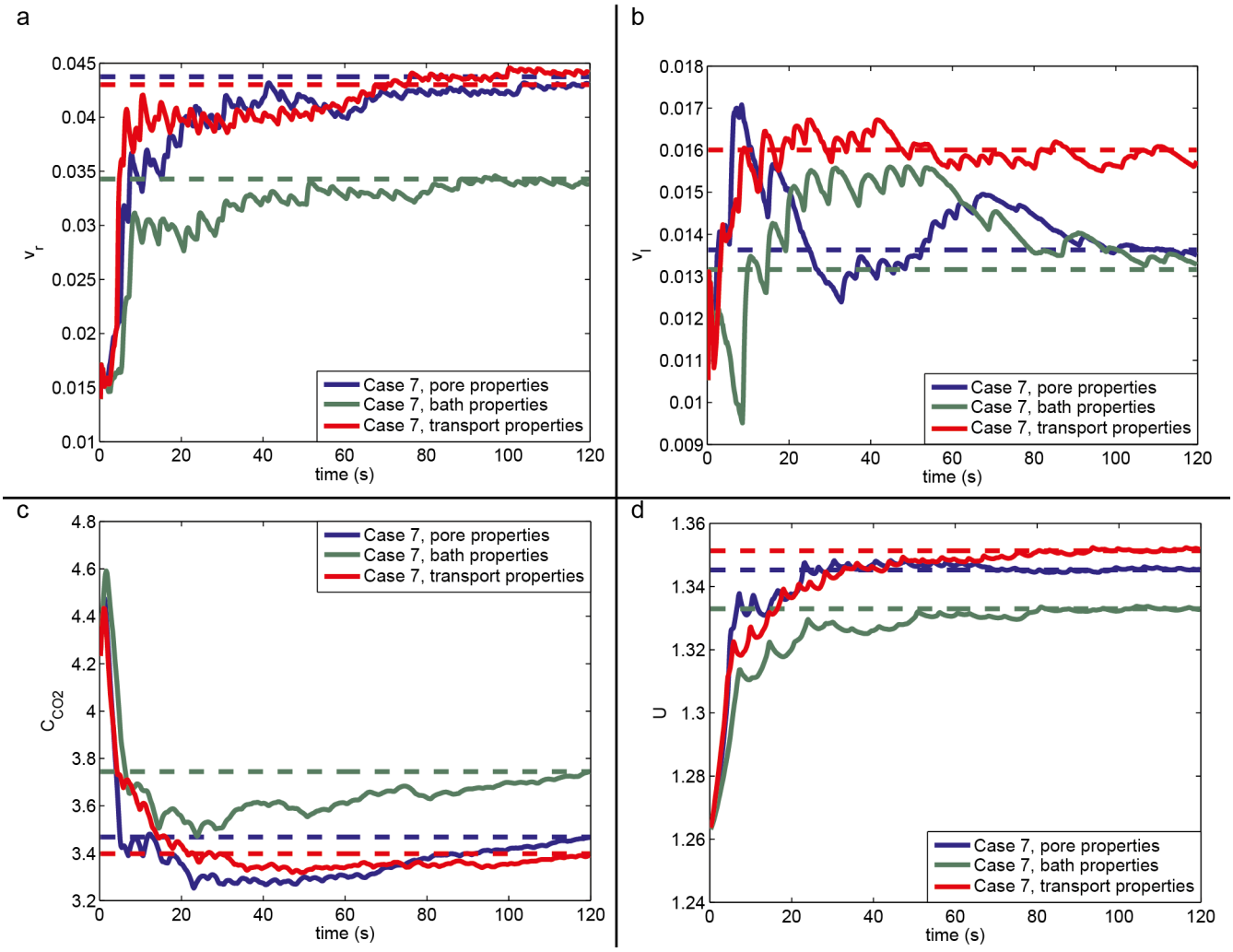

Figure 16.11: Integral mean values (solid lines) and arithmetic averages (dashed lines) for velocity in right channel (v_r) ,(a), velocity in left channel (v_l), (b), mean CO_2 concentration on anode surface (C_{CO2}), (c), and voltage (U), (d), for three selected cases.

surface have not reached a fully steady state for the time interval considered (80-120 s), values increasing steadily, although at a rate slower than that observed at earlier stages. Increased concentrations at the anode surface will enhance the driving force for mass transfer, ΔC_{CO_2}, comparable to the influence of the saturation concentration (cf. table 16.11). Hence, frequencies presented in previous sections are expected to increase (slightly) as the concentrations reach a statistically steady state.

16.3.5 Grid dependence

The macroscopic gas bubbles generated in the current simulations are resolved only to a minimal level; typically each bubble consists only of 6-12 cells with phase fraction unity. As a result, phenomena such as wall adhesion are resolved only to a minimal level. Also, as seen in Appendix A, the action of the surface tension is also greatly influenced by the mesh density. Hence, a grid dependency study is required in order to determine if this is critical for the *global* properties of the voltage signal.

For a multiscale approach such as the one presented here, mesh refinement is not straight forward as sub-grid models necessarily are inherently coupled to the grid, as this determines whether an entity is sub-grid or not. Some grid dependence is thus *expected* and the following simulations are performed to determine how sensitive results are to grid resolution, compared to other factors.

Case 7 of the pore property study is considered for reference and the mesh in the proximity of the anode is refined on three levels, with properties summarized in table 16.20.

Table 16.20: Mesh size in proximity of anode. Case (+,+) is the original mesh.

Case	Δx (mm)	Δy (mm)
(+,+)	3	1
(-,+)	1.5	1
(+,-)	3	0.5
(-,-)	1.5	0.5

Figure 16.12 shows sample voltage curves for each of the cases given in the above table. Details regarding frequencies, amplitudes and mean voltages are given in table 16.21.

As expected, the resolution influences both local and global features of the voltage signal. However, as seen from table 16.21, the difference between the various resolutions is not as significant as one might expect, *averaged* properties differing by less than 10% for cases (-,-) and (-,+). Case (+,-) shows the greatest difference from the default case, averaged frequencies being 20% lower. Considering the mesh quality, this particular case is the worst of the four cases considered, due to the considerable aspect ratio of the cells close to the anode, a critical issue for successful VOF-simulations.

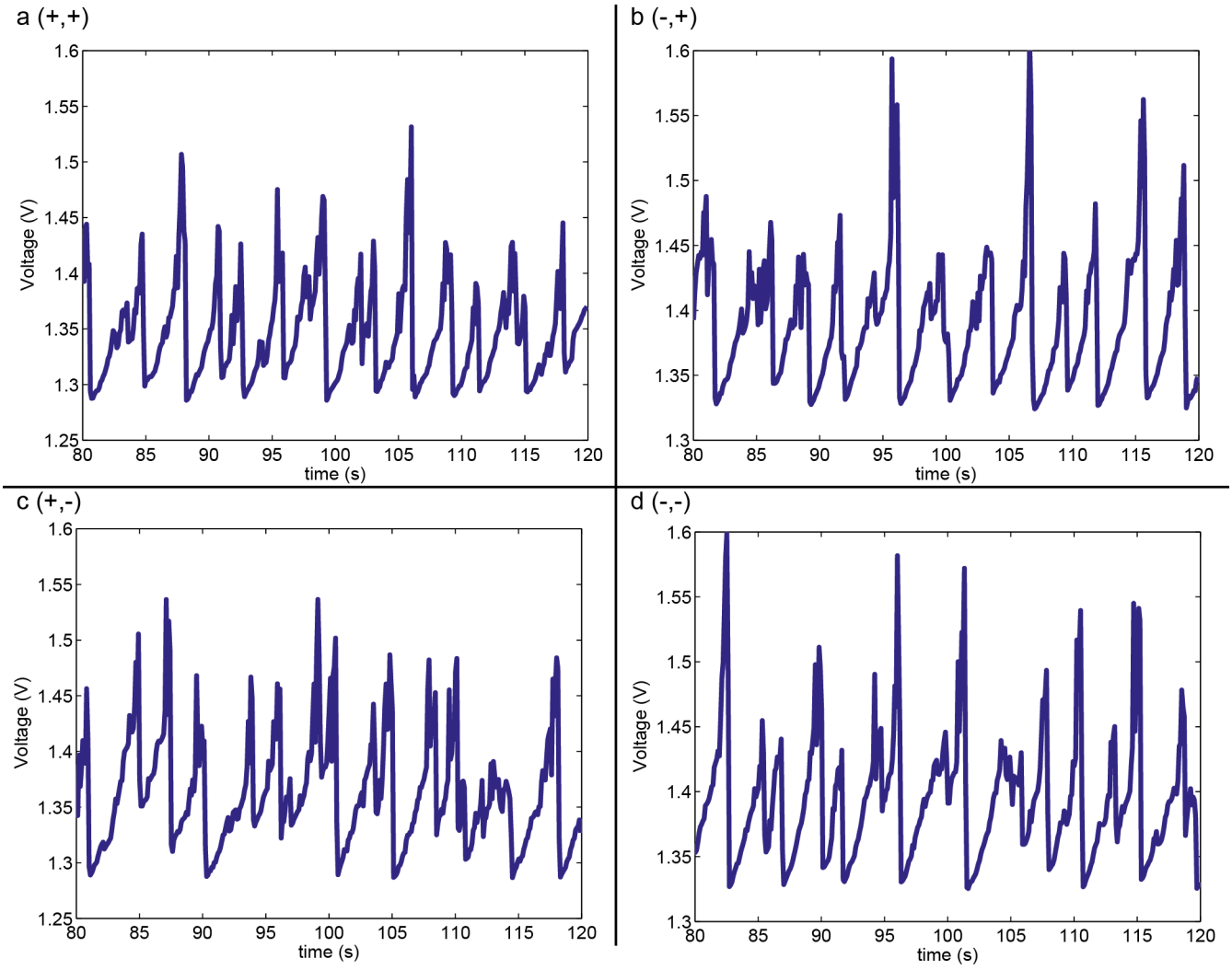

Figure 16.12: Sample voltage curves for three different levels of resolution corresponding to table 16.20.

Table 16.21: Summary of factors, frequencies, signal domain and mean voltages obtained when varying grid resolution.

Name	Factor		Frequency replicate				Signal domain	Mean voltage
	Δx	Δy	f_v^1 (Hz)	f_v^2 (Hz)	f_g^1 (Hz)	f_g^2 (Hz)	ΔU (V)	$\bar{U}$ (V)
Case (-,-)	-	-	0.22	0.43	0.22	0.27	0.19	1.39
Case (+,-)	+	-	0.22	0.33	0.22	0.20	0.19	1.36
Case (-,+)	-	+	0.27	0.25	0.27	0.33	0.20	1.39
Case (+,+)	+	+	0.27	0.33	0.27	0.33	0.22	1.35

For all the cases considered, frequencies and amplitudes tend to decrease with increasing resolution, the dependency upon wall normal resolution (Δy) being the strongest. The mean voltage show the strongest dependency upon the horizontal resolution (Δx), due to the improved prediction of horizontal currents entering the *cathode* through its corners (cf. figure 16.8).

16.3.6 Sensitivity analysis

Data provided in tables 16.7, 16.8 and 16.9, and corresponding tables for other properties, give the influence of a given factor when it is allowed to vary between high and low levels. Hence, it gives an indication of the sensitivity related to the *uncertainty* of a given factor and not the sensitivity to the factor itself, for which a relative percentwise change is required.

Consider for instance the minimum pore density and maximum pore density, i.e. factors A and B. Table 16.7 indicates that the influence of factor A is greater than that of factor B, average frequencies from A+ -cases being 26% higher than the corresponding A–cases, while the relative change between high and low levels is only 15% when considering factor B. The relative change in the factors is however different, high levels being 250% and 29% higher, respectively, than the corresponding low levels for factors A and B. Hence, the sensibility to the two factors cannot be compared directly.

Assuming a linear response and negligible coupling between factors, the relative percentwise change, β_i^{RPC}, is introduced to enable direct comparison of factors, defined as

$$\beta_i^{RPC} = \frac{F^- \left(R_i^+ - R_i^-\right)}{R_i^- \left(F^+ - F^-\right)}, \tag{16.7}$$

where R_i^+, R_i^-, F^+ and F^- respectively represent the response to high and low values of a factor F, for a property (i.e. frequency or amplitude) i. A relative percentwise change of unity thus indicates that 1% change in the parameter in question, yields a corresponding change in the response of the property.

The relative percentwise change, and thus sensitivity, for the factors described in the factorial design is given in table 16.22 and corresponding results for grid sensitivity are shown in table 16.23.

Table 16.22: Relative percentwise change in frequency f, domain ΔU and mean voltage $\bar{U}$ due to different properties.

	Pore properties			Bath properties			Transport properties		
Factor	β_f^{RPC}	$\beta_{\Delta U}^{RPC}$	$\beta_{\bar{U}}^{RPC}$	β_f^{RPC}	$\beta_{\Delta U}^{RPC}$	$\beta_{\bar{U}}^{RPC}$	β_f^{RPC}	$\beta_{\Delta U}^{RPC}$	$\beta_{\bar{U}}^{RPC}$
A	0.11	0.08	0.00	-0.37	0.21	0.01	0.77	0.02	0.01
B	0.51	-0.11	0.01	-0.96	0.29	0.01	-0.14	-0.07	-0.01
C	-0.37	-0.22	-0.02	-0.09	-0.03	0.00	0.32	-0.32	0.03
D	-	-	-	0.45	0.06	0.01	-	-	-

Table 16.23: Relative percentwise change in frequency f, domain ΔU and mean voltage $\bar{U}$ due to different mesh resolution.

Factor	β_f^{RPC}	$\beta_{\Delta U}^{RPC}$	$\beta_{\bar{U}}^{RPC}$
Δx	-0.04	0.05	0.03
Δy	0.10	0.09	0.00

As seen from tables 16.22 and 16.23, the frequencies of the simulated signals show the greatest sensitivity to the various factors considered. The most significant factors are the contact angle, Sherwood number and maximal pore density. As measured values of these factors reported in the literature show considerable variation, extensive experiments are required in order to reduce the *uncertainty* of the proposed model.

Considering the domain of the signal, the bubble detachment diameter, contact angle and pore diameter appear to have the strongest influence. However, due to the strong coupling between the various factors (cf. tables 16.8, 16.13 and 16.18), this result is only indicative.

As indicated previously, the mean voltage is relatively insensitive to the factors considered here, as it is governed by other conditions (cf. section 16.5).

16.4 Influence of MHD-forces

As seen in section 13.2, the current passing through the lab scale cell results in a tangential magnetic field and corresponding *radial* Lorentz-force. As a full 3D simulation is required to capture the complete MHD picture, the following 2D approximation serves as an estimate to determine the importance of MHD-forces.

Assuming a uniform current density $-j_0\hat{\boldsymbol{y}}$ in the interpolar region, the magnetic field in the xy-plane is given as

$$\boldsymbol{B}_{ind} = \begin{cases} -\frac{\mu_0 j_0}{2} x\hat{\boldsymbol{z}} & \text{if} \quad |x| < r_0 \\ -\frac{\mu_0 j r_0^2}{2x^2} x\hat{\boldsymbol{z}} & \text{if} \quad |x| \geq r_0 \end{cases} \tag{16.8}$$

for a anode with diameter $2r_0$, where $\hat{\boldsymbol{z}}$ is a unit vector pointing into the paper plane, as shown schematically in figure 16.13.

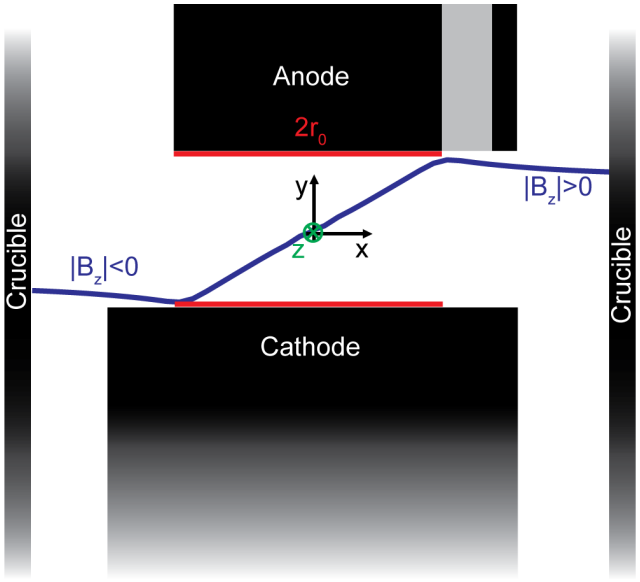

Figure 16.13: Sketch of 2D lab scale geometry with magnetic field given by equation 16.8, resulting from a uniform current density $-j_0\hat{\boldsymbol{y}}$ in the interpolar region. The unit vector $\hat{\boldsymbol{z}}$ points into the paper plane.

The Lorentz force is calculated as

$$\boldsymbol{f}_L = \boldsymbol{j} \times \boldsymbol{B}, \tag{16.9}$$

where $\boldsymbol{j}$ is the *local* current density obtained from the simulation at every time step. This 2D approximation is thus a zero order approach, as the magnetic field is specified and induction currents are neglected. As both the local current densities and the magnetic field are strongly related to j_0, the resulting Lorentz force, and thus its action, is expected to scale as $\boldsymbol{f}_L \sim j_0^2$. For simplicity, only the linear part of the magnetic field is considered, as

the current density and hence the Lorentz forces outside the interpolar region is negligible, as seen in chapter 13.

Experiments 8 and 31 and 22 and 44 (cf. table 9.1) are chosen for comparison, as these cases have the largest difference in current density and also the largest ACD, thus allowing for MHD related bath flow in a larger region.

Pore-, bath- and transport properties correspond to Case 7 of the pore property study. Figure 16.14 shows sample voltage curves as well as dominating frequencies for each of the two current densities, with and without Lorentz forces enabled.

As seen from figure 16.14, the inclusion of Lorentz forces shows a considerable influence upon the voltage curves, particularly when considering the most dominating frequencies of the signal, which *increase* for both of the cases considered with 22 and 32%, respectively, compared to the simulations without MHD. The enhanced bubble departure can be understood by comparing figures 13.4 and 16.8, showing an enhanced (MHD-induced) pressure gradient at the right edge of the anode (figure 13.4) which corresponds to the region typically having the highest density of *macroscopic* bubbles (cf. figure 16.8), owing to the tilting of the anode. The Lorentz forces thus behave as an additional buoyancy force, allowing large bubbles to round the anode corner more easily.

The enhanced motion of the bath also influences other features, such as mass transfer, allowing the system to reach a statistically steady state *faster* than corresponding simulations without Lorentz forces present, as shown in figure 16.15.

Comparing the most dominating frequencies provided in figure 16.14, it is evident that increasing current densities increases the bubble departure rates, as expected from the enhanced production of gas on a molecular level. Considering the cases without Lorentz forces (frames a and c), the increase in the most dominant frequencies is 14%, while the increase in current density is 37%. Correspondingly, the increase in dominant frequencies is 25% for cases *with* Lorentz forces activated, that is, the contribution due to MHD on bubble departure frequencies is comparable to that of increased gas production.

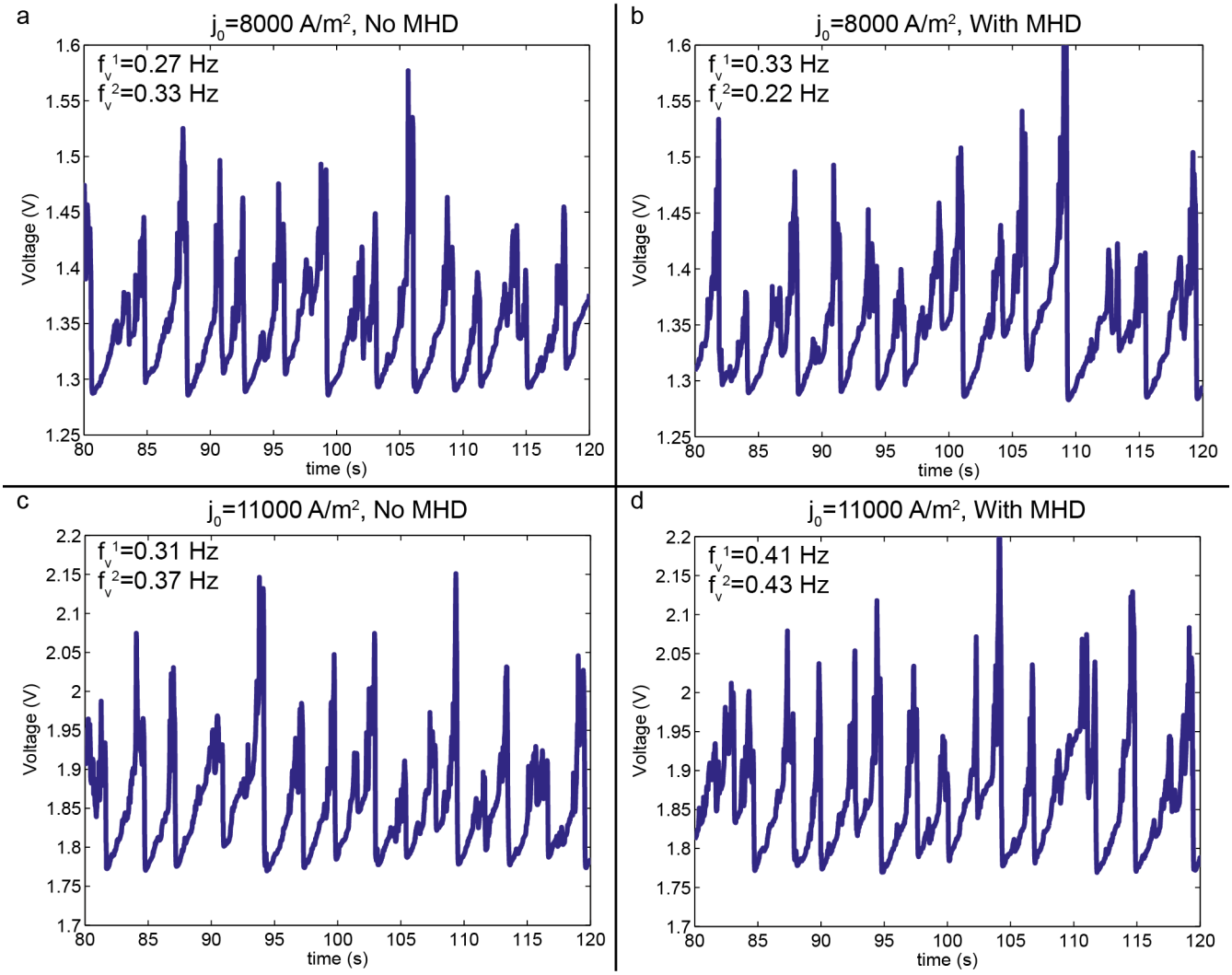

Figure 16.14: Influence of Lorentz forces on voltage signal. Figure shows voltage signal for current densities $j_0 = 8000$ A/m^2, with and without Lorentz forces (a and b) and corresponding curves for current densities $j_0 = 11000$ A/m^2 (c and d) and first and second most dominating frequencies, f_v^1 and f_v^2, respectively.

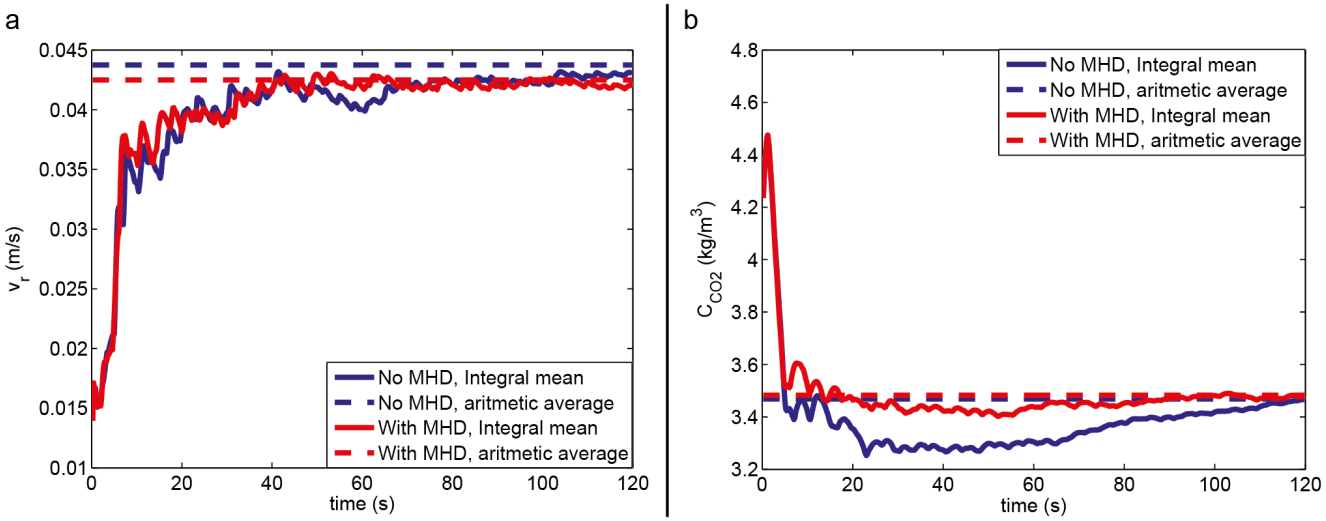

Figure 16.15: Integral mean values (solid lines) and arithmetic averages (dashed lines) for velocity in right channel (a) and CO_2 concentration on anode surface (b) for simulations at $j_0 = 8000$ A/m^2 with and without Lorentz forces, red and blue lines, respectively.

16.5 Full validation study

The final validation of the proposed (2D) model is based on the experimental results given in table 9.1. In addition, extended simulations are performed in order to further investigate the influence of anode inclination. Pore-, bath- and transport properties are chosen corresponding to case 7 in the study of pore properties, while operational parameters are varied according to experiments. Lorentz forces are simulated for each of the cases considered, following the same procedures as described in section 16.4, i.e. a zero order approach.

Conditions for each of the simulations as well as essential results (corresponding to those given in table 9.1) are given in table 16.24. Selected voltage curves are shown in figure 16.16.

As seen from table 16.24, the typical frequencies for the cases considered correspond well to those obtained experimentally. Higher frequencies are found at higher current densities and greater anode inclinations.

Considering the voltage losses neglected in the current simulations (of order 2 V), mean voltages are within the expected order. Evidently, the mean voltage changes according to the ACD and current densities. For cases 3 and 4, operating with a current density of 8000 A/m^2, the mean voltage increases with 0.54 V with a 2 cm increase of the ACD. The

Table 16.24: Results from simulations corresponding to lab scale experiments, table 9.1, cases 1–5, and simulations related to increasing inclination angle, cases 6 and 7.

Case (#)	CD A/cm^2	ACD (cm)	inc (°)	$\bar{U}$ (V)	f_v^1 (Hz)	f_v^2 (Hz)	ΔU (V)
1	0.95	3	4	1.25	0.45	0.37	0.14
2	1.10	2	2	1.11	0.37	0.35	0.35
3	0.80	4	2	1.35	0.33	0.22	0.19
4	0.80	2	2	0.81	0.29	0.39	0.32
5	1.10	4	2	1.86	0.41	0.43	0.29
6	0.80	4	4	1.32	0.35	0.45	0.10
7	0.80	4	6	1.31	0.25	0.51	0.06

experimental result (cf. table 9.1) is 0.48 V. Analogously, for a current density of 11000 A/m^2, simulated and experimental values both give 0.75 V. Considering an increase in current density of 37% (as for instance between cases 2 and 4), the corresponding increase in mean voltage is 37%, as expected, as the simulated voltage consists only of Ohmic contributions.

Similarly to simulations presented previously in this chapter, the magnitude of the voltage oscillations are somewhat over predicted, particularly for the low ACD cases.

The trend of the fluctuations is however similar to that found in experiments, higher current densities promoting higher amplitudes, while greater anode inclinations significantly reduce the bandwidth of the signal, as seen from cases 3, 6 and 7. The simulations also indicate a strong dependency upon ACD, amplitudes increasing as the ACD decreases. As this effect is not (clearly) seen in the experiments, it is possible that this effect is a numerical artifact arising due to the uniform current density enforced on the cathode, impeding the redistribution of electrical current expected to occur in reality.

Increasing anode inclinations tend to increase the frequencies of the signal, although the trend is not as strong as for the bandwidth, as seen from table 16.24. As seen from the data provided for case 7, the most dominating frequency *decreases* significantly when compared to cases 3 and 6, as opposed to the expected behaviour. Considering the actual voltage curve, figure 16.16d, it is however evident that the signal in fact is fluctuating more significantly than cases with lower inclination (i.e. case 6). The voltage curve from case 7 also shows low frequency oscillations superimposed on the faster fluctuations, indicated by the moving average in figure 16.16d, possibly shifting dominating frequencies in the FFT (which assumes oscillations around a constant mean) towards lower values.

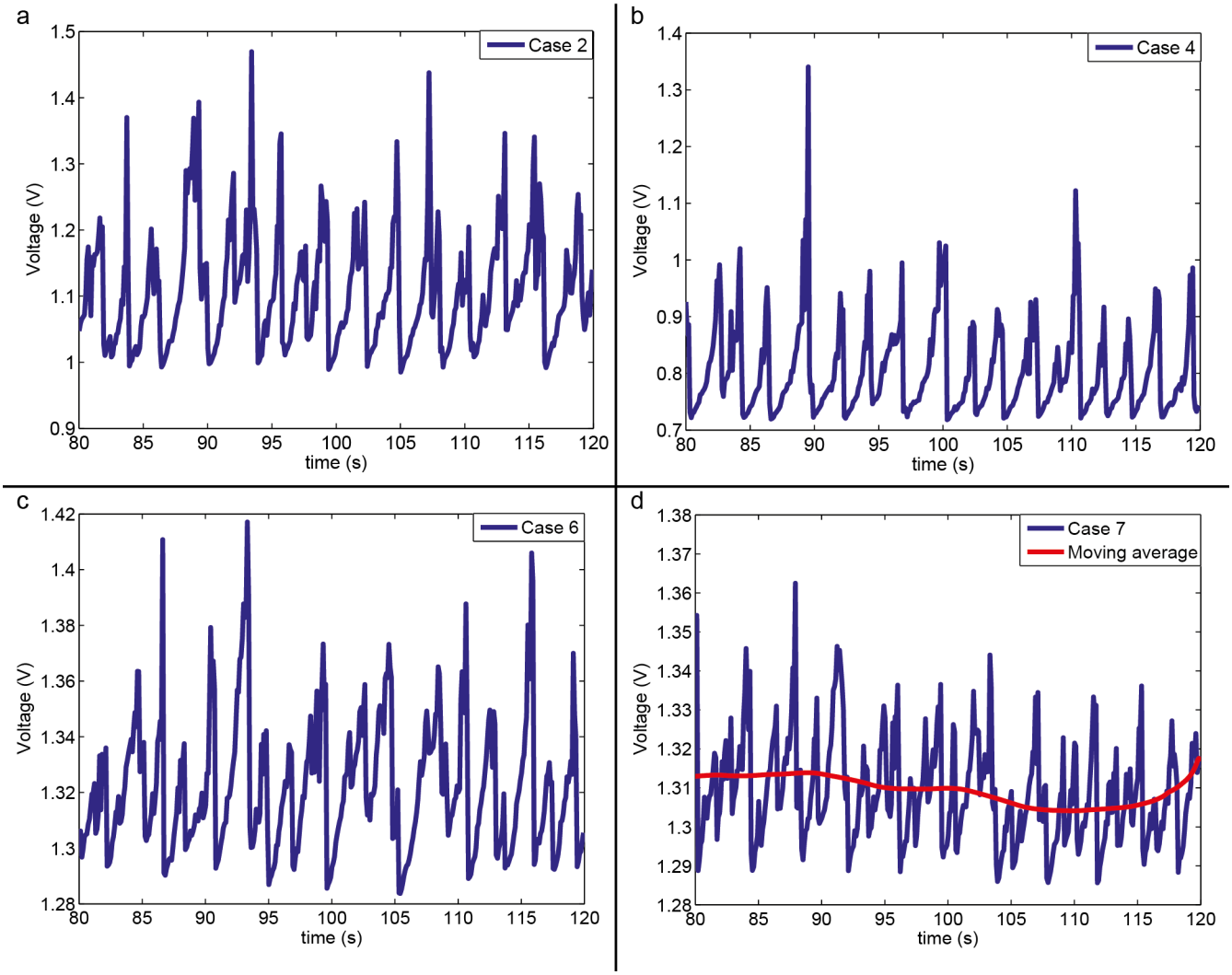

Figure 16.16: Voltage curves from selected simulations presented in table 16.24.

16.6 Mass transport in the interpolar region

As seen from figures 16.11c and 16.15b, the CO_2 concentration on the anode surface, which governs nucleation and mass transfer to the majority of the microbubbles, is close to a statistically steady state. Hence, bubble production can assumed to be steady, as indicated by the corresponding steady state curves for voltage. A statistically steady state is however *not* reached when considering the system as a whole. Figure 16.17 shows the total mass of dissolved CO_2 in the bath, compared to that produced by Faraday's law, i.e. expected mass of CO_2 if no bubble production is present.

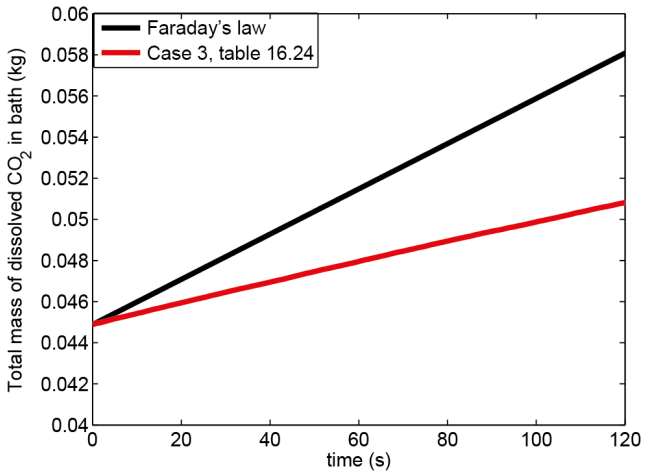

Figure 16.17: Total mass of dissolved CO_2 for case 3, table 16.24 (red line), compared to that predicted by Faraday's law (black line).

As seen from the above figure, the total mass of dissolved CO_2 in the bath is *increasing* steadily, although at a lower rate than that predicted by Faraday's law. The rate of the simulated curve is approximately 40% of Faraday's law, indicating that 60% of the (molecular) gas produced is evolved as bubbles. Hence, the present simulations indicate that a statistically steady state on the anode surface does *not* imply a complete transfer of dissolved gas to bubbles, rather an equilibrium between gas and bubble generation and transport away from the anode by means of diffusion (mainly turbulent) and advection, as indicated in figure 16.18.

The steady state behaviour illustrated in figure 16.18 corresponds well to the analytical predictions of Vogt [125]-[129]. Vogt [127] indicates that 30% (or less) of the molecular gas is evolved *at the anode surface*, i.e. by nucleation. The higher gas evolution efficiency indicated in figure 16.17 is due to mass transfer to microbubbles in the proximity of the anode, an effect not considered in [127].

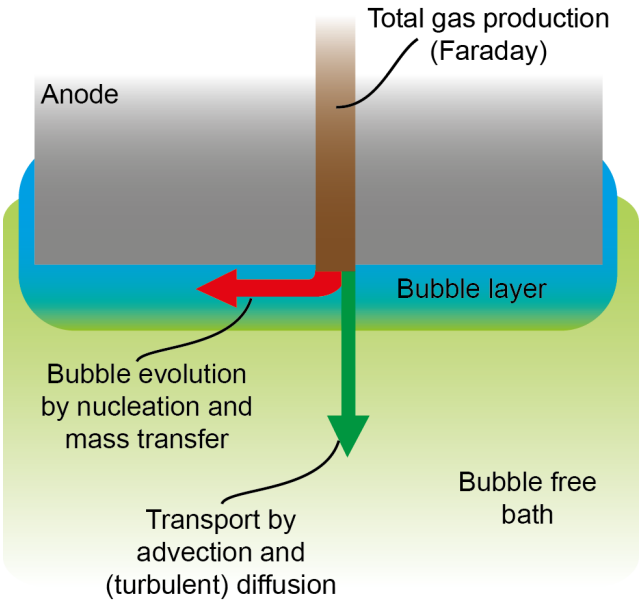

Figure 16.18: Sketch of steady state bubble production. The total amount of produced CO_2 by Faraday's law (brown) is separated between bubble evolution (red), occuring in the bubble layer with close proximity to the anode, and transport into the remaining (essentially bubble free) bath by advection and diffusion (green).

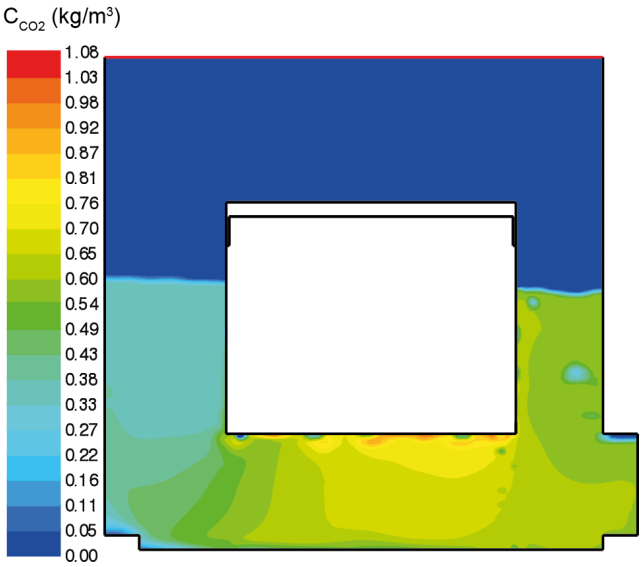

Figure 16.19: Snapshot of dissolved CO_2 distribution for case 3, table 16.24, at t=120 s. The uniform initial value (C_{CO_2}=4 kg/m^3) has been subtracted from the result for visualization purposes.

Figure 16.19 shows the distribution of C_{CO_2} for case 3, table 16.24, at t=120 s. Although the greatest (and smallest, due to local production) concentrations are present in close proximity of the anode, figure 16.19 indicates that the remaining bath contains considerable amounts of CO_2, typically greater than the saturation concentration.

Evidently, reducing the ACD brings the CO_2 enriched region closer to the cathode, thus increasing the typical CO_2 concentrations in this region, as shown in figure 16.20.

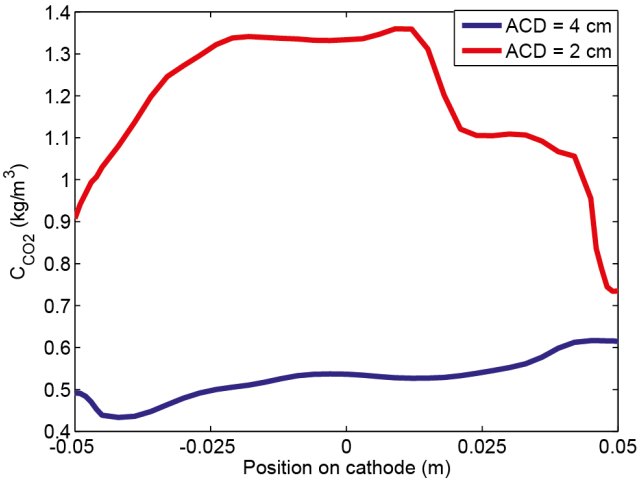

Figure 16.20: Concentration of CO_2 on cathode at t=120 s for cases 3 and 4, table 16.24, with ACD 4 and 2 cm, respectively.

The presence of CO_2 in proximity of the cathode could in principle initiate the back reaction (equation 5.15), thus lowering the overall current efficiency. As CO_2 concentrations in this region increase with reduced ACD, as indicated in figure 16.20, the bath-transport mode of CO_2 appears to yield a possible explanation to the significantly reduced current efficiency observed experimentally, if the ACD is reduced below a certain limit.

In a real setting, the bath cannot absorb unlimited amounts of CO_2, as is the case in the current simulations. The presence of alumina particles, dust and the remaining boundaries of the system are likely to provide sufficient porous structures for heterogeneous nucleation of bubbles to occur. Additionally, the dissolved gas can be freed at the interface of large bubbles (as of equation 14.43), further depleting the surrounding bath. The concentrations shown in figure 16.20 are thus expected to be greatly exaggerated compared to reality. Nevertheless, it is interesting to note that the rigourous mixing arising due to the bubbles allows the concentration field of dissolved CO_2 to extend far outside the typical bubble layer thickness, possibly allowing for the back reaction (equation 5.15) *without* (resolved) bubbles coming in contact with the metal pad.

Chapter 17

3D case study

Although the simulations presented in the previous chapters adequately reproduce the sought experimental behaviour, the 2D approach has some shortcomings, besides the (obvious) fact that a 2D-simulation *always* is an idealization of the real 3D problem. The main shortcomings of the 2D approach are:

- Bubbles in a 2D simulation are neccessarily represented as cylinders, spanning infinitely into the paper plane, as sketched in figure 17.1 An aritificial self-organization is thus enforced on the bubble flow due to the 2D approximation.
- Owing to the cylindrical shape of the bubbles, a stronger redistribution of the electrical current is expected, as it cannot pass through a plane parallell to the bubble.
- Surface and contact forces are neccessarily different in 2 and 3 dimensions, again owing to the cylindrical shape imposed by the 2D-approximation.
- The MHD phenomena occuring in the cell are 3D, due to the tangential direction of the magnetic field. In addition, the reduced redistribution of current density in 3D will result in a different distribution of Lorentz forces, compared to 2D cases.

The first three of the above points are illustrated further in figure 17.1.

Despite the above shortcomings, the proposed model is able to adequately reproduce the essential properties of the voltage signal in 2D. This is expected to be due to the particular geometry used in the lab scale experiments, essentially forcing all the gas in one direction due to inclination and the plates fixed to the sides of the anode (cf. figure 16.1), resulting in bubble behaviour much similar to that observed in water model experiments (cf. Einarsrud [30]), which is well represented by a 2D approach.

For the general case, however, a 3D validation of the model is required. Due to limited computing capacity, the following 3D-study is restricted to a simplified case, rather than a full validation.

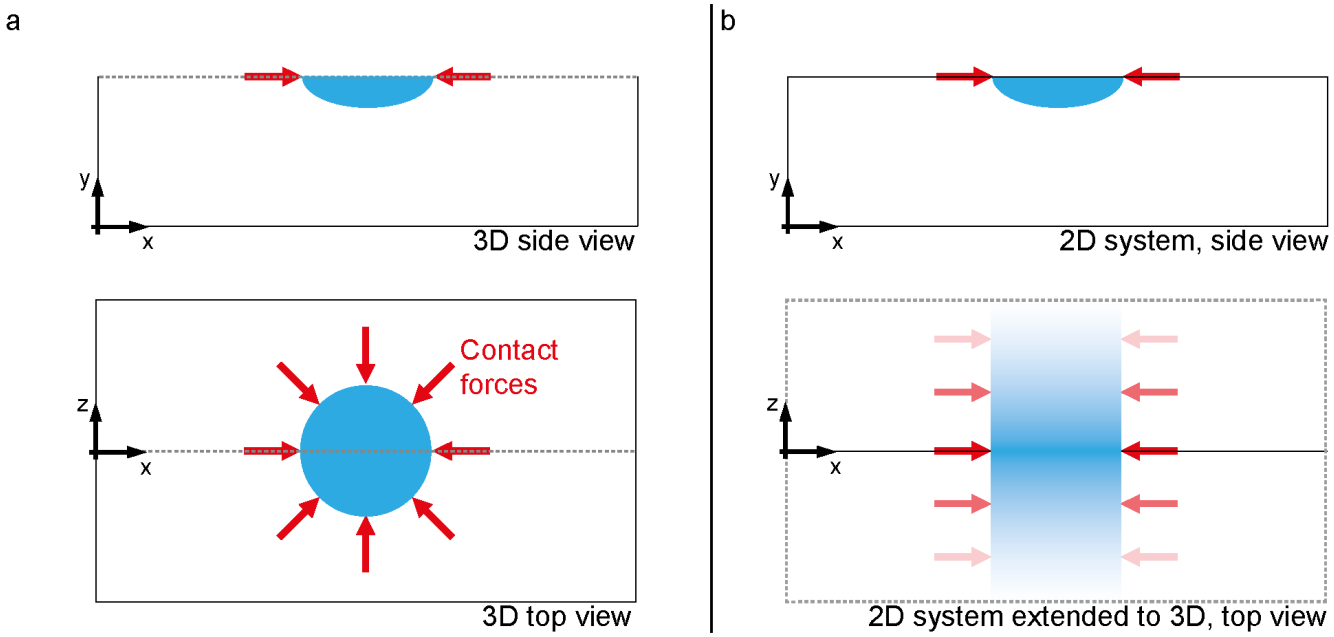

Figure 17.1: Comparison of single bubble in 3D (a) and 2D (b). Although the side view (top frames) is identical for both approaches, the top view is not. For the 3D bubble, the electrical current can circumvent the bubble in the z-direction. As this is not possible in 2D, a stronger redistribution of the electrical current is expected.

17.1 Geometry and setup

Considering the 2D cases presented previously, typically consisting of 6000–8000 cells, the typical simulation time (on a single CPU) to reach 120 s flowtime is 72 hours. A pure extrusion of the geometry presented in figure 16.3, will typically involve 30 times more cells with the given resolution, indicating that long term 3D simulations of the full lab cell, with the current hardware, is impractical. Furthermore, preliminary simulations indicate that significantly lower time-steps are required for 3D simulations than in 2D, due to the complex motion of the top bath-gas interface as bubbles are released. While this results in a Courant number just below unity in 2D, Courant numbers above 10 are observed in 3D, seriously impeding convergence and leaving the time accuracy of the solution highly questionable.

Consequently, in order to reduce the computational cost of the 3D-simulations, the lab-cell geometry is simplified further, as shown in figure 17.2.

The cross section shown in figure 17.2 is extruded ± 5 cm in the z-direction in order to represent the full lab scale anode surface. The anode connection rod, with a specified

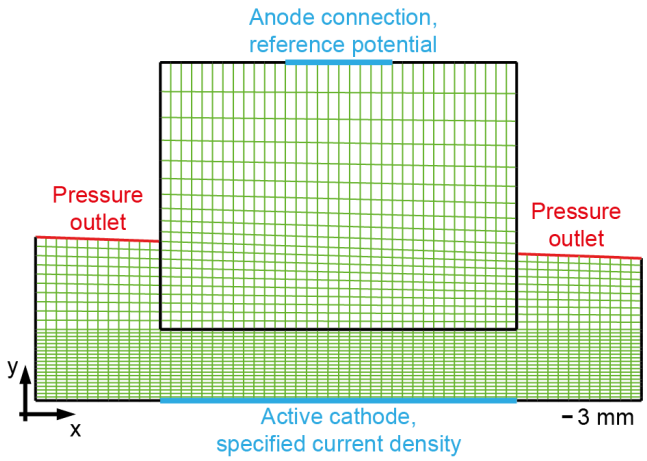

Figure 17.2: Cross section of simplified 3D model showing mesh and essential boundary conditions. Outlet surfaces are inclined corresponding to experiments in order to have equal gauge pressure.

reference potential of 0 V, spans ±1.5 cm. Mesh properties under the anode correspond to those used in the 2D simulations. The resolution in the z-direction is identical to the x-direction, i.e. $\Delta x = \Delta z$=3 mm. All bounding surfaces are treated as in the 2D-simulations, i.e. zero flux, no-slip walls, except for the active cathode, where a current density of 8000 A/m^2 is specified. Solver settings and model parameters correspond to those used in section 16.5.

As MHD is expected to be of importance, the full second order formulation based on the magnetic vector potential is adopted. Analytical Dirichlet boundary conditions, equation 11.17, are used on all external surfaces for the main component of the magnetic vector potential (A_y), while appropriate academic boundary conditions (cf. section 11.4 for definition) are imposed on internal surfaces and for the remaining components, analogously to simulations performed in chapter 13.

The simplified geometry described in figure 17.2 imposes two constraints on the bath flow. As the free surface is not present, the typical recirculation pattern observed in the side channel (cf. figure 17.3 and [30], [31]) is expected to be limited. In addition, the presence of two outlets will increase the "rigidity" of the system, as opposed to the (full) 2D simulation, where a pressure imbalance in one channel can be equalized by moving the interface in the other channel accordingly.

In order to save additional CPU-resources, the following study is performed with an ACD of 2 cm. Results should thus correspond to those obtained for case 4, table 16.24.

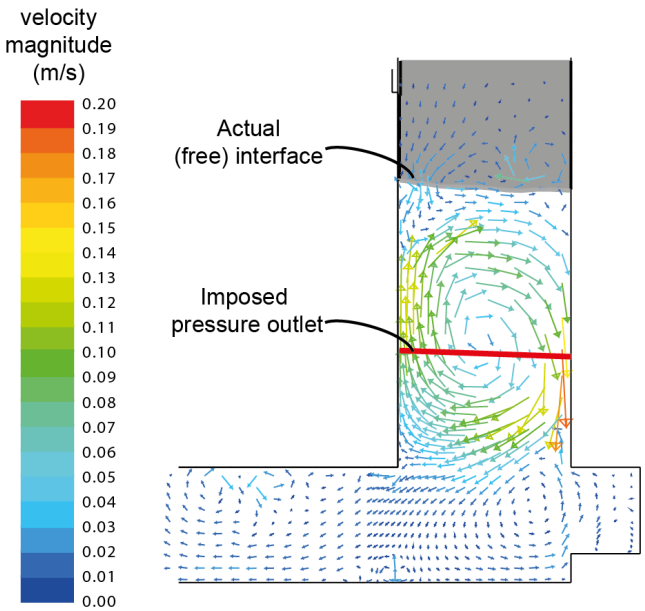

Figure 17.3: Typical velocity distribution in gas escape channel, case 4, table 16.24, and position of pressure outlet in simplified geometry.

17.2 Validity of simplified geometry

As the geometry is slightly different for the simplified 3D case compared to that used in case 4, table 16.24, a 2D simulation is performed on the geometry shown in figure 17.2 in order to ensure that the simplfied geometry (qualitatively) yields the expected results. Figure 17.4 shows voltage curves obtained from simulations on the simplified geometry compared to the one obtained from case 4, table 16.24.

The voltage curved shown in figure 17.4 indicate that the simplified geometry influences the resulting voltage curve, which necessarily is expected from the strong dependency upon geometry reported in the literature. Due to the additional constraints on the bath flow, the signal obtained from the simplified geometry shows lower frequencies ($f_v^1 = 0.22$ Hz, $f_v^2 = 0.37$ Hz) than the corresponding data given in table 16.24. The mean voltage ($\bar{U}$=0.81 V) and amplitudes ($\Delta U = 0.31$ V) correspond well to that expected.

Qualitatively, the expected behaviour is sufficiently reproduced, suggesting that a 3D simulation on the simplified geometry also should correspond to that obtained for case 4, table 16.24.

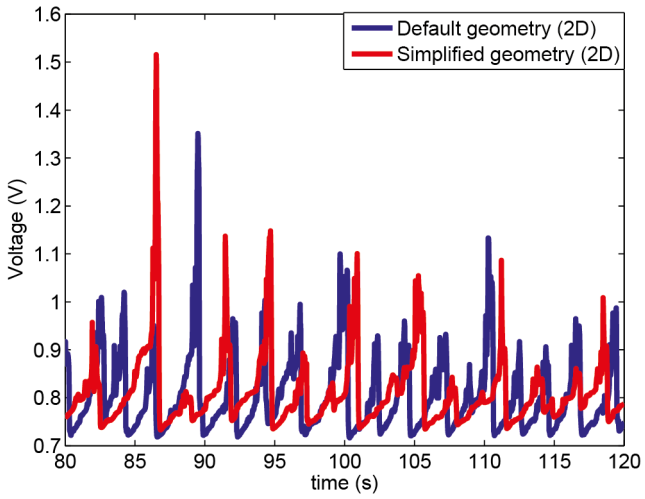

Figure 17.4: Comparison between voltage signal in default (blue) and simplified geometry (red).

17.3 Results from 3D simulation

Figure 17.5 shows the evolution of voltage (a) and gas coverage fraction (b) for the 3D simulations, compared to results obtained on the corresponding simplified 2D geometry. Due to limited computer resources, the 3D simulation is limited to 60 s flowtime[1]. Although not sufficient to obtain a statistically steady state, *representative* fluctuations are obtained on this interval for 2D simulations and thus gives a strong indication of future bubble evolution.

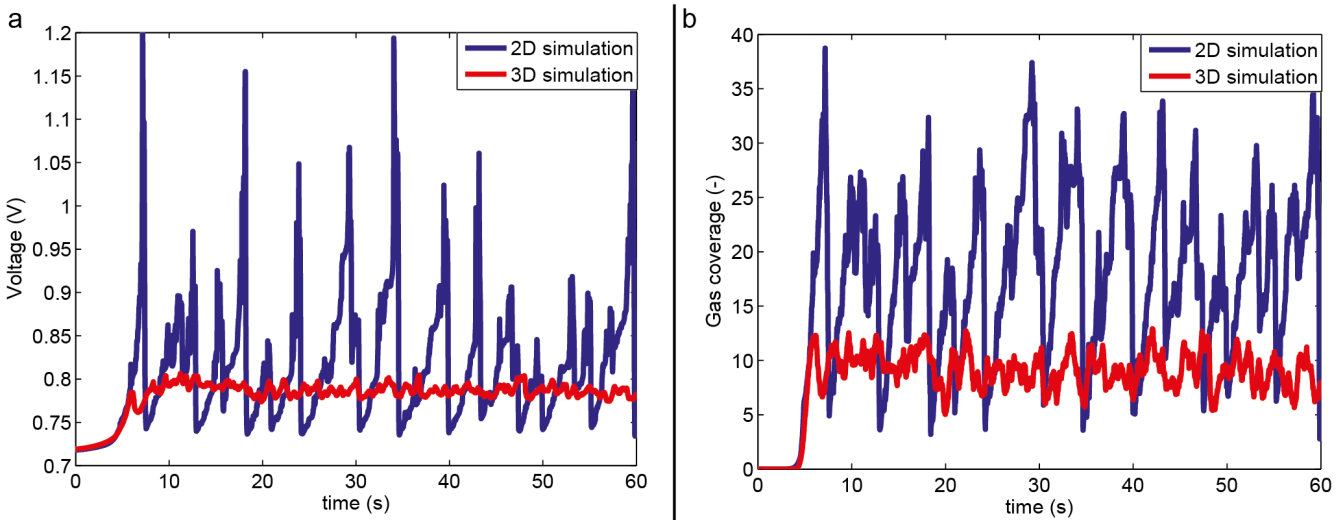

Figure 17.5: Comparison between voltage signal (a) and gas coverage fraction (b) for 2D (blue) and 3D (red) simulations on simplified geometry (figure 17.2).

Evidently, as seen from figure 17.4, there is a significant difference between the behaviour obtained in 2- and 3D simulations. While the typical bubble fluctuations are achieved already in the first cycle in 2D, 3D simulations show random-like, low amplitude fluctuations throughout the whole time interval, corresponding to that shown in figure 7.6b for multiple bubbles failing to reach a self-organised state.

Figure 17.6 shows the details of the voltage signal and gas coverage for the first bubble cycle.

It is clear that the initial behaviour (up to $t \approx 6$ s) is similar in 2 and 3D. However, bubbles appear to detach and slide along the anode surface more easily in the 3D simulations, allowing for less gas to accumulate under the anode and consequently resulting in significantly lower amplitudes. That the 2 and 3D approaches produce similar results up to the point at which the presence of macroscopic bubbles becomes significant indicates that the challenges in 3D are related to the macroscopic VOF bubbles, possibly due to

[1]Even on the simplified geometry, this simulation requires approximately 2000 CPU-hours to complete.

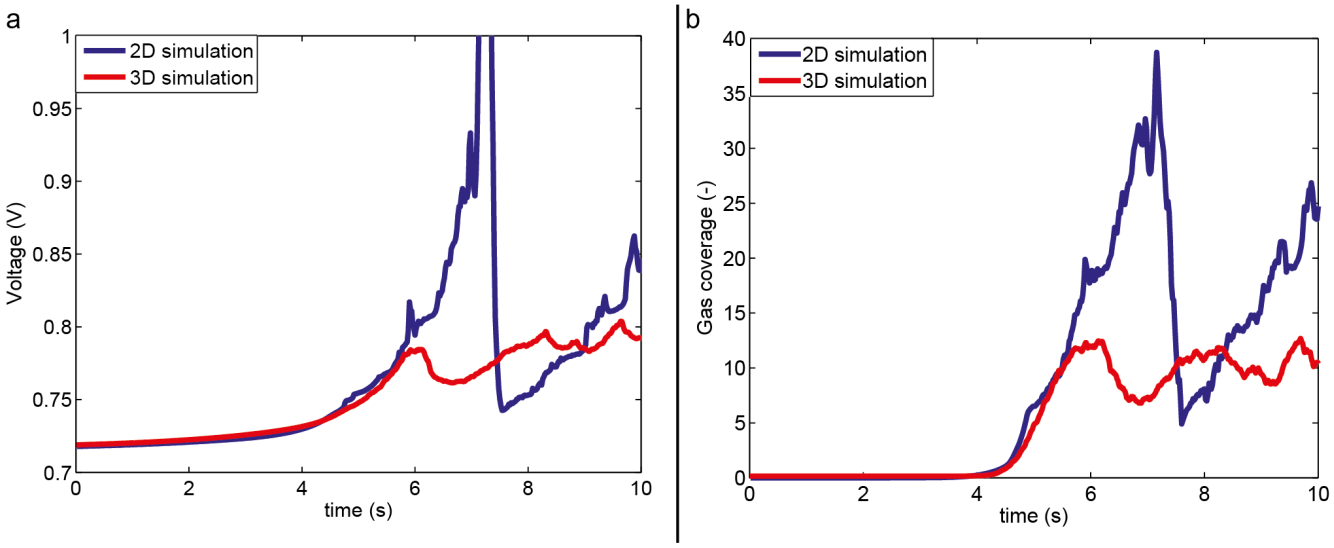

Figure 17.6: Comparison between first voltage (a) and gas coverage (b) cycle for 2D (blue) and 3D (red) simulations on simplified geometry (figure 17.2).

surface tension (and resulting surface forces), which, as shown in appendix A, is strongly influenced by whether the simulation is run in 2 or 3D.

Figure 17.7 shows the evolution of bubbles under the anode for a selected 4 s interval. As seen from the figure, macroscopic bubbles form several small clusters, typically extending 4x4 cells, which evolve more or less independently of other clusters present. This behaviour is significantly different from that obtained in corresponding 2D simulations, where small clusters remain close to stationary until sufficient amounts are present, resulting in the formation of a single large bubble which is released in the gas escape channel (cf. figure 16.8).

Although the 2D simulations impose an artificial self-organised state, likely to be extreme compared to that occuring in a real cell, results indicate that this at least is *closer* to reality than the lack of self-organisation observed in the current 3D simulation. Whether the lack of a self-organised state in 3D is a transient phenomenon, inadequate choice of parameters or due to some unknown factor enforcing self-organisation (or a combination) can be determined only by extended simulations.

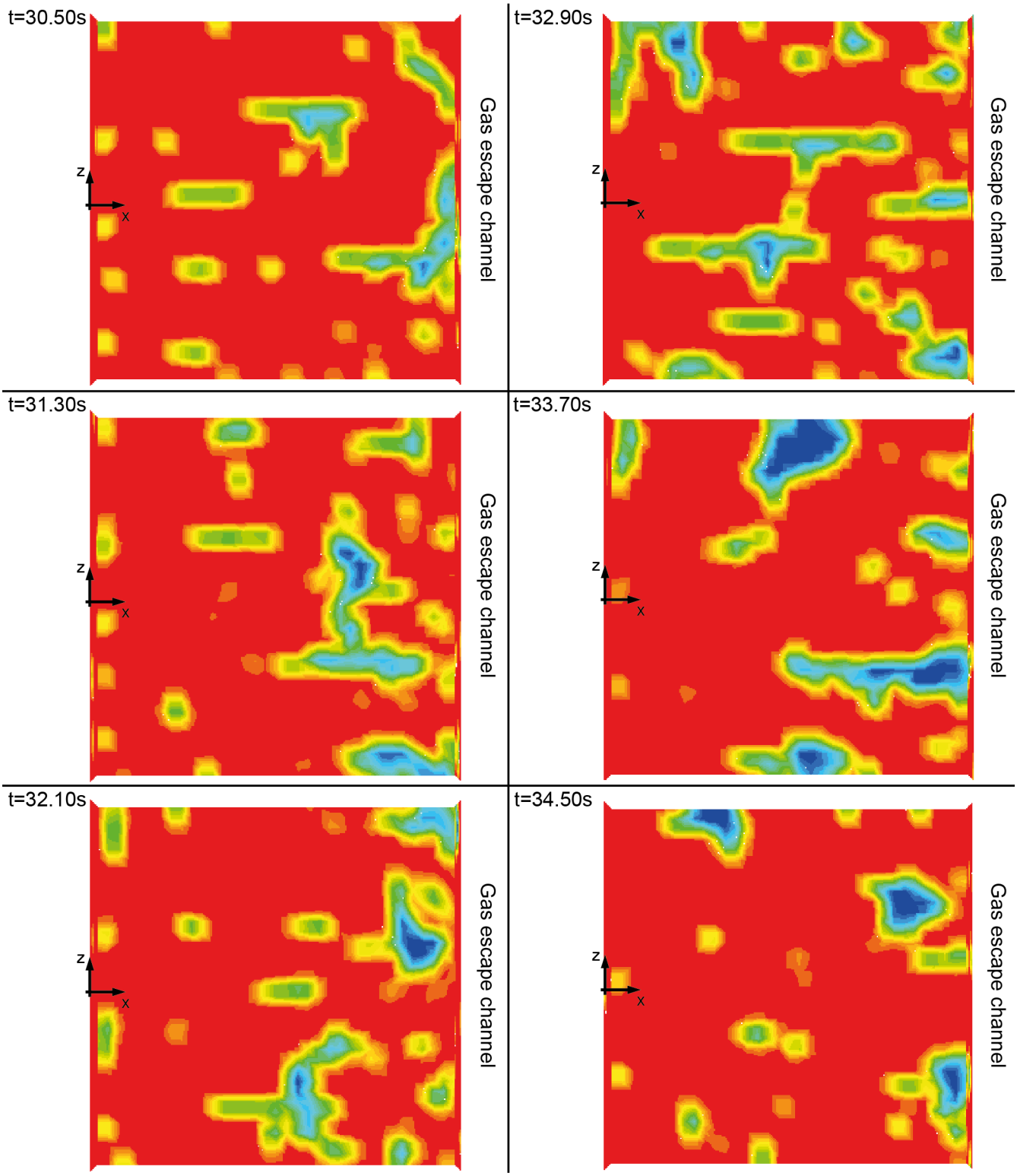

Figure 17.7: Sample evolution of anodic bubbles (blue) in 3D simulation.

Part V: Conclusions

Outline of Part V

Part V provides a conclusive summary and states the most important limitations of the models presented this thesis. Finally, suggestions for future research are given.

Chapter 18

Concluding remarks and limitations

This thesis contributes to the understanding of mechanisms for mass transport in aluminium electrolysis cells. Fundamental studies are undertaken of flow patterns and mass transport in the interpolar region under various operating conditions. A coupled model predicting the turbulent electrolyte flow, under the influence of both electromagnetism and forces from buoyant gas bubbles, crucial for better prediction of mass transfer mechanisms and voltage oscillations, has been developed from first principles. The model is validated against experiments performed on a lab scale electrolysis cell. Both modelling and experiments are performed within the scope of the thesis.

The control of aluminium reduction cells relies almost exclusively on the continuous sensing of potline current and cell voltage. Voltage oscillations arise due to several sources, both internal and external. One such source is the continuous production and departure of anodic bubbles, typically yielding frequencies in the order of 1 Hz. As bubbles influence the voltage signal, the voltage could thus in principle be used to map the bubble behaviour in a cell, without the need for invasive techniques.

Voltage measurements have been performed on both lab and industrial scales, supplied with high speed video recordings of the bath surface in order to relate the measured voltage signal to bubble departure on the anode.

The following conclusions can be drawn from the industrial scale experiments:

- Voltage signals have distinct low frequency components in the range 0.5 to 2.0 Hz, with amplitudes up to $\pm 5\%$ around the mean voltage, due to bubbles departing from the anode.
- The frequency and magnitude of the bubble induced oscillations are found to increase with anode age, due to the rounding of the anode edges and diminishing influence of slots.
- No significant correlation in the voltage signal between anode pairs is identified,

indicating that stand alone models of bubble phenomena on industrial anodes are meaningful, provided that the *global* bath and metal flow is adequately described.

- Bubbles are found to depart from the anode at a higher rate than the typical frequencies found in the voltage signal. The measured fluctuations can qualitatively be reproduced from observed departure rates by accounting for the time a bubble spends beneath the anode. This procedure indicates that several large bubbles can coexist under the anode and that the measured voltage signal thus is due to the collective behaviour of several bubbles, rather than single bubbles as commonly described in physical model experiments.
- Due to the multitude of simultaneous phenomena occurring on an industrial scale, results can at best be used for qualitative validations of a numerical model.

A series of lab scale experiments have been conducted in order to obtain data from which a quantitative validation can be performed. The following conclusions can be drawn from the lab-scale experiments:

- Voltage signals show distinct low frequency components in the range 0.2 to 1.0 Hz, with amplitudes up to $\pm 4\%$ around the mean voltage.
- Increasing current densities increases the frequency and amplitudes of the voltage signal, as expected from increased production rates.
- Increased inclination angles increases the frequency and decreases the domain of the voltage signal, indicating a complex interaction between bubble topology and governing forces.
- No general dependence upon the ACD is identified with respect to the signal properties considered, other than the expected reduction in *mean* voltage with reducing ACD. It should be noted that this result is greatly influenced by the wettable cathode used in the experiments, resulting in negligible bath metal interface effects.
- The signal domain is found to decrease with increasing anode age due to rounding of initially sharp edges. Results indicate that higher frequencies also are to be expected with increasing anode age, although the trend is not as clear as for the signal domain.
- There is a good correspondence between observed bubble departure and voltage fluctuations, observed events accounting for approximately 95% of the fluctuations with amplitude larger than $\pm 2.5\%$ of the average voltage. In can thus be concluded that the measured fluctuations are directly related to bubbles departing from the anode.
- Large variations in bubble release times are observed, resulting in an aperiodic signal, thus leaving the *physical* interpretation of the FFT questionable.
- Due to the aperiodic nature of the voltage curves a description of the signal based solely on FFT-frequencies is not sufficient. Consequently, simulations should be closely assessed in order to ensure that the full complexity of the signal is captured.

Chemical reactions in the Hall-Héroult cell are driven by an imposed electrical current, which, due to the dual nature of electromagnetism, induces a magnetic field in the surrounding medium. Interacting electromagnetic fields yield Lorentz forces, resulting in pressure gradients and motion in the medium; magnetohydrodynamics (MHD). In order to ensure compatibility with other models, a MHD framework is developed from first principles. The main conclusions from the development of the MHD framework are:

- A formalism based the magnetic vector potential $\boldsymbol{\mathcal{A}}$ and the electrical potential ϕ incorporates all relevant physics through two simple Poisson equations. As the magnetic vector potential is parallel to the electrical current, determining boundary conditions is more straightforward than for an approach based directly on the magnetic field.
- The $\boldsymbol{\mathcal{A}} - \phi$ model yields a direct decoupling of induced- and external magnetic fields for cases in which this is important.
- Implementing the governing equations through the UDS framework in FLUENT reproduces expected behaviour, provided that an appropriate weighting is used for the interpolation of the electrical field across sharp interfaces. A conductivity weighted interpolation ensures conservation of electrical charge.
- For cases in which boundary conditions for the magnetic vector potential are unknown, academic boundary conditions (i.e. $\mathcal{A}_i = 0$ or $\partial_n \mathcal{A}_i = 0$) yield a good approximation, with absolute error less than 15% compared to analytic results, if Dirichlet and Neumann boundary conditions are applied to insulating and conducting surfaces, respectively.
- For an *isolated* bubble, the influence of MHD is negligible compared to other forces present.
- The presence of a bubble does however have a significant influence on the voltage of the system. The resulting voltage is due to a complex interaction between Ohmic screening and current deflection, i.e. both the projected area of the bubble and its typical thickness is important.
- Considering MHD effects on the lab scale cell, the presence of Lorentz forces result in a slightly favourable pressure gradient and flow field, enhancing bath and bubble transport towards the anode edges. The magnitude of the MHD induced velocities is typically 1-10% of that obtained by buoyant bubbles, indicating that the flow in the bath is mainly controlled by the bubbles.

A phenomenological, coupled, model for the creation and transport of anodic gas bubbles has been developed from first principles. The proposed model is a multiscale approach in which molecular species are produced by Faraday's law and transported by diffusion and advection through a supersaturated electrolyte. Sub grid bubbles are allowed to form through non-classical nucleation on the anode surface and the resulting bubble population evolves through mass transfer and coalescence. As sub grid bubbles reach a certain size

they are transferred to a macroscopic phase which evolution is governed by the volume of fluid method, thus allowing for the treatment of complex bubble topology.

The model is validated against results from the lab scale experiments in a 2D geometry, showing that essential features of the voltage signal can be reproduced by the proposed approach. The influence of various parameters such as bath properties, anode microstructure and mass transfer properties are investigated by means of a factorial design analysis.

The following conclusions can be drawn from the coupled bubble model:

- Bubble evolution by means of CO_2 transport through a supersaturated bath is both possible and plausible, despite very low molecular diffusivities in the bath.
- Due to the low diffusivity, the bath in proximity of the anode surface quickly becomes supersaturated. Expected levels of supersaturation are significant, typically five to ten times the saturation concentration.
- Voltage fluctuations correspond well to variations in gas coverage under the anode.
- The main factors influencing the gas release frequencies are the contact angle, the Sherwood number (i.e. the mass transfer coefficient) and the porosity of the anode. Considering operational parameters, the gas release frequency is found to increase with increasing current densities and anode inclination.
- The amplitudes of the voltage signal are most sensitive to the bubble detachment diameter, contact angles and the mean pore diameter on the anode. Amplitudes however show significant dependence upon coupling between different factors, indicating that the amplitudes of the voltage oscillations is more complex than the frequencies. Regarding operational parameters, amplitudes are found to increase with increasing current densities, while decreasing with increasing anode inclination.
- The mean voltage is relatively insensitive to the (non-operational related) factors investigated in the current study. As expected by Ohm's law, it increases with increasing current densities and ACD.
- Magnetohydrodynamics appear to have a considerable influence upon the bubble evolution, the inclusion of Lorentz forces yielding enhanced gas departure rates comparable to that arising due to increased current densities. The enhanced bubble departure rates appear to be due to slightly favourable pressure gradients at the anode edges, where the concentration of large bubbles is most significant, thus acting as an additional source of buoyancy, allowing bubbles to round the anode corners more easily. The enhanced dynamics of the interpolar region also influence concentration fields, indicating that MHD is highly relevant, also in the bath.
- Simulations compare well to experimental results and appears to handle different operational parameters reasonably for a given set of properties. The amplitudes of the voltage oscillations are however over predicted compared to experiments. The qualitative behaviour is however consistent, indicating that the elevated amplitudes

are due to some systematic error such as system geometry (for instance the lack of rounded corners) or 3D effects not accounted for.

- Steady state bubble production on the anode does not imply a direct transfer of all the molecular gas to bubbles. Instead, a balance between bubble production and transport by diffusion and advection away from the anode appears to describe this state, resulting in a CO_2 supersaturated region greatly extending the bubble layer. The presence of a CO_2 enriched region yields a possible explanation to the observed (significant) reduction of current efficiency if the ACD is reduced beyond a critical limit.

The main constraint of the model is that alumina concentrations are assumed to be constant during each simulation. Hence, important features such as alumina dependent bath properties (which is the case for almost all properties) and the anode effect have not been modelled at the present time. The presence of sufficient amounts of alumina is, necessarily, also crucial for the formation of CO_2. Although the assumption of homogenous (and constant) alumina concentrations is likely to be valid for short time intervals, it cannot be the case in the long run. The current model is thus limited to relatively short time intervals, typically a fraction of the alumina feeding cycle.

As seen in Thonstad et al. [116], the contact angle is strongly dependent upon local alumina content and current densities. The lack of a general model incorporating these effects is most certainly a critical issue, as simulations show a strong dependence upon the contact angle, here treated as a constant value.

Owing to the current focus, i.e. the formation and evolution of bubbles on the anode surface, the bath outside the immediate neighbourhood of the anode is allowed to absorb unlimited amounts of CO_2, if flow conditions are such that advection and diffusion away from the anode are favourable. The proposed model will however (greatly) over predict the CO_2 concentrations outside the bubble layer, as secondary mass transfer to macroscopic bubbles and nucleation on particles suspended in the bath is neglected in the current implementation.

Microscopic bubbles are in the current approach, for simplicity and (numerical) stability reasons, only allowed to influence the conductivity of the bath. However, the presence of bubbles will most definitely influence other parameters as well, most notably the density and also the viscosity, corresponding to the shear induced turbulent viscosity (cf. for instance Zhang et al. [146]). Considering the density and assuming a homogeneous mixture, a sub-grid bubble volume fraction of 0.1 (essentially the largest allowed value) will, approximately, reduce the density of the bath by a corresponding factor, thus allowing for additional buoyancy, not considered in the current approach.

Due to the multiscale nature of the proposed model and challenges related to surface tension, grid dependence is observed. As grid convergence is not achieved at the current time, successive refinements of the mesh does not guarantee that the numerical solution approaches the physical solution, whatever it may be. Until these challenges are resolved,

parameters will have to be adjusted according to experimental observations for a given computational mesh.

Although validated for a selected range of parameters, extended validation studies are required to determine the influence of additional parameters such as for instance different models for electrical conductivity, number of classes in the PBM, turbulence models, different approaches for surface tension, different models for the Sherwood number and altered anode topologies, in particular rounded anode corners. In addition, long term simulations are required in order for all simulations to reach a statistically steady state, provided that this state can be reached without violating the time constraints due to the assumption of constant alumina levels.

Another important limitation is that the proposed model is relatively CPU-intensive, due to the strong coupling between the various fields, resulting in slow convergence, and the long simulation times required to reach a statistically steady state. Considering the 2D cases, typically consisting of 7000–8000 cells, the typical simulation time (on a single CPU) to reach 120 s flowtime is 72 hours. A 3D-model of the (simplified) lab-scale anode will typically consist of approximately 30 times more cells (with the current resolution), making 3D-parametric studies highly time consuming. A 3D extension to a full scale electrolysis cell (or even a full anode) is thus (at best) impractical, at least without access to a supercomputing facility.

Due to the above limitation, a full 3D validation of the lab-scale cell has not been performed in this thesis. Instead, a time limited 3D simulation is performed on a simplified geometry. A self-organized state is not achieved for this simulation, voltage curves showing seemingly random, low amplitude fluctuations. Comparing to experimental voltage curves, however, a form of self-organisation is most definitely present. The 2D simulations induce an artificial self-organised state as bubbles essentially are formed on lines passing into the paper plane. Although this is believed to be somewhat extreme compared to the phenomena occuring in a real cell, results indicate that this at least is *closer* to reality than a complete lack of self-organisation. Whether the lack of a self-organised state in the 3D simulations is a transient phenomenon, inadequate choice of parameters or due to some unknown driving force (or a combination) can be determined only by extended simulations. Consequently, until these exist, the proposed model remains unvalidated for 3D applications.

Despite the above limitations, the proposed model is able to adequately reproduce essential properties of the voltage signal (for 2D simulations), thus providing the basis for a framework in which the evolution of anodic bubbles and their interaction with, and impact on, other phenomena can be studied.

Chapter 19

Topics for further research

1. **Fractal analysis:** Both experimental and simulated voltage curves deviate from periodicity, thus leaving the *physical* interpretation of an FFT questionable. Advanced signal processing tools such as for instance fractal analysis (cf. for instance Wornell [138]) could provide additional useful information regarding the nature of the signal, as these methods are not limited to periodic signals. However, fractal signal analysis requires larger datasets and significantly higher sampling rates than those considered here.

2. **Extended experiments I:** Simulations reveal a strong dependency upon parameters for which values reported in the literature vary significantly. This is in particular the case for wetting properties and the diffusivity of CO_2 in the bath (i.e. mass transfer). If a model such as the one presented in this thesis is to be used as a tool for future cell design, extensive experimental work is required to reduce the uncertainty of governing parameters, and consequently the uncertainty of model output.

3. **Extended experiments II:** The successful simulations performed in this thesis indicate that bubble evolution by means of gas transport through the bath is possible. However, the anode transport mode (cf. Kiss et al. [62]) also provides plausible results. In order to determine the dominating mode of gas transport, dedicated experiments must be conducted. Comparable to the supersaturation required in the bath transport mode, gas transport through the anode would require elevated pressures within the anode pore system, which in principle can be measured. Correspondingly, for the bath transport mode, the supersaturation concentrations should be determined by some appropriate measuring technique. Evidently, measuring these non-equilibrium quantities in the harsh environment of the Hall-Héroult cell will pose tremendous experimental challenges. These must however be met, if the true nature of gas evolution is to be determined.

4. **Extended experiments III:** If experiments reveal that gas transport through the bath dominates the process, the influence of CO_2 concentrations upon bath proper-

ties, if any, should be determined, either by classical or numerical experiments.

5. **Extension of model I:** As the main constraint of the proposed model is that alumina concentrations are assumed to be constant and homogeneous, a natural extension of the model is to include transport of alumina. As a first approach, alumina transport can be simulated by means of a UDS, similarly to the current treatment of dissolved CO_2. For a complete description, however, more advanced models dealing with for instance dissolution of alumina must be included.

6. **Extension of model II:** The influence (or presence) of secondary nucleation and mass transfer should be investigated in detail, in order to determine realistic CO_2 concentrations outside the bubble layer. Combined with an implementation of the back-reaction, the extended model will allow for an estimate of the current efficiency and consequently an additional experimental parameter to which the model can be validated. A model allowing for accurate predictions of the current efficiency would also necessarily be a useful tool for the industry, in order to determine the influence of alternative cell and process design.

7. **Extension of model III:** With access to a high performance computing facility a full 3D-validation of the model should be performed, as 2D cases are limited in the sense of MHD effects and impose artificial conditions for self-organization of the bubbles. Extended simulations will also allow for studies on the factors which govern the onset to a self-organised state in 3D, a critical issue not resolved in the current thesis.

8. **Modelling a full cell:** Owing to the relatively high computational requirements of the proposed model, a direct application to a full scale cell (or even a full size anode) is unrealistic. Details obtained from the proposed model can however be used to determine realistic input parameters for a full scale model, for instance typical time-scales, momentum and mass transfer rates, bubble distribution and mean concentration fields. On the other hand, the output from a full scale model would provide typical (global) flow conditions, which in turn can serve as realistic boundary conditions for a smaller scale model used to describe features on a selected portion of the anode.

   Ultimately, a model allowing for a (semi) continuous coupling between small and large scale phenomena should be developed, thus allowing for detailed interpretations and potential improvements of the process as a whole.

Bibliography

[1] ANSYS. Ansys - Simulation Driven Product Development. `http://www.ansys.com/`, May 2012.

[2] ANSYS. ANSYS FLUENT User's Guide. `http://www.ansys.com/`, May 2012.

[3] S. K. Banerjee and J. W. Evans. Further results from a physical model of a Hall-Héroult cell. *Light Metals*, pages 247–255, 1987.

[4] G. Bearne, A. Jenkin, L. Knapp, and I. Saeed. The Impact of Cell Geometry on Cell Performance. *Light Metals*, pages 375–380, 1995.

[5] M. M. Bilek, W. D. Zhang, and F. J. Stevens. Modelling of Electrolyte Flow and Its Related Transport Processes in Aluminium Reduction Cells. *Light Metals*, pages 323–331, 1994.

[6] R. B. Bird, W. E. Stewart, and E. N. Lightfoot. *Transport Phenomena: Revised Second Edition*. John Wiley & Son, 2007.

[7] V. Bojarevics and K. Pericleous. Solutions for the metal-bath interface in aluminium electrolysis cells . *Light Metals*, pages 569–574, 2009.

[8] V. Bojarevics and A. Roy. Bubble transport by electro-magnetophoretic forces at anode bottom of aluminium cells. *Light Metals*, pages 549–554, 2011.

[9] J. U. Brackbill, D. B. Kothe, and C. Zemach. A continiuum method for modeling surface tension. *Journal of Computational Physics*, 100:335–354, 1992.

[10] C. E. Brennen. *Fundamentals of Multiphase Flow*. Cambridge University Press, 2006.

[11] D. A. G. Bruggeman. Berechnung verschiedener physikalischer Konstanten von heterogenen Substanzen. I. Dielektrizittskonstanten und Leitfhigkeiten der Mischkrper aus isotropen Substanzen. *Annalen der Physik*, 416(7):636–664, 1935.

[12] A. Caboussat, L. I. Kiss, J. Rappaz, K. Vekony, A. Perron, S. Renaudier, and O. Martin. Large gas bubbles under the anodes of aluminium electrolysis cells. *Light Metals*, pages 581–586, 2011.

[13] H. B. Callen. *Thermodynamics and an introduction to thermostatistics, 2nd edition.* Wiley, 1985.

[14] L. Cassayre, T. A. Utigard, and S. Bouvet. Visualizing Gas Evolution on Graphite and Oxygen-Evolving Anodes. *Journal of Metals*, 5:41–45, 2002.

[15] D. C. Chenosis and A. F. LaCamera. The Influence of Gas-driven Circulation on Alumina Distribution and interface Motion in a Hall-Héroult Cell. *Light Metals*, pages 211–220, 1990.

[16] A. K. Chesters. The Modelling of Coalescence Processes in Fluid-Liquid Dispersions: A Review of Current Understanding. *Chemical Engineering Research and Design*, 69:259–270, 1991.

[17] C. Y. Chow. Flow around a Nonconducting Sphere in a Current-Carrying Fluid. *The Physics of Fluids*, 9(5):933–936, 1966.

[18] C. Y. Chow and D. F. Billings. Current-Carrying Fluid Past a Nonconducting Sphere at Low Reynolds Number. *The Physics of Fluids*, 10(4):871–873, 1967.

[19] R. Clift, J. R. Grace, and M. E. Weber. *Bubbles, Drops and Particles, Dover Edition.* Dover Publishing, 2005.

[20] COMSOL. Comsol - Multiphysics Modeling and Simulation Software. `http://www.comsol.com/`, May 2012.

[21] M. A. Cooksey, M. P. Taylor, and Chen J. J. J. Resistance Due To Gas Bubbles in Aluminium Reduction Cells. *Journal of Metals*, 2:51–57, 2008.

[22] M. A. Cooksey and Yang W. PIV Measurements on Physical Models of Aluminium Reduction Cells. *Light Metals*, pages 359–365, 2006.

[23] A. Dahlkild. Modelling the two-phase flow and current distribution along a vertical gas-evolving electrode. *Journal of Fluid Mechanics*, 428:249–272, 2001.

[24] P .A. Davidson. *Turbulence: An introduction for scientists and engineers.* Oxford University Press, 2004.

[25] E. Dernedde and E. L. Cambridge. Gas induced circulation in an aluminium reduction cell. *Light Metals*, pages 111–122, 1975.

[26] M. A. Doheim, A. M. El-Kersh, and M. M. Ali. Computational Modeling of Flow in Aluminium Reduction Cells Due to Gas Bubbles and Electromagnetic Forces. *Metallurgical and Materials Transactions B*, 38B:113–119, 2007.

[27] R. C. Dorward. Reaction Between Aluminum and Graphite in the Presence of Cryolite. *Metallurgical Transactions*, 4:386–388, 1973.

[28] D. A. Drew and S. L. Passmann. *Theory of Multicomponent Fluids. Applied Mathematical Sciences, Vol 135.* Springer, 1999.

[29] I. Eick, A. Klaveness, C. Rosenkilde, M. Segatz, H. Gudbrandsen, A. Solheim, E. Skybakmoen, and K. E. Einarsrud. Voltage and Bubble Release Behaviour in a Laboratory Cell at Low Anode-Cathode Distance. *10th AASTC, Launceston, Tasmania*, pages –, 2011.

[30] K. E. Einarsrud. The effect of detaching bubbles on alumunium-cryolite interfaces: An experimental and numerical investigation. Master's Thesis, Norwegian University of Science and Technology (NTNU), 2008.

[31] K. E. Einarsrud. The effect of detaching bubbles on alumunium-cryolite interfaces: An experimental and numerical study. *Metallurgical and Materials Transactions B*, 41(3):560–573, 2010.

[32] K. E. Einarsrud and S T. Johansen. On the Modelling of Anodic Bubbles in Hall-Héroult cells . *Proceedings of the 8th Int. Conf. on CFD in Oil & Gas, Metallurgical and Process Industries, SINTEF/NTNU, Trondheim, Norway*, page 135, 2011.

[33] K. E. Einarsrud and S T. Johansen. Modelling of bubble behaviour in aluminium reduction cells. *Progress in Computational Fluid Dynamics*, 12(2/3):119–130, 2012.

[34] K. E. Einarsrud, S. T. Johansen, and I. Eick. Anodic bubble behaviour in Hall-Héroult cells. *Light Metals*, pages 875–880, 2012.

[35] K. E. Einarsrud and E. Sandnes. Anodic Voltage Oscillations in Hall-Héroult Cells . *Light Metals*, pages 555–560, 2011.

[36] J. W. Evans and D. P. Ziegler. The Electrolytic Production of Aluminium. *Electrochemical engineering*, 5(4), 2007.

[37] P. Fellner, K. Grjotheim, and H. Kvande. Current Efficiency Measurements in Laboratory Aluminium Cells – VI. Back Reactions. *Canadian Metallurgical Quarterly*, 23(4):421–425, 1984.

[38] S. Fortin, M. Gerard, and A. J. Gesing. Physical Modelling of Bubble Behaviour and Gas Release from Aluminium Reduction Cell Anodes. *Light Metals*, pages 721–741, 1984.

[39] GAMBIT. GAMBIT - Geometry And Mesh Building Intelligent Toolkit. `http://www.fluentusers.com/`, May 2012.

[40] B. Gao, X. Hu, J. Xu, Z. Shi, Z. Wang, and Qiu Z. Study on Bubble Behavior on Anode in Aluminum Electrolysis-Part II. *Light Metals*, pages 467–470, 2006.

[41] J. F. Gerbeau, T. Lelievre, and C. Le Bris. *Mathematical Methods for the Magnetohydrodynamics of Liquid Metals*. Oxford Science Publications, 2003.

[42] J. P. Givry. Computer Calculation of Magnetic Effects in the Bath of Aluminum Cells. *Trans. Met. Soc. AIME*, 239:1161–1166, 1967.

[43] D. J. Griffiths. *Introduction to Electrodynamics, Third edition*. Prentice Hall, 1999.

[44] K. Grjotheim, C. Krohn, M. Malinovský, K. Matiasovský, and J. Thonstad. *Aluminium Electrolysis - Fundamentals of the Hall-Héroult Process, 2nd edition.* Aluminium-Verlag, 1982.

[45] K. Grjotheim, C. Krohn, R. Næumann, and K. Tørklep. On the application of Radiotracers in the aluminium industry. *Light Metals*, pages 133–145, 1971.

[46] K. Grjotheim and H. Kvande. *Understanding the Hall-Héroult Process for Production of Aluminium.* Aluminium Verlag, 1986.

[47] K. Grjotheim and H. Kvande. *Introduction to Aluminium Electrolysis, 2nd edition.* Aluminium Verlag, 1993.

[48] T. Haarberg, A. Solheim, S. T. Johansen, and P. A Sollie. Effect of Anodic Gas Release on Current Efficiency in Hall-Héroult Cells. *Light Metals*, pages 475–481, 1998.

[49] S. Hardt and F. Wondra. Evaporation model for interfacial flows based on a contiuum-field representation of the source terms . *Journal of Computational Physics*, 227:5871–5895, 2008.

[50] C. W. Hirt and B. D. Nichols. Volume of Fluid (VOF) Method for the Dynamics of Free Boundaries. *Journal of Computational Physics*, 39:201–225, 1981.

[51] M. J. Hounslow, l R. L. Ryal, and V. R. Marshall. A Discretized Population Balance for Nucleation, Growth and Aggregation. *AIChE Journal*, 34(11):1821–1832, 1998.

[52] J. Hua and C.H. Wang. Numerical simulation of bubble-driven liquid flows. *Chemical Engineering Science*, 55:4159–4173, 2000.

[53] T. M. Hyde and B. J. Welch. The Gas under Anodes in Aluminium Smelting Cells Part I: Measuring and Modelling Bubble Resistance under Horizontally Oriented Electrodes. *Light Metals*, pages 333–340, 1997.

[54] International Aluminium Institute. `http://www.world-aluminium.org/`, May 2011.

[55] S. T. Johansen, J. Wu, and W. Shyy. Filter-based unsteady rans computations. *International Journal of Heat and Fluid Flow*, 25:10–21, 2004.

[56] S. T. Johansen, T. Ytrehus, and K. E. Einarsrud. Modeling of Multiphase Flows. Lecture notes EP8404, PhD Course, Norwegian University of Science and Technology (NTNU), January 2011.

[57] S. F. Jones, G. M. Evans, and K. P. Galvin. Bubble nucleation from gas cavities - a review . *Advances in Colloid and Interface Science* , 80:27–50, 1999.

[58] S. F. Jones, G. M. Evans, and K. P. Galvin. The cycle of bubble production from a gas cavity in a supersaturated solution . *Advances in Colloid and Interface Science* , 80:51–84, 1999.

[59] J. T. Keniry, G. C. Barber, M. P. Taylor, and Welch B. J. Digital processing of anode current signals: An opportunity for improved cell diagnosis and control. *Light Metals*, pages 1225–1232, 2001.

[60] L. I. Kiss. Transport processes and bubble driven flow in the Hall-Héroult cell. *5th Int. Conf. on CFD in Proc. Ind., CSIRO, Melbourne, Australia*, pages 1–7, 2006.

[61] L. I. Kiss, S. Poncsak, D. Toulouse, A. Perron, A. Liedtke, and V. Mockowiak. Detachment of bubbles from their nucleation sites. *Multiphase Phenomena and Simulation in Materials Processes*, pages 159–168, 2004.

[62] L. I. Kiss and Poncsák S. Effect of the bubble growth mechanism on the spectrum of voltage fluctuations in the reduction cell . *Light Metals*, pages 217–223, 2002.

[63] L.I Kiss, S. Poncsák, and J. Antille. Simulation of the Bubble Layer in the Aluminum Electrolysis Cells. *Light Metals*, pages 559–564, 2005.

[64] A. Kisza, J. Kazmierczak, J. Thonstad, T. Eidet, and J. Hives. The Kinetics and Mechanism of the Electrode Reactions in Aluminium Electrolysis. *Light Metals*, pages 423–428, 1999.

[65] A. Kisza, J. Thonstad, and J. Hives. Mechanism and Kinetics of the Anodic Reaction in Cryolite Melts. II. The influence of AlF_3 (11 wt %) at Different Al_2O_3 Content. *Polish Journal of Chemistry*, 74:1003–1010, 2000.

[66] P. Kloucek and M. V. Romerio. The detachment of bubbles under a porous rigid surface during aluminium electrolysis . *Mathematical Models and Methods in Applied Sciences*, 12(11):1617–1652, 2002.

[67] O. Kobbeltvedt. Dissolution kinetics for alumina in cryolite melts. Distribution of alumina in the electrolyte of industrial aluminium cells. PhD thesis 1997:37, Norwegian University of Science and Technology (NTNU), 1997.

[68] O. Kobbeltvedt and B. P. Moxnes. On the Bath Flow, Alumina Distribution and Anode Gas Release in Aluminium Cells. *Light Metals*, pages 369–376, 1997.

[69] N. I. Kolev. *Multiphase Flow Dynamics 3: Turbulence, Gas Absorption and Release, Diesel Fuel Properties*. Springer, 2007.

[70] R. Kuboi, I. Komasawa, and T. Otake. Collision and Coalescence of Dispersed Drops in Turbulent Liquid Flow. *Journal of Chemical Engineering of Japan*, 4(5):423–424, 1972.

[71] L. D. Landau and Lifshitz E. M. *Fluid Mechanics, 2nd Edition, Course of Theoretical Physics, Volume 6*. Elsevier, 1987.

[72] B. E. Launder, G. J. Reece, and W. Rodi. Progress in the development of a reynolds-stress turbulent closure. *Journal of Fluid Mechanics*, 68(3):537–566, 1975.

[73] J. A. Leistra and P. J. Sides. Hyperpolarization at Gas Evolving Electrodes - II: Hall-Héroult Electrolysis. *Electrochimica Acta*, 33(12):1761–1766, 1988.

[74] A. Linnerud. CFD Analysis of a Microfluidics Lab-on-a-Chip Component. MSc thesis, Norwegian University of Science and Technology (NTNU), 2010.

[75] P. Liovic and D. Lakehal. Interface-turbulence interactions in large-scale bubbling processes. *International Journal of Heat and Fluid Flow*, 28(1):127–144, 2007.

[76] P. Liovic and D. Lakehal. Multi-physics treatment in the vicinity of arbitrarily deformable gas-liquid interfaces. *Journal of Computational Physics*, 222:504–535, 2007.

[77] P. Liovic, M. Rudman, J. L. Liow, D. Lakehal, and D. Kothe. A 3d unsplit-advection volume tracking algorithm with planarity-preserving interface reconstruction. *Computers & Fluids*, 35:1011–1032, 2006.

[78] L. P. Lossius. Hydro Aluminium, Årdalstangen, Norway. Private communication, 2010.

[79] H. Luo. Coalescence, Breakup and Liquid Circulation in Bubble Column Reactors. PhD Thesis 105, Norwegian Institute of Technology (NTH), 1993.

[80] MATLAB. MATLAB - the language of scientific computing. `http://www.mathworks.com/products/matlab/`, May 2012.

[81] J. C. Maxwell. *A Treatise on Electricity and Magnetism, Unabridged 3rd edition.* Dover Publishing, 1954.

[82] D. Montgomery. *Design and analysis of experiments.* Wiley and Sons, 2009.

[83] M. J. Moran and H. N. Shapiro. *Fundamentals of Engineering Thermodynamics, Fifth Edition.* John Wiley and Sons, 2008.

[84] R. J. Moreau and J. W. Evans. An Analysis of the Hydrodynamics of Aluminum Reduction Cells. *Journal of the Electrochemical Society*, 131(10):2251–2259, 1984.

[85] H. Numata and J. O'M. Bockris. Interactions of Gases in Molten Salts: Carbon Dioxide and Oxygen in Cryolite Alumina Melts. *Metallurgical and Materials Transactions B*, 15(1):39–46, 1984.

[86] H. Oertel. *Prandtl's Essentials of Fluid Mechanics, Second Edition.* Springer, 2004.

[87] E. Olsen, S. Rolseth, and B. P. Moxnes. Probe for assessing the height of gas induced waves at the bath-metal interface in Hall-Héroult cells. *Light Metals*, pages 27–41, 1999.

[88] openFOAM. openFOAM - open source CFD. `http://www.openfoam.com/`, May 2012.

[89] K. Outsuki, Y. Nakagawa, and K. Nakazawa. Artificial Acceleration in Accumulation Due to Coarse Mass-Coordinate Divisions in Numerical Simulation. *ICARUS*, 83:205–215, 1990.

[90] K. A. Paulsen. Light Metal Electrolysis II. Lecture notes, Norwegian University of Science and Technology (NTNU), May 2009.

[91] A. Perron, K. I. Kiss, and Poncsak S. Regimes of the Movement of Bubbles under the Anode in an Aluminium Electrolysis Cell. *Light Metals*, pages 565–570, 2005.

[92] A. L. Perron, L. I. Kiss, and S. Poncsák. Mathematical model to evaluate the ohmic resistance caused by the presence of a large number of bubbles in Hall-Héroult cells . *Journal of Applied Electrochemistry*, 37:303–310, 2007.

[93] S. Poncsák, Kiss L. I., and Bui R. T. Mathematical modelling of the growth of gas bubbles under the anode in the aluminium electrolysis cells. *Light Metals (Met. Soc.)*, pages 57–72, 1999.

[94] S. Poncsák, L. Kiss, D. Toulouse, A. Perron, and S. Perron. Size Distribution of the Bubbles in the Hall-Héroult cells. *Light Metals*, pages 457–462, 2006.

[95] K. Popov, S. Djokic, and Grgur B. *Fundamental Aspects of Electrometallurgy*, pages 272–289. Springer, 2002.

[96] V. Potocnik. Modelling of Metal-Bath Interface Waves in Hall-Héroult Cells using ESTER/PHOENICS. *Light Metals*, pages 227–235, 1988.

[97] S. Prasad. Studies on the Hall-Héroult Aluminum Electrowinning Process . *Journal of Brazilian Chemical Society*, 11:245–251, 2000.

[98] W. H. Press, S. A. Teukolsky, W. T. Vetterling, and B. P. Flannerly. *Numerical Recipies in C++: The Art of Scientific Computing, second edition.* Cambridge University Press, 2005.

[99] M. J. Prince and H. W. Blanch. Bubble Coalescence and Break-Up in Air Sparged Bubble Columns. *AIChE Journal*, 36(10):1485–1499, 1990.

[100] J. M. Purdie, M. Bilek, M. P. Taylor, Zhang W. D., B. J. Welch, and J. J. Chen. Impact of Anode Gas Evolution on Electrolyte Flow and Mixing in Aluminium Electrowinning Cells. *Light Metals*, pages 355–360, 1993.

[101] Alcorn T. R., C. J. McMinn, and A. T. Tabereaux. Current Efficiency in Aluminium Electrolysis by Anode Gas Analysis. *Light Metals*, pages 683–695, 1988.

[102] S. Rørvik and H. A. Øye. A method for characterization of anode pore structure by image analysis. *Light Metals*, pages 561–568, 1996.

[103] P. G. Saffman and J. S. Turner. On the collision of drops in turbulent clouds. *Journal of Fluid Mechanics*, 1:16–30, 1956.

[104] P. Sagaut. *Large Eddy Simulation for Incompressible Flows: An Introduction.* Springer Verlag, 2005.

[105] R. Scardovelli and S. Zaleski. Direct Numerical Simulation of Free-Surface and Interfacial Flow. *Annual Review of Fluid Mechanics*, 31:567–603, 1999.

[106] L. E. Scriven. On the dynamics of phase growth. *Chemical Engineering Science*, 10(1):1–18, 1959.

[107] M. Segatz, D. Vogelsang, C. Droste, and P. Baeckler. Modelling of Transient Magneto-Hydrodynamic Phenomena in Hall-Héroult Cells. *Light Metals*, pages 361–368, 1993.

[108] D. S. Severo, V. Gusberti, A. F. Schneider, E. C. V. Pinto, and V. Potocnik. Comparison of various methods for modeling the metal-bath interface. *Light Metals*, pages 413–418, 2008.

[109] T. H. Shih, W. W. Liou, A. Shabbir, Z. Yang, and J. Zhu. A New k-ϵ Eddy-Viscosity Model for High Reynolds Number Turbulent Flows - Model Development and Validation. *Computers & Fluids*, 24:227–238, 1995.

[110] A. Solheim. The Density of Molten NaF-LiF-AlF_3-CaF_2-Al_2O_3 in Aluminium Electrolysis. *Aluminum Transactions*, 2(1):161–168, 2000.

[111] A. Solheim, S. T. Johansen, S. Rolseth, and J. Thonstad. Gas induced bath circulation in aluminium reduction cells. *Journal of Applied Electrochemistry*, 19:703–712, 1989.

[112] K. Stüben. A review of algebraic multigrid. *Journal of Computational and Applied Mathematics*, 128:281–309, 2001.

[113] G. Suttner and H. W. Yorke. Early dust evolution in protostellar accreation disks. *The Astrophysical Journal*, 551:461–477, 2001.

[114] H. Q. Tang and N. Urata. Metal Pad Wave Analysis Using a Fast Anode Lowering Method. *Light Metals*, pages 387–394, 1997.

[115] H. Tennekes and J. L. Lumley. *A first course in turbulence, Eighteenth printing.* The MIT press, 2001.

[116] J. Thonstad, P. Fellner, G. M Haarberg, J. Híves, H. Kvande, and Å. Sterten. *Aluminium Electrolysis - Fundamentals of the Hall-Héroult Process, 3rd edition.* Aluminium Verlag, 2001.

[117] J. Thonstad, H. D. Kleinschrodt, and H. Vogt. Improved design equation for the interelectrode voltage drop in industrial aluminium cells. *Light Metals*, pages 427–432, 2004.

[118] M. Thumfart. Surface Tension Dominated Flows: Observations with ANSYS FLUENT. Ansys: Multiphase Flows, 23rd - 24th June, 2010.

[119] K. Tøerklep, K. Kalgraf, and T. Nordbø. Alumina distribution in point-fed Hall-Héroult cells. *Light Metals*, pages 377–386, 1997.

[120] K. Tørklep and H. A. Øye. Viscosity of NaF-AlF_3-Al_2O_3 melt mixtures. *Electrochimica Acta*, 25(2):229–235, 1980.

[121] A. Troshko and S. Mohan. Drag laws. *Fluent News - Summer 2005*, pages 34–35, 2005.

[122] T. A. Utigard and J. M. Toguri. Maragoni Flow in the Hall-Héroult Cell. *Light Metals*, pages 273–281, 1991.

[123] K. Vasshaug. The influence of the formation and dissolution of aluminium carbide on the cathode wear in aluminium electrolysis cells. PhD thesis No. 106, Norwegian University of Science and Technology (NTNU), 2008.

[124] H. K. Versteeg and Malalasekera W. *An Introduction to Computational Fluid Dynamics: The Finite Volume Method, second edition.* Pearson Education Limited, 2007.

[125] H. Vogt. On the supersaturation of gas in the concentration boundary layer of gas evolving electrodes. *Electrochimica Acta*, 25:527–531, 1980.

[126] H. Vogt. The rate of gas evolution at electrodes-I: An estimate of the efficiency of gase evolution from the supersaturation of electrolyte adjacent to a gas-evolving electrode. *Electrochimica Acta*, 29(2):167–173, 1984.

[127] H. Vogt. Studies on gas-evolving electrodes: The concentration of dissolved gas in electrolyte bulk. *Electrochimica Acta*, 30:265–270, 1985.

[128] H. Vogt. Contribution to the interpretation of the anode effect. *Electrochimica Acta*, 42:2695–2705, 1997.

[129] H. Vogt and J. Thonstad. The voltage of alumina reduction cells prior to the anode effect. *Journal of Applied Electrochemistry*, 32:241–249, 2002.

[130] Y. G. Waghmare, C. A. Dorao, H. A. Jakobsen, C. F. Knopf, and R. G. Rice. Bubble Size Distribution for A Bubble Column Reactor Undergoing Forced Oscillations. *Industrial and Engineering Chemistry Research*, 48:1786–1796, 2009.

[131] W. E. Wahnsiedler. Hydrodynamic modeling of commercial Hall-Héroult Cells. *Light Metals*, pages 269–287, 1987.

[132] X. Wang, R. D. Peterson, and A. T. Tabereaux. A Multiple Regression Equation for the Electrical Conductivity of Cryolite Melts. *Light Metals*, pages 247–255, 1993.

[133] X. Wang and A. T. Taberaux. Anodic phenomena - Observations of anode overvoltage and gas bubbling during aluminium electrolysis. *Light Metals*, pages 239–247, 2000.

[134] Z. Wang, B. Gao, H. Li, Z. Shi, X. Lu, and Qiu Z. Study on Bubble Behavior on Anode in Aluminum Electrolysis-Part I. *Light Metals*, pages 463–466, 2006.

[135] F. M. White. *Fluid Mechanics, Fifth Edition.* McGraw-Hill, 2003.

[136] D. C. Wilcox. Re-assessment of the scale-determining equation for advanced turbulence models. *AIAA Journal*, 26:1414–1421, 1988.

[137] M. W. Williams, D. B. Kothe, and E. G. Puckett. *Accuracy and convergence of continuum surface-tension models. In: W. Shyy and R. Narayanan, Editors, Fluid Dynamics at Interfaces*, pages 294–305. Cambridge University Press, 1998.

[138] G. Wornell. *Signal Processing with Fractals: A Wavelet based approach.* Cambridge, 1995.

[139] J. Xue and H. A. Øye. Bubble behaviour - Cell voltage oscillation during aluminium electrolysis and the effects of sound and ultrasound. *Light Metals*, pages 265–271, 1995.

[140] V. Yakhot, S. A. Orszag, S. Thangam, T. B. Gatski, and C. G. Speziale. Development of turbulence models for shear flows by a double expansion technique. *Physics of Fluids A*, 4(7):1510–1520, 1992.

[141] W. Yang and M. A. Cooksey. Effect of Slot Height and Width on Liquid Flow in Physical Models of Aluminium Reduction Cells. *Light Metals*, pages 451–456, 2007.

[142] D. L. Youngs. *Time-dependent multi-material flow with large fluid distortion, in Numerical Methods for Fluid Dynamics*, pages 273–285. Academic Press, 1982.

[143] C. Zhang. Liquid metal flows driven by gas bubbles in static magnetic fields. PhD thesis, TU Dresden, 2008.

[144] C. Zhang, S. Eckert, and G. Gerbeth. Experimental study of single bubble motion in a liquid metal column exposed to a DC magnetic field. *International Journal of Multiphase Flow*, 31:824–842, 2005.

[145] C. Zhang, S. Eckert, and G. Gerbeth. The flow structure of a bubble-driven liquid metal jet in a horizontal magnetic field. *Journal of Fluid Mechanics*, 575:57–82, 2008.

[146] D. Zhang, N. G. Deen, and J. A. M. Kuipers. Numerical simulation of the dynamic flow behaviour in a bubble column: A study of closures for turbulence and interface forces . *Chemical Engineering Science*, 61(23), 2006.

[147] K. Zhang, Y. Feng, P. Schwarz, M. Cooksey, and Z. Wang. Numerical Investigation of Bubble Dynamics in Aluminium Electrolytic Cells. *Light Metals*, pages 881–886, 2012.

[148] W. D. Zhang, Chen J. J. J., and Taylor M. P. Similarity Analysis of Gas Induced Bath Flow in Hall-Héroult cells. *CHEMCEA 90*, pages 1–8, 1990.

[149] J. Zoric, R. I. Rousa, and J. Thonstad. Mathematical modelling of industrial aluminium cells with prebaked anodes Part I: Current distribution and anode shape. *Journal of Applied Electrochemistry*, 27:916–927, 1997.

[150] J. Zoric and A. Solheim. On gas bubbles in industrial aluminium cells with prebaked anodes and their influence on the current distribution . *Journal of Applied Electrochemistry*, 30:787–794, 2000.

Appendix A

Surface Tension in FLUENT

Several industrial immiscible flows are at an initial stage dominated by surface tension, for instance the formation of bubbles in metallurgical flows (Thumfart [118]) and capillary effects in microfluidics (Linnerud [74]). A common approach to these kinds of problems is to use a Volume of Fluid (VOF) method, with sharp interfaces (Hirt and Nichols [50]), in conjecture with a Contiuum Surface Force (CSF) as propsed by Brackbill et al. [9]. Although the VOF-CSF model has successfully been adopted to problems where surface tension effects are secondary, surface tension driven flows appear to be prone to instabilities and inaccuracies as shown by for instance Thumfart [118].

One possible explanation for the observed discrepancies are the so called parasitic currents (cf. Williams et al. [137]) originating from the CSF formulation, in which the surface tension is represented as a continuous volumetric force which acts in the immediate neighborhood of the interface. The CSF formulation relies upon an accurate representation of the interface curvature, typically determined by means of the gradient in volume fraction. Hence, a well resolved interface is crucial in order for surface tension to behave as expected. As shown by Williams et al. [137], the resolution requirement can be relaxed by describing the curvature by means of a higher order method. However, at the current time, these high order methods are unavailable in FLUENT.

In practical calculations, the computational domain typically consists of more than one bubble and simulations are often run for long times in order to obtain average properties. In order to minimize the computational cost, the required resolution is often relaxed, resulting in the inaccuracies reported in the literature. In the following, the influence of the various parameters and models available in FLUENT, for a surface tension dominated system, are investigated.

A.1 Model setup

All of the following simulations are performed in a rectangular geometry as sketched in figure A.1. Gravity is disabled, so that a (stable) cavity placed in the domain should retain its original position and shape. Three different mesh densities are used; $a = 20,\ 40,\ 60$.

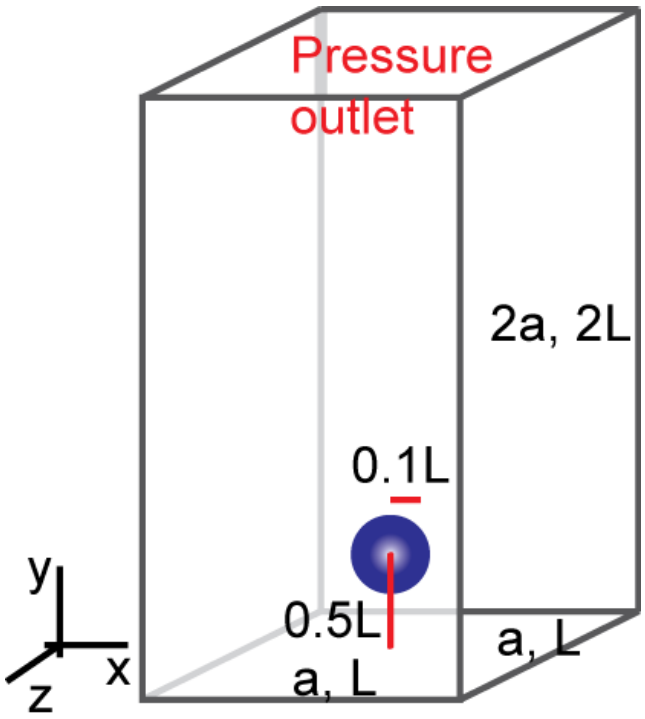

Figure A.1: Sketch of rectangular geometry used in simulations. A gas cavity (blue) with radius $0.1L$ is patched into the domain $0.5L$ above the bottom surface. The z-direction is used only in 3D-simulations. For all cases, $L = 10$ cm.

Simulations are run using the transient formulation with a constant time step of 0.001 s until a final time of 1 s is reached. The multiphase nature is modeled by the explicit, two-phase VOF model, using the implicit body force formulation, to increase stability further. The phase fraction equation is discretized by means of the Geo-reconstruct (PLIC) scheme of Hirt and Nichols [50]. The gaseous phase (secondary phase) is patched into the domain and the RP-command (*rpsetvar 'patch/vof? #t*) is used in order to initially obtain a smooth surface. All other settings are kept at their default values, unless otherwise noted.

The liquid phase is assumed to have a density of 2000 kg/m^3 and viscosity $2.5{\cdot}10^{-3}$ Pa·s, while the gaseous phase is given a density of 1 kg/m^3 and viscosity $2{\cdot}10^{-5}$ Pa·s. The surface tension is set to 0.1 N/m.

A.2 Results

A.2.1 The influence of resolution

Figures A.2 and A.3 show the evolution of the bubble surface over time using different resolution in 2 and 3D, respectively, compared to the bubble surface when surface tension is deactivated (using a=40).

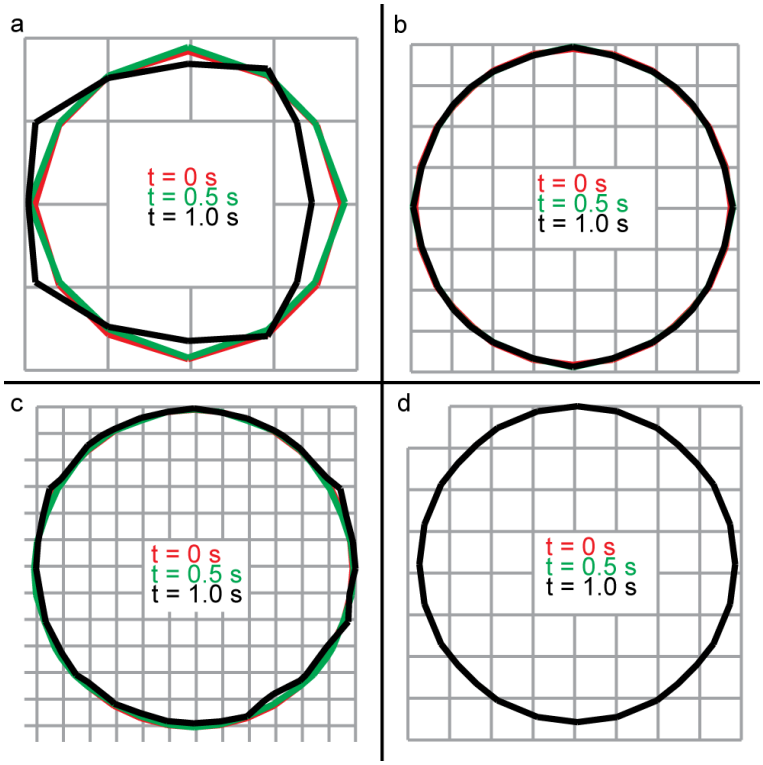

Figure A.2: Results from 2D simulation. Simulated bubble surface at three different time instances for three different mesh densities, a = 20, 40 and 60 shown in figures a-c, respectively, compared to the case of no surface tension (figure d).

Evidently, as seen from figures A.2 and A.3, the mesh density has a significant impact on the predicted bubble surface. For the 2D simulations, the case with a=40 appears to predict a stable bubble surface. The finest resolution (a=60) does however show some tendency to instability. Considering the simulations shown in figures A.2a and A.2b, the (global) CFL number is (on average) in the range of 0.01, while it is 0.1 in figure A.2c. Reducing the time-step for the 2D simulations, in order to obtain similar CFL numbers, does not change the predicted surface significantly. The interfaces shown in figure A.2 show some discrepancies, they are all in of the same order of the grid resolution and thus acceptable.

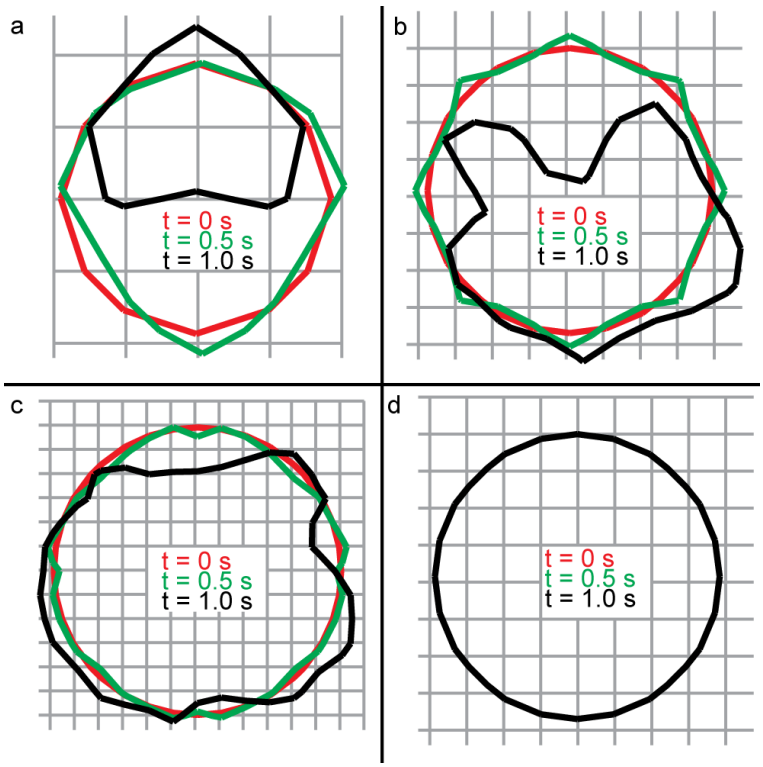

Figure A.3: Results from 3D simulation. Simulated bubble surface at three different time instances for three different mesh densities, $a = 20$, 40 and 60 shown in figures a-c, respectively, compared to the case of no surface tension (figure d).

Considering the 3D simulations shown in figure A.3, the discrepancies are large and bubbles become strongly deformed as time passes. Allowing the simulation to evolve further entirely disrupts the bubble, hence violating mass conservation.

Although the current time step is thought to be acceptable, simulations are performed with a reduced time step, $\Delta t = 0.0001s$, for comparison. Figure A.4 shows the evolution of the interface on the a=40 mesh.

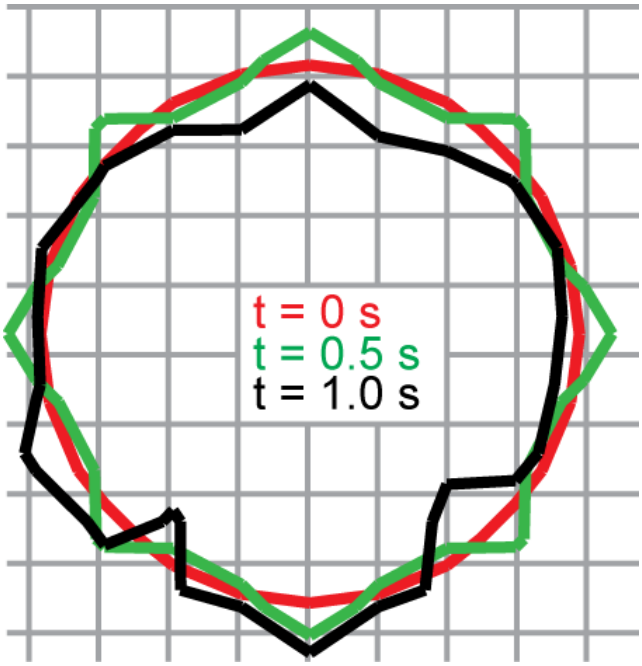

Figure A.4: 3D simulation of bubble on medium mesh (a=40) using reduced time-step (Δt = 0.0001s).

As seen from figure A.4, the predicted interface is somewhat improved by using a smaller time-step (compared to figure A.3b). However, non-physical deformations persist, in addition to increased computational time.

A.2.2 The influence of discretization

Figure A.5 shows the final surface of a 3D-bubble using the $a = 40$ mesh using the four different discretization schemes available for the VOF-model in FLUENT.

As seen from figure A.5, the choice of VOF-discretization has a huge impact upon the predicted interface. The diffusive nature of the non-sharp schemes is clearly visible as the bubbles appear to contract (i.e. the volume-fraction is smeared across more cells). Although the shape of the bubble is somewhat better represented using the non-sharp

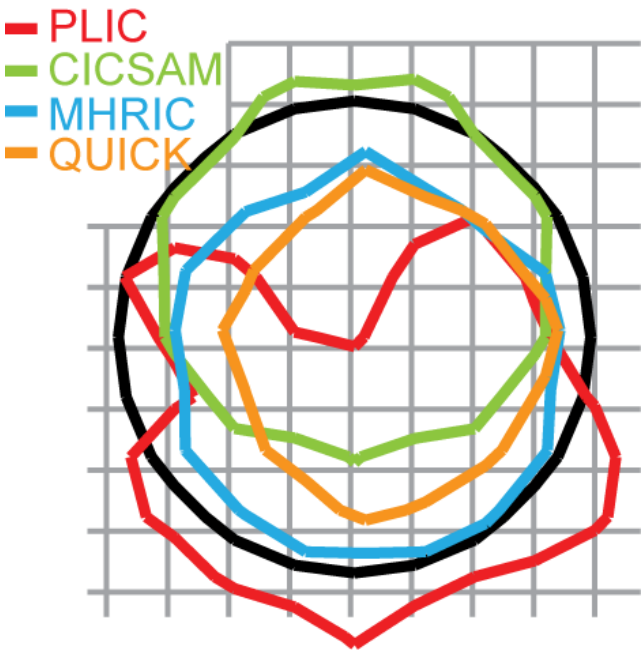

Figure A.5: 3D simulation of bubble on medium mesh (a=40) using different discretization schemes for VOF, compared to the initial bubble surface (black).

schemes, the position of the interface becomes less accurate; a critical issue for the application of mass transfer and force distribution on the surface.

A.2.3 The continuum surface stress model

A promising improvement to the above CSF-model is the continuum surface stress model (CSS) introduced in FLUENT 14 (released Q1-2012), which does not require an explicit calculation of surface curvature. Hence, it is expected to perform *more* physically in under-resolved regions [2]. Figure A.6a shows the evolution of a bubble on the a=20 mesh (in 3D).

Evidently, as seen from the figure, the CSS formulation *greatly* improves the stability of the interface. Spurious currents are however still present, but reduced by approximately 40% compared to the CSF formulation.

Figure A.6b shows the evolution of the bubble with both the CSS-method and the surface tension limiter introduced in equation 16.5 enabled. As seen from the figure, the final state is comparable to that of the pure CSS-approach. The intermediate interphase position, i.e. t=0.5 s, is however better, only deviating slightly from the initial value. Moreover, spurious velocities are reduced by 50% compared to the CSF formulation.

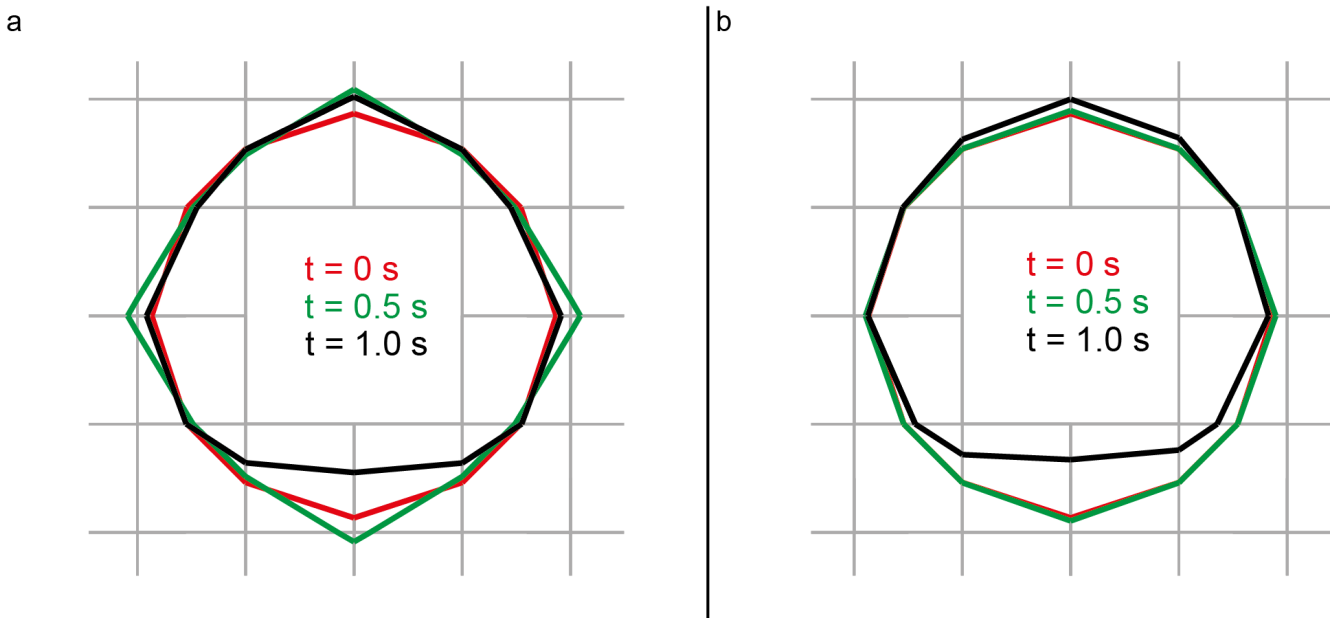

Figure A.6: 3D simulation of bubble on coarse mesh (a=20) using the CSS-method (a) and a combination of the CSS-method and the surface tension limiter defined in equation 16.5 (b).

A.3 Closing remarks regarding surface tension

It is shown that the stability of the interface is coupled to the spatial and temporal resolution as well as the number of dimensions used in the simulation. The deformation of the interface is most strong for 3D simulations, even when these are run with identical settings as the 2D cases.

As expected, 3D simulations are improved with a finer resolution, but necessarily comes with a higher computational cost. The choice of discretization schemes for the phase fraction influences the overall shape of the interface, but neither of the schemes investigated here stand out as being superior.

The newly released CSS-model provides a significant improvement over the traditional CSF, both with respect to interface stability and reduction of spurious velocities. As the CSS-model can handle variable surface tension, additional improvements can be made by introducing limiters on the surface tension, ensuring that it is active only in regions of interest.

Appendix B

Enhanced PBM evolution due to discretization

As shown by Outsuki et al. [89], studying the evolution of galaxies by means of a PBM, the choice of the discretization factor q, (cf. equation 14.45) can severely influence the accuracy of a calculation. The system studied by Outsuki et al. [89] is of astronomical proportions; particle classes spanning 20 orders of magnitude and time scales of the order 10^5 years. In this case, the typical time required to form the largest particle class differed by a factor of 10 when comparing a $q = \sqrt{2}$ distribution to a coarse $q = 8$ distribution. Based on their findings, Outsuki et al. [89] conclude that the ratio should be $\sqrt{2}$ at most.

Although the above astronomical system is somewhat extreme, enhanced evolution due to discretization is believed to occur in the current system as well as it is a mathematical, rather than a physical effect. However, due to the typically smaller system size and shorter time intervals its relative importance is expected to be smaller than that observed by Outsuki et al. [89], as seen from results obtained using a $q = 2$ distribution on small systems (cf. Hounslow et al. [51] and Waghmare et al. [130]), obtaining good accordance with experimental results.

For the current PBM model, a discretization factor of $q = \sqrt{2}$ is inadequate when dealing with coalescence, as it results in idle bubble classes. For instance, considering a population with volumes V_i=1, $\sqrt{2}$, 2 ..., an interaction between two bubbles of volume V_1 results in a bubble of volume V_3, thus leaving the class with volume V_2 idle. Hence, the finest distribution used in the present case is $q = 2$. In the following, the $q = 2$ distribution is compared results obtained with $q = 4$ in three separate cases.

In order to investigate acceleration in cases relevant to coupled simulations, the number of bubble classes is kept relatively low; 9 classes in the $q = 2$ and 5 classes in the $q = 4$ class, resulting in a maximal bubble volume $V_M = 256V_0$ in both cases. The smallest bubble class is given a diameter of 0.5 mm, corresponding to the smallest bubbles observed by Xue and Øye, [139]. Although both distributions start and end with the same *mean* values,

the internal boundaries of each class is different as shown in figure 14.13. This neccesarily results in a different *internal* distribution of bubbles.

All results presented in the following are obtained using the ODE45 solver in MATLAB, with initial bubble distribution $n_1 = 0.9$. All other bubble classes are initialized to zero.

B.1 Evolution by coalescence with contant kernel

Consider first a system which evolves as a result of coalescence. Assuming a constant coalescence kernel given as $\Gamma = 10^{-6}$ m^3/s with no other interactions, the overall behaviour of the system should be similar to that shown in figure 14.15, that is, the global *number density* should decrease as time increases, while the system mass should be constant. Figure B.1 shows a comparison between the total number density with fine and coarse distribution.

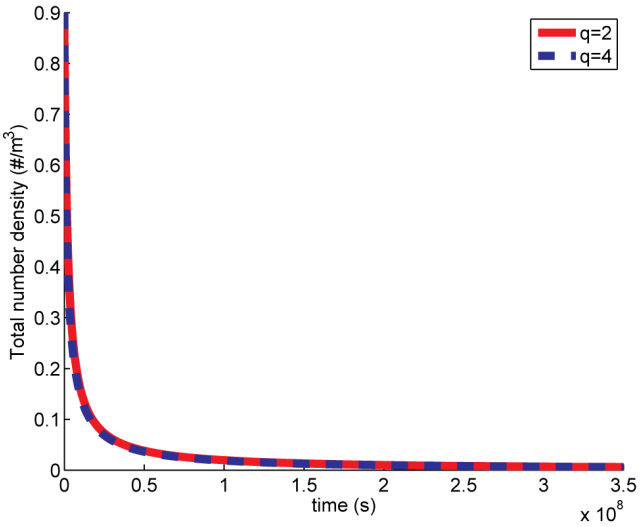

Figure B.1: Comparison between total bubble number density obtained by fine (solid line) and coarse (dashed line) discretization.

As seen from figure B.1, the evolution of the coarse distribution is only slightly enhanced compared to the fine one, with an average difference of 3% for intermediate times shown in the figure. Both distributions neccesarily approach the same asymptotic value of $n_1/256$, but again at slightly different times. Figure B.2a shows a comparison between the mass contained in the final bubble class. Evidently, the difference is larger than for the total number density and the accumulation in the largest bin is significantly faster for the coarse distribution.

The reason for this apparent discrepancy is that the largest class in the $q = 4$ class actually covers 80% of the *second* largest class in the $q = 2$ distribution (in addition to the largest

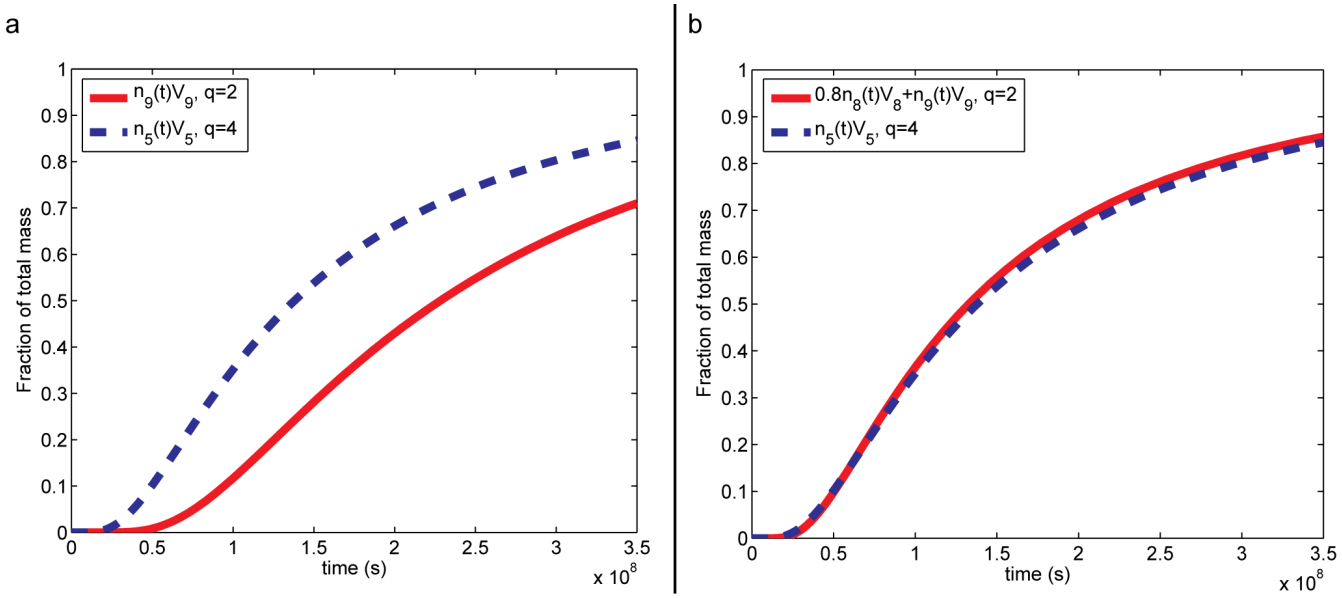

Figure B.2: Comparison between total mass in final bin (a) and equivalent bins (b) obtained by fine (solid line) and coarse (dashed line) discretization.

class, cf. figure 14.13). Figure B.2b shows a comparison of the mass in the largest bin for the coarse case to the corresponding mass distribution in the fine case, i.e. $0.8n_8V_8 + n_9V_9$. The difference between the two cases is comparable to that of the total number density (figure B.1).

The uncertainties related to discretization are considered to be negligible in the case of a constant coalescence kernel, as it is of a smaller magnitude than the sensitivity of the coalescence kernel itself.

B.2 Evolution by coalescence with physical kernel

For the next case, consider a physical kernel on the form

$$\Gamma_{ij} = \Omega_{ij} P_{ij}^{C}, \tag{B.1}$$

where the coalescence probability is set to unity and the collision frequency of Luo [79] (equation 14.58) is chosen for comparison. The turbulent dissipation rate is set to unity for all cases. With a physical coalescence kernel, the bubble diameter is coupled directly to the collision frequency and the effect of enhanced evolution is expected to be stronger than in the constant kernel case. In figure B.3a, the total number density is compared using a fine and coarse distribution.

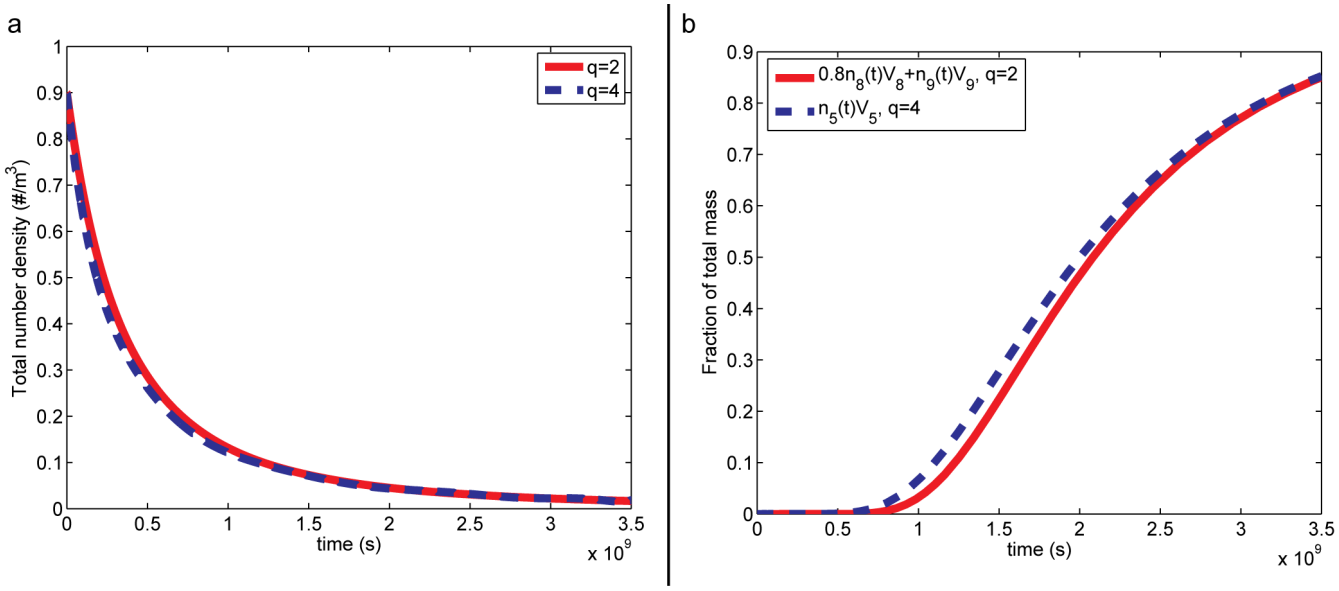

Figure B.3: Comparison between total bubble number density (a) and total mass in final class (dashed line) and its equivalent (solid line) (b) obtained by fine (solid line) and coarse (dashed line) discretization.

The mean average difference between the two discretizations is 6%, which is higher than the sensitivity on the value of ϵ_t (cf. equation 14.58), which results in an average difference of 2% with an change of 10%. The mean average difference between the total mass present in the final class with the coarse- and fine discretization is 3%.

B.3 Evolution by mass transfer

Finally, consider a population evolving due to mass transfer from a reservoir with constant saturation $\Delta C = 0.1$ kg/m^3. The proportionality coefficient, K_2 is assumed to be $2.3{\cdot}10^{-6}$ m^5/(kg·s). In such a system, the total number of bubbles is constant, but the total mass (for the bubbles) increases as long as the surrounding fluid is supersaturated. As ΔC is constant in this case, the population will evolve until it reaches a total mass of $256n_1(0)V_1$. Figure B.4a shows a comparison between the total mass attained by coarse and fine discretizations, while figure B.4b shows the fraction of the maximal attainable mass present in the largest bubble class (for the coarse distribution) and its equivalent for the fine distribution.

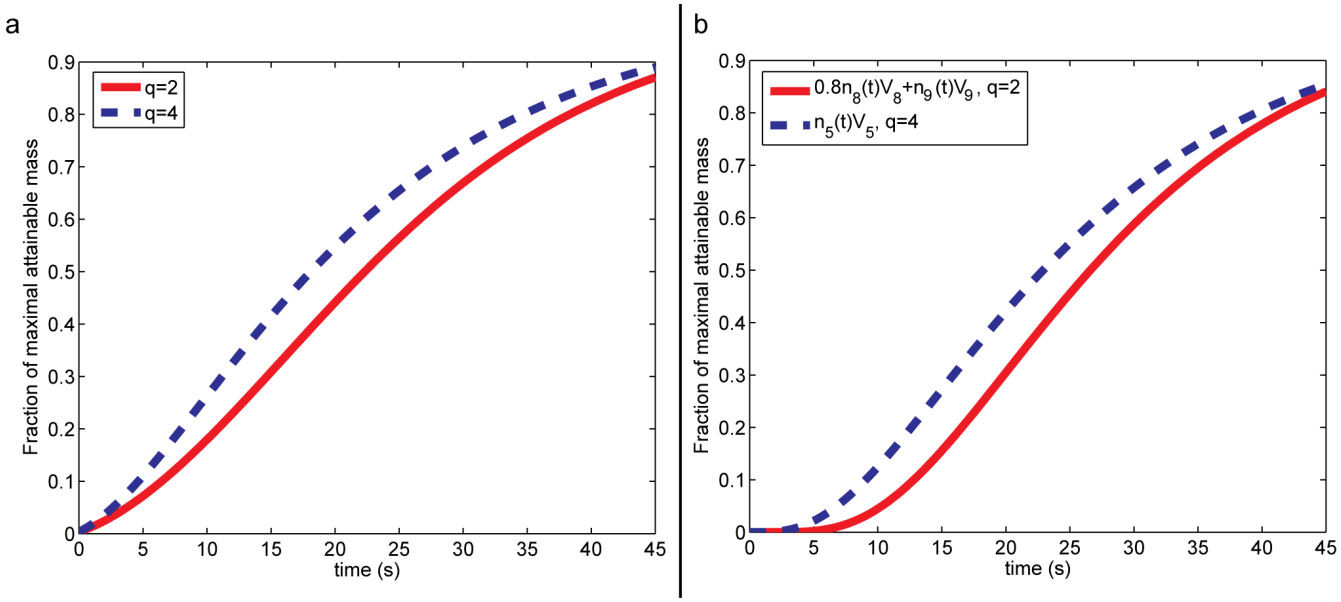

Figure B.4: Comparison between total mass, $\Sigma n_i V_i/256n_1(0)V_1$, (a) and total mass in final class, $n_M V_M/256n_1(0)V_1$, (dashed line) and its equivalent (solid line) (b) obtained by fine (solid line) and coarse (dashed line) discretization.

As seen from the above figures, the coarse distribution is accelerated compared to the fine one, with mean average difference of 10%. This is comparable to the sensitivity of the coefficient K_2; a 10% change resulting in a 7% average difference.

B.4 Closing remarks regarding acceleration

As seen from the above cases, a coarse distribution does indeed lead to an artificial enhanced evolution of the population towards the largest classes. The effect is however significantly smaller than that found by Outsuki et al. [89]. The effect is larger, the stronger the

governing equations are coupled to the discretization. Changing the discretization from $q = 2$ to $q = 4$ changes the solution by 10% in the case of mass transfer. Compared to the large uncertainty in the mass transfer coefficient, the error introduced by a coarse distribution can be neglected.